



HAL
open science

Design of tunnels using the hyperstatic reaction method

Dianchun Du

► **To cite this version:**

Dianchun Du. Design of tunnels using the hyperstatic reaction method. Chemical and Process Engineering. Université Grenoble Alpes, 2019. English. NNT : 2019GREAI063 . tel-02452288

HAL Id: tel-02452288

<https://theses.hal.science/tel-02452288>

Submitted on 23 Jan 2020

HAL is a multi-disciplinary open access archive for the deposit and dissemination of scientific research documents, whether they are published or not. The documents may come from teaching and research institutions in France or abroad, or from public or private research centers.

L'archive ouverte pluridisciplinaire **HAL**, est destinée au dépôt et à la diffusion de documents scientifiques de niveau recherche, publiés ou non, émanant des établissements d'enseignement et de recherche français ou étrangers, des laboratoires publics ou privés.

THÈSE

Pour obtenir le grade de

DOCTEUR DE LA COMMUNAUTE UNIVERSITE GRENOBLE ALPES

Spécialité : **IMPE2/Matériaux, Mécanique, Génie civil,
Electrochimie**

Arrêté ministériel : 25 mai 2016

Présentée par

Dianchun DU

Thèse dirigée par **Daniel DIAS**
et codirigée par **Ngocanh DO**

préparée au sein du **Laboratoire Sols, Solides,
Structures et Risques**
dans l'**École Doctorale I-MEP2 - Ingénierie - Matériaux,
Mécanique, Environnement, Energétique, Procédés,
Production**

**Conception de tunnels au moyen de la méthode
hyperstatique aux coefficients de réaction**

**Design of tunnels using the Hyperstatic Reaction
Method**

Thèse soutenue publiquement le **7 Novembre 2019**,
devant le jury composé de :

M. Pierpaolo ORESTE

Président du jury, Professeur à Politecnico di Torino-Italie

M. Richard GIOT

Rapporteur du jury, Professeur à Université de Poitiers

M. Hussein MROUEH

Rapporteur du jury, Professeur à Université Lille 1

M. Daniel DIAS

Directeur de thèse, Professeur à Université Grenoble Alpes

Mme Orianne JENCK

Examineur, Professeur Assistant à Université Grenoble Alpes

M. Ngocanh DO

Co-directeur de thèse, Professeur à Hanoi Université de Mining et
Geology



Design of Tunnels using the Hyperstatic Reaction Method

ACKNOWLEDGEMENTS

Firstly, I would like to thank my supervisors, Professor Daniel Dias and Professor Ngocanh Do. Their professional guidance and willingness are crucial to the completion of this thesis. They are very supportive and give me a lot of advices during the period of this work. They push me to achieve my full potential. I wish to express my sincere appreciation of their help. Three years of my PhD study under their supervisions will be unforgettable experience in my life.

I would like to thank the Laboratory 3SR for offering me a good research environment and every colleague at this lab for their help during these three years. They give me a good memory in Grenoble and I am so proud of being one of them.

The financial support from China Scholarship Council is gratefully acknowledged.

Finally, I am deeply indebted to my family who made this research possible by their unconditional support, patience and love. Special gratefulness goes to my parents, my wife and her parents, and my daughter for their endless love and infinite understanding. This research would never have been completed without their support and this thesis belongs to them.

CONTENTS

ACKNOWLEDGEMENTS	I
CONTENTS	II
LIST OF FIGURES	V
LIST OF TABLES	X
ABSTRACT	XI
RÉSUMÉ.....	XII
GENERAL INTRODUCTION	1
CHAPTER 1 LITERATURE VIEW	5
1. Procedure for tunnel lining design	6
2. Effect of tunnel shape on the lining behaviour	7
3. Design methods of non-circular tunnels	17
3.1 Experimental studies	17
3.2 Theoretical and analytical methods	28
3.3 Numerical analysis methods.....	33
4. Conclusions	48
CHAPTER 2 BEHAVIOUR ANALYSIS OF U-SHAPED TUNNEL SUPPORTS (WITH INVERT).....	50
1. Mathematical expression of hyperstatic reaction method	52
1.1 Ground-support interaction.....	56
1.2 Active loads.....	57
2. Calculation code and the dimensioning of support	58
3. Validation of the HRM method	62
4. Parametric analysis and design figures	65
5. Conclusions	70
CHAPTER 3 BEHAVIOUR OF TWO DIFFERENT U-SHAPED TUNNEL LININGS (WITH AND WITHOUT INVERT)	72
1. Introduction	72

2. Validation of the HRM method for a U-shaped tunnel without invert arch	74
2.1 Calculation code and the dimensioning of the support.....	74
2.2 Validation of the HRM method for a U-shaped tunnel without invert arch.....	79
3. Results and parametric analysis for U-shaped tunnel without invert arch	83
4. Conclusions	89
CHAPTER 4 EFFECT OF MULTI-LAYERED SOILS ON THE DESIGN OF TWO KINDS OF U-SHAPED TUNNEL LININGS	
	90
1. Introduction	90
2. Tunnel design models	92
3. Estimation the performance of the HRM Method	96
4. Results and parametric analysis	98
4.1. One soil (constant parameters)	98
4.2. One soil with a linear cohesion variation with depth	100
4.3. Two-layered soil (contact surface located at the spring line of tunnel).....	103
4.4. Three-layered soil.....	104
5. Conclusions	108
CHAPTER 5 EFFECT OF A SURCHARGE LOADING ON HORSESHOE SHPAED TUNNELS EXCAVATED IN SATURATED GROUND.....	
	109
1. Introduction	109
2. Design model of tunnel and validation	112
2.1 Design model of tunnel	113
2.2 Validation of the HRM method	114
3. Results analysis of the parametric studies	116
4. Conclusions	122
CHAPTER 6 OPTIMIZATION OF SUB-RECTANGULAR TUNNEL USING HYPERSTATIC REACTION METHOD.....	
	124
1. Introduction	124
2. Optimization of sub-rectangular tunnel shape	125
2.1 Determining the static area of a sub-rectangular tunnel and establishing optimizing procedure	125

2.2 Reference case	130
3. Parametric analyses	133
3.1 Effect of the tunnel depth on the lining forces and on the sub-rectangular tunnel shapes	134
3.2 Effect of coefficient of lateral earth pressure on internal forces and shape of sub-rectangular tunnel	137
3.3 Effect of Young's modulus E_s of soil on internal forces and shape of sub-rectangular tunnel	141
3.4 Effect of surface loads on internal forces and shape of sub-rectangular tunnel	143
4. Conclusions	147
CHAPTER 7 THERMO-MECHANICAL BEHAVIOUR OF TUNNELS	149
1. Introduction	149
2. Hyperstatic reaction method considering the temperature	150
2.1 Additional thermal loads	151
3. Effect of the temperature change on the tunnel lining forces	155
3.1 Considering only the additional thermal loads of lining	155
3.2 Considering the additional thermal loads of the soil mass and lining	157
3.3 Effect of other factors on the tunnel lining forces	158
4. Effect of a fire on the tunnel lining forces	162
4.1 Effect of a fire on the lining elastic modulus.....	163
4.2 Effect of a fire on the tunnel lining forces	163
5. Conclusions	166
GENERAL CONCLUSIONS	168
REFERENCES	172

LIST OF FIGURES

Fig. 1-1 Flow chart of tunnel lining design (ITA-Group2, 2000).....	7
Fig. 1-2 Effect of tunnel shape on the stresses of lining (Shin et al., 2005)	8
Fig. 1-3 Shape and dimensions of the tunnel cross-section (González-Nicieza et al., 2008)	9
Fig. 1-4 Radial displacement vs. distance x from working face (González-Nicieza et al., 2008)	9
Fig. 1-5 Convergence $u_R(\theta)$ for the three types of tunnel at depth of 250m (González-Nicieza et al., 2008).....	9
Fig. 1-6 Typical tunnel cross sections (Yoon et al., 2014)	10
Fig. 1-7 Normal force for each tunnel shape (Yoon et al., 2014).....	11
Fig. 1-8 Lining bending moment for each tunnel shape (Yoon et al., 2014)	12
Fig. 1-9 Lining stresses for each tunnel shape (Yoon et al., 2014).....	13
Fig. 1-10 Lining Deformation for Each Tunnel Shape (Yoon et al., 2014).....	13
Fig. 1-11 Layout of different shape of twin tunnels (Eman et al., 2013).....	14
Fig. 1-12 Finite elements mesh of different shape of twin tunnels (Eman et al., 2013)	14
Fig. 1-13 Distribution of the bending moment M in the different shapes of tunnels at D=8 m, t/r =0.1(Eman et al., 2013)	14
Fig. 1-14 Distribution of normal forces N in the different shapes of tunnels at D=8 m, t/r=0.1(Eman et al., 2013).....	15
Fig. 1-15 Distribution of shear forces S in the different shapes of tunnels at D=8 m, t/r=0.1 (Eman et al., 2013)	15
Fig. 1-16 Effect of the change in the diameter (D) on the bending moment at upper crown point of the tunnels (cr) at different t/r ratios (Eman et al., 2013).....	15
Fig. 1-17 Effect of the change in the thickness-radius ratios (T/R) on the normal force at the upper crown point of the tunnel (cr) at different diameters (Eman et al., 2013)	16
Fig. 1-18 Lining structures in section (Nakamura et al., 2003)	17
Fig. 1-19 Results of loading tests on composite segments (Nakamura et al., 2003).....	18
Fig. 1-20 Results of loading tests on DC segments (unsymmetrical pressure load) (Nakamura et al., 2003)	18
Fig. 1-21 Structure layout of the testing segmental lining (Huang et al., 2018)	19
Fig. 1-22 Measured internal forces distribution (Huang et al., 2018).....	20
Fig. 1-23 Measured overall deformation of middle lining ring (black line is the original segmental outline) (Huang et al., 2018).....	21
Fig. 1-24 Schematic diagram of test tunnel ring (a) and division of load points (b) (Liu et al., 2018).....	22
Fig. 1-25 Load-convergence deformation of long axis curves of three test rings (Liu et al., 2018).....	22
Fig. 1-26 Comparison of load-convergence deformation curves of three test rings (Liu et al., 2018)	23
Fig. 1-27 Load-rebar strain of inner and outer side of two rings (Liu et al., 2018)	24
Fig. 1-28 Size of the inside segment and the outside shield (Ding et al., 2019)	24
Fig. 1-29 Arrangement diagram of grouting pressure gauges in the steel segment (Ding et al., 2019).....	25
Fig. 1-30 Distribution of grouting pressure ground the segment lining in the toroidal direction (Ding et al., 2019)	25
Fig. 1-31 Pressure curves around the steel segments (Ding et al., 2019)	26
Fig. 1-32 Measuring points layout of the layered settlement test (Ding et al., 2019).....	26
Fig. 1-33 Settlement curves of A1 in Section A and B5 in Section B (Ding et al., 2019).....	27
Fig. 1-34 Total settlement curves of Section A (a) and Section B (b) at 15:00 on 27/ 10/2015 (mm) (Ding et al., 2019) .	27
Fig. 1-35 Toulon (left) and Pech–Brunet (right) tunnels (Oreste and Dias, 2012)	29

Fig. 1-36 Discretization technique for the collapse mechanism of a non-circular tunnel (Pan and Dias, 2017)	30
Fig. 1-37 Safety factor as a function of the ratio L/H (Pan and Dias, 2017)	31
Fig. 1-38 Failure mechanism generated by the discrete technique (Du et al., 2018).....	32
Fig. 1-39 Numerical methods and models for tunnel engineering (ÜÇER, 2006).....	33
Fig. 1-40 Tunnel Geometry and loading conditions (Leca and Clough, 1992)	34
Fig. 1-41 Influence of softening factor on liner bending moment (Leca and Clough, 1992)	34
Fig. 1-42 A finite domain for the design of optimal reinforcements (Yin and Yang, 2000)	36
Fig. 1-43 Rock strata surrounding the tunnel (Yin and Yang, 2000).....	36
Fig. 1-44 Optimal distribution of reinforcing material for the passive loading case (Yin and Yang, 2000)	37
Fig. 1-45 Optimal distribution of reinforcing material for the active loading case (Yin and Yang, 2000).....	37
Fig. 1-46 Deformations of the tunnel profiles under the initial and the optimal designs for the passive loading case (Yin and Yang, 2000).....	38
Fig. 1-47 Deformations of the tunnel profiles under the initial and the optimal designs for the active loading case (Yin and Yang, 2000).....	38
Fig. 1-48 Detail of the mesh of the numerical method developed to study the illustrated example (Oreste, 2003)	39
Fig. 1-49 Final vertical displacements for case (a) of the illustrated example (Oreste, 2003).....	39
Fig. 1-50 Layout of the model, horizontal (q_h) and vertical loads (q_v) and node numbers (R = 5.75 m) (Barpi et al., 2011)	40
Fig. 1-51 Membership functions for K_n , K_t and E_s for case 1 (a, c, e) and case 2 (b, d, f); μ means the grade of membership (Barpi et al., 2011)	41
Fig. 1-52 Bending moment vs. normal force for shotcrete (a) and steel ribs (b) (case 1) (Barpi et al., 2011).....	42
Fig. 1-53 Bending moment vs. normal force for shotcrete (a) and steel ribs (b) (case 2) (Barpi et al., 2011).....	42
Fig. 1-54 Cross-section of the FLAC tunnel model with displacement and fluid flow boundary conditions (Prasetyo and Gutierrez, 2016).....	43
Fig. 1-55 Plots of inward radial displacements around the tunnel boundary after surface loading in both cases (Prasetyo and Gutierrez, 2016)	44
Fig. 1-56 Plots of normal force for (a) clay and (b) granite in Case 1 at both states (Prasetyo and Gutierrez, 2016)	44
Fig. 1-57 Plots of the induced bending moment in the liner (a, b) after surface loading and (c, d) at the steady-state in both cases (Prasetyo and Gutierrez, 2016)	45
Fig. 1-58 Comparison of the liner interaction diagrams (Prasetyo and Gutierrez, 2016).....	46
Fig. 1-59 (a) Structure design of the front tunnel; (b) stress distribution of the front tunnel; (c) deformation of the front tunnel; (d) optimized structure of the front tunnel; (e) stress distribution of the optimized front tunnel; (f) deformation of the optimized front tunnel (Li, 2017).....	47
Fig. 2-1 Calculation scheme of U-shaped support structures with the HRM	51
Fig. 2-2 Scheme of the behaviour of a beam-type finite element with reference to the local Cartesian coordinates	52
Fig. 2-3 Scheme of the ground–support interaction through springs connected to the support nodes.....	53
Fig. 2-4 Relationship between reaction pressure p and support deformation δ	56
Fig. 2-5 Support geometry considered in the HRM calculation code.....	59
Fig. 2-6 Type of constraint foreseen (vertical clamped-roller) for the initial node and final node of geometry.....	59
Fig. 2-7 Positive direction of the structural forces and displacements	59

Fig. 2-8 Comparisons of results obtained from the calculation for the two cases of loads.....	60
Fig. 2-9 Bending moments with the cover-to-diameter ratio C/D	62
Fig. 2-10 Numerical geometry model considered in the analysis.....	63
Fig. 2-11 Two-dimensional numerical mode (a) and U-shaped tunnel (b).....	63
Fig. 2-12 Displacements of the tunnel support, comparison between the HRM and the FLAC ^{3D} model.....	64
Fig. 2-13 Structural forces in the tunnel support, comparison between the HRM and FLAC ^{3D} model.....	65
Fig. 2-14 Behaviour of the tunnel support considering the tunnel dimensions, support thickness and reduction factor of rigidity, η , (Ground type B - case 3) at the tunnel invert arch	67
Fig. 2-15 Behaviour of the tunnel support considering the tunnel dimensions, support thickness and reduction factor of rigidity, η , (Ground type B - case 3) at the tunnel sidewall	68
Fig. 2-16 Behaviour of the tunnel support considering the tunnel dimensions, support thickness and reduction factor of rigidity, η , (Ground type B - case 3) at the tunnel crown.....	69
Fig. 3-1 Calculation scheme of two different U-shaped support structures with the HRM.....	73
Fig. 3-2 Support geometries considered in the HRM calculation codes.....	75
Fig. 3-3 Type of constraints.....	75
Fig. 3-4 Comparisons of results obtained from two different U-shaped tunnels with only normal springs and normal springs plus shear springs	77
Fig. 3-5 Effect of constraint conditions on the tunnel lining behaviour of Geometry2	78
Fig. 3-6 Comparisons of the results between circular and two different U-shaped tunnels obtained by the HRM	79
Fig. 3-7 Numerical geometry model of the U-shaped tunnel without invert arch	80
Fig. 3-8 Numerical model.....	81
Fig. 3-9 Comparison of structural forces and displacements in the U-shaped tunnel support (Geometry2 in Fig.3) between the HRM and FLAC ^{3D} modelt	83
Fig. 3-10 Structural forces and displacement (Case1)	85
Fig. 3-11 Structural forces and displacement (Case3).....	86
Fig. 3-12 Structural forces and displacement (Case5).....	87
Fig. 3-13 Structural forces and displacement (Case7).....	88
Fig. 4-1 Two different U-shaped tunnel linings	91
Fig. 4-2 Support geometries considered in the analysis	92
Fig. 4-3 Layered soil cases of U-shaped tunnel with invert arch.....	95
Fig. 4-4 Numerical geometry model of U-shaped tunnel with invert arch	96
Fig. 4-5 Numerical model in FLAC ^{3D}	96
Fig. 4-6 Comparisons of internal forces and displacements in the U-shaped tunnel support	97
Fig. 4-7 Comparisons of the HRM results between two different U-shaped tunnels	99
Fig. 4-8 Effect of constraint types on the tunnel lining behaviour of Geometry2	100
Fig. 4-9 Comparisons of the HRM results between two different U-shaped tunnels of cases 1 and 2	101
Fig. 4-10 Effect of constraint conditions on the tunnel lining behaviour of Geometry2	102
Fig. 4-11 Comparisons of the HRM results of Geometry2 under the cases 1 and 2.....	102
Fig. 4-12 Comparisons of the HRM results between two different U-shaped tunnels	103

Fig. 4-13 Effect of constraint types on the tunnel lining behaviour of Geometry2	104
Fig. 4-14 Comparisons of the HRM results between two different U-shaped tunnels	105
Fig. 4-15 Effect of constraint types on the tunnel lining behaviour of Geometry2	106
Fig. 4-16 Effect of the position and thickness of layer2 on the tunnel lining behaviour of Geometry1	107
Fig. 5-1 Schematic diagram for a horseshoe shaped tunnel lining	110
Fig. 5-2 Pore water pressure	111
Fig. 5-3 Cross-section of the numerical adopted model with the adopted boundary conditions	112
Fig. 5-4 Numerical model in FLAC ^{3D}	114
Fig. 5-5 Location θ (degrees).....	114
Fig. 5-6 Comparison of structural forces and displacements between the HRM and numerical model	116
Fig. 5-7 Behaviour of tunnel lining considering and without considering the pore water pressure.....	117
Fig. 5-8 Behaviour of tunnel lining when considering both the surcharge loading P_0 and the pore pressure.....	118
Fig. 5-9 Behaviour of tunnel lining when considering only the surcharge loading	120
Fig. 5-10 Effect of the surcharge load width on the tunnel behaviour without considering the pore water pressure	121
Fig. 5-11 Effect of phreatic surface position on tunnel behaviour.....	122
Fig. 6-1 An illustrate of sub-rectangular support structures in the HRM method	125
Fig. 6-2 Tunnel construction clearance (mm) of twin lanes metro tunnels	126
Fig. 6-3 Simplified considered tunnels	127
Fig. 6-4 Entire tunnel lining obtained by optimization.....	127
Fig. 6-5 Optimization procedure of sub-rectangular tunnels	130
Fig. 6-6 Schematic diagram of sub-rectangular and soil parameters in the optimization	131
Fig. 6-7 Numerical model as $C=5D_0$	132
Fig. 6-8 Effect of tunnel depth C on the internal forces of sub-rectangular tunnel obtained by FLAC ^{3D} and HRM.....	133
Fig. 6-9 Effect of tunnel depth C on the Maximum internal forces obtained by HRM	134
Fig. 6-10 Effect of the tunnel depth C on the minimum M_{max} value and on the sub-rectangular tunnel shape.....	135
Fig. 6-11 Optimum sub-rectangular tunnel shapes and internal forces as $C=D_0$ and $C=30D_0$, respectively.	136
Fig. 6-12 Comparison between the results of HRM and FLAC ^{3D} in terms of bending moments and normal forces along the whole tunnel for the case of $C/D_0=5$	137
Fig. 6-13 Internal forces of sub-rectangular tunnel considering different K_0	138
Fig. 6-14 Effect of K_0 on minimum M_{max} and sub-rectangular tunnel shape	139
Fig. 6-15 Optimum sub-rectangular tunnel shapes and internal forces as $K_0=0.25$ and $K_0=1.5$, respectively.....	140
Fig. 6-16 Effect of Young's modulus E_s of soil on the Maximum internal forces	141
Fig. 6-17 Effect of Young's modulus E_s of soil on minimum M_{max} and sub-rectangular tunnel shape	142
Fig. 6-18 Optimum sub-rectangular tunnel shapes and internal forces as $E_s=10$ MPa and $E_s=200$ MPa, respectively	143
Fig. 6-19 Effect of Surface loads on the Maximum internal forces considering different C	145
Fig. 6-20 Distributions of bending moment considering different surface loads when $C/D_0=5$	146
Fig. 6-21 Distributions of normal force considering different surface loads when $C/D_0=5$	146

Fig. 7-1 Simplified structure of circular tunnel considering additional thermal loads caused by the temperature change in the HRM method	151
Fig. 7-2 Positive direction of the structural forces (bending moment M, normal force N)	154
Fig. 7-3 Effect of the temperature change on the incremental tunnel lining forces when only considering the additional lining thermal loads	157
Fig. 7-4 Effect of the temperature change on the tunnel lining forces of when considering the additional thermal loads of the soil mass and lining	158
Fig. 7-5 Effect of the temperature change on the tunnel lining forces at the tunnel crown while considering the lining thickness	160
Fig. 7-6 Effect of the temperature change on the tunnel lining forces at the tunnel crown considering different elastic modulus of lining	161
Fig. 7-7 Effect of the temperature change on the tunnel lining forces at the tunnel crown while considering different soil coefficients of thermal expansion	162
Fig. 7-8 Young's modulus lining used in analysis (Aslani and Samali, 2014)	163
Fig. 7-9 Effect of the temperature change on the tunnel lining forces at the tunnel crown considering different coefficient of thermal expansion.....	165
Fig. 7-10 Temperature-time ETK/ISO curve (Kaundinya, 2006).....	166

LIST OF TABLES

Table 1-1 Obtained safety factors for Toulon’s tunnel (Pan and Dias, 2017)	30
Table 1-2 Comparison of earth pressure q (kPa) (Du et al., 2018).....	32
Table 2-1 Geometric parameters of the Toulon tunnel	60
Table 2-2 Details of the cases adopted for the parametric analyses	66
Table 3-1 Geometric parameters of the Toulon tunnel (Oreste and Dias, 2012).....	76
Table 3-2 Details of the cases adopted for the parametric analyses	83
Table 4-1 Tunnel parameters used in this chapter	92
Table 4-2 Soil mass properties	93
Table 5-1 Tunnel parameters	113
Table 6-1 Comparison of internal forces of HRM and FLAC considering different tunnel depth C in terms of normal forces (T) and bending moment (M).....	133
Table 6-2 Optimum internal forces considering different tunnel depth C obtained by present method.....	137
Table 6-3 Optimum internal forces considering different K_0	140
Table 6-4 Optimum internal forces considering different Young’s modulus of soil E_s	142
Table 6-5 Effect of surface loads on internal forces and shape of sub-rectangular tunnel considering different C	145
Table 7-1 Properties of the materials used in Luo et al. (2010)	153
Table 7-2 Inner thermal forces of lining concrete (Luo et al. 2010)	153
Table 7-3 Properties of the materials used in the analysis	154

ABSTRACT

This research work aims to present the design of tunnel by means of the Hyperstatic Reaction Method (HRM). The models developed by the HRM method are firstly proposed for investigating the behaviour of U-shaped tunnels under different conditions, considering two load cases, two different geometries of U-shaped tunnel lining, two different cases of springs, change of the spring stiffness, multi-layered soil conditions, surcharge loading, and saturated soil masses. The presented models permit to obtain good predictions with a high computational efficiency in comparison to finite difference numerical modelling. Then a parametric analysis has permitted to estimate the U-shaped tunnel lining behaviour in a large number of cases which cover the conditions that are generally encountered in practice. Thereafter, taking a twin-lane metro tunnel as an example, a series of mathematical functions used in the optimization progress of sub-rectangular tunnel shape is deduced, which gives tunnel designers a theoretical support to choose the optimal sub-rectangular tunnel shape. The effect of different parameters, like the lateral earth pressure factor, soil Young's modulus, tunnel depth, surface loads, on the internal forces and shape of sub-rectangular tunnel is then given. In the last part of the manuscript, the influence of a temperature change on the lining forces of circular tunnel by means of the HRM method is investigated, considering different factors, such as the tunnel lining thickness, lining elastic modulus and ground coefficient of thermal expansion.

Keywords: tunnel design, hyperstatic reaction method, multi-layered soils, surcharge loading, saturated ground, optimization, sub-rectangular tunnel, thermo-mechanical behaviour

RÉSUMÉ

Ce travail de recherche a pour objectif de présenter la conception de tunnels au moyen de la méthode hyperstatique aux coefficients de réaction (HRM). Les modèles développés par la méthode HRM sont tout d'abord proposés pour étudier le comportement de tunnels en forme de fer à cheval inversé dans différentes conditions, par exemple en considérant deux cas de charge, deux géométries différentes de revêtement de tunnel, deux cas de coefficients de réaction différents, changement de la rigidité des coefficients de réaction, conditions de sol multicouches, surcharges en surface et sol saturés. Les modèles présentés permettent d'aboutir à des prévisions qualitatives avec une efficacité de calcul élevée par rapport à la modélisation numérique en différences finies. Une analyse paramétrique est ensuite réalisée pour estimer le comportement du revêtement de tunnel en forme de fer à cheval dans un grand nombre de cas couvrant les conditions généralement rencontrés dans la pratique. Ensuite, en prenant comme exemple un tunnel métropolitain à deux voies, une série de fonctions mathématiques est déduite et utilisée dans le processus d'optimisation d'un tunnel de forme complexe, ce qui offre aux concepteurs de tunnels un support théorique leur permettant de choisir la forme optimale du tunnel à mettre en oeuvre. L'effet de différents paramètres, tels que le coefficient des terres au repos, le module d'Young du sol, la profondeur du tunnel, les surcharges en surface, sur les efforts internes et la forme du tunnel. Dans la dernière partie du manuscrit, l'influence d'un changement de température sur les efforts dans le revêtement d'un tunnel circulaire au moyen de la méthode HRM est étudiée en tenant compte de différents facteurs, tels que l'épaisseur du revêtement de tunnel, le module d'élasticité du revêtement et le coefficient de dilatation thermique du sol.

Mots-clés: conception de tunnels, méthode aux coefficients de réaction hyperstatique, sols multicouches, surcharges en surface, sol saturé, optimisation, tunnel de forme complexe, comportement thermo-mécanique

GENERAL INTRODUCTION

As civil engineering structures, tunnels are widely used in the construction of underground infrastructures. One of the most important issues in tunnel engineering is the appropriate tunnel lining design. The design of tunnels requires a proper estimate of lining forces and displacements. In engineering practice, different design methods tend to be used, varying from simple empirical and analytical formulations to advanced numerical analyses. Although tunnelling is a three-dimensional (3D) problem, the 3D models are computationally expensive and difficult to be built. The simplified two-dimensional (2D) models are therefore often used.

The behaviour analysis of tunnels presented in this manuscript is based on a 2D numerical approach named the hyperstatic reaction method (HRM). The HRM method was proposed and developed by some researchers ([Duddeck and Erdmann 1985](#); [Leca and Clough 1992](#); [Oreste 2007](#); [Do et al., 2014b, 2014d](#)). In this method, the interaction between the support and rock surrounding the tunnel is simulated through independent “Winkler” type springs. It is particularly suitable for the estimation of tunnel lining behaviour, in terms of structural forces and lining displacements along the support profile. Another advantage of the HRM method is the fact that it necessitates a short calculation time. Therefore, it can be extended to do the reliability analysis which requires a high number of deterministic calculations.

This thesis mainly focuses on the lining behaviour study of non-circular tunnels, like U-shaped tunnel and sub-rectangular tunnel, under different conditions. Besides, the behaviour of circular tunnel linings is also investigated considering the effect of temperature change using the present method. Since the HRM method was mainly used for the behaviour analysis of circular tunnel lining before, therefore and firstly, the developed models are extended to investigate the behaviour of U-shaped tunnels. The proposed models in this thesis are validated by the finite difference program $FLAC^{3D}$ in some cases. Moreover, as sub-rectangular tunnel cross-sections are increasingly used for underground engineering projects recently, this kind of geometry is also investigated. Actually, very limited studies have dealt with the design of this kind of non-circular tunnels. Therefore, a series of mathematical functions used in an optimization progress of sub-rectangular tunnel shapes are deduced, which gives tunnel designers a theoretical support to choose the optimal sub-rectangular tunnel shape. Lastly, the attention is given to thermal stresses in circular tunnels

caused by temperature change. Thermal stresses generated by temperature change may cause cracking and damage to the lining and surrounding ground. In the case of large enough thermal stresses, e.g. when caused by fire, they can be a major factor to the damage of tunnels. So the influence of temperature change on the lining forces of circular tunnel by means of the HRM method is investigated. This thesis is organized in seven chapters as follows:

The first chapter presents a literature review on the design methods of non-circular tunnels. The procedure of tunnel lining design is firstly introduced. Then the tunnel shape effect on the lining behaviour is summarized. Lastly, the tunnel design methods are presented, which include experimental studies, theoretical analytical methods and numerical analysis methods. The advantages and limitations of these methods are discussed.

The second chapter presents the 2D improved numerical approach to the HRM for the analysis of U-shaped tunnel supports. The mathematical expression in detail of the HRM in this chapter is given, which is also used in the following chapters. When the tunnels are located at shallow depth, e.g. the cover-to-diameter ratio $C/D < 2$, the gravity effect on the change in external loads acting on the tunnel lining could be significant and the vertical stress variation should be considered. Therefore, two cases of loads, constant loads and varying loads, are taken into consideration in this chapter.

The third chapter studies the behaviour of two different U-shaped tunnel linings (with and without invert arch). To investigate the difference of the results between two U-shaped tunnels and a circular tunnel, a comparison is made. The toe constraint conditions effect on the behaviour of U-shaped tunnel linings without invert arch is also studied. An extensive parametric analysis is presented to highlight the influence of different stiffness of the springs, different loads on the support, different geometries and different bending stiffness of the support structures on the structural forces and displacements.

In practical engineering, the tunnels are usually not excavated in only one homogeneous soil layer, but in multi-layered soils. Therefore, the fourth chapter aims to investigate the effect of multi-layered soils on the design U-shaped tunnel linings. Different stratified soil conditions are considered to investigate the U-shaped tunnel lining behaviour: one homogeneous layer, one layer with a linear cohesion with depth, two layers, and three layers considering a variation of the position and of the thickness of the intermediate layer. The results

of two different U-shaped tunnels are compared and analysed for these different stratified soils. In the case of a U-shaped tunnel without invert, the effect of the lining constraint conditions is also investigated.

Tunnels are popular in urban areas due to the development of modern societies. They are inevitably constructed under existing buildings or beneath the phreatic surface. In the fifth chapter, the surcharge loading effect on a horseshoe shaped tunnel excavated in saturated soil masses is investigated, in which the effects of different factors, such water pressure, surcharge loading, surcharge loading width and phreatic surface position, on the internal forces and displacements of tunnel lining are discussed.

Compared with a conventional circular cross-section tunnel, the sub-rectangular cross-section is more economic. In spite of this, there is no efficient way to design sub-rectangular tunnels. In the sixth chapter, the optimization process of sub-rectangular tunnels in terms of tunnel lining forces is presented using the HRM method. A series of mathematical functions considering the tunnel shape are deduced and the optimization of sub-rectangular tunnels shape is realized. The effect of different parameters, such as the lateral earth pressure factor, Young's modulus of soil, tunnel depth, surface loads on the internal forces and shape of sub-rectangular tunnel is then investigated.

During the service time of a tunnel, the temperature changes in the tunnel lining and in the surrounding ground. Thermal stresses generated by temperature change will induce the variation of the tunnel lining forces and displacements. In the last chapter of this manuscript, the HRM method is used to investigate the thermo-mechanical behaviour of a circular tunnel lining. The implementation of the thermal behaviour of the tunnel lining and surrounding mass is presented. The effective strain coefficient β_{Tl} of lining is deduced from the literature and used to calculate the effective lining thermal stresses combined with the mechanical ones. A parametric study is proposed to investigate the effect of temperature change on the tunnel lining internal forces by means of the present HRM method. Several factors are considered, such as the tunnel lining thickness, lining elastic modulus and ground coefficient of thermal expansion. Thereafter, the effect of fire on the tunnel lining forces is presented.

In conclusion, this thesis presents improved models to investigate the behaviour of U-shaped tunnel lining under different conditions. An optimization of the sub-rectangular tunnel shape and the effect of temperature change on the circular tunnel behaviour are presented. Based on the HRM method, parametric

analyses are developed to show the effect of different parameters of tunnel support and of ground mass on the tunnel behaviour.

CHAPTER 1 LITERATURE VIEW

The growth of urban populations and economic development in the last decades have triggered a rising demand for infrastructure construction within the context of a valuable and densely constructed urban space (Andre, 2004). On the one hand, it causes a serious shortage of urban land resources and the prominent conflict between the supply and demand of space. On the other hand, some urban problems come out, such as traffic congestion, pollution and noise nuisance. Underground space exploitation and utilization is a possible solution to these urban problems. Specially, tunnels become an important part of public underground infrastructure. Besides, tunnelling may be the most practical and effective way to cross the obstacles from mountains, rivers and seas during building roads or railways.

As civil engineering structures, tunnels are widely used in the construction of underground infrastructure for the purpose of securing space in the ground (Lanka, 2018), especially the use of non-circular tunnels is becoming popular in the urban areas over decades years. One of the most important issues for the construction of tunnels is the appropriate design of tunnel lining. However, there is no one method which can be used to precisely and effectively estimate the behaviour of non-circular tunnels in the preliminary design phase considering different design factors, e.g. ground load, underground water, stratified ground, types of soil, etc. Therefore, it is urgent to find an effective and efficient method which can be used to analyse the internal forces and displacement of non-circular tunnel lining in the tunnel design phase. The Hyperstatic Reaction Method (HRM), a numerical method, is particularly suitable for the estimation of tunnel lining behaviour, in terms of structural forces, and lining displacements along the support profile but with a short calculation time. Therefore, the target of this manuscript is the design of tunnel lining based on the HRM method, which focuses on the analysis of U-shaped tunnel behaviour in terms of the internal forces and displacement of lining under different conditions (Chapters 2-5), the optimization of sub-rectangular tunnel shape (Chapter 6) and the effect of temperature change on circular tunnel lining behaviour (Chapter 7).

The rest of this chapter is devoted to present an overview of relevant researches about the methods of non-circular tunnel design. The procedure of tunnel lining design is firstly introduced. Then effect of tunnel

shape on the lining behaviour is summarized. Lastly, the tunnel design methods are presented, which include the experimental studies, theoretical analytical methods and numerical analysis methods.

1. Procedure for tunnel lining design

According to [ITA-Group2 \(2000\)](#), the guidelines for the design of tunnel lining is summarized in detail as follows:

1) Referring to specifications, codes or standards. Tunnels should be designed on the basis of the appropriate specification standards, codes or standards, which are determined by the persons in charge of the project or decided by discussion between project managers and the designers.

2) Determining the inner dimension of tunnel. The inner diameter of the tunnel should be decided in consideration of the space that is demanded by the functions of the tunnel. The space can be determined by the traffic volume and number of lanes for the case of road tunnels; the discharge for the case of water tunnels and sewer tunnels.

3) Determining the load condition. The loads acting on the lining including earth pressure, water pressure, dead loads, surcharges and efforts due to the tunnel construction.

4) Determining the lining conditions. The lining conditions, like dimension of the lining (thickness), strength of material, arrangement of reinforcement, should be selected.

5) Computing the internal forces of lining. The internal forces such as bending moments, normal forces and shear forces of the lining should be computed by using appropriate models and design methods.

6) Checking the safety of lining. The safety of the lining should be checked against the computed internal forces.

7) Reviewing. If the designed lining is not safe against design loads or if the designed lining is safe but not economical, the lining conditions should be changed and the lining should be redesigned.

8) Approving the design. Once the designer judges that the designed lining is safe, economical and optimally design, the design could be approved by the persons who are in charge of the project.

Those steps are shown in Fig. 1-1 on a flow chart for designing tunnel lining. It can be found that the computation of forces of lining plays a key role in the tunnel design.

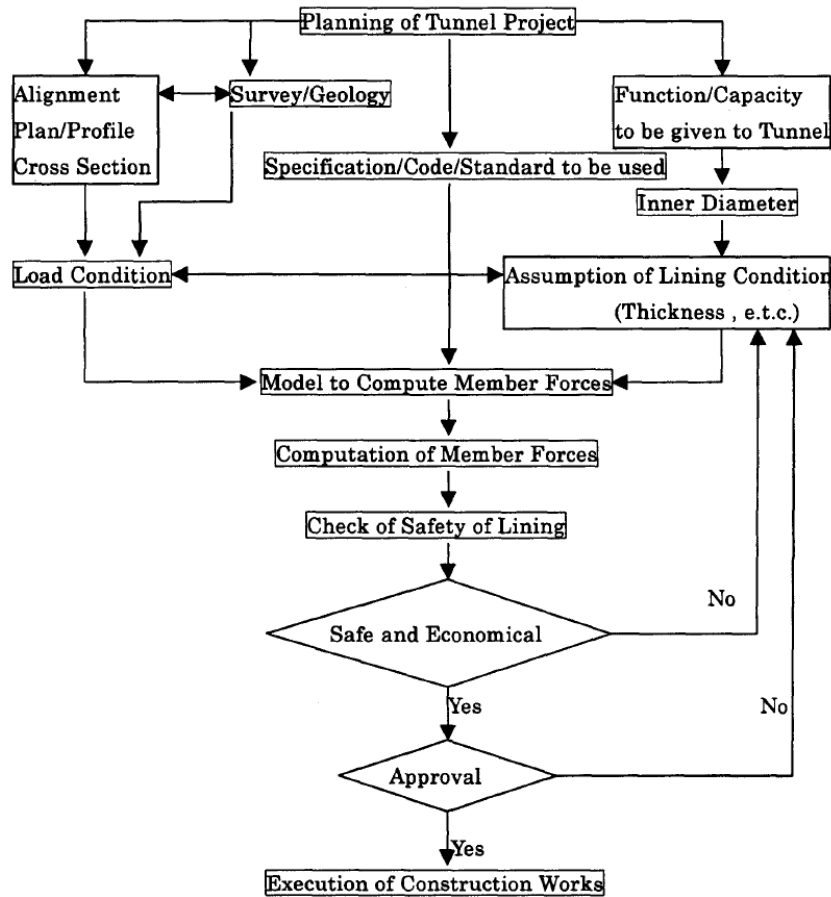


Fig. 1-1 Flow chart of tunnel lining design (ITA-Group2, 2000)

2. Effect of tunnel shape on the lining behaviour

The tunnel structures can be divided into two main types (British Tunnelling Society, 2001): 1. the flexural structure, e.g. rectangular tunnels, and 2. the compression structure, e.g. circular tunnels. In practice, a circular tunnel is usually adopted to avoid the generation of stress concentration and tensile stress in the lining. However, the conventional circular tunnel is unsuitable in some cases because a large amount of the excavated soil is required and lots of space is unutilized. In order to overcome these problems, the noncircular cross sections, e.g. horseshoe-shaped or sub-rectangular-shaped, are taken into consideration instead. Tunnel shapes have considerable influence on the lining behaviour. To investigate the mechanical behaviour of different kinds of tunnel shape, some studies have been done. Many authors have indicated that the active load may cause considerable bending moments in a noncircular tunnel, resulting in tensile stresses and a reduction in structural resistance (Peck, 1969; O'Rourke, 1984).

Shin et al. (2005) found that the tunnel shape is an important factor governing structural behaviour. They showed that although the active loads are applied as a constant tendency in the case of a horseshoe-shaped cross section, it causes the stress concentration because of an increase of bending moments at corners. To quantify the effect of tunnel shape, the lining behaviour analysis of an equivalent circular tunnel with the same cross-sectional area as that of the horseshoe-shaped tunnel was performed and the results were compared with those of the horseshoe-shaped tunnel. Geological conditions, tunnel depth, and all modelling methods were the same as those used for the horseshoe-shaped tunnel. Fig. 1-2 presents the distributions of maximum principal stress, assuming tension is positive, around the lining for both circular and horseshoe-shaped tunnels. It can be found that for the circular tunnel, the maximum principal stresses are everywhere compressive, whereas in the lower part of the tunnel wall of the horseshoe-shaped tunnel tensile stresses are observed. Also, the stress concentration occurs at corners of the horseshoe-shaped tunnel.

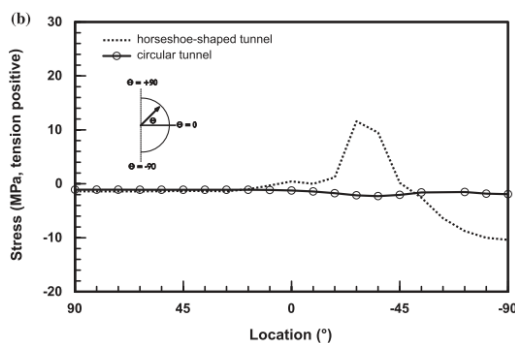


Fig. 1-2 Effect of tunnel shape on the stresses of lining (Shin et al., 2005)

González-Nicieza et al. (2008) proposed a modification of the convergence-confinement method (CCM) to investigate the influence of the shape of a tunnel on the radial displacements of the tunnel. An expression was established that enables the convergence to be determined as a function of the shape of the tunnel cross-section and of the point considered within the perimeter of the cross-section. Three typical tunnel cross-section shapes, circular (Type I), cart (Type II), U-shaped (Type III), were considered for the three-dimensional analysis using FLAC^{3D}. The dimensions of each type of tunnel are shown in Fig. 1-3 along with the origin of the angles.

The radial displacement curves were obtained as a function of the distance to the face x , at uniformly distributed points along the cross-section. Fig. 1-4 shows the calculated radial displacement, as a function of

the distance x to the face, registered in the floor and in the crown for a circular tunnel (Type I) and a cart tunnel (Type II).

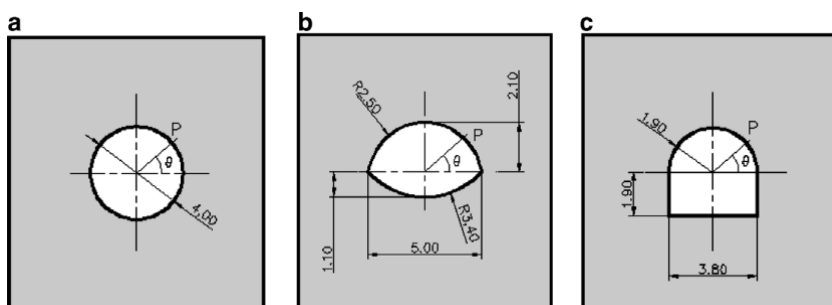


Fig. 1-3 Shape and dimensions of the tunnel cross-section. (a) Tunnel Type 1; (b) tunnel Type 2; (c) tunnel Type 3 (González-Nicieza et al., 2008)

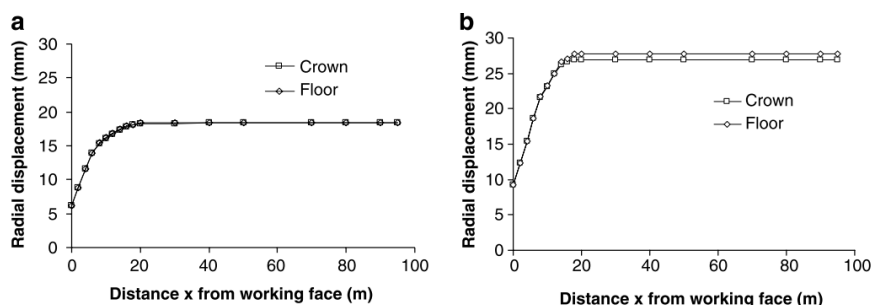


Fig. 1-4 Radial displacement vs. distance x from working face. (a) Type I tunnel; (b) Type II tunnel (González-Nicieza et al., 2008)

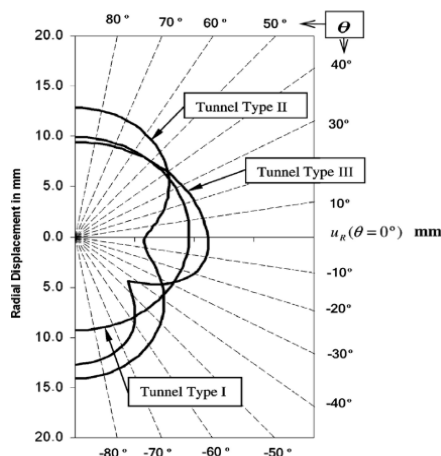


Fig. 1-5 Convergence $u_R(\theta)$ for the three types of tunnel at depth of 250m (González-Nicieza et al., 2008)

In Fig. 1-5, the displacements obtained in the three-dimensional modeling are compared for the three types of tunnel. It was shown that the radial displacements in the crown or in the side walls are significantly different for non-circular excavations, which decisively conditions the taking of decisions on tunnel stability.

Also, the radial displacements of non-circular shapes are much larger than those of circular tunnels. According to the general shape function of González-Nicieza et al. (2008), once the type of tunnel and the zone to be considered are established, the value of the radial displacement may be estimated.

Considering the water pressure, Yoon et al. (2014) investigated the effect of tunnel cross section on the lining behaviour using a coupled numerical analysis. Three typical tunnel cross sections, namely, circular, egg-shaped, and horse shoe-shaped, are considered, as shown in Fig. 1-6. Chosen architectural limits, which determine the scale of the tunnel’s cross section, are of a width of 9 m and a height of 4.8 m. To compare shape effect, shape factor (sf) which is defined as the ratio of height to width.

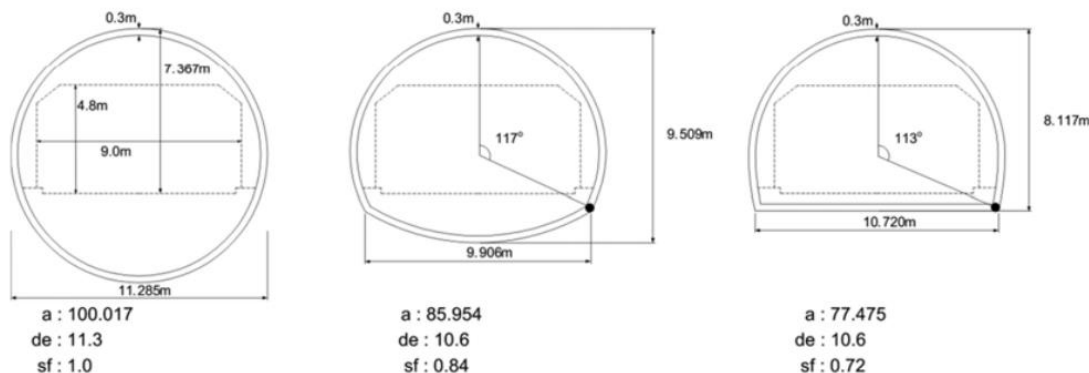
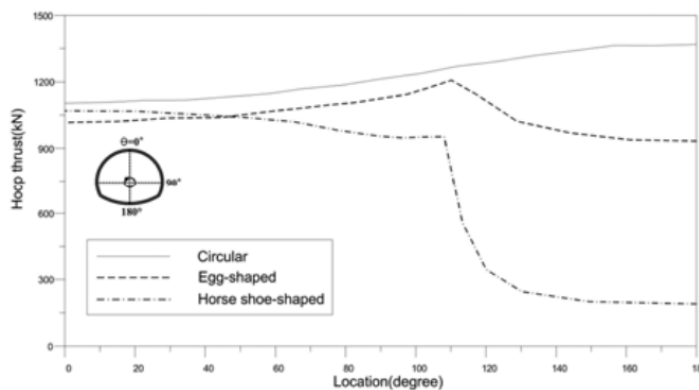
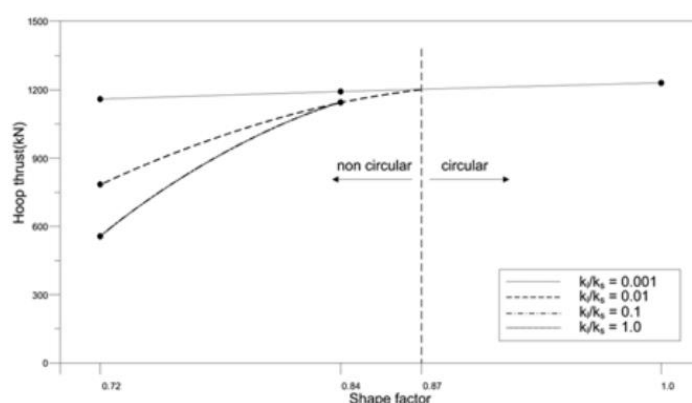


Fig. 1-6 Typical tunnel cross sections: (a) Circular, (b) Egg-shaped, (c) Horse shoe-shaped (a: Area (m²), de: Equivalent diameter (m), sf: Shape Factor (Height/Width)), (Yoon et al., 2014)

Fig. 1-7(a) shows the representative normal forces distribution for each tunnel shape. Although the influence of tunnel shapes on normal force from the crown to corners is not significant, significant changes occur at the corners and invert. Non-circular shapes have shown a considerably lower normal force at the invert. Fig. 1-7(b) shows the maximum normal forces around corners for each tunnel shape. In non-circular tunnels, hydraulic deterioration results in the increases of the maximum normal force. If the shape factor (sf) is higher than 0.87, the influence of hydraulic deterioration in maximum normal force can be neglected.



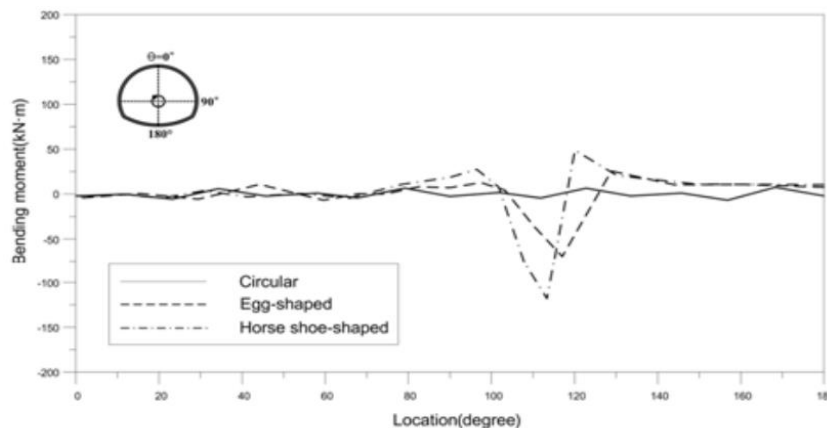
(a)



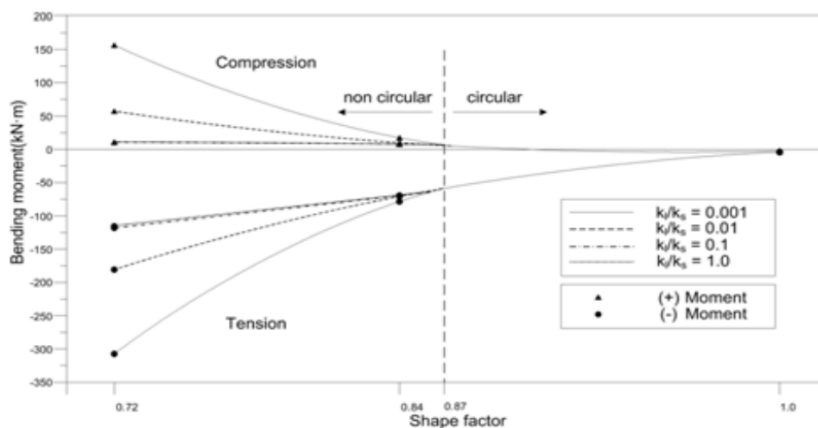
(b)

Fig. 1-7 Normal force for each tunnel shape: (a) Normal forces in lining ($k_l/k_s = 0.1$), (b) Maximum normal force (around corner). k_l and k_s are the permeability of lining and soil respectively, (Yoon et al., 2014)

The lining bending moment distribution for each cross section is shown in Fig. 1-8(a). In case of the circular shape, the bending moment is small and constant throughout the lining. The egg-shaped and horseshoe-shaped cross sections show drastic changes in bending moments from negative (-) to positive (+) values around corners. The minimum and maximum bending moment values around corners of the linings for each tunnel shape are shown Fig 1-8(b). The absolute values of the maximum bending moment increase with the pore water pressure resulting from hydraulic deterioration, especially in the cases of the non-circular tunnels. There is almost no influence of the relative permeability (k_l/k_s) on the bending moment when the shape factor (sf) is more than 0.87.



(a)

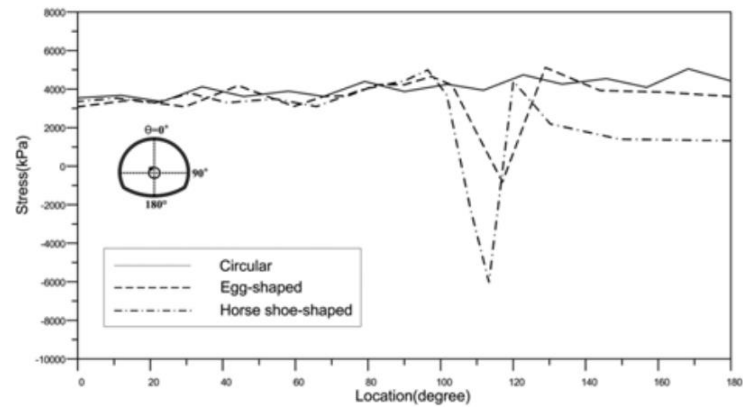


(b)

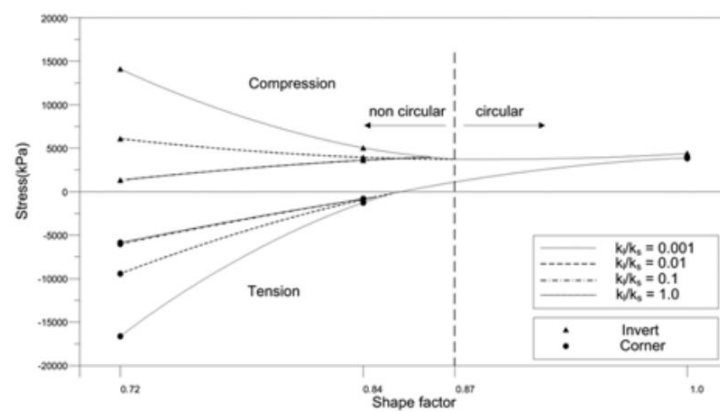
Fig. 1-8 Lining bending moment for each tunnel shape: (a) Lining bending moments ($k_1/k_s = 0.1$), (b) Maximum bending moments (around corner), (Yoon et al., 2014)

The lining stresses for each tunnel shape considering the combined effect of the normal force and bending moment are shown in Fig. 1-9(a). The circular tunnel shows no significant changes in the lining stress; however, the egg-shaped and horseshoe-shaped tunnels have shown high negative stresses, which imply tensile stress in the groundside around corners. This denotes structural weakness due to stress concentration around corners.

Fig. 1-9(b) shows the stresses at the corners and inverts with the progress of hydraulic deterioration for the tunnel cross sections. The influence of hydraulic deterioration is significant for non-circular shapes. In particular, the tensile stress increases significantly with hydraulic deterioration. For a shape factor higher than 0.87, or shapes close to the circular shape, there is almost no influence of hydraulic deterioration at the corner and the invert.



(a)



(b)

Fig. 1-9 Lining stresses for each tunnel shape: (a) Lining stresses ($k_i/k_s = 0.1$), (b) Maximum lining stresses (around corner), (Yoon et al., 2014)

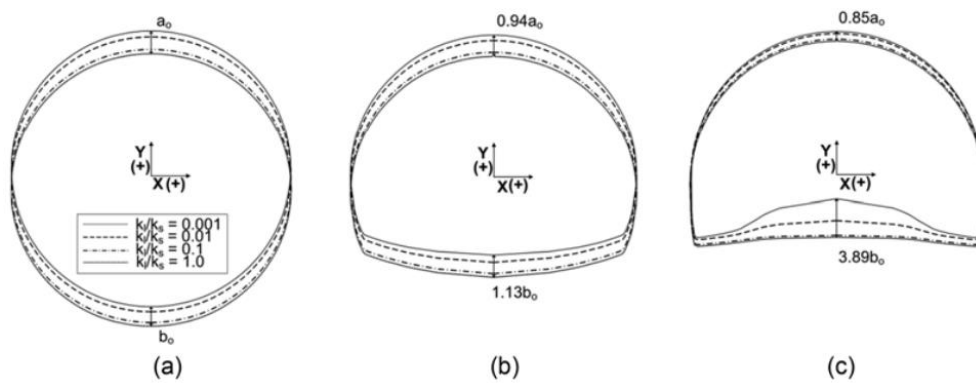


Fig. 1-10 Lining Deformation for Each Tunnel Shape: (a) Circular, (b) Egg-shaped, (c) Horseshoe-shape, (Yoon et al., 2014)

Fig. 1-10 shows the lining displacement with the progress of hydraulic deterioration for each tunnel shape. In general, as the relative permeability (k_i/k_s) decreases, tunnels move upward owing to the buoyant force. The

extents of vertical movements are in the following descending order: circular, egg-, and horseshoe-shaped tunnels at the crown; and horseshoe-, egg-shaped, and circular tunnels at the invert. In particular, the horseshoe-shaped tunnel shows a significant increase in displacement at the centre of the invert.

Eman et al. (2013) investigated the behaviour of two adjacent different shapes of tunnels in soft clay soil using finite element software with three shapes (circular, elliptical and rectangle with arch) as shown in Fig. 1-11. Each shape of twin tunnels was studied by varying its diameter D and wall-thickness ratio (t/r). Fig. 1-12 gives the finite elements mesh of different shape of twin tunnels.

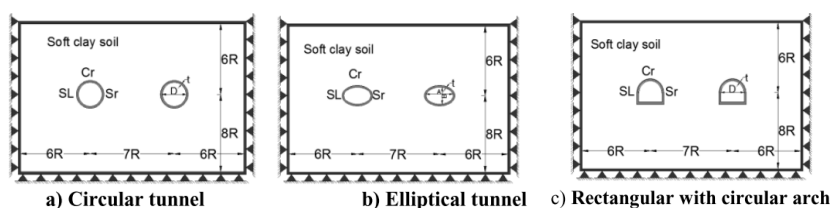


Fig. 1-11 Layout of different shape of twin tunnels: (SL) is the left spring point, (Cr) is the crown point and (Sr) is the right spring point of the tunnel (Eman et al., 2013)

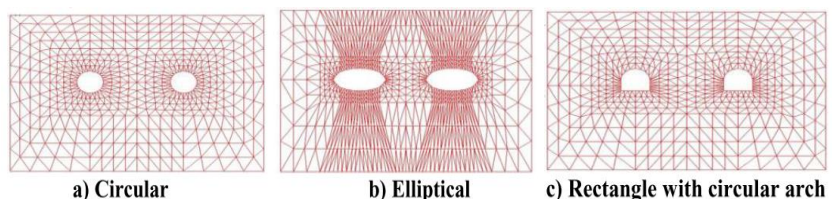


Fig. 1-12 Finite elements mesh of different shape of twin tunnels (Eman et al., 2013)

Figs. 1-13 to 1-15 show the distribution of the internal forces (bending moment M , normal force N , and shear force S) for the different shapes of tunnels at the thickness-radius ratio (t/r) = 0.1. It can be found that the shapes of the tunnel in the soft clay soil have a significant effect on the internal forces.

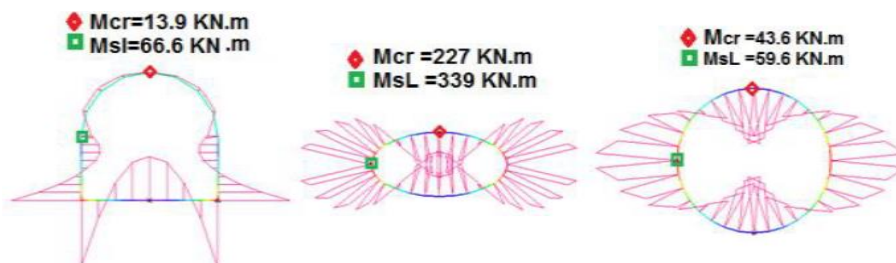


Fig. 1-13 Distribution of the bending moment M in the different shapes of tunnels at $D=8\text{ m}$, $t/r = 0.1$ (Eman et al., 2013)

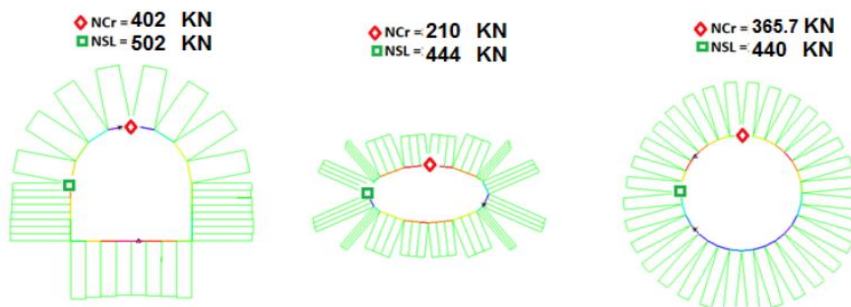


Fig. 1-14 Distribution of normal forces N in the different shapes of tunnels at D=8 m, t/r=0.1(Eman et al., 2013)

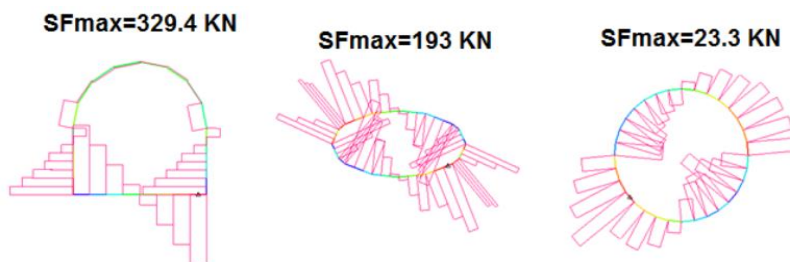


Fig. 1-15 Distribution of shear forces S in the different shapes of tunnels at D=8 m, t/r=0.1 (Eman et al., 2013)

Figs. 1-16 and 1-17 indicate the effect of change in diameter (D) on the bending moment and normal forces at the upper crown point of the tunnel with different thickness–radius ratios (t/r) for three shapes of tunnels in soft clay soil. It shows that for all shape of tunnels, the bending moment ratio (M/M_0) increases up to 40% due to increase the diameters of tunnel from 8 to 12m. However, it increases up to 15% as the wall-thickness ratios (t/r) increase as shown in Fig. 1-16.

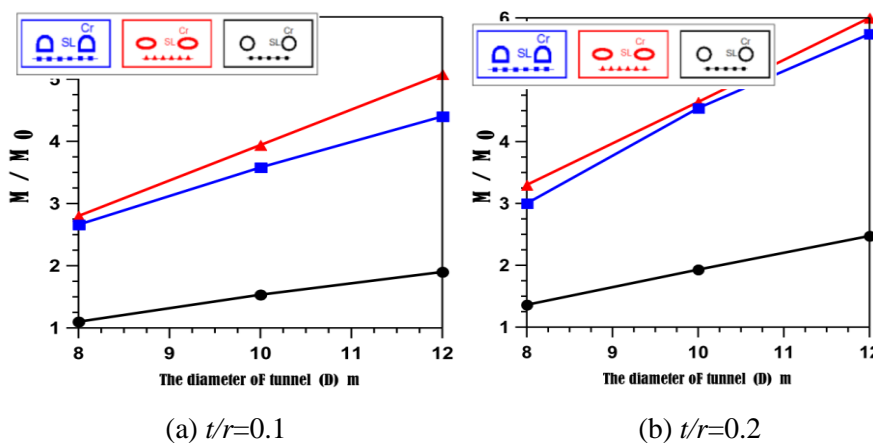


Fig. 1-16 Effect of the change in the diameter (D) on the bending moment at upper crown point of the tunnels (cr) at different t/r ratios (Eman et al., 2013)

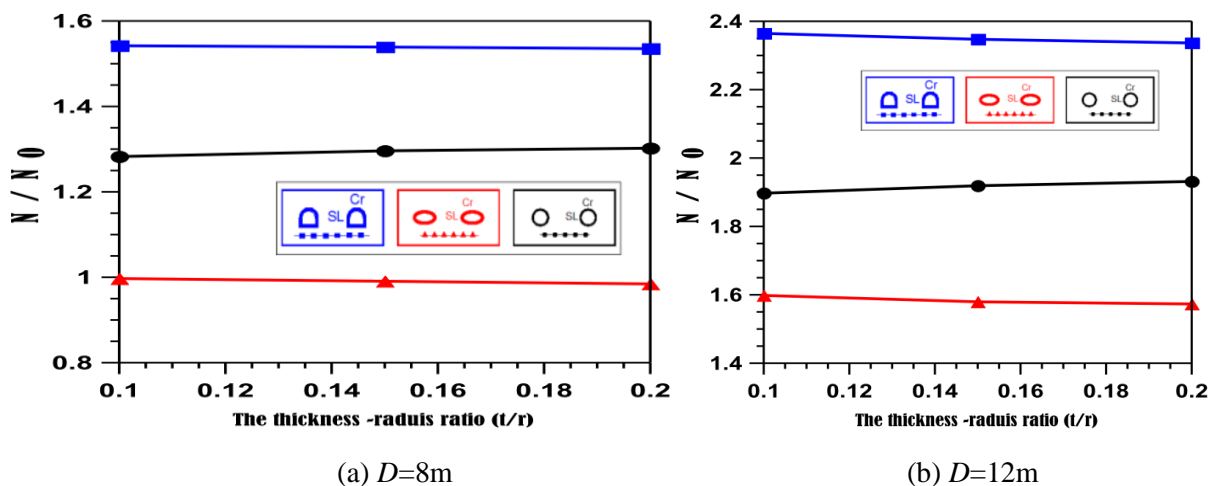


Fig. 1-17 Effect of the change in the thickness-radius ratios (T/R) on the normal force at the upper crown point of the tunnel (cr) at different diameters (Eman et al., 2013)

Fig. 1-17 indicates that the normal forces ratios (N/N_0) are rarely affected by the increase of (t/r) ratios, however increase up to 50% as the tunnel diameter D increases.

Summary

This section gives the studies about the effect of tunnel shape on the lining behaviour. Generally, when the tunnel shape becomes flat, the normal force becomes dominant part to support the tunnel. Specially, stress concentration around corners increases sharply as the tunnel shape becomes non-circular. For the case of same tunnel width and lining thickness, the noncircular tunnel has less stability than the circular one. However, as a large amount of the excavated soil is generated and lots of space is unutilized, the circular cross section is not efficient and not economic space.

Compared with traditional circular tunnels, the non-circular cross-section tunnels have several advantages including the facts that 1) underground space can be more effectively utilized by designing the tunnel to have a configuration that matches the purpose of the tunnel, 2) the degree of adverse impact from the surrounding environment can be decreased, and 3) the quantity of excavation can be reduced. In addition, as one kind of non-circular tunnels, the quasi-rectangular tunnel is a new type of structure in tunnelling. It combines the advantages of circular and rectangular tunnel, and will surely be widely used in the future (Liu et al., 2018). However, so far few studies have been given to non-circular cross-section tunnels.

3. Design methods of non-circular tunnels

The design of tunnels requires a proper estimate of the structural displacements and internal forces in the linings. There are various methods for designing tunnel linings. This section introduces the design methods of non-circular tunnels.

The practice of designing tunnel linings needs experience, practical and theoretical knowledge. Therefore, the difficulties of designing tunnel support arise mainly from the inadequate knowledge of the soil behaviour under conditions associated with tunnel driving, insufficient data of the natural soil state of stress, and the fact that it is a three-dimensional problem. Generally, the methods for designing non-circular tunnel lining can be classified into three categories: experimental studies, theoretical and numerical analysis methods.

3.1 Experimental studies

In situ monitoring data or experimental results of tunnels are relatively rare, but it is important to collect field measurement data or experimental results to predict tunnel displacements, lining efforts and also to validate analytical and numerical tools. The experimental methods usually provide the simplest calculation.

Nakamura et al. (2003) performed full-scale loading tests on non-circular tunnel lining segments to confirm the adequacy of their design. Two kinds of non-circular lining structures (Fig. 1-18), composite segments and DC segments, were tested in their investigation. In the loading tests, the safety of the linings and the reliability of the design method were evaluated by directly applying to single segment and full segment rings loads were approximately equal to the design loads.

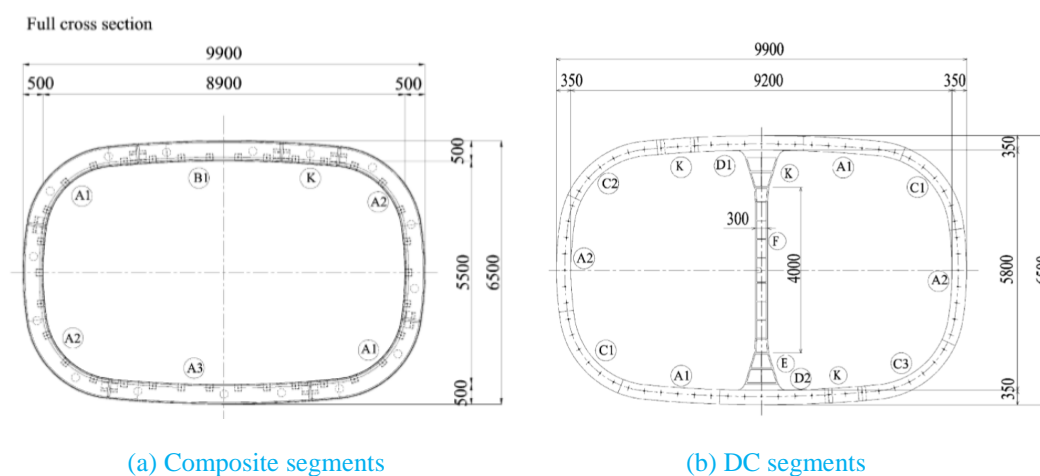


Fig. 1-18 Lining structures in section (Nakamura et al., 2003)

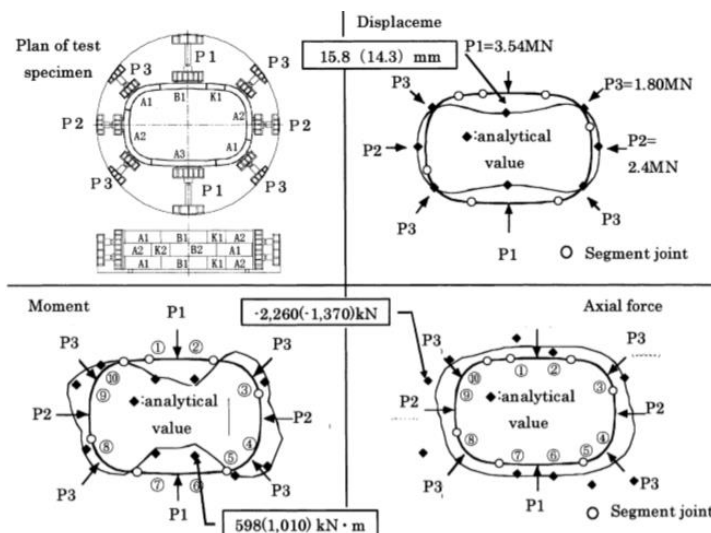


Fig. 1-19 Results of loading tests on composite segments (Nakamura et al., 2003)

Loads nearly equivalent to the design loads were applied to the composite segment rings from eight directions (Fig. 1-19). In these tests, the amounts of lining displacement and bending moment were generally close to the analytical values, thus confirming the adequacy of the analytical method. However, the amount of normal force had relatively large dispersion, but the effect of such dispersion is not very large because the stress generated by normal force is on the order of 10% of the maximum stress. Both strain and displacement almost returned to their origins after the loading was removed, and it was judged that no extraordinary strain or deformation will develop.

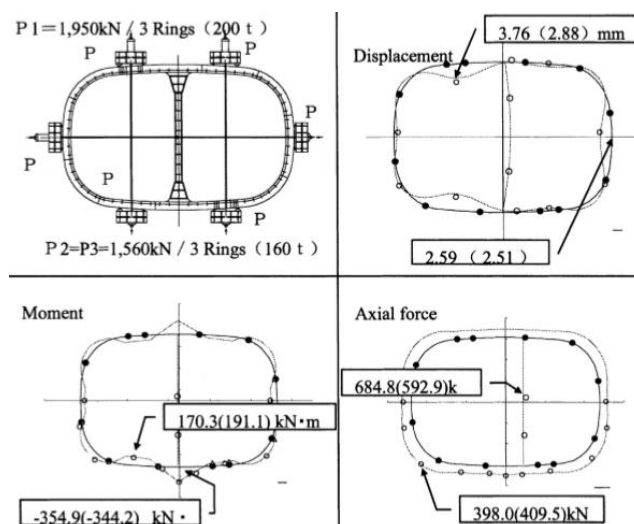


Fig. 1-20 Results of loading tests on DC segments (unsymmetrical pressure load) (Nakamura et al., 2003)

The distribution of bending moment, normal force and displacement of DC segments are shown in Fig. 1-20 in comparison with the results of analysis. The measured values and analytical values are generally close to each other, thus indicating that the beam and spring model satisfactorily simulates the behaviour of the rectangular lining.

Huang et al. (2018) developed a novel loading setup for performing full-scale loading tests on ‘standing’ segmental lining of a sub-rectangular tunnel, which allows the mechanical behaviour of segmental lining subject to self-weight to be assessed in terms of the radial deformation and internal forces of the lining. Granular rubber bearings with an equivalent coefficient of subgrade reaction close to hard plastic clay were used to simulate subgrade soils. The experimental data were compared with the numerical simulation (shell-spring model) results.

The cross-sectional outline of a testing full lining ring is composed of eight arcs (Fig. 1-21). A full ring is fabricated from six element blocks. The lining ring has an outer dimension of 10.2m×7.7m with a thickness of 0.5m and a width of 1.2m. Stagger fabrication method is adopted to enhance the longitudinal rigidity. The segments are connected by four M30 straight bolts at each joint between adjacent blocks and the neighboring rings are connected by 26M33 bent bolts in the longitudinal direction. The testing unit is composed of a middle full ring confined by two half rings at the front and the rear, which is the smallest unit of a stagger lining system.

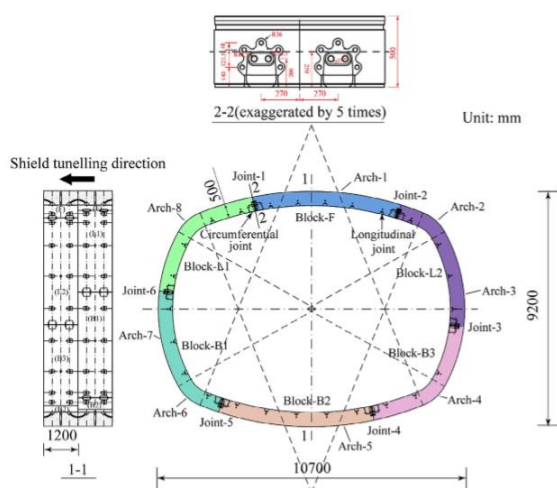


Fig. 1-21 Structure layout of the testing segmental lining (Huang et al., 2018)

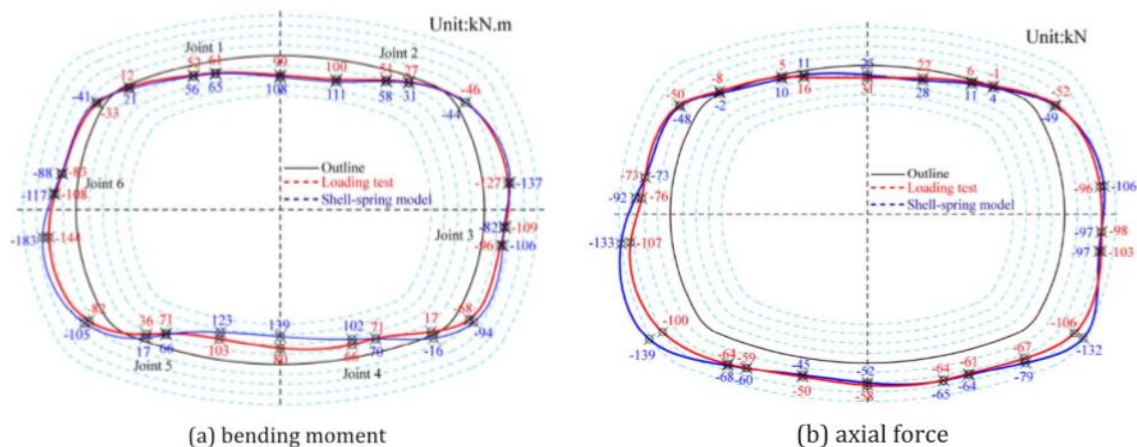


Fig. 1-22 Measured internal forces distribution (Huang et al., 2018)

The distributions of bending moment and normal force within the middle full ring are presented in Fig. 1-22. The cross symbols mark the locations of measurement points. The numbers aside the cross symbols indicate the measured values. The bending moment/normal force values between measurement points are estimated by spline line fitting. It can be found that the laboratory test results and the numerical simulation data agree quite well with each other. The maximum positive bending moment occurs close to the middle points of the crown and invert areas, and the largest negative moment is present close to the waist areas; whereas the bending moment at the four corners is small. Due to the presence of joints, the distribution of bending moment/normal force is not axisymmetric with respect to the vertical central axis of the lining ring. The presence of joints lowers down the local stiffness, which leads to the reduction of bending moment in areas close to the joint. Therefore, the largest negative bending moment on the left waist occurs slightly below the horizontal central line, while the largest negative bending moment on the right waist occurs slightly above the horizontal central line. As shown in Fig. 1-22b, subject to self-weight loading, the normal force within the lining ring is not universally compressive, with small tensile forces present at some locations in the crown areas. This is attributable to the absence of lateral confinement and the consequent large deformation at the lining waist. Similar to the distribution of bending moment, the distribution of normal force is also nonsymmetrical but depends on the joint locations.

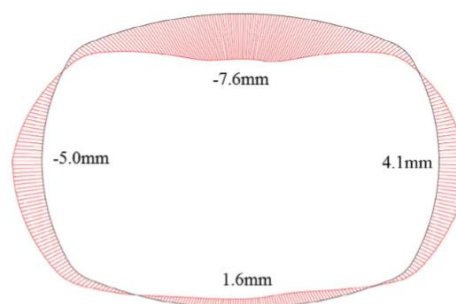


Fig. 1-23 Measured overall deformation of middle lining ring (black line is the original segmental outline) (Huang et al., 2018)

The overall deformation of the middle lining ring after removal of inner support frame is shown in Fig. 1-23. The deformation is obtained by comparing the inner outline of the lining ring scanned after removal of inner support frame with the designed outline. In the absence of lateral confinement, the lining ring can deform freely in the lateral direction and the largest outward deformation takes place close to the waists. The outward deformation of the left waist is slightly larger than that of the right waist as the negative bending moment on the left waist is slightly larger than that on the right waist as shown in Fig. 1-22. The total amount of lateral outward displacement (sum of the displacement at the left and right waists) is 9.1mm, which is close to that of the total vertical inward displacement (9.2mm, sum of the displacement at the middle point of crown and that at the middle point of the invert). The inward displacement at the invert (1.6mm) is much smaller than that at the crown (7.6mm). The experimental results confirmed the previous numerical observations that the convergence deformation of lining ring and the joint deformation caused by self-weight during fabrication are non-negligible. Therefore, Huang et al. (2018) suggested that the influence of self-weight should be considered in future full-scale loading tests, especially for shallowly-buried tunnels.

To investigate the bearing mechanical behaviour of a quasi-rectangular segmental tunnel lining, Liu et al. (2018) conducted a full-scale ring test of corresponding lining structure. Based on the first full-scale ring test of a quasi-rectangular segmental tunnel lining, the ultimate bearing capacity of the tunnel was reached. The bearing mechanism and weakness of the lining were revealed. In a tunnel lining, a ring is composed of a number of segments and neighboring segments are connected by longitudinal joints. Then based on the results of the first full-scale ring test, two more full-scale ring tests were carried out by improving the reinforcement of the segment and optimizing the position of the longitudinal joint bolt to investigate the influence of

segmental reinforcement, longitudinal joint position and shear bearing capacity of a T block on the mechanical behaviour of a quasi-rectangular segmental tunnel lining. Based on the fact that shear failure phenomenon appeared at the haunch of T2 block in the first full-scale ring test, shear stirrup at two T blocks is strengthened in the third test to increase the shear bearing capacity.

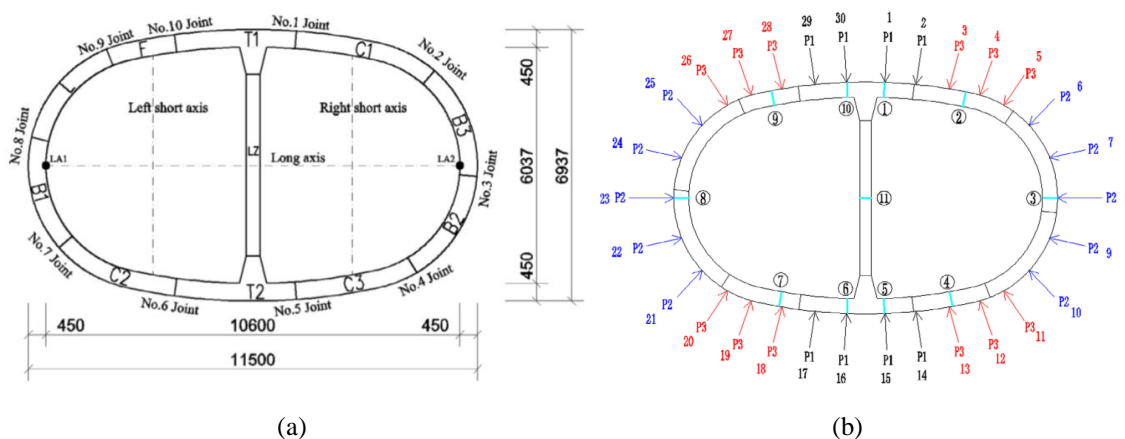


Fig. 1-24 Schematic diagram of test tunnel ring (a) and division of load points (b) (Liu et al., 2018)

The failure process, structural convergence deformation, joint deformation and bolt strain of the lining structure were obtained.

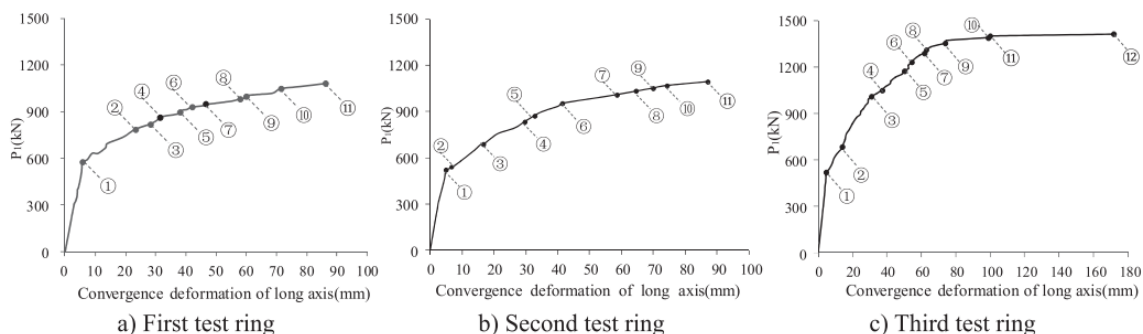


Fig. 1-25 Load-convergence deformation of long axis curves of three test rings (Liu et al., 2018)

The failure process of the three test linings under whole process limit condition is shown in Fig. 1-25. Throughout the entire loading process, the load-convergence deformation curves have two typical stages: elastic and plastic (working with cracks) stages. Here the convergence deformation refers to the deformation of the deformed structure relative to the initial state.

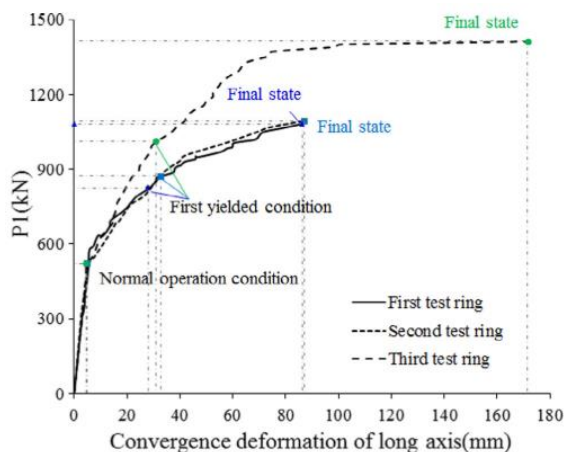
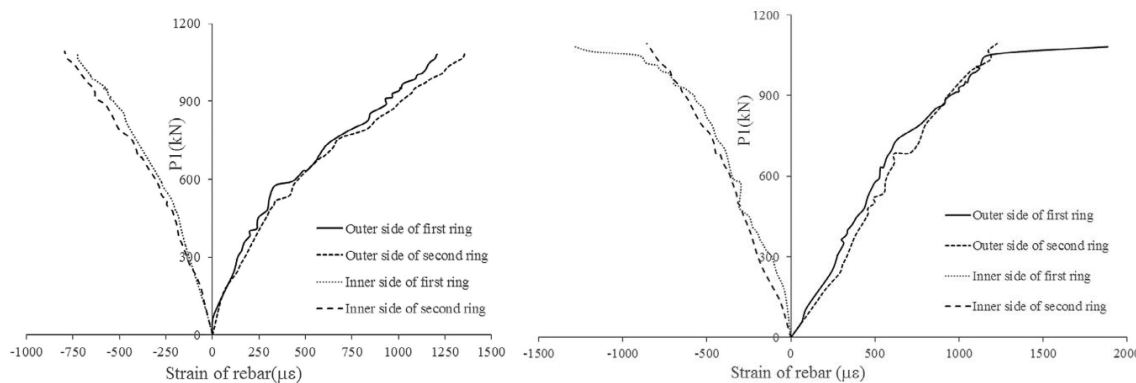


Fig. 1-26 Comparison of load-convergence deformation curves of three test rings (Liu et al., 2018)

The load-long axis convergence deformation curves of the three test rings are illustrated in Fig. 1-26. The performance points (normal operation condition, first yielded condition, final state) are shown in the same Figure. As shown in Fig. 1-26, the three test rings have similar mechanical behaviour at elastic stage. After entering the plastic stage, the curves of the first and second rings are similar to each other. However, the curve of the third ring is significantly different from the other two. In comparison, the performance point (first yielded condition) of the first ring appears the earliest while that of the third appears last. When the convergence deformation of the three test rings reaches about 30 mm, the structure first develops local yielded phenomenon.

The load-rebar strain curves of critical cross-section 1 and critical cross-section 6 (Fig. 1-24b) are shown in Fig. 1-27. As for critical cross-section 1, the development of rebar strain of two rings shows the same tendency and the curve of the second ring grows a little faster. The development rule of the rebar located at critical cross-section 6 is similar to that located at cross-section 1. According to the monitoring results, none of the rebars are yielded at the end of the whole process limit condition. The results show that an increase in reinforcement causes the internal force on the segment to be slightly increased. The failure of the second ring is due to the local damage at T block and the bearing capacity of the joints is not fully utilized. However, considering the quasi-rectangular tunnel lining is governed by joint failure and shear bearing failure of T blocks, an increase in reinforcement has little influence on the ultimate bearing capacity of the structure when the longitudinal joint design remains unchanged.



(a) Critical cross-section 1

(b) Critical cross-section 6

Fig. 1-27 Load-rebar strain of inner and outer side of two rings (Liu et al., 2018)

Although based on the three full-scale ring tests, the influence of segmental reinforcement and longitudinal joint bolt position on the mechanical behaviour of a quasi-rectangular segmental tunnel lining was investigated by Liu et al. (2018), corresponding parameter analysis has not been carried out to obtain an optimal decision.

Synchronous grouting in a quasi-rectangular shield tunnel plays an important role in construction. For example, synchronous grouting can control stratum deformation, ensure uniform stress on a segment lining, improve the tunnel anti-permeability and fix the position of a segment lining. Ding et al. (2019) investigated the behaviour of synchronous grouting in a quasi-rectangular shield tunnel based on a large visualized model test. Their experiment used an integrated simulative experimental platform in the form of a large-sized quasi-rectangular shield tunnelling machine to simulate the synchronous grouting process. The purpose of their research was to fully understand the grout flow path and the grouting pressure distribution mechanism to guide the selection of the grouting parameters and the shield type and to provide references for the design of a shield tunnel. The detailed sizes of the inside segment and the outside shield are shown in Fig. 1-28.

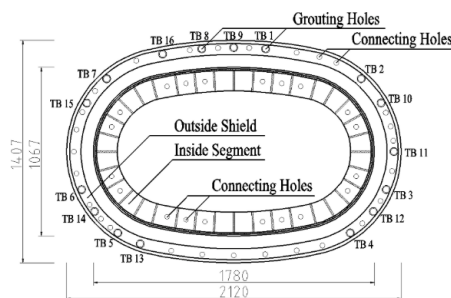


Fig. 1-28 Size of the inside segment and the outside shield (Ding et al., 2019)

The measured parameters during the test include the grouting pressure change, the grouting pressure distribution in the toroidal direction along the segment, the influence of the grouting on settlement and the relationship between the grouting pressure and the final grout shape. The grouting pressure and settlement of each soil layer were measured throughout the entire experimental process, and the grout flow path was recorded by cameras. Moreover, the upper covering soil was removed after the test to survey the final shape of the solid grout.

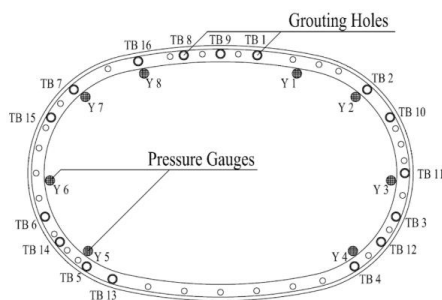


Fig. 1-29 Arrangement diagram of grouting pressure gauges in the steel segment (Ding et al., 2019)

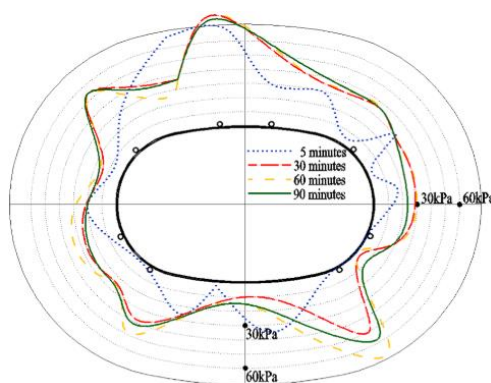


Fig. 1-30 Distribution of grouting pressure ground the segment lining in the toroidal direction (Ding et al., 2019)

There are four curves of the pressure distribution in the toroidal direction shown in Fig. 1-30. Different curves represent different grouting pressures at different times after the shield tail passes: 5 min, 30 min, 60 min, and 90 min. The data in the curve of 60 min is taken to be analysed. The grouting pressure near the grouting hole is higher than that far from the grouting hole. The grouting pressure near the grouting hole is as high as 62.5 kPa. The grouting pressure far from the grouting hole is in the range of 20-30 kPa or even less. In the experiment, the buried depth is shallow, and the inside segment is fixed between the inward and outward doors. Therefore, the average pressure on the top of the segment is higher than that at the bottom of the segment. However, in practical engineering, the pressure on the top is lower than that at the bottom, primarily

because of the weights of the tunnel and the soils. Comparing the lines at different times, they found that the pressure circle increases between 5 and 60 min, whereas the value at 90 min is smaller than that at 60 min.

Ding et al. (2019) also investigated the pressure distribution around the steel segment. They found that in the steel segment, the arrangement of pressure gauges is similar to that of the traditional method. As shown in Fig. 1-29, eight pressure gauges are arranged sparsely around the inside segment in each cycle. The pressure curves in the toroidal direction are shown in Fig. 1-31. Similar to the change rule in the vitreous segment, the grouting pressure on the top is higher than that at the bottom. The grouting pressure at the top of segment is between 35 kPa and 51 kPa, and the grouting pressure at the bottom of the segment is between 19 kPa and 38 kPa.

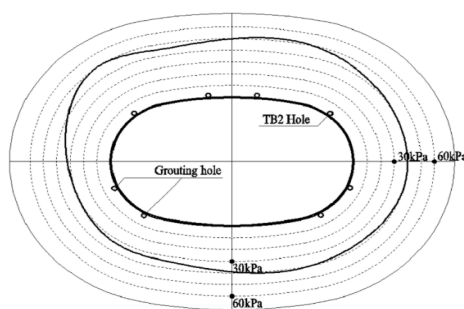


Fig. 1-31 Pressure curves around the steel segments (Ding et al., 2019)

The settlement of each soil layer measurement consists of pipelines and magnetic rings, which are deployed in the upper covering soil. The layout of the measuring points is shown in Fig. 1-32. Before the synchronous grouting test, the data were measured twice every day; the rate of measurement is increased to once every hour during and after the synchronous grouting test.

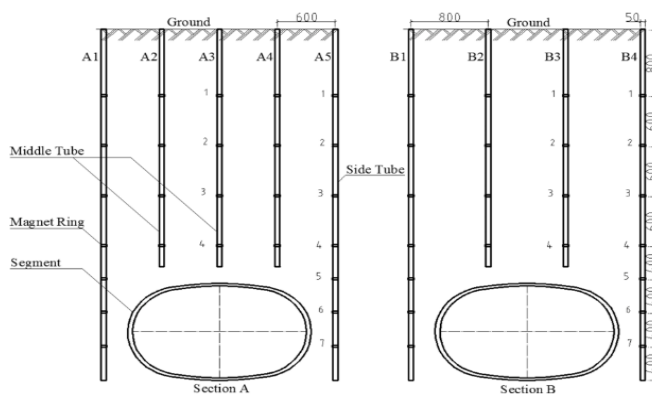


Fig. 1-32 Measuring points layout of the layered settlement test (Ding et al., 2019)

The settlement curves in different points of A5 and B1 over time are shown in Fig. 1-33. The soil finishes filling into the test zone at 15:00 21/ 10/2015, which is set as the time origin. First, the layer settles gradually because of the consolidation itself. The surface settlement reaches the highest value of approximately 10mm and then tends to be stable over the next 5 days. Since the start of the excavation, the layer uplifts first because of the filling grout. The largest value of upheaval is nearly 28 mm. Subsequently, the layer settles gradually. The maximum value of settlement is approximately 15 mm, and the minimum value of settlement is approximately 4 mm. The settlement differs from the layer depth. The uplift value on the ground surface is far less than the uplift value near the segment, and the filling grout cannot completely compensate for the settlement in ground surface because the uplift of soil is substantial near the segment but diffuses only minimally to the far areas.

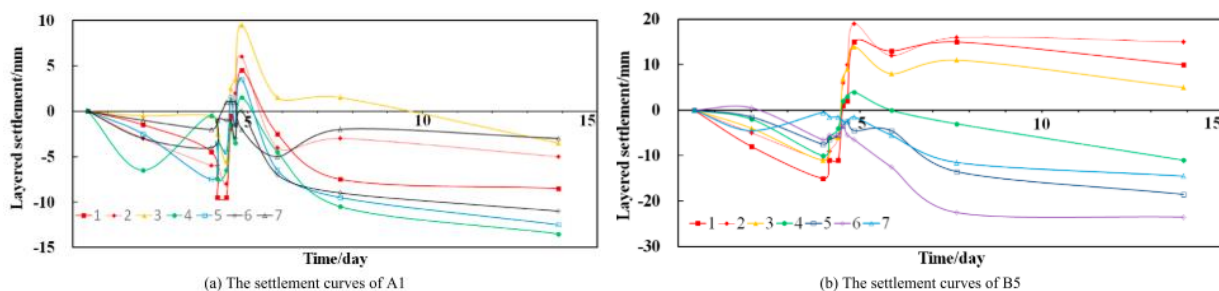


Fig. 1-33 Settlement curves of A1 in Section A and B5 in Section B (Ding et al., 2019)

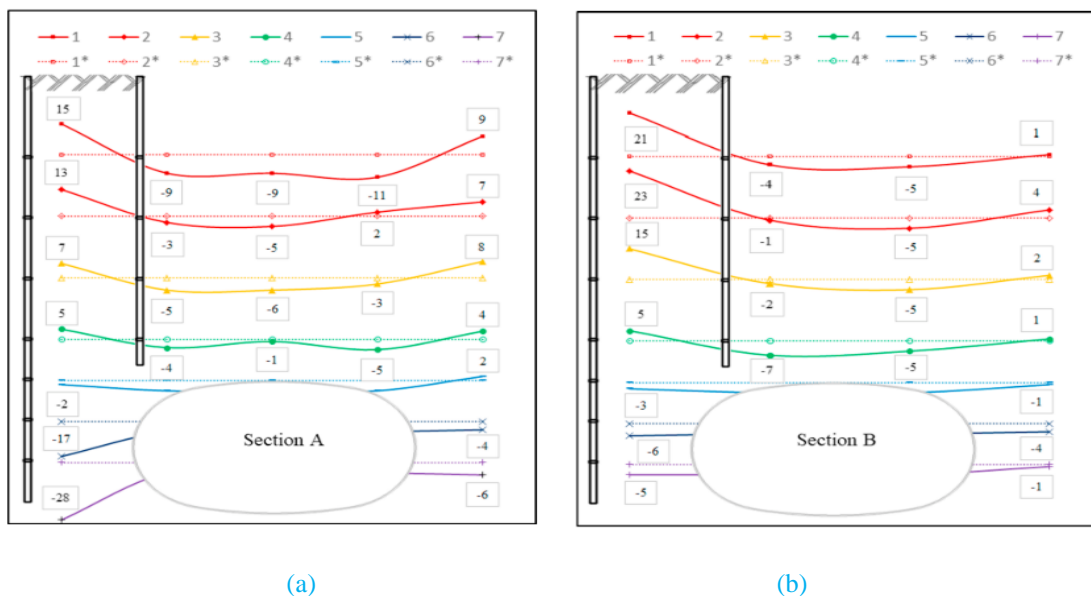


Fig. 1-34 Total settlement curves of Section A (a) and Section B (b) at 15:00 on 27/ 10/2015 (mm) (Ding et al., 2019)

Fig. 1-34 shows the settlement curves observed at different depths of Section A and Section B. The dotted lines represent the initial position at different depths, and the solid lines represent the final position at different depths. The positive value represents upheaval, whereas the negative value represents settlement. In the area above the segment, the soil settles, and the value is less than 10 mm. However, in the area beside the segment, the soil uplifts, and the most value reaches nearly 23 mm. The stratum settles in the middle area of segment apparently and the stratum beside the segment does not settle obviously and even uplifts in some regions.

The investigation results of [Ding et al. \(2019\)](#) demonstrate that the key parameters of synchronous grouting in a quasi-rectangular tunnel are the grouting ratio and the position of the grouting holes. It should be noted that all the analyses of their test are based on the gray clay, so their results have some limitations. When it used to other soil layers, it should be modify.

Summary

Because of the expensive costs, the experimental studies are rare. Also they are heavily subjected to some important limitations, including their applicability to different tunnel geometries, soil properties, and construction procedures. Despite this, the experimental studies are still useful for comparing the results with the numerical methods and analytical solutions for validation purpose of a model.

3.2 Theoretical and analytical methods

The problem of tunnel design is a three-dimensional model for analysis with some specific assumptions. Some attempts have been made to develop simple closed-form analytical solutions or theoretical solutions for estimating the behaviour of non-circular tunnels.

For example, [Oreste and Dias \(2012\)](#) found that even though face reinforcement with fibreglass dowels has proved to be efficient, there is still no reliable routine design method available. Therefore, they illustrated a calculation procedure for the analysis of face reinforcement with fibreglass dowels in shallow non-circular tunnels. The procedure is based on the limit equilibrium method (LEM), which is able to offer a detailed evaluation of the interaction between each reinforcement element and the surrounding rock. The main calculation result concerns the safety factor of the excavation face with dowel reinforcement. Using the proposed calculation method, it is possible to quickly obtain the definition of the reinforcement lengths and

the number of dowels required to obtain the desired safety factor of the excavation face. The proposed method was applied to two road tunnels in France: the Toulon and Pech–Brunet tunnels (Fig. 1-35), which have also been studied using tridimensional numerical methods. The results have shown that the safety factors of both cases obtained through the proposed calculation method are similar to those obtained by means of 3D numerical methods. This important result validates their developed analytical approach.

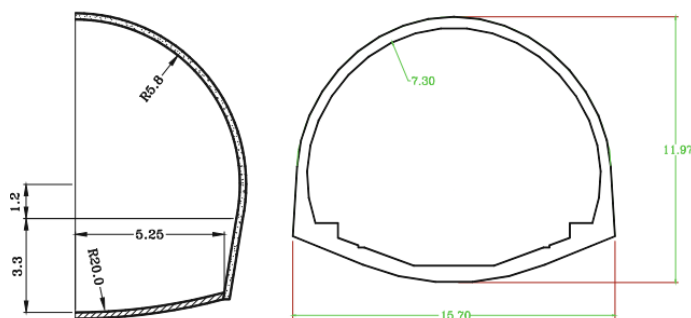


Fig. 1-35 Toulon (left) and Pech–Brunet (right) tunnels: geometry of the sections (Oreste and Dias, 2012)

It should be noted that the main simplifying hypotheses on which the LEM is based are:

- The potential unstable mass is represented by one or more blocks that maintain their initial volume and shape;
- The kinematic mechanism of each block occurs through sliding along its lateral surfaces;
- It is a static analysis and only the possibility of the initial displacement of the rock blocks is dealt with;
- The possibility of a progressive break along the sliding surfaces is not considered.

It is evident that the LEM is based on particular simplifications of the instability mechanisms, and the results should be interpreted very carefully. However, use of the LEM in the analysis of many instability mechanisms is very common in geotechnical engineering due to its simplicity, the intuitive nature of the approach and the possibility of evaluating the degree of stability with safety factors.

As the safety factor is an important and appropriate factor for the design in the open-face tunnelling and the cross section of a NATM tunnel is often a non-circular shape (horse-shoe, elliptical or more complex shape), [Pan and Dias \(2017\)](#) estimated the safety factor of a non-circular tunnel section using the upper-bound limit analysis in combination with the strength reduction technique. The strength reduction method (SRM) is an effective technique to define a safety factor, in which the safety factor is the ratio of the real shear strength

of the material to the critical shear strength which corresponds to the limit equilibrium state. The spatial discretization technique was extended to generate an advanced 3D rotational collapse mechanism for a non-circular NATM tunnel face. The non-circular tunnel of height H and width L is sketched in Fig. 1-36. The whole failure mechanism rotates around a horizontal axis passing through point O with an angular velocity ω . For any point of the failure mechanism, the velocity is equal to the product of the angular velocity and the distance between the rotating centre and the point under consideration.

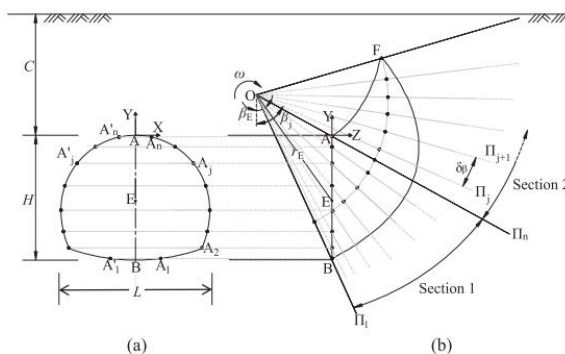


Fig. 1-36 Discretization technique for the collapse mechanism of a non-circular tunnel. Points A, B and E representing, respectively, the crown, invert and centre of the tunnel face; C being the tunnel buried depth (Pan and Dias, 2017)

The safety factors obtained by their proposed approach and by the 3D numerical calculations with $FLAC^{3D}$ were compared (Table 1-1).

Table 1-1 Obtained safety factors for Toulon’s tunnel (Pan and Dias, 2017)

Methods	Safety factor		Difference (circular section/ non circular section)
	Circular section	Non-circular section	
$FLAC^{3D}$	2.15	2.49	13.7%
Kinematical approach	2.38	2.60	8.5%
Difference ($FLAC^{3D}/KA$)	9.7%	4.2%	-

The safety factors obtained from their proposed kinematical approach agree reasonably well with those provided by the finite difference method using $FLAC^{3D}$ both in terms of the full face excavation and the top heading excavation. Only a maximum difference of 9.7% occurs in the case of top heading excavation. This has shown that their proposed method is an effective approach to evaluate the safety factor for a tunnel face with a non-circular cross section. In addition, a comparison with other approaches indicates that their presented approach gives conservative results (Fig. 1-37a).

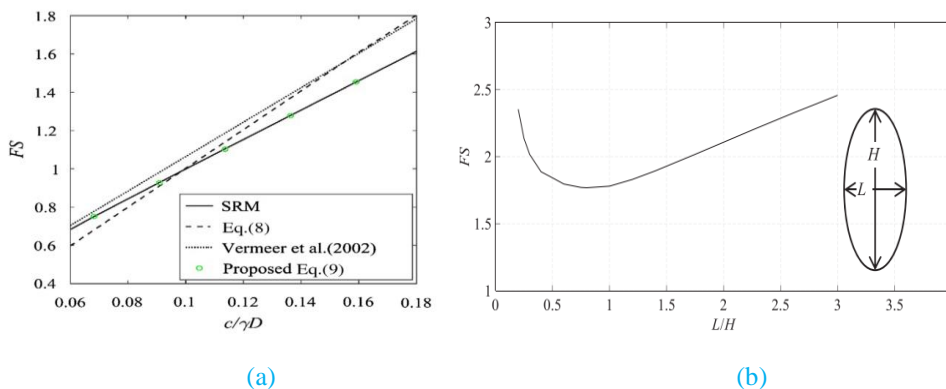


Fig. 1-37 Safety factor as a function of the ratio L/H (Pan and Dias, 2017)

Pan and Dias (2017) also discussed the effect of the cross-sectional tunnel shape on the safety factor. Fig. 1-37b shows the safety factors obtained by the proposed method as a function of the ratio L/H . The ratio of the width L to the height H of the cross section is investigated in the range from 0.2 to 3.0. As seen in Fig. 1-37b, the cross-section tunnel shape significantly influences the safety factor. The safety factor firstly drops with the ratio L/H and then increases with it. The minimum safety factor occurs at a point close to 1.0 at which the elliptic section is reduced to a circular shape. The safety factor decreases 24.3%, from 2.35 at $L/H = 0.2$ to 1.78 at $L/H = 1.0$, and then increases 27.6% from 1.78 to 2.46 at $L/H = 3.0$. These differences are large and cannot be neglected in real engineering problems. The cases near the circular one ($L/H = 1.0$) are the worst in terms of safety due to the fact that the opening span is the same in all the directions.

On the basis of the upper bound theorem of limit analysis, the influence of the anisotropy and non-homogeneity of soil on the earth pressure of shallow square tunnels was studied by Du et al. (2018). Their analysis was based on the assumptions that the surrounding soil mass is assumed to be a perfectly plastic material with an associated flow rule and the failure block is regarded as rigid. The failure mechanism of the surrounding soil for shallow square tunnels was firstly generated by the discrete method (Fig. 1-38). The work rate of external forces and the internal energy dissipation were calculated considering the anisotropy and non-homogeneity of soil cohesion. Then the earth pressure formula was derived and the optimal solution was obtained.

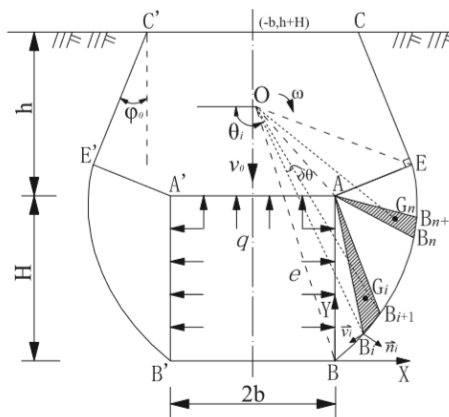


Fig. 1-38 Failure mechanism generated by the discrete technique: h is the overburden; H is the height of the tunnel; $2b$ is the width of the tunnel, and $2b=H$; $e=Kq$, where K is the ratio of horizontal force e to vertical force q (Du et al., 2018).

Table 1-2 Comparison of earth pressure q (kPa) (Du et al., 2018)

Ratio K	Yang [12]	Present results	Difference/%
0.6	243.2	232.5	4.4
0.8	199.1	189.5	4.8
1.0	169.3	160.0	5.5
1.2	147.7	138.4	6.3

Compared to other results (Table 1-2), it is shown that their present approach is feasible and effective. After discussing the impact of the anisotropy and the non-homogeneity of soil on earth pressure, the tunnel stability was studied with the presence of the pore water pressure. They also investigated the effect of pore water pressure and the change of the water table level on the behaviour of a square tunnel. Lastly, they give the following conclusions:

- (1) The earth pressure increases as the anisotropy of soil cohesion increases.
- (2) The earth pressure decreases linearly as the coefficient of cohesion non-homogeneity increases.
- (3) The increase of pore water pressure causes the increase of the earth pressure.
- (4) The earth pressure usually decreases as the coefficient of changing water table increases.

Summary

It can be found that the analytical methods do lead to the effective evaluation of the stress and strain state of the tunnel lining. Analytical formulations have a number of advantages over numerical and experimental methods such as:

- (1) they provide insight into the problem;

- (2) have low computational cost with a good accuracy;
- (3) are very useful to identify the most important variables for a given problem;
- (4) can be used to verify and calibrate complex numerical models.

Also, analytical solutions are desirable in direct applications or in the validation and verification of numerical models for their advantages of conciseness and convenience. However, as analytical formulations are usually derived on the basis of some simplifying assumptions to the problem, this kind of methods could only be applicable for the corresponding specific types of case. In fact, since the physical and mechanical properties of soil and rock, also the geometrical properties of tunnel varies from site to site, no one analytical method can be applicable to all type of case and cannot deal with complex situations. As for more complicated scenarios, a numerical model would be more flexible.

3.3 Numerical analysis methods

Recently, with the rapid development of computational tools, user-friendliness and ability to account for the complex tunnel geometries and ground profiles the numerical methods are becoming more popular. Many limitations of the proposed empirical and analytical methods can also be overcome by the numerical methods.

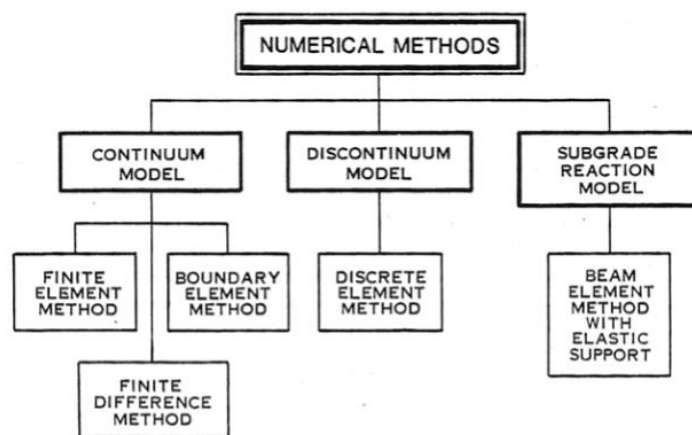


Fig. 1-39 Numerical methods and models for tunnel engineering (ÜÇER, 2006)

Numerical methods used for tunnel engineering are shown in Fig. 1-39. These models are: Continuum Models, Dis-continuum Models, and Subgrade Reaction Models (ÜÇER, 2006). The numerical methods associated with these models are: Beam Element Method with Elastic Support, Finite Element Method (FEM), Finite Difference Method (FDM), Boundary Element Method (BEM), and Discrete Element Method (DEM).

The strengths and weaknesses of each method mentioned above have been introduced specifically by ÜÇER (2006). In the following part of this section, only the applications of those methods related to the non-circular tunnels are described.

Leca and Clough (1992) did a parametric study of the excavation and support of a shallow NATM tunnel using the finite element method (FEM). The results were cast in a form so that the bending moments and thrusts in a proposed liner can be easily obtained. The softening technique, used for the analysis of NATM tunnels, was improved to better account for the three-dimensional deformation of the ground around the face and was applied to ovoid transportation tunnels (Fig. 1-40) constructed in undrained clays. A simplified method was provided for the preliminary design of the NATM tunnel support, which allows the estimation of bending moments and thrusts acting on the liner for a range of commonly encountered conditions and provides information to help guide better use of the more sophisticated analyses. The analysis is limited to single tunnels, but the results are applicable to cases of double tunnels, provided the pillar width over diameter ratio is larger than 2.0.

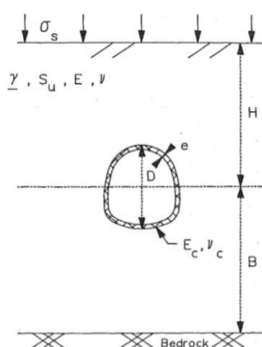


Fig. 1-40 Tunnel Geometry and loading conditions (Leca and Clough, 1992)

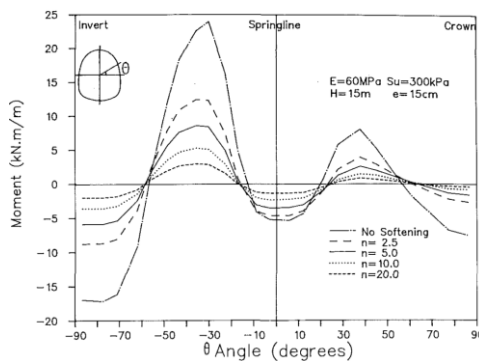


Fig. 1-41 Influence of softening factor on liner bending moment (Leca and Clough, 1992)

Fig. 1-41 shows the liner bending moments that were computed for a tunnel driven at 15 m in elastic ground (Young's modulus of ground $E = 60$ MPa and lateral earth pressure of ground $K_0 = 0.5$) and lined with 15 cm of shotcrete. The location along the liner is determined by the angle θ ($\theta = -90^\circ$ corresponds to the invert, $\theta = 0^\circ$ to the spring line, and $\theta = 90^\circ$ to the crown). Five different values of the softening factor n (including no softening) were considered. The five plots in Fig. 1-41 show a similar pattern of bending moment variation with θ , with a maximum at haunch level (θ is about 35°). When normalized to their maximum, the five moment profiles are almost identical. Fig. 1-41 shows a definite influence of the softening coefficient n on maximum liner bending moments, with liner bending moments being smaller when the level of softening is increased.

Tunnel construction commonly proceeds in an environment of layered geological formation. Design for tunnel support relies on the tunnel location and the mismatch of different layers. [Yin and Yang \(2000\)](#) proposed a topology optimization method for the design of tunnel support. The design domain is discretized by finite elements (Fig. 1-42). An element is composed of the original rock (hard or soft) and the reinforcing material (rock reinforced by grouting or bolting). The design issue involves the distribution of reinforcements. The ratios of two phases in various elements are optimized to minimize the deformation of the tunnel. The method enables a computer-aided design for the supports of underground tunnels embedded within layered geological structures. The reinforced areas for the tunnel are displayed under the passive geological stress and the active external loading. Four kinds of rock formations, homogeneous rock, hard-soft-hard (HSH) sandwich structure, two-layer structure with the soft rock at the top and the hard rock at the bottom (SH), and the one with the hard rock at the top and the soft rock at the bottom (HS) (Fig. 1-43), are examined. The simulation reveals the high efficiency of tunnel support by optimizing its topologies.

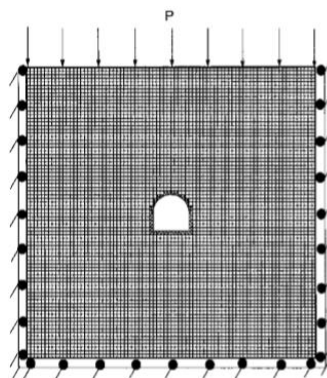


Fig. 1-42 A finite domain for the design of optimal reinforcements. The inner layer of the tunnel is replaced by a strong material, the square elements outside represent the area to be designed (Yin and Yang, 2000)

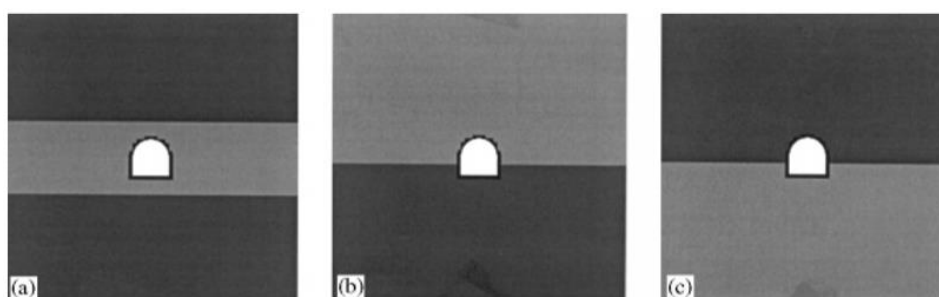


Fig. 1-43 Rock strata surrounding the tunnel for: (a) HSH; (b) SH; and (c) HS cases (Yin and Yang, 2000)

Fig. 1-44 shows the result of design under passive loading with four types of rock strata. In the reinforcement plots, the dark gray colour denotes the elements occupied by the reinforcing material, and the light gray colour denotes those still occupied by the original rock mass, and the black colour denotes the rim of the tunnel that is initially replaced by the strong material. The plots only display the domain near the tunnel, with the understanding that the region outside the displayed domain is not reinforced. The reinforcements tend to be distributed around the tunnel. In the homogeneous case, the reinforcements locate near the two floor corners of the tunnel and guard the two sides. In the HSH cases, the floor corner reinforcements connect to the hard rock stratum at the bottom. In the SH case, the hard-rock stratum occupying the lower half of the ground forces the reinforcement to spread, forming a reinforcing shape of two limbs of a butterfly. In the HS case, the reinforcement distribution resembles that of the homogenous case but is truncated above by the hard-rock stratum. Among the four configurations, the HS case suffers the largest deformation, and the HSH case achieves the smallest. The tunnel would deform less by putting it on top of the hard stratum.

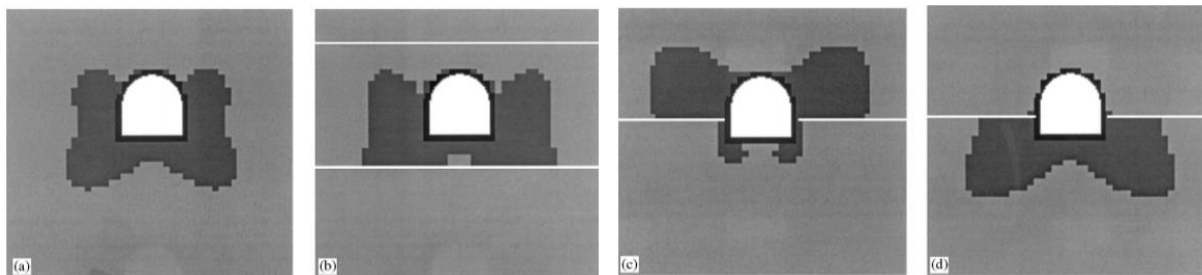


Fig. 1-44 Optimal distribution of reinforcing material for the passive loading case. The four graphs correspond to: (a) homogeneous; (b) HSH; (c) SH; and (d) HS host ground (Yin and Yang, 2000)

The case of active loading was also discussed. Distributions of reinforcement for four types of rocks are shown in Fig. 1-45. They are similar to their respective counter parts in Fig. 1-44 under passive loading. The values of the objective functions, however, follow a rather different trend. Among the four configurations, the homogeneous case suffers the largest deformation, and the HS case achieves the smallest. Since the global deformations of the geological structures are not excluded, the tunnel would deform more when situated within the soft stratum. As anticipated, the deformations under active loading exceed those under passive loading.

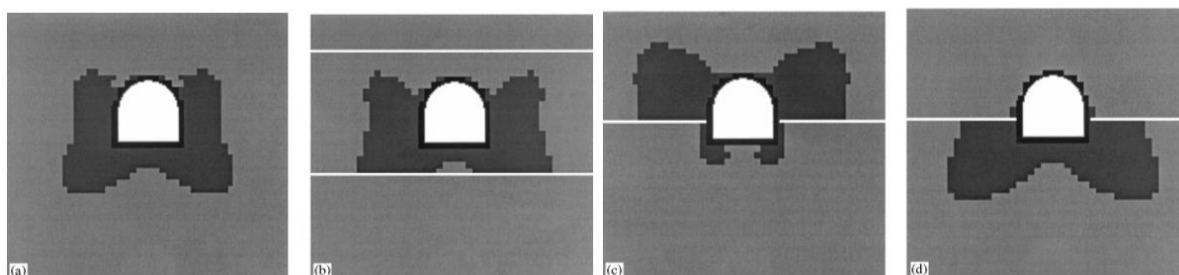


Fig. 1-45 Optimal distribution of reinforcing material for the active loading case. The four graphs correspond to: (a) homogeneous; (b) HSH; (c) SH; and (d) HS host ground (Yin and Yang, 2000)

To reveal the practical implications given in Figures 1-44 and 1-45, the tunnel deformations under initial designs with those under the optimal designs were compared. Figs 1-46 and 1-47 delineate the initial profiles (dashed lines), the deformed profiles under the initial design (dotted lines), and the deformed profiles under optimal design (solid lines) of the tunnel. The figures clearly demonstrate the reduction of tunnel deformation by optimizing the tunnel support.

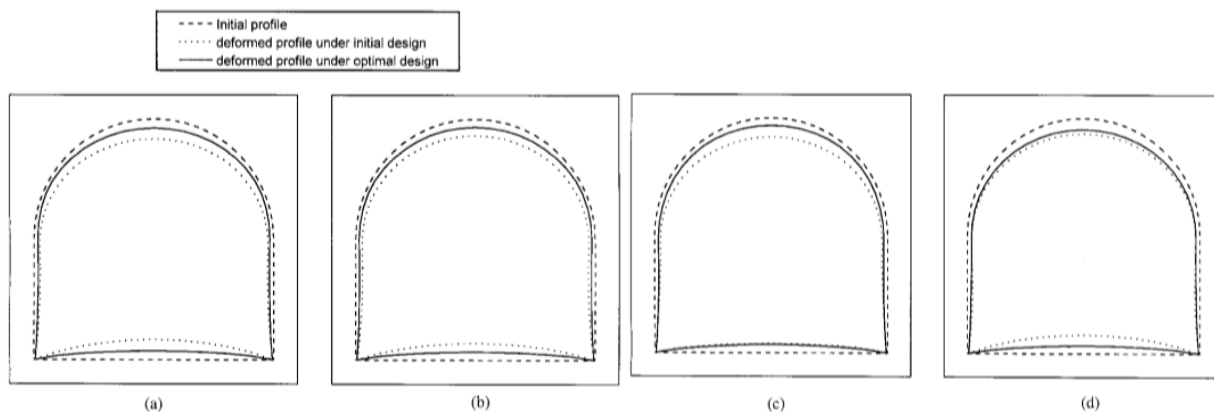


Fig. 1-46 Deformations of the tunnel profiles under the initial and the optimal designs for the passive loading case. The four graphs correspond to: (a) homogeneous; (b) HSH; (c) SH; and (d) HS host ground (Yin and Yang, 2000)

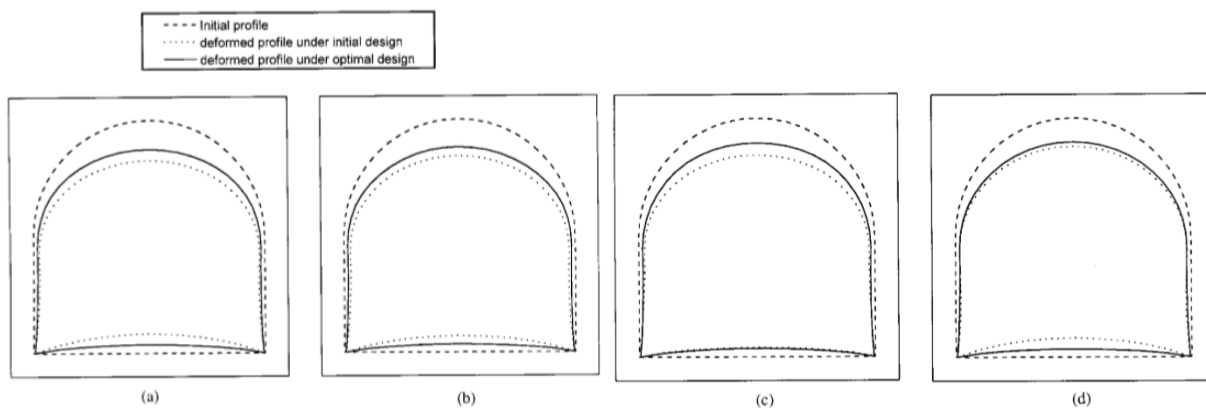


Fig. 1-47 Deformations of the tunnel profiles under the initial and the optimal designs for the active loading case. The four graphs correspond to: (a) homogeneous; (b) HSH; (c) SH; and (d) HS host ground (Yin and Yang, 2000)

Oreste (2003) illustrated the importance of the distance at which the supports are installed using FLAC when studying the interaction of support structures in tunnels. The numerical model is of a tunnel 12-m width, 10-m height, 140-m depth, which is assumed to be excavated in a weak rock mass (friction angle 30° ; cohesion 0.1 MPa, deformation modulus 5000 MPa, the *in situ* coefficient of horizontal stress K 0.5). The detail of the mesh of the numerical model adopted is shown in Fig. 1-48. Two cases were considered: firstly, steel sets installed at a short distance (1.5 m) from the face (case a); secondly, steel sets installed at great distance from the face (7m) (case b).

The final vertical displacements around the tunnel for case (a) are reported in Fig. 1-49. From these results Oreste (2003) found that the efficiency of the second support decreases with the distance of the point

of installation from the face: the final displacement of the tunnel increase; and final vertical load on the support system decrease.

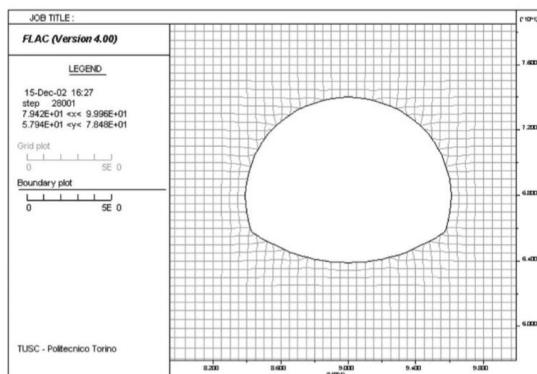


Fig. 1-48 Detail of the mesh of the numerical method developed to study the illustrated example (Oreste, 2003)

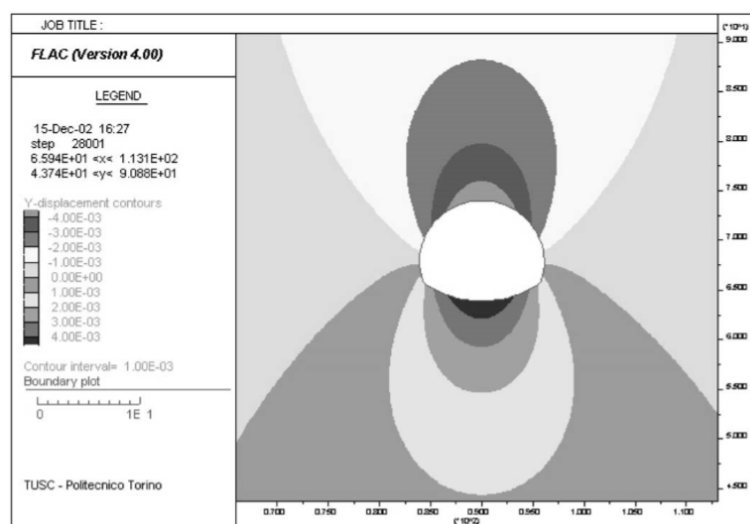


Fig. 1-49 Final vertical displacements for case (a) of the illustrated example (Oreste, 2003)

In order to provide a simple procedure and tool for tunnel designers, Barpi et al. (2011) carried out a study on the effect of non-circular tunnel boundary conditions (Fig. 1-50), based on a fuzzy model, using a bedded-beam-spring model. The study of the ground-tunnel interaction was presented and discussed by introducing a predetermined degree of variation (fuzziness) in some parameters of the chosen model. Their research came from the consideration that tunnel model parameters and geometry are usually affected by a degree of uncertainty, mainly due to construction imprecision and the great variability of rock mass properties. The research has been developed by using the fuzzy set theory assuming that the model parameters are

affected by a certain amount of uncertainty (defined by the so-called membership functions). The response of the numerical model is calculated by solving the fuzzy equations for different shapes of the membership functions.

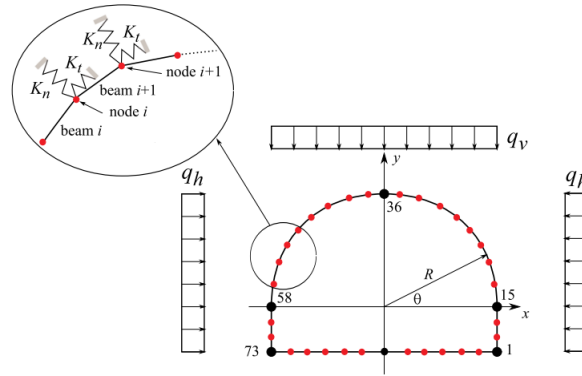


Fig. 1-50 Layout of the model, horizontal (q_h) and vertical loads (q_v) and node numbers ($R = 5.75$ m) (Barpi et al., 2011)

The parameters, e.g. the stiffnesses of the springs K_n , K_t and the elastic modulus of ground E_s , are considered to be fuzzy and associated with given membership functions. The variables of interest (output of the model), for instance the internal forces (bending moment $M(\theta)$ and normal force $N(\theta)$), are expressed by fuzzy numbers (q is represented in Fig. 1-50). The same applies to any other output of the model, i.e., stresses in the boundary elements or in the structural elements. It means that $M(\theta)$ and $N(\theta)$ are associated with a certain membership function to be determined by finding, for each level $0 \leq \alpha \leq 1$:

$$\min/\max M(\theta; K_n^\alpha; K_t^\alpha; E_s^\alpha; \dots) \quad \alpha \in [0,1]$$

$$\min/\max N(\theta; K_n^\alpha; K_t^\alpha; E_s^\alpha; \dots) \quad \alpha \in [0,1]$$

The solution is found by minimizing and maximizing the fuzzy variables and calculating displacements, stresses, internal forces (or any other parameters of interest) for each level of α .

Two different tunnel shapes were examined to assess the influence of shape. Each of them is described by the membership functions with symmetrical triangular shape with respect to the reference values shown in Fig. 1-51.

In rock tunnels the lining is usually made of steel ribs and shotcrete and in the design the steel ribs are usually considered in contact with the rock along its whole length. The results of the analyses in terms of M , and N on element 48 (located at the base of the arch, i.e., for $q = 0$ in Fig. 1-50) for shotcrete and steel ribs are then shown in Fig. 1-52 (case 1) and Fig. 1-53 (case 2).

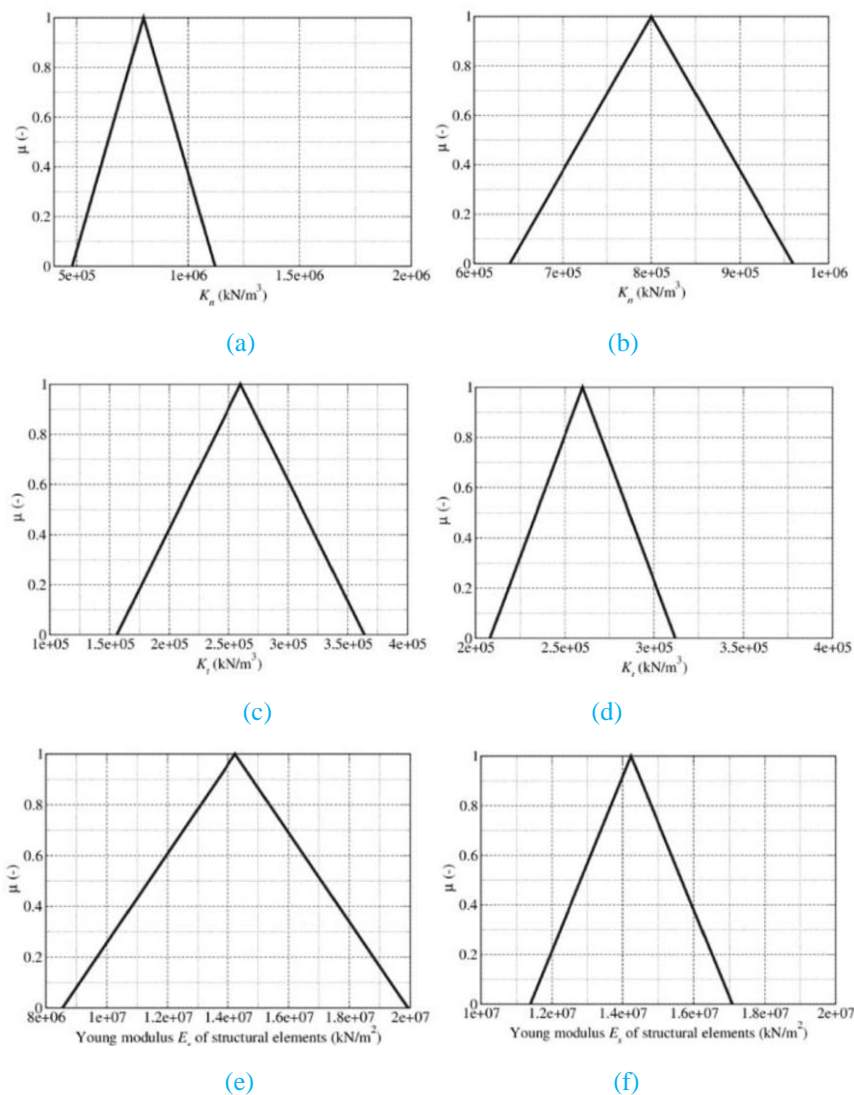


Fig. 1-51 Membership functions for K_n , K_t and E_s for case 1 (a, c, e) and case 2 (b, d, f); μ means the grade of membership (Barpi et al., 2011)

By using a safety factor of 1.5, some points for shotcrete fall outside the diagram, which means a bending failure (Fig. 1-52). Similar considerations apply to Fig. 1-53 based on the membership functions represented in Fig. 1-51. It must be pointed out that the data represented in Figs. 1-52 and 1-53 are related to the values of $\alpha=0$ and 1 (the minimum and the maximum α in the triangular used membership function of input parameters). The computed results (bending moments, normal force and shear force) are therefore represented by two different values: the minimum and the maximum that correspond to the chosen α -cut. Since the chosen membership function of input parameters is of triangular shape, for $\alpha =0$ there are the two values of the computed results while for $\alpha = 1$ (the reference values) the two values are coincident.

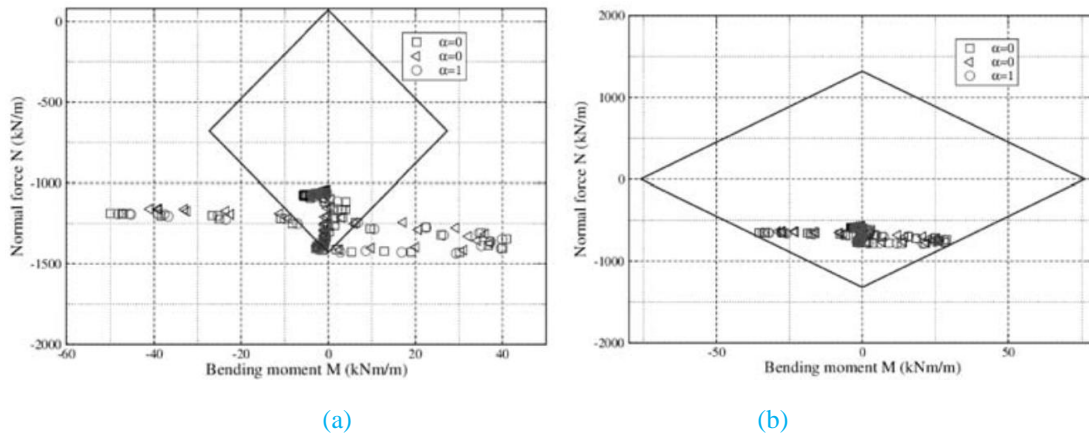


Fig. 1-52 Bending moment vs. normal force for shotcrete (a) and steel ribs (b) (case 1) (Barpi et al., 2011)

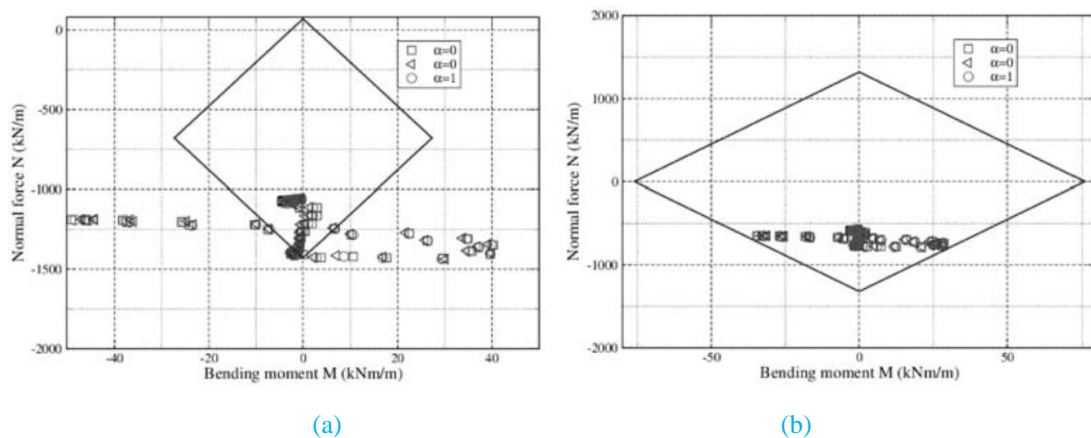


Fig. 1-53 Bending moment vs. normal force for shotcrete (a) and steel ribs (b) (case 2) (Barpi et al., 2011)

Lastly, they given the conclusion that if the average thickness is not considered, a wrong design could be obtained since the designed lining could be not adequate to support the applied loads, and cracks and damages could occur.

Prasetyo and Gutierrez (2016) carried out a series of numerical studies to examine the effect of surface loading on the hydro-mechanical (H-M) response of a horseshoe-shaped tunnel in saturated ground. Two tunnel models were created in the computer code Fast Lagrangian Analysis of Continua (FLAC). One model represented weak and low permeability ground (stiff clay), and the other represented strong and high permeability ground (weathered granite). Each of the models was run under two liner permeabilities: permeable and impermeable. Two main cases were compared. In Case 1, the surface load was applied 10

years after tunnel construction. In Case 2, the surface load was applied after the steady state pore pressure condition was achieved.

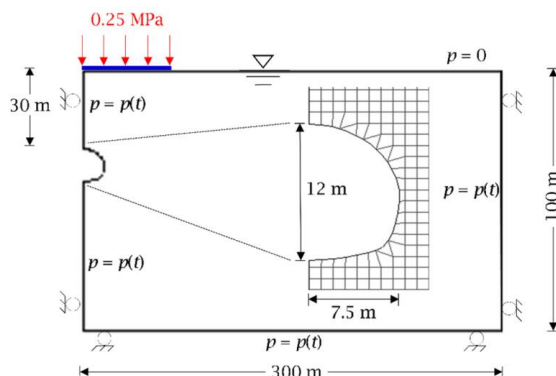


Fig. 1-54 Cross-section of the FLAC tunnel model with displacement and fluid flow boundary conditions (Prasetyo and Gutierrez, 2016)

The tunnel model in their study was built in FLAC under the plane-strain condition as a 12 m by 15 m horseshoe-shaped tunnel that was externally loaded with a surface pressure of 0.25 MPa over a width of 30 m (Fig. 1-54). Due to the assumption of vertical symmetry in the problem, only half of the problem was modelled. The model boundary was 100 m by 300 m, with the tunnel located 30 m below the groundwater table. For the mechanical boundary conditions, the horizontal displacement at the left and far-field boundaries and the vertical displacement at the bottom boundary were fixed. For the hydraulic boundary conditions, the pore pressure was free to change at the left, far-field, and bottom boundaries but fixed at zero at the top of the model. The pore pressure boundary at the tunnel boundary was either fixed at zero or free depending on the liner permeability used (permeable or impermeable). The results of the simulations for the two main cases were presented.

Fig. 1-55 shows the inward radial displacements around the tunnel boundary after surface loading in both cases. It can be found that the surface loading in Case 2 uniformly increased the inward deformations in the permeable tunnels in both grounds. The inward deformations in clay (Fig. 1-55a) and granite (Fig. 1-55b) were uniformly larger by -2.8 cm and -0.5 cm than those in Case 1, respectively. These deformations generated vertical closures of -6.5 cm for clay and -2.5 cm for granite. For the impermeable tunnels, the surface loading in Case 2 also induced substantial compression at the crown and heave at the invert, generating larger vertical closure than in Case 1. In clay, the surface loading in Case 2 induced vertical closure of up to -13.7 cm, which was -6.4 cm larger than that in Case 1 (-7.3 cm). In granite, the closure was -5.9 cm,

which was -1.3 cm larger than that in Case 1 (-4.6 cm). These results show that the liner permeability played an important role in the deformation behaviour around the tunnel. This was particularly obvious in Case 2, in which the vertical closures for the impermeable tunnels were approximately twice as large as those in permeable tunnels in both grounds.

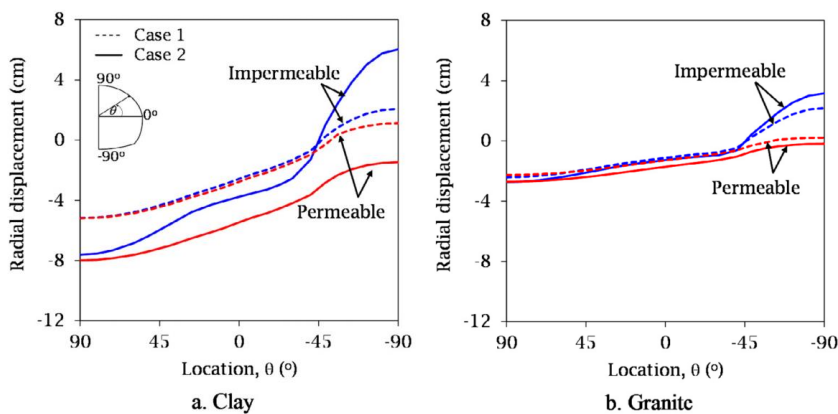


Fig. 1-55 Plots of inward radial displacements around the tunnel boundary after surface loading in both cases (Prasetyo and Gutierrez, 2016)

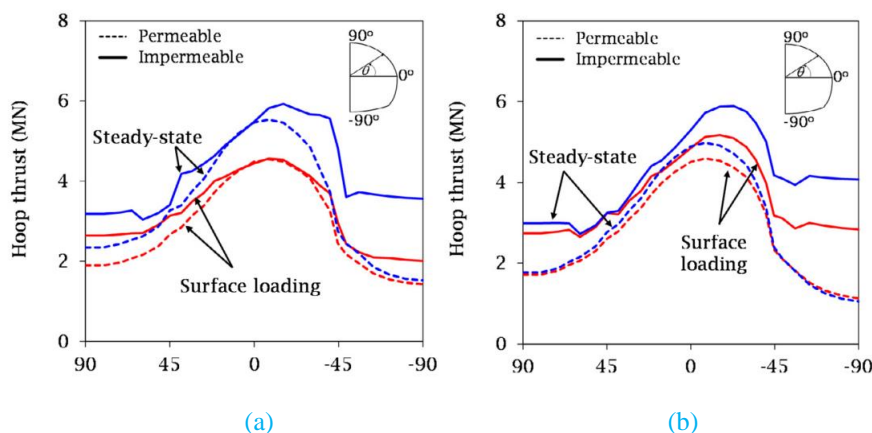


Fig. 1-56 Plots of normal force for (a) clay and (b) granite in Case 1 at both states (Prasetyo and Gutierrez, 2016)

In terms of the induced thrusts and bending moments in the liners, the results in Case 1 showed that the bending moment largely determined the liner stability. The induced normal forces in the liner in Case 1 were still far beyond the compressive yield strength of the liner (Fig. 1-56). In Case 2, a similar situation was observed for the normal forces. Hence, they only gave the induced bending moments and compared to those in Case 1 (Fig. 1-57). After the surface load was applied, the induced bending moments in the permeable liners between Case 1 and Case 2 were similar in each ground (Fig. 1-57a and b). However, in the impermeable liners, the bending moments in Case 2 were larger than those in Case 1, particularly for the tunnels in clay. In

this ground, the inward bending moment at the invert in Case 2 (3.3 MN.m) was up to 3.5 times larger than that in Case 1 (0.9 MN.m), while it was only 1.4 times larger than that in granite (1.3 MN.m in Case 1 and 1.9 MN.m in Case 2). At steady state, the differences in long-term bending moments between Case 1 and Case 2 were negligible (Fig. 1-57c and d). However, in both cases, the long-term bending moments in the impermeable liners were higher than those after the surface load was applied. In the permeable liners, the variations were not significant.

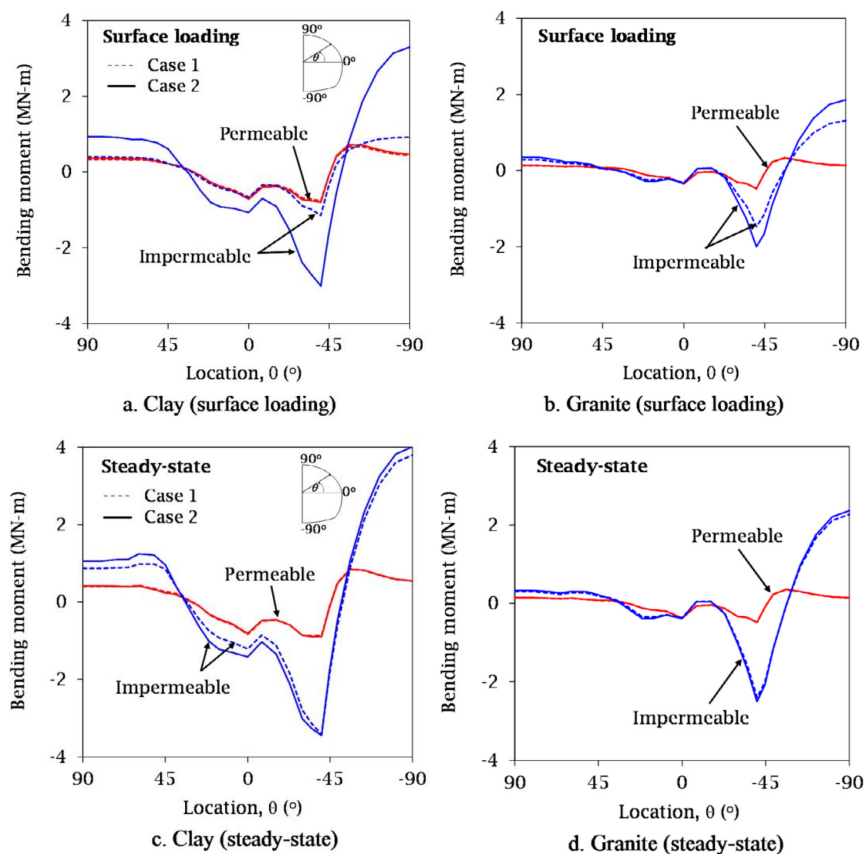


Fig. 1-57 Plots of the induced bending moment in the liner (a, b) after surface loading and (c, d) at the steady-state in both cases (Prasetyo and Gutierrez, 2016)

The short- and long-term liner stability under surface loading and at steady state in each case was then compared (Fig. 1-58). In clay (Fig. 1-58a and b), the long-term liner stability for the permeable tunnel was poorer than that after the surface load was applied, but not significantly poorer. The tunnel was unstable at both states, and there was no difference in the stability condition between the tunnels in Case 1 and in Case 2. For the impermeable tunnel, the short-term stability condition in Case 2 was significantly poorer than that in Case 1. However, the difference in the stability condition became insignificant at steady state because of the

worsening condition in Case 1 due to the continuous tunnel closure. In granite (Fig. 1-58c and d), the permeable tunnel in Case 2 was able to withstand the short- and long-term H-M responses induced by surface loading. The combination of thrusts and bending moments for the tunnel in Case 2 stayed within the envelope for a factor of safety 1.5, which was similar to the trend observed in Case 1. For the impermeable tunnels, there was a minor difference in the stability conditions between the two cases after the surface load was applied. However, at steady state, the difference became negligible. Nevertheless, the tunnels in both cases were unstable in the short term and long term.

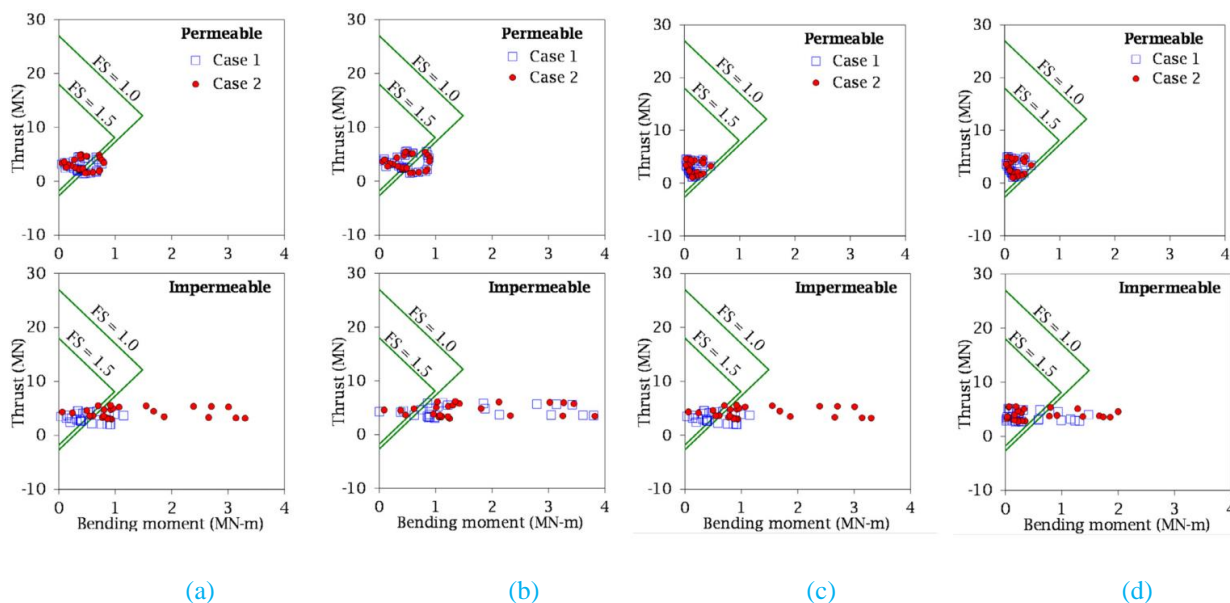


Fig. 1-58 Comparison of the liner interaction diagrams (a) clay with surface loading, (b) clay with steady-state, (c) granite with surface loading and (d) granite with steady-state in both cases (Prasetyo and Gutierrez, 2016)

The simulation results show that tunnels with impermeable liners experienced the most severe influence from the surface loading, large inward displacement around the tunnels, and high bending moments in the liner. In addition, the severity of the response increased toward steady state. This induced H-M response was worse for tunnels in clay than for those in granite. Furthermore, the long-term liner stabilities in Case 1 and Case 2 were similar, indicating that the influence of the length of time between when the tunnel was completed and when the surface load was applied was negligible. These findings suggest that under surface loading, tunnel stability in saturated ground is largely influenced by liner permeability and the long-term H-M response of the ground.

In order to provide a set of feasible solutions for the design, manufacture, and construction of non-circular TBMs, Li (2017) investigated the optimization design of the non-circular tunnel structure. The front tunnel is designed as a quasi-rectangle with an upper arch, which consists of a tapered front cross-section and a box-type rear cross-section in order to improve the mechanical behaviour (Fig. 1-59a). According to the finite element analysis of the front tunnel, it is found that the maximum stress of the front tunnel should be less than 85.329 MPa (Fig. 1-59b) in order to satisfy the operating requirements. The maximum deformation of the front tunnel is 4.6134 mm, and is located at the middle of the rear part of the front tunnel (Fig. 1-59c). In order to improve the mechanical behaviour and deformation of the tunnel, it is recommended to increase the vertical support beam between the gusset plates to enhance structural stiffness (Fig. 1-59d). The stress distribution and deformation of the front tunnel after optimization are shown in Fig. 1-59e and f, respectively, under the same load condition.

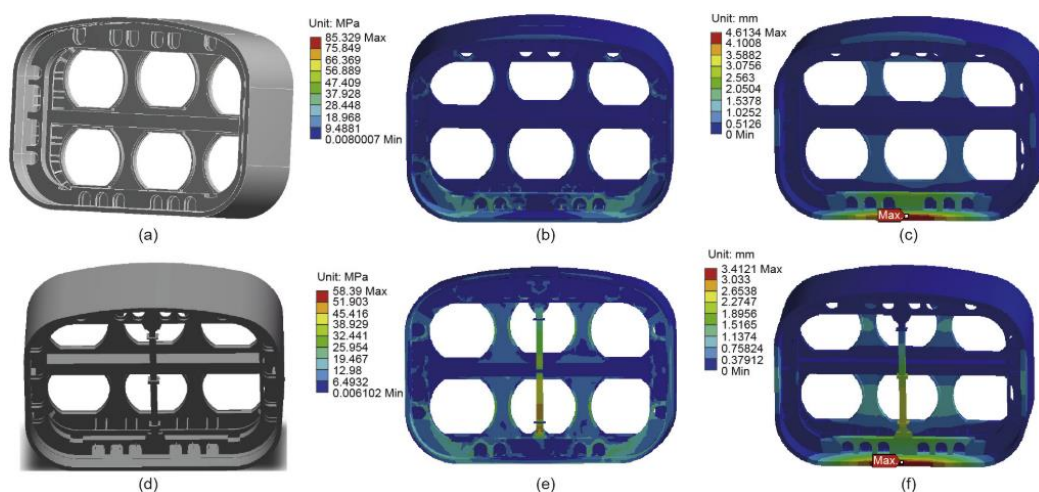


Fig. 1-59 (a) Structure design of the front tunnel; (b) stress distribution of the front tunnel; (c) deformation of the front tunnel; (d) optimized structure of the front tunnel; (e) stress distribution of the optimized front tunnel; (f) deformation of the optimized front tunnel (Li, 2017)

Summary

The numerical analysis methods can deal with various soil and rock properties, geometrical properties, and complex boundary conditions, especially when a complex three-dimensional problem is studied. Numerical simulations can be used for both two-dimensional (2D) and three-dimensional (3D) studies of

tunnel design. Generally, the most numerical models are usually time-consuming comparing with the analytical methods. Although tunnel excavation is a 3D problem and the 3D numerical simulation could be the better way to simulate a tunnel excavation, the 3D models usually takes much more time than 2D ones. Therefore, the 2D simulations are sometimes a better choice when the requirement for the accuracy of calculation is not high. Although most numerical simulations are time-consuming, they can be desirable in the validation and verification of analytical solutions.

4. Conclusions

This chapter mainly presents a literature review on the design methods of non-circular tunnels. In the first section, the procedure of tunnel lining design is introduced in details according to the [ITA-Group2 recommendations \(2000\)](#). It can be divided into 8 steps, in which the computation of forces of lining plays a key role in the tunnel design.

In the second section, the effect of tunnel shape on the lining behaviour is summarized. Generally, the circular tunnels have more stability than the non-circular ones. When the tunnel shape becomes flat, the normal force becomes the dominant part to be supported by the tunnel. Specially, stress concentration around corners increases sharply as the tunnel shape becomes non-circular. However, as a large amount of the excavated soil is generated and lots of space is unutilized, the circular cross section is not so useful in terms of space use. Compared with traditional circular tunnels, the non-circular cross-section tunnels have several advantages: 1) underground space can be more effectively utilized by designing the tunnel to have a configuration that matches the tunnel purpose, 2) the degree of adverse impact from the surrounding environment can be decreased, and 3) the quantity of excavation can be reduced. In addition, as one kind of non-circular tunnels, the quasi-rectangular tunnel is a new type of structure in tunnelling. It combines the advantages of circular and rectangular tunnel, and will surely be widely used in the future.

The third section introduces the design methods of non-circular tunnels. The methods are classified into three categories: experimental studies, theoretical and numerical analysis methods. The applications of three categories of lining design methods are described separately. Compared with the analytical and numerical methods, the experimental studies are generally more expensive. The theoretical analysis models have an advantage of rather low computational cost with a good accuracy. However, those analytical methods could

only be used for the corresponding specific types of case due to those assumptions on which they are based. In contrast, the numerical analysis methods can deal with various soil and rock properties, geometrical properties, complex boundary condition, but the most numerical models are time-consuming.

In practical engineering, it is required that the internal force and displacements of the tunnel lining should be estimated quickly and effectively facing different geological conditions in the preliminary tunnel design stage. Although the existing design methods of non-circular lining mentioned above are given considering different conditions, e.g. surface loading, underground water, stratified ground, etc, these methods are either time-consuming or complex. No one of them can be used to consider all kind of design factors. As non-circular tunnels are increasingly encountered in practice, there is a need to find an effective and efficient method which could be used to analyse the internal forces and displacement of non-circular tunnel lining in the preliminary design. The hyperstatic reaction method (HRM) method is particularly suitable for the precise and effective estimation of tunnel lining behaviour, in terms of structural forces and lining displacements along the support profile with a short calculation time (several seconds). Therefore, the objectives of this research are mainly to improve and develop a new computational tool based on the HRM method for the study of the non-circular tunnel lining behaviour, which consist of the analysis of U-shaped tunnel behaviour in terms of the internal forces and displacement of tunnel lining under different conditions (Chapters 2-5), and to optimize the sub-rectangular tunnel shape (Chapter 6). In addition, the temperature change may have an effect on circular tunnel lining behaviour. Therefore, in the last chapter of this manuscript, the thermo-mechanical behaviour of a circular tunnel is investigated by means of the HRM method.

CHAPTER 2 BEHAVIOUR ANALYSIS OF U-SHAPED TUNNEL SUPPORTS (WITH INVERT)

As U-shaped tunnels are often encountered in practice, there is a need to find an effective and efficient method which can be used to analyse the behaviour of this kind of tunnel in the preliminary design of a tunnel. For the dimensioning of support structures, a simplified analytical method, convergence-confinement method (CCM) (Hoek and Brown 1980; Brown et al. 1983; Panet 1995; Oreste 2003), can be used. This method is able to simulate the displacements and the loads of the supports, but the internal forces used to determine the correct dimensioning of the support structures are not given. Einstein and Schwartz (1979) presented the other simplified approach to get the axial forces and bending moments of the circular tunnels support structures in elastic medium. Their method, however, neglected the relaxation process induced by the excavation around the tunnel before the support structure installation.

The development of computers and limitations of analytical methods have led to an increase of the use of numerical methods for designing tunnel support. Although the numerical analysis methods can deal with various soil and rock properties, geometrical properties, complex boundary condition, most numerical models are time-consuming. As a numerical method, the hyperstatic reaction method (HRM) (Duddeck and Erdmann 1985; Leca and Clough 1992; Oreste 2007; Do et al., 2014d) is different from the other numerical methods. Lots of independent Winkler-spring methods are used in the HRM method to simulate the interaction between the support and the soil mass surrounding the tunnel. The HRM method could be effectively used to design support structures with a very short calculation time. It is particularly suitable for analyses with many calculations and for the estimation of the tunnel lining behaviour, in terms of structural forces, lining displacement and passive ground pressure along the support profile. Also, the effective geometry of the support and the horizontal active loads could be considered in the HRM code. The HRM method requires the definition of the active loads applied directly to the support structure by the rock mass. Those loads can be estimated using different methods that were already presented in the literature or they can be estimated backwards on the basis of in situ monitoring, using back-analysis procedures.

Oreste (2007) investigated the behaviour of a circular tunnel on the basis of the HRM method. The interaction of ground and structure was described only by normal springs. Design tables were drawn up to summarise the results of the parametric analyses. From these tables, it is possible to verify the influence of the

various calculation parameters on the dimensioning of the support structure and to obtain indications on the support structures behaviour in the preliminary stages of a project. Although a useful step forward, the solution proposed by Oreste (2007) does not consider the tangential stiffness of the tunnel-soil interaction. Do et al. (2014d) extended the HRM approach proposed by Oreste (2007) to study the behaviour of segmental tunnel support considering the normal and shear springs.

The main purpose of this chapter is to present an improved numerical approach to the HRM for the analysis of U-shaped tunnel supports. The present model is developed on the basis of the ones proposed by Oreste (2007) and Do et al. (2014d). Unlike the model of Oreste (2007), since the tunnel bottom usually bears the active loads applied by the soil, an active external load applied at the tunnel bottom in the upward direction (Fig. 2-1) is considered to improve the model. In addition, as the structure may have strain in the tangential direction, therefore, the presence of tangential springs has also been taken into consideration to simulate the same external load scheme as the one used in the model of Do et al. (2014d).

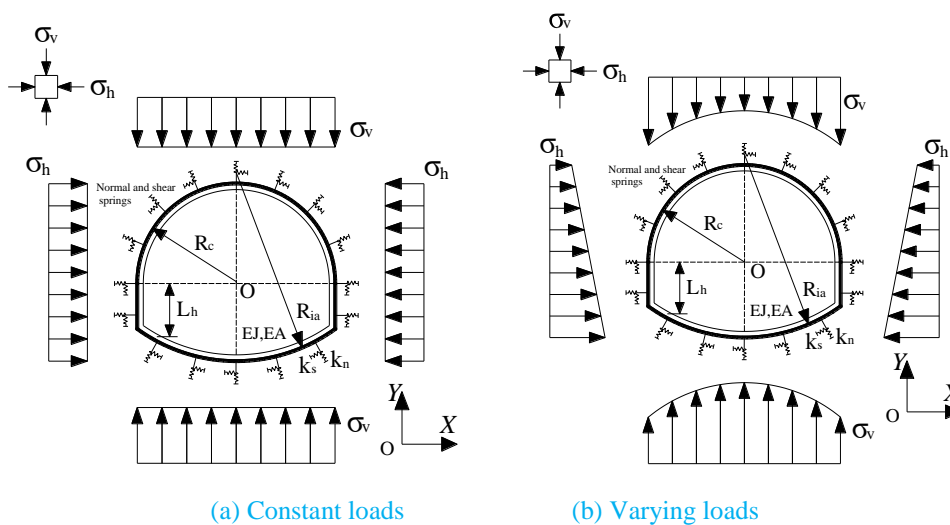


Fig. 2-1 Calculation scheme of U-shaped support structures with the HRM. With: σ_v : vertical stress; σ_h : horizontal stress; k_n and k_s : stiffness of the Winkler-springs; R_{ia} : radius of the invert arch; R_c : crown radius; L_h : vertical length from the point of tunnel cross-section to x axis; EJ and EA : bending and normal stiffness of support

When the tunnels are located at shallow depths, e.g. the cover-to-diameter ratio $C/D < 2$, the gravity effect on the change in external loads acting on the tunnel lining could be significant and the vertical stress variation should be considered. Therefore, two different loads are taken in this chapter, one represented by constant loads (Fig. 2-1a - case of deep tunnels), the other one considers the effect of the gravity over the

tunnel height (Fig. 2-1b - case of shallow tunnels). A comparison between the results of the HRM method and those of a numerical model based on the finite difference program FLAC^{3D} is made. Only some small discrepancies for those two methods are found, which allows the present method to be validated.

An extensive parametric analysis is developed to study the effect of the ground mass properties, tunnel support stiffness, applied loads and tunnel dimensions on the behaviour of tunnel lining. Some conclusions are obtained in terms of the influence of the parameters on the tunnel lining support design.

1. Mathematical expression of hyperstatic reaction method

One fundamental hypothesis, on which the numerical approach to the hyperstatic reaction method is based, is to subdivide the support structures into a finite number of linear sub-domains, named elements (which make it possible to describe the stress-strain law by a simple way). The support structure could therefore be represented by some mono-dimensional elements that are able to develop bending moments, axial forces and shear forces in the calculation (Fig. 2-2). They are connected to the outside through springs that are distributed over the nodes.

The beam element i is defined by means of the following parameters: the inertia modulus J and area A of the transversal section, the elastic modulus E of the constituent material and length L_i (distance between the terminal connecting nodes). In bi-dimensional methods, reference is made to a unitary thickness and therefore the parameters J and A should also be calculated considering the sum of the inertia modules and the areas that are involved in the support for a unitary length in the direction of the tunnel axis.

Therefore, the ground mass interacts with the support in two ways: through normal and tangential springs connected to the nodes of the structure and through applied active loads (Fig. 2-3).

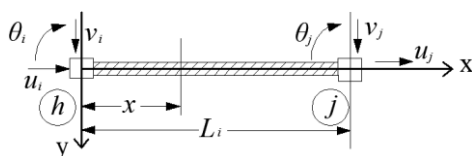


Fig. 2-2 Scheme of the behaviour of a beam-type finite element with reference to the local Cartesian coordinates With: h : initial node; j : final node; u : axial displacement; v : transversal displacement; θ : rotation; x and y : local Cartesian coordinates; L_i : the length between the terminal connecting nodes

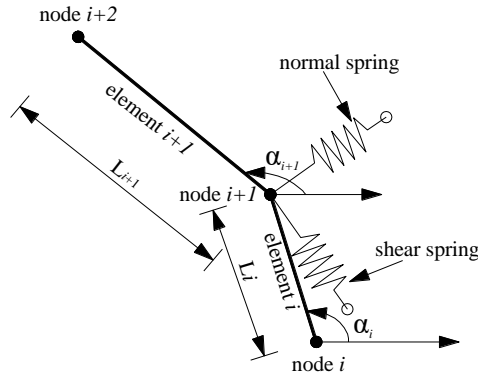


Fig. 2-3 Scheme of the ground–support interaction through springs connected to the support nodes

The unknowns of the problem are the displacement components of the nodes of those elements. The stresses inside each element and along the entire support structure could be obtained after these unknown displacements determined. The evaluation of the unknown displacements is made by defining the global stiffness matrix of the entire structure. The global stiffness matrix is assembled using the local stiffness matrices of each single element as illustrated in Huebner et al. (2001).

The local stiffness matrix Z_i of the i element in the local Cartesian reference system could be achieved by equating the work of the inner forces of the finite element to the ones of the external nodal forces, which is evaluated according to a local reference system (Huebner et al., 2001).

$$Z_i = \begin{bmatrix} \frac{EA}{L_i} & 0 & 0 & -\frac{EA}{L_i} & 0 & 0 \\ 0 & \frac{12EI}{L_i^3} & \frac{6EI}{L_i^2} & 0 & -\frac{12EI}{L_i^3} & \frac{6EI}{L_i^2} \\ 0 & \frac{6EI}{L_i^2} & \frac{4EI}{L_i} & 0 & -\frac{6EI}{L_i^2} & \frac{2EI}{L_i} \\ -\frac{EA}{L_i} & 0 & 0 & \frac{EA}{L_i} & 0 & 0 \\ 0 & -\frac{12EI}{L_i^3} & -\frac{6EI}{L_i^2} & 0 & \frac{12EI}{L_i^3} & -\frac{6EI}{L_i^2} \\ 0 & \frac{6EI}{L_i^2} & \frac{2EI}{L_i} & 0 & -\frac{6EI}{L_i^2} & \frac{4EI}{L_i} \end{bmatrix} \quad (2-1)$$

Therefore, one can obtain:

$$Z_i \cdot S_i = G_i + R_i \quad (2-2)$$

with S_i : the vector of the displacement at nodes h and j of the element i , evaluated according to the local reference system:

$$S_i = [u_{h,i} \ v_{h,i} \ \theta_{h,i} \ u_{j,i} \ v_{j,i} \ \theta_{j,i}]^T \quad (2-3)$$

with u and v : the axial and transversal displacement in the local reference system, θ : the rotation of the element in correspondence to the nodes. G_i and R_i : the external nodal forces and the nodal forces applied by the neighboring elements. In the global Cartesian reference system, the nodal displacements $q_{h \div j, i}$ are connected to S_i through the λ_i , which is the transformation matrix:

$$S_i = \lambda_i \cdot q_{h \div j, i} \quad (2-4)$$

where:

$$q_{h \div j, i} = \begin{bmatrix} w_{h, i} \\ z_{h, i} \\ \varphi_{h, i} \\ w_{j, i} \\ z_{j, i} \\ \varphi_{j, i} \end{bmatrix} = [q_{i+1}] \quad (2-5)$$

$$\lambda_i = \begin{bmatrix} \cos \alpha_i & \sin \alpha_i & 0 & 0 & 0 & 0 \\ -\sin \alpha_i & \cos \alpha_i & 0 & 0 & 0 & 0 \\ 0 & 0 & 1 & 0 & 0 & 0 \\ 0 & 0 & 0 & \cos \alpha_i & \sin \alpha_i & 0 \\ 0 & 0 & 0 & -\sin \alpha_i & \cos \alpha_i & 0 \\ 0 & 0 & 0 & 0 & 0 & 1 \end{bmatrix} \quad (2-6)$$

with $q_{h \div j, i}$: the vector of the nodal displacements of element i ; q_i : the vector of the nodal displacements of node i ; w and z : the displacements along axis x and along axis y of the global Cartesian reference system; φ : rotation of node in the global Cartesian reference system; α_i : the angle between the local Cartesian reference system of element i and the global Cartesian reference system.

The nodal forces G_i and R_i are given by the following matrix expressed in the global Cartesian reference system:

$$G_i = \lambda_i \cdot F_{h \div j, i} \quad (2-7)$$

$$R_i = \lambda_i \cdot Q_{h \div j, i} \quad (2-8)$$

Making the necessary substitutions, the following equation in the global Cartesian reference system could be obtained:

$$k_i \cdot q_{h \div j, i} = F_{h \div j, i} + Q_{h \div j, i} \quad (2-9)$$

The local stiffness matrix k_i of element i in the global Cartesian reference system:

$$k_i = \lambda_i^T \cdot Z_i \cdot \lambda_i \quad (2-10)$$

The global stiffness matrix K is assembled by the local stiffness matrix k_i ($i=1, 2, 3, \dots, n$ in the analysis) of i^{th} element in the global Cartesian reference system by means of the criteria described in Huebner et al. (2001). The global stiffness matrix K is constituted by $(3n+3) \times (3n+3)$ elements, where n is the total number of nodes.

$$K \cdot q = F \quad (2-11)$$

$$\begin{bmatrix} k_{1,a} & k_{1,b} & 0 & 0 & 0 & 0 \\ k_{1,c} & k_{1,d} + k_{2,a} & k_{2,b} & 0 & 0 & 0 \\ 0 & k_{2,c} & k_{2,d} + k_{3,a} & k_{3,b} & 0 & 0 \\ 0 & 0 & k_{3,c} & k_{3,d} + k_{4,a} & \dots & 0 \\ 0 & 0 & 0 & \dots & \dots & k_{n,b} \\ 0 & 0 & 0 & 0 & k_{n,c} & k_{n,d} \end{bmatrix} \cdot \begin{bmatrix} q_1 \\ q_2 \\ q_3 \\ \dots \\ q_{n+1} \end{bmatrix} = \begin{bmatrix} F_1 \\ F_2 \\ F_3 \\ \dots \\ F_{n+1} \end{bmatrix} \quad (2-12)$$

with $k_{i,a}$, $k_{i,b}$, $k_{i,c}$, $k_{i,d}$ are the sub-matrices of k_i , each of which is of 3×3 dimension; $q_1, q_2, q_3, \dots, q_{n+1}$ are the sub-vectors of the three displacements of each node and $F_1, F_2, F_3, \dots, F_{n+1}$ are the sub-vectors of the three external forces applied to each node in the global Cartesian reference system.

Some elements of the global stiffness matrix K need to be modified along the diagonal due to the presence of normal and tangential node springs (Fig. 2-3). These changes are considered by modifying the corresponding elements in function of the stiffness of the normal (k_n) and shear (k_s) interaction springs of each node and the angle between the local and global reference systems (α) for each element.

$$K_{3i-2,3i-2}^* = K_{3i-2,3i-2} + k_{n,i} \cdot \cos^2 \left(\frac{\alpha_{i+1}}{2} + \frac{\alpha_i}{2} - \frac{\pi}{2} \right) + k_{s,i} \cdot \sin^2 \left(\frac{\alpha_{i+1}}{2} + \frac{\alpha_i}{2} - \frac{\pi}{2} \right) \quad (2-13)$$

$$K_{3i-1,3i-1}^* = K_{3i-1,3i-1} + k_{n,i} \cdot \sin^2 \left(\frac{\alpha_{i+1}}{2} + \frac{\alpha_i}{2} - \frac{\pi}{2} \right) + k_{s,i} \cdot \cos^2 \left(\frac{\alpha_{i+1}}{2} + \frac{\alpha_i}{2} - \frac{\pi}{2} \right) \quad (2-14)$$

$$K_{3i-1,3i-2}^* = K_{3i-1,3i-2} + (k_{n,i} - k_{s,i}) \cdot \sin \left(\frac{\alpha_{i+1}}{2} + \frac{\alpha_i}{2} - \frac{\pi}{2} \right) \cdot \cos \left(\frac{\alpha_{i+1}}{2} + \frac{\alpha_i}{2} - \frac{\pi}{2} \right) \quad (2-15)$$

$$K_{3i-2,3i-1}^* = K_{3i-2,3i-1} + (k_{n,i} - k_{s,i}) \cdot \sin \left(\frac{\alpha_{i+1}}{2} + \frac{\alpha_i}{2} - \frac{\pi}{2} \right) \cdot \cos \left(\frac{\alpha_{i+1}}{2} + \frac{\alpha_i}{2} - \frac{\pi}{2} \right) \quad (2-16)$$

where: i is the number of the generic node; $k_{n,i}$ is the stiffness of the normal interaction spring connected to node i ; $k_{s,i}$ is the stiffness of the tangential interaction spring connected to node i ; α_i and α_{i+1} are respectively the angles between the local and global reference systems, for element i and for element $i+1$ (Fig. 2-3).

Once the vector S is obtained, a conversion of the nodal displacements at the local reference system of the element is easily achieved. Then the characteristic of nodal stresses can immediately be determined through the local stiffness matrix.

1.1 Ground-support interaction

In the HRM model, the structure support interacts with the surrounding mass in two ways: through springs connected to the nodes of the structures (Fig. 2-3) and through the applied active loads.

A nonlinear (hyperbolic) pressure-displacement ($p - \delta$) relation was introduced by Oreste (2007) to describe the relation between the reaction pressure p and the support deformation δ :

$$p = p_{lim} \cdot \left(1 - \frac{p_{lim}}{p_{lim} + \eta_0 \cdot \delta}\right) \quad (2-18)$$

where p_{lim} is the maximum reaction pressure offered by the ground mass and η_0 is the initial stiffness (when the value of δ is close to 0) of the ground mass.

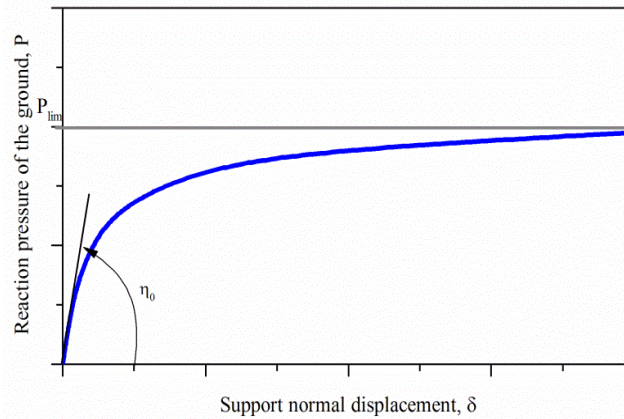


Fig. 2-4 Relationship between reaction pressure p and support deformation δ

The apparent stiffness η^* of the ground mass which is not constant is given by the p/δ ratio obtained at each node of the support structure:

$$\eta^* = \frac{p_{lim}}{\delta} \cdot \left(1 - \frac{p_{lim}}{p_{lim} + \eta_0 \cdot \delta}\right) \quad (2-19)$$

The initial normal ground stiffness $\eta_{n,0}$ can be determined by this empirical formula detailed in [Müller \(2006\)](#):

$$\eta_{n,0} = \beta \frac{1}{1+\nu_s} \cdot \frac{E_s}{R} \quad (2-20)$$

with E_s : initial elastic modulus of the ground mass; R : tunnel radius (radius of the crown tunnel); ν_s : Poisson's ratio of the ground mass; β : dimensionless factor. It should be noticed that the value of β depends on soil and structural parameters, and it is difficult to determine the exact β value. In this analysis, its value is chosen based on the comparison between the results of the HRM and the FLAC.

The shear stiffness at the support-ground interface is quite hard to estimate. In this analysis, the following simple relationship between the normal stiffness (η_n) and tangential stiffness (η_s) was adopted ([Mashimo and Ishimura, 2005](#); [Plizzari and Tiberti 2006](#); [Arnau and Molins 2011](#); [Barpi et al. 2011](#)):

$$\eta_s = \frac{1}{3} \eta_n \quad (2-21)$$

The maximum normal reaction pressure $p_{n,lim}$ depends on the cohesion c , friction angle φ , Poisson's ratio ν_s of the ground, and active loads:

$$p_{n,lim} = \frac{2 \cdot c \cdot \cos \varphi}{1 - \sin \varphi} + \frac{1 + \sin \varphi}{1 - \sin \varphi} \cdot \frac{\sigma_h + \sigma_v}{2} \cdot \frac{\nu_s}{1 - \nu_s} \quad (2-22)$$

The maximum shear reaction pressure $p_{s,lim}$ is estimated by:

$$p_{s,lim} = \frac{\sigma_h + \sigma_v}{2} \cdot \tan \varphi \quad (2-23)$$

Then the normal stiffness $k_{n,i}$ and shear stiffness $k_{s,i}$ of each spring are given by the formulas:

$$k_{n,i} = \eta_{n,i}^* \cdot \left[\frac{(L_{i-1} + L_i)}{2} \cdot 1 \right] = \frac{p_{n,lim}}{\delta_{n,i}} \cdot \left(1 - \frac{p_{n,lim}}{p_{n,lim} + \eta_{n,0} \cdot \delta_{n,i}} \right) \cdot \frac{(L_{i-1} + L_i)}{2} \quad (2-24)$$

$$k_{s,i} = \eta_{s,i}^* \cdot \left[\frac{(L_{i-1} + L_i)}{2} \cdot 1 \right] = \frac{p_{s,lim}}{\delta_{s,i}} \cdot \left(1 - \frac{p_{s,lim}}{p_{s,lim} + \eta_{s,0} \cdot \delta_{s,i}} \right) \cdot \frac{(L_{i-1} + L_i)}{2} \quad (2-25)$$

Clearly, the stiffness $k_{n,i}$ and $k_{s,i}$ of each spring connected to the nodes of the structure are functions of the unknown nodal displacements q_i .

1.2 Active loads

[Duddeck \(1988\)](#) proposed that a bedded-beam model or a continuum model without a reduction of ground pressure at the crown should be considered in design for shallow tunnels. Most models in the studies

of Einstein and Schwartz (1979), Duddeck and Erdmann (1985), Mödler (2006), Oreste (2007), and Do et al. (2014d) adopted the same vertical pressure loads at upper and lower parts of the tunnel support. For example, the tunnel supports of model mentioned by Oreste (2007) and Do et al. (2014d), were applied by the vertical constant loads, which are given by:

$$\sigma_v = \gamma \cdot H \quad (2-26)$$

with γ : the volumetric weight of ground; H : the depth of tunnel. The horizontal loads working on the tunnel support are also constant and can be written as:

$$\sigma_h = K_0 \cdot \sigma_v \quad (2-27)$$

where K_0 : the lateral earth pressure coefficient.

If the overburden thickness is two times larger than the lining external diameter, an effective depth h_0 is considered. It is determined by means of the formula:

$$h_0 = \frac{B_1(1-c/(B_1\gamma_s))}{K_0 \cdot \tan\varphi} (1 - e^{-K_0 \cdot \tan\varphi \cdot (H/B_1)}) + \frac{P_0}{\gamma_s} \cdot (e^{-K_0 \cdot \tan\varphi \cdot (H/B_1)}) \quad (2-28)$$

$$B_1 = R_0 \cdot \cot(\pi/4 + \varphi/2) \quad (2-29)$$

where P_0 is the surcharge load.

In this analysis, the first case of loading conditions considers constant loads acting on the tunnel support (Fig. 2-1a). In the second case, considering the difference of the loads at the top and the bottom of tunnel support due to gravity, the linear variable loads applied on the tunnel support are also studied (Fig. 2-1b). In the proposed U-shaped tunnel HRM model shown in Fig. 2-1b, the vertical ground loads on the support vary and can be estimated as: $\sigma_v = \gamma \cdot (H + L_h)$, where L_h : the vertical length from the point of tunnel cross-section to the x axis (L_h is negative for the sections above the x axis). A comparison between the results obtained from both two cases of external loads is presented as well.

2. Calculation code and the dimensioning of support

The HRM calculation code is able to consider the support geometry (Fig. 2-5) and the type of constraint at the base of the tunnel support (Fig. 2-6). Due to the symmetry of the problem, only half of the tunnel is considered. The HRM method is particularly suitable for the dimensioning of preliminary supports and concrete final linings, due to considering the geometric shape and the stress field in the calculation code.

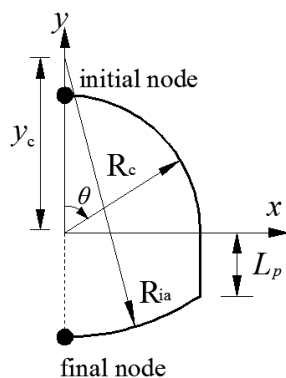


Fig. 2-5 Support geometry considered in the HRM calculation code. With: R_{ia} : radius of the invert arch; R_c : crown radius; L_p : sidewall length; y_c : height of the invert arch centre; θ : the angle between the vertical axis of cross-section of tunnel and the element axis, (θ is 0° at the initial node, θ is 90° at the connection of sidewall and crown)

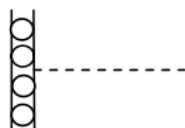


Fig. 2-6 Type of constraint foreseen (vertical clamped-roller) for the initial node and final node of geometry

Fig. 2-7 shows the positive direction of the structural forces and displacements (bending moment M , normal force N) in the analysis.

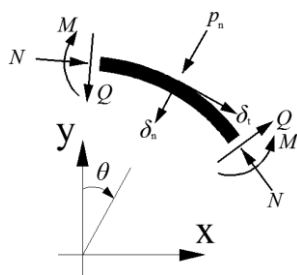


Fig. 2-7 Positive direction of the structural forces (M , N , Q), normal support displacement (δ_n), tangential support displacement (δ_t) and normal pressure (p_n)

It is possible to obtain the bending moments M , the normal forces N and the shear forces Q along the support profile, when the geometrical and mechanical parameters that influence the problem are defined. An analysis for the verification of the preliminary support is here given as an example (Toulon tunnel, France) using the HRM calculation code. The geometrical parameters of the tunnel, the soil parameters and of the adopted support structure are shown in Table 2-1. When the loads are constant, the vertical loads used in this calculation are equal to 0.88MPa, while the horizontal ones are equal to 0.44MPa.

Table 2-1 Geometric parameters of the Toulon tunnel

Parameter	Symbol	Value	Unit
<i>Properties of tunnel</i>			
Crown radius	R_c	6.02	m
Invert arch radius	R_{ia}	20.22	m
Height of the invert arch centre	y_c	15.00	m
Height of the sidewall	L_p	3.80	m
External diameter	D	10.74	m
Scale parameter in the x direction	m_x	1.00	-
Scale parameter in the y direction	m_y	1.00	-
Support thickness	t	0.22	m
Poisson's ratio	ν	0.15	-
Elastic modulus of concrete	E_0	35,000	MPa
<i>Properties of the ground</i>			
Cohesion	c	0.05	MPa
Unit weight	γ_s	22	kN/m ³
Poisson's ratio	ν_s	0.3	-
Internal friction angle	φ	20	°
Elastic modulus	E	300	MPa
Lateral earth pressure factor	K_0	0.5	-
Overburden	H	40	m

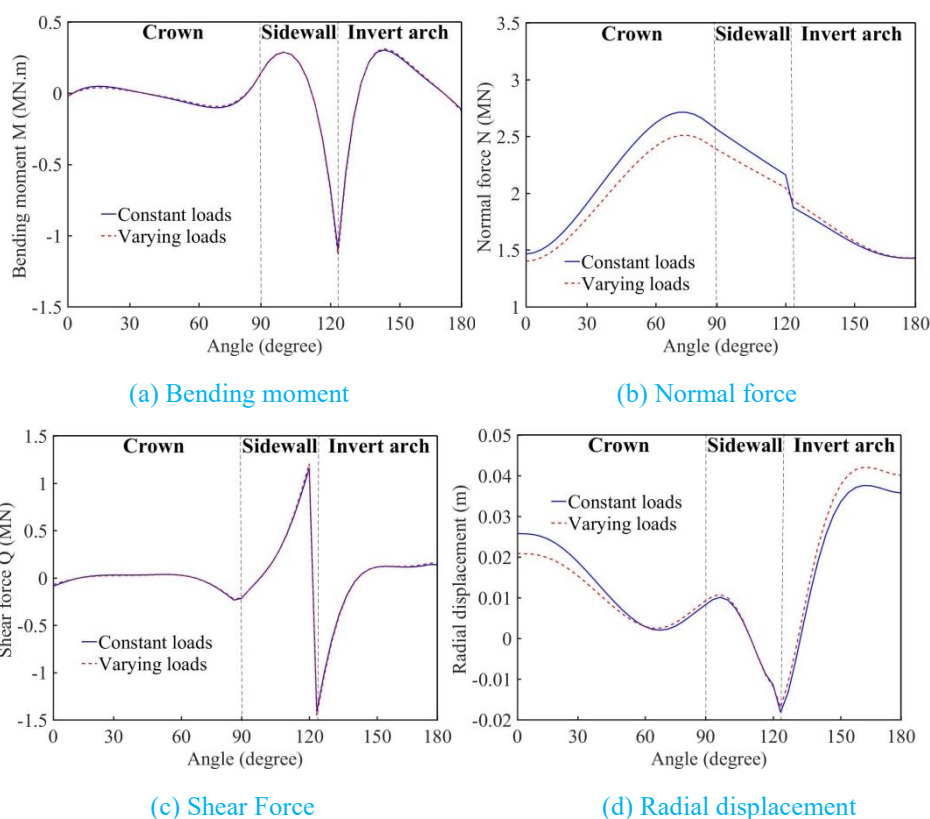
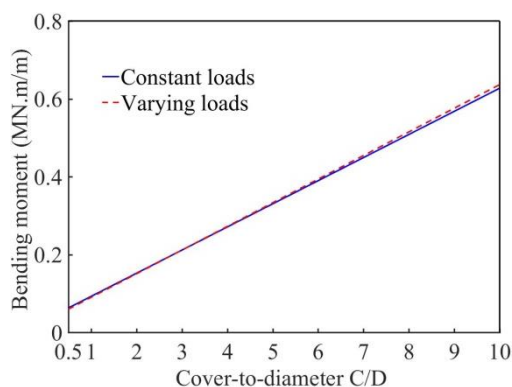


Fig. 2-8 Comparisons of results obtained from the calculation for the two cases of loads

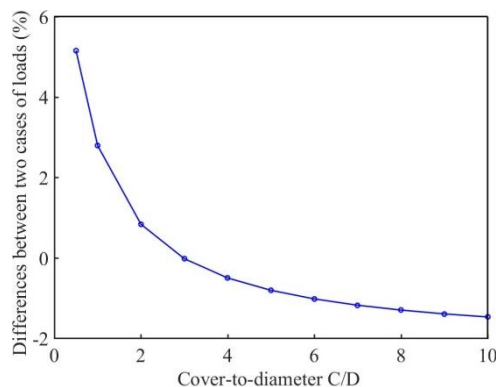
The comparisons of the results obtained from the calculations for the cases of constant loads and varying loads are shown in Fig. 2-8. It can be seen in Fig. 2-8 that the maximum moment M (in absolute value) is

located at the connection between the sidewall and invert arch. The other local maximum moments could be found at the invert arch and on the sidewalls. The normal forces show a peak value near the crown-sidewall connection. The normal forces almost have the same values at the centre of the crown and that of the invert arch. The shear forces show a peak value at the connection between the invert arch and the sidewall. They are almost constant in the sidewalls. The maximum radial displacement is located at the centre of the invert arch and the other local maximums can be found on the crown-sidewall connection and at the centre of the crown.

From Fig. 2-8, one can find that the internal forces and displacements, calculated by the two different load cases, have the similar trend. The solution of constant loads almost gives the same values of bending moments and shear forces as the varying loads case. However, the solution of constant loads gives higher values of normal forces than the one with varying loads at the crown and on the sidewall. Both these two loads cases give more less the same values at the tunnel invert arch. The maximum absolute discrepancy (7.9%) for normal forces is near the crown-sidewall connection. The values of radial displacements obtained from the constant load case are higher than the ones obtained with the varying load at the tunnel crown. However, the values of the varying load case are higher than the ones of the constant load case at the tunnel invert arch. The maximum absolute discrepancy for radial displacements is of 19.1% at the centre of the tunnel crown.



(a) Bending moments comparison at the crown-sidewall connection with the C/D



(b) Differences between the two load cases (taking the constant load case as a reference)

Fig. 2-9 Bending moments with the cover-to-diameter ratio C/D

In addition, a comparison of the bending moments at the crown-sidewall connection of the tunnel, under constant and varying loads, with the cover-to-diameter ratio is also made in Fig. 2-9a. The parameters used in the comparison are the same as presented in Table 2-1. Several values of C/D were studied. The differences between the two load cases with the cover-to-diameter ratio are also shown in Fig. 2-9b.

It can be seen from Fig. 2-9a that the absolute discrepancy between the two solutions becomes smaller with the increase of the cover-to-diameter C/D ratio when $C/D < 3.0$. Otherwise, the absolute discrepancy becomes higher with the cover-to-diameter ratio increase for $C/D \geq 3.0$. It means that the constant load case and the varying load one almost give the same values in terms of bending moments, 0.2213 MN.m when $C/D = 3.0$. The varying loads case is used in the following analysis of this chapter.

3. Validation of the HRM method

A comparison between the HRM and a numerical method is presented in this section, which makes it possible to estimate the accuracy that can be achieved by means of the present improved HRM. This numerical simulation has been done using the finite difference program FLAC^{3D} (Itasca Consulting Group, 2012). Parameters from the Toulon tunnel project in the city of Toulon have been adopted for evaluation purpose (Oreste, 2012). The geo-mechanical parameters of the ground and tunnel support are shown in Table 2-1.

The 2D numerical model has been shown in Figs. 2-10 and 2-11, assuming plane-strain conditions. The FLAC^{3D} model is 60m long in the z -direction, 240m wide in the x -direction. In directions perpendicular to the

x - z and the y - z planes (i.e. $y=0$, $y=1$, $x=-120$ and $x=120$) the nodes were fixed. The nodes at the base of this numerical model ($z=-20$) were also fixed in the z -direction. The numerical model is constituted of around 6,100 zones and 12,400 grid points. The volume of the model was discretized into hexahedral zones in this study. And the tunnel support has been modelled using linear-elastic embedded liner elements. A continuous support is simulated to compare with the results of the HRM in this work.

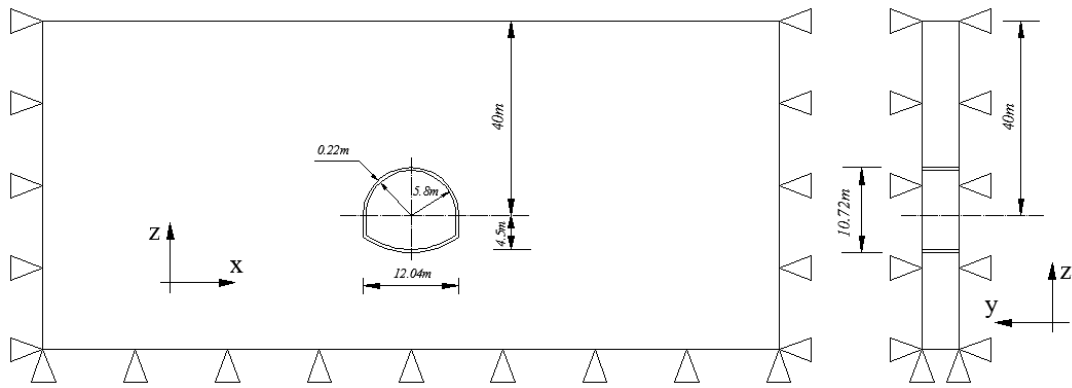


Fig. 2-10 Numerical geometry model considered in the analysis

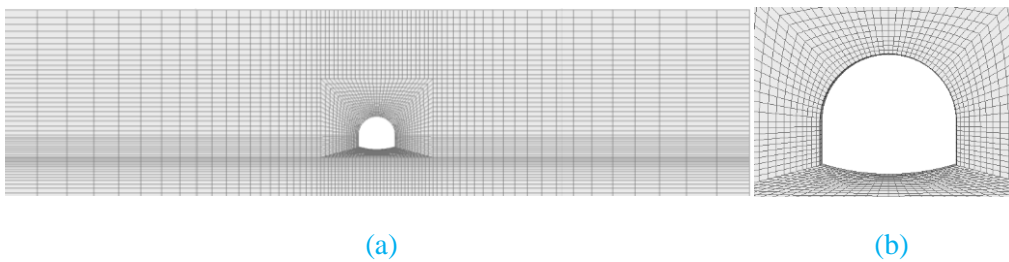


Fig. 2-11 Two-dimensional numerical mode (a) and U-shaped tunnel (b)

Liner elements are embedded along the tunnel boundary, and attached to the surrounded ground zones. The liner elements can slide and/or open relative to the surrounding zones (Itasca Consulting Group, 2012). Using a good rule-of-thumb in which k_n and k_s (normal stiffness k_n and tangential stiffness k_s , respectively) are set to one hundred times the equivalent stiffness of the neighbouring zone, the liner-zone interface stiffness is chosen. The apparent stiffness (expressed in stress-per-distance units) of a zone in the direction normal to the surface is calculated using the following formula:

$$\max\left[\frac{(K+\frac{4}{3}G)}{\Delta z_{min}}\right] \tag{2-30}$$

where, K and G : the bulk and shear modulus, respectively; z_{min} : the smallest dimension of an adjoining zone in the normal direction.

Fig. 2-12 and Fig. 2-13 illustrate the displacements and structural forces of the tunnel support, respectively. It is shown in Fig. 2-12 that both radial and tangential displacements obtained with HRM have the same trend with the ones obtained with the FLAC^{3D} model. The absolute discrepancies in terms of radial displacements between these two methods are clear when θ (Fig. 2-7) is lower than 120° (corresponding to the tunnel invert arch). The values of radial displacement obtained with HRM are a slightly higher than the FLAC^{3D} ones near the crown-sidewall connection. The maximum absolute discrepancy for radial displacement is equal to 12.2 mm at the centre of the invert arch. Both these two methods give more or less the same values of tangential displacements at the tunnel invert arch and sidewall. In addition, noticeable differences for tangential displacements obtained with the two methods can also be observed at the tunnel invert arch. The maximum absolute discrepancy of tangential displacement is of 6.1 mm. This could be caused by the fact that the loading condition on the tunnel support is not the same in the two methods. The external loads caused by the soil gravity act directly and explicitly on the beam elements in the HRM method. In contrast, the external loads are implicitly applied on the tunnel support through the continuous soil in the numerical method using FLAC^{3D}. The arching effect of tunnel, which can be developed in the soil surrounding tunnel in the FLAC^{3D}, is not taken into account in HRM.

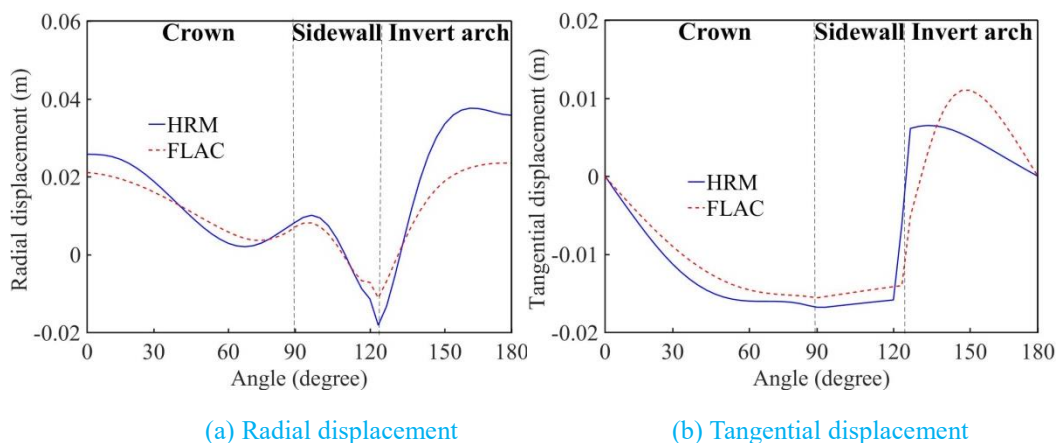


Fig. 2-12 Displacements of the tunnel support, comparison between the HRM and the FLAC^{3D} model

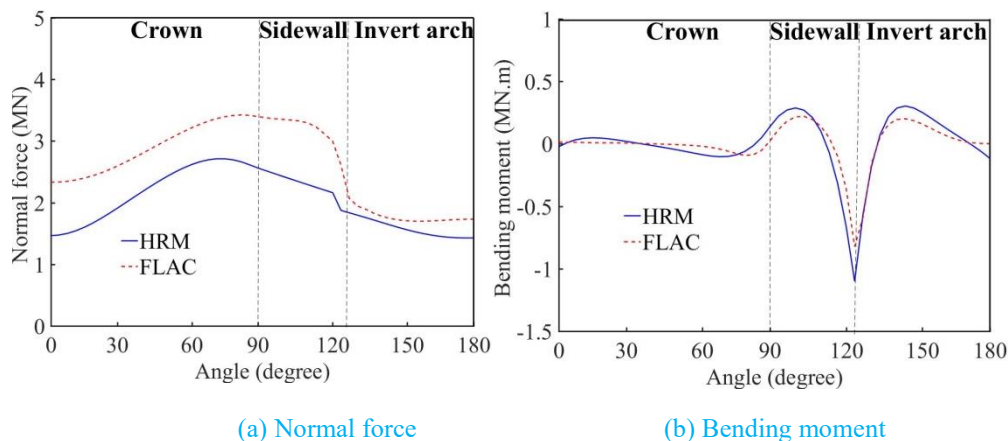


Fig. 2-13 Structural forces in the tunnel support, comparison between the HRM and FLAC^{3D} model

Structural forces on the tunnel support are presented in Fig. 2-13. It can be seen that the normal forces obtained with the HRM method are lower than the FLAC^{3D} ones for the whole tunnel. The differences are clear at the tunnel crown and sidewall. The absolute maximum discrepancy is equal to 0.979 MN. The bending moments calculated by HRM almost have the same trend compared with the FLAC^{3D} ones for the whole tunnel. However, noticeable differences in terms of bending moments can be observed at the sidewall and at the invert arch. The absolute discrepancy is equal to 0.278 MN.m at the invert arch-sidewall connection. The differences for the normal forces and bending moments could also be attributed to the effect of external loads on the tunnel support, which are not similar in those two methods.

Based on the results mentioned above, it is therefore reasonable to conclude that the support displacement and structural internal force results obtained using the HRM are basically in good agreement with the ones of the numerical FLAC^{3D} with respect to the position along the tunnel boundary.

4. Parametric analysis and design figures

An extensive parametric analysis was developed to study the effect of the ground mass properties, tunnel support stiffness, applied loads and tunnel dimensions on the bending moments, the shear forces, the normal forces and the normal support displacement developed in the support structures. Details of the cases adopted for the parametric analyses are shown in Table 2-2. Three different types of ground are therefore considered in this analysis. Two values of lateral earth pressure factor K_0 are considered ($K_0=0.5$ and 1.5). The tunnel dimension, represented here by the crown radius R_c , is in a range between 3.4m and 5.8m. The diameter of U-

shaped tunnel D is 1.8 times R_c and the height of the invert arch centre y_c is 2.5 times R_c . The parametric analyses are done (648 different cases) using the HRM code, which is therefore be able to cover most of the possible situations encountered in design practice.

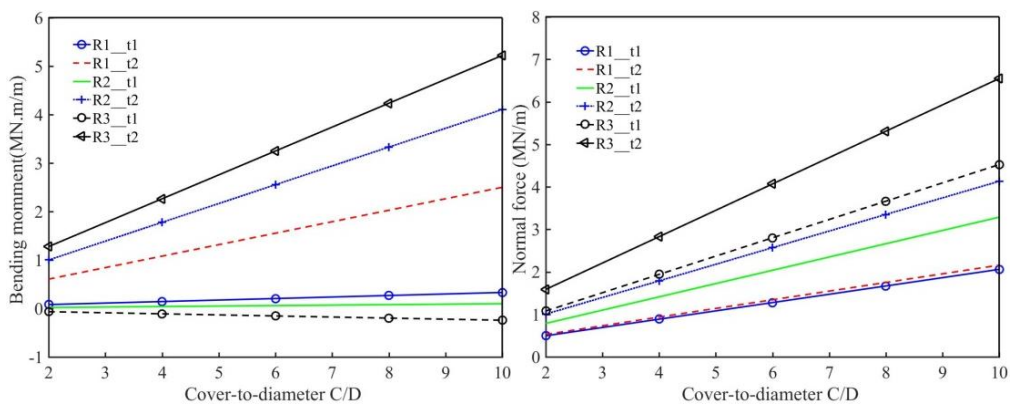
Table 2-2 Details of the cases adopted for the parametric analyses

Descriptions/Case	1	2	3	4	5	6
Properties of tunnel	A	A	B	B	C	C
Ground Elastic modulus E_s (MPa)	50	50	150	150	500	500
Liner Young's modulus E_s' (GPa)	35					
Friction angle φ (degree)	28		31		35	
Cohesion c (MPa)	0.005		0.02		0.5	
Unit weight γ (kN/m ³)	22					
Lateral earth pressure factor K_0	0.5	1.5	0.5	1.5	0.5	1.5
Tunnel crown radius R_c (m)	Changed for three cases: $R_1=3.4\text{m}$; $R_2=4.6\text{m}$; $R_3=5.8\text{m}$					
Cover-to-diameter C/D values	Five values were considered: 2, 4, 6, 8, 10					
Support thickness t (m)	Two cases were considered: $t_1=0.20\text{m}$; $t_2=0.50\text{m}$					

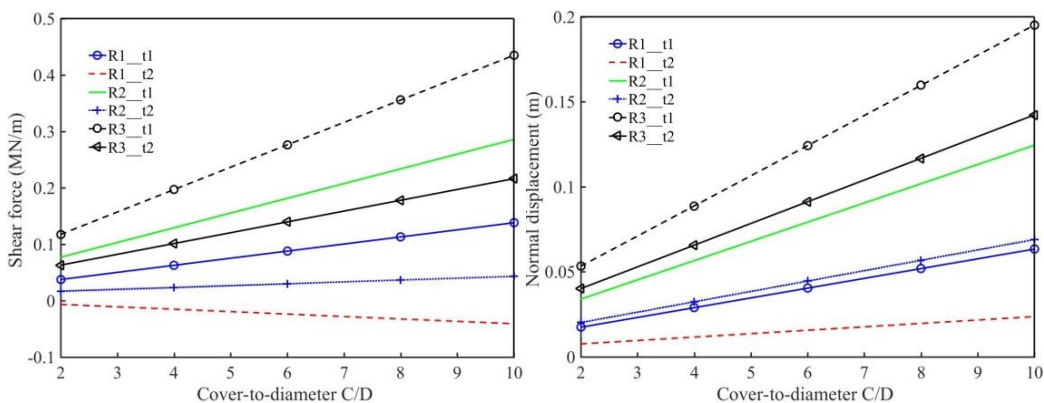
The values of the bending moments, normal forces, shear forces and normal displacements at the tunnel invert arch, the right sidewall and the tunnel crown have been determined. To decrease the length of the chapter, only the results obtained from the case 3, which represent the results obtained with the ground mass (B in Table 2-2), have been illustrated in Fig. 2-14 to Fig. 2-16. Some interesting conclusions are obtained from the parametric analyses:

- (1) The higher the ground mass quality, the lower the support displacements, bending moments, shear forces and normal forces. The thicker the tunnel support, the lower the shear forces and tunnel support displacements, but the higher the normal forces and bending moments;
- (2) The dependency of the bending moments to the cover-to-diameter C/D is almost linear and can be expressed by a relationship equation of the following type $M=aC/D+b$. The absolute values of the bending moments increase with the increase of C/D . The larger the tunnel diameter and the thinner the tunnel support are, the higher the effect of C/D on the bending moment values is for the tunnel crown and invert arch. The influence of the support thickness on the bending moment is higher for large tunnels ($R_c=5.8\text{ m}$) than the ones induced on smaller tunnels ($R_c=3.4\text{ m}$). For instance, with the input data of case 3, the absolute value of a in the above relationship equation applied for the bending moment at the tunnel crown changes from 9.03 kN.m to 9.37 kN.m when the tunnel crown radius is equal to 3.4m and the support thickness changes from 0.2m to 0.5 m, respectively. On the other hand, when $R_c=5.0\text{ m}$, the

absolute value of a changes from 0.000467 to 0.1304 (Fig. 2-16a);

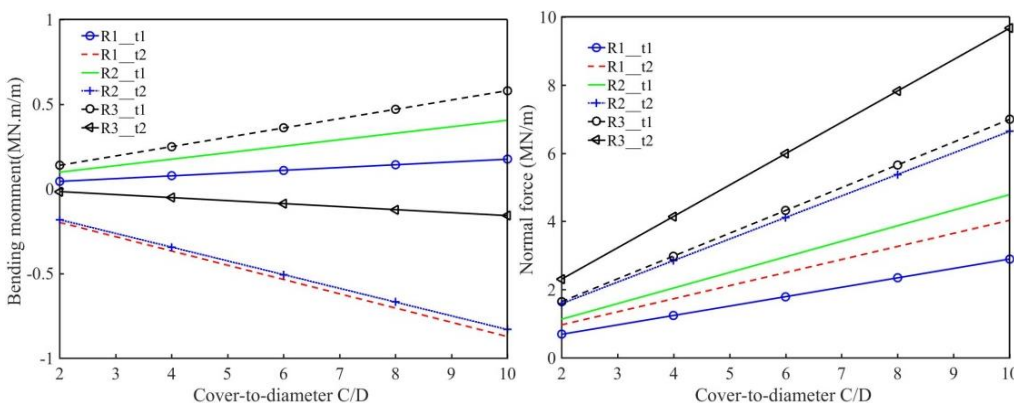


(a) Bending moments at the tunnel invert arch (b) Normal forces at the tunnel invert arch

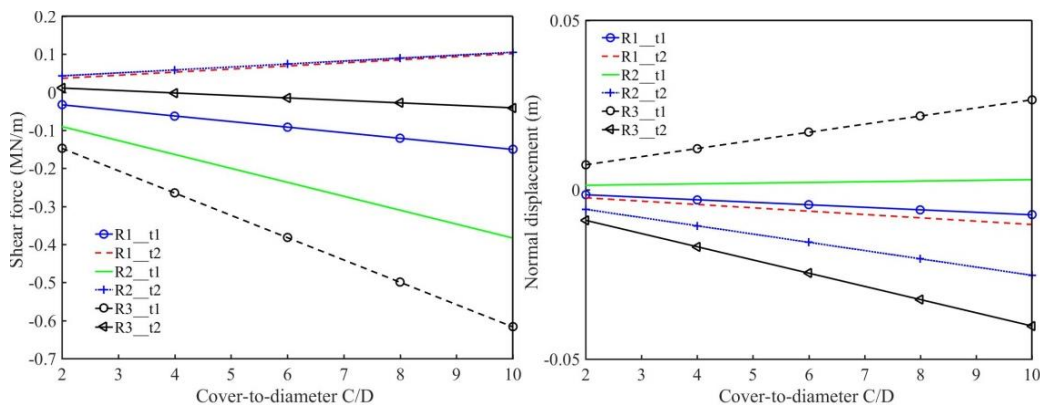


(c) Shear forces at the tunnel invert arch (d) Normal displacements at the tunnel invert arch

Fig. 2-14 Behaviour of the tunnel support considering the tunnel dimensions, support thickness and reduction factor of rigidity, η , (Ground type B - case 3) at the tunnel invert arch



(a) Bending moments at the tunnel sidewall (b) Normal forces at the tunnel sidewall



(c) Shear forces at the tunnel sidewall (d) Normal displacements at the tunnel sidewall

Fig. 2-15 Behaviour of the tunnel support considering the tunnel dimensions, support thickness and reduction factor of rigidity, η , (Ground type B - case 3) at the tunnel sidewall

- (3) The higher the ground quality, the lower the effect of C/D on the bending moments. For example, the absolute maximum a values in the relationship equation applied for the bending moment induced at the spring line of the tunnel crown, obtained with a tunnel radius of 5.80 m and a support thickness of 0.5 m are about 0.3366 MN.m, 0.1304 MN.m and 0.04275 MN.m, for case 1 (ground type A), case 3 (ground type B), case 5 (ground type C), respectively;
- (4) The absolute values of the normal forces increase with the increase of C/D when the support thickness changes from 0.20 m to 0.50 m (Fig. 2-14b, Fig. 2-15b and Fig. 2-16b);
- (5) The absolute discrepancies of the normal forces at the tunnel crown and invert arch are slightly higher than those of the normal forces at the tunnel sidewall when the support thickness changes from 0.20m to 0.50m. For example, with the case 3 input data, the absolute discrepancy of the normal force induced at the tunnel crown and invert arch are 31.6% and 30.9%, respectively, when $C/D=10$ and $R_c=5.80$ m. The corresponding value for absolute discrepancy of the normal forces at the tunnel sidewall is 27.6% (Fig. 2-14b, Fig. 2-15b and Fig. 2-16b);
- (6) The impact of C/D on the normal displacement depends to a great extent on the tunnel dimensions and support thickness. An increase in C/D values and a decrease in support thickness cause an increase in normal displacement. The dependency of the normal displacement to the cover-to-diameter C/D is almost linear and can also be expressed by a relationship equation $\delta_n=aC/D+b$. For case 3, the absolute a values in the relationship equation at the tunnel crown changes from 0.001701 to 0.003434 when the tunnel

crowns radius is equal to 3.4m and the support thickness changes from 0.5m to 0.2m. On the other hand, when $R_c=5.0m$, the value of a changes from 0.008390 to 0.01216 (Fig. 2-16d);

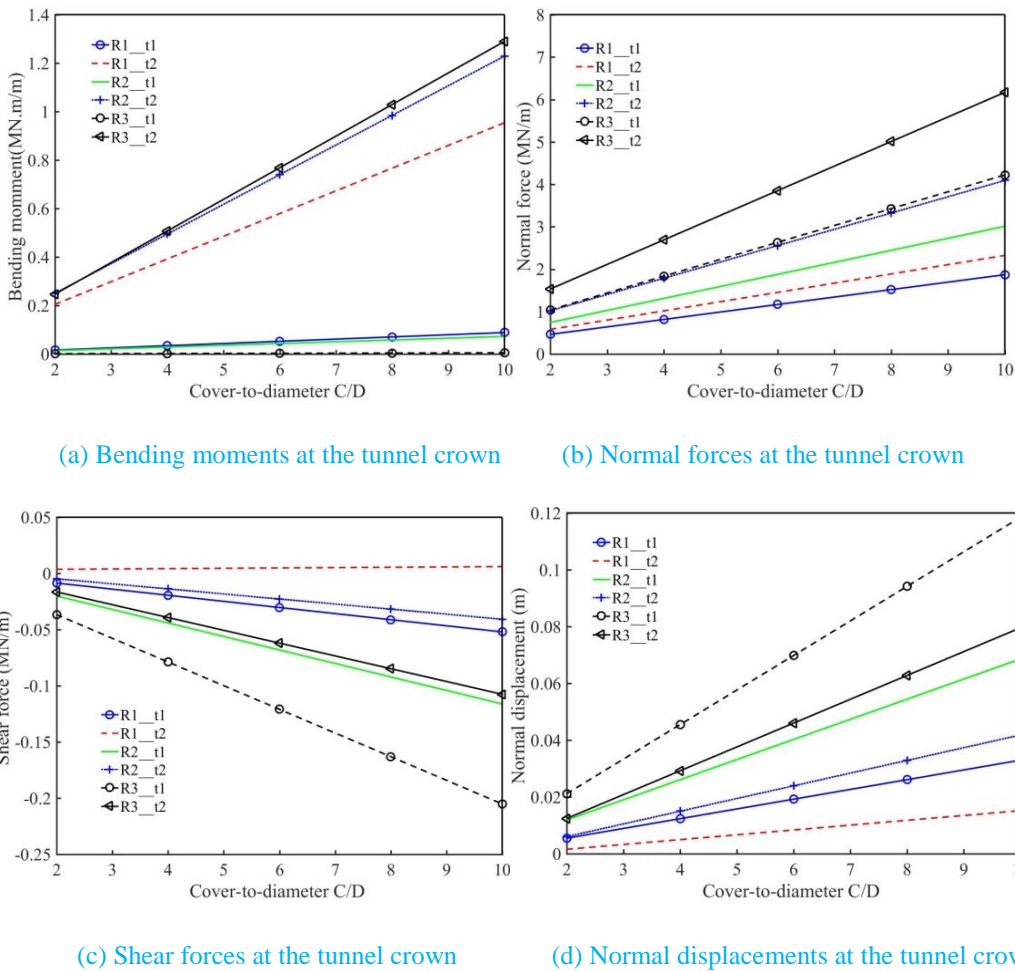


Fig. 2-16 Behaviour of the tunnel support considering the tunnel dimensions, support thickness and reduction factor of rigidity, η , (Ground type B - case 3) at the tunnel crown

(7) The larger the tunnel dimensions, the higher the impact of the support thickness on the shear forces and the higher the dependency of the shear forces with the C/D ratio. Generally, an increase of the C/D values leads to an increase in shear forces. This relation can also be expressed by a relationship equation of the following type $Q=aC/D+b$. The larger the tunnel dimension is, the higher the absolute value of a . For example, for case 3, the absolute values of a at the tunnel crown, when R_c is 3.4 m or 5.8 m are respectively equal to 0.00544 and 0.0211, (Fig. 2-16c - thickness equal to 0.20m).

In this parametric analysis, the ground parameters, the tunnel dimensions, the support thickness and the value of the cover-to-diameter C/D ratio, are assumed to be known. The structural internal forces and support

displacements can then be estimated. It is therefore possible to conduct a detailed design of the support structure of a U-shaped tunnel and then decided such as necessary reinforcements, concrete quality, etc. According to the proposed design figures, it is also possible to verify the effect of the various calculation parameters on the structure behaviour for a U-shaped tunnel support. The preliminary results acquired from the design figures help to start with further numerical calculations considering types of support structures. It permits thus to save a lot of time.

5. Conclusions

An improved numerical method to the HRM developed on the basis of the model proposed by [Oreste \(2007\)](#) and [Do et al. \(2014d\)](#), which is suitable for the dimensioning of U-shaped support structures, has been developed in this chapter.

The mathematical procedure adopted and the parameters used in the analysis, are also given. The results of the HRM method are compared with the ones of the numerical model $FLAC^{3D}$. There are some small discrepancies for those two methods, which allows the HRM method to be validated. As for the reason of the discrepancies, on one hand, this could be caused by the fact that the loading condition on the tunnel support is not the same in the two methods. The external loads caused by the soil gravity act directly and explicitly on the beam elements in the HRM method. In contrast, the loads of the numerical method using $FLAC^{3D}$ are applied at the tunnel support through the continuous soil. On the other hand, the arching effect of tunnel, which can be developed in the soil surrounding tunnel in the $FLAC^{3D}$ model, should not be neglected.

The parametric analysis has made it possible to estimate the U-shaped tunnel support behaviour in a large number of cases which cover the conditions that are generally encountered in practice. The effect of three typical types of grounds, of two values of lateral earth pressure coefficient K_0 , of three values of tunnel crown radius R_c , of two values of tunnel support thickness t and of five values of cover-to-diameter C/D , have been investigated. The results presented as design figures can be used for preliminary estimation of the structural internal forces, support displacement induced in the U-shaped tunnel support under the action of active loads. Before using these figures for a preliminary U-shaped tunnel support design, the external loads applied to the tunnel structure should be known, in terms of vertical load σ_v and lateral earth pressure coefficient K_0 . In addition, a comparison of two different active loads, constant and varying loads, is also made. This

comparison shows that the absolute discrepancy of two solutions obtained from the two different loads is almost zero when $C/D = 3.0$.

Some main points can be drawn from this chapter:

- The higher the ground mass quality, the lower the support displacements, bending moments, shear forces and normal forces;
- The thicker the tunnel support, the lower the shear forces and tunnel support displacements, but the higher the normal forces and bending moments. The influence of the support thickness on the bending moment is higher for large tunnels than the ones induced on smaller tunnels;
- The absolute values of the bending moments increase with the increase of C/D ; the higher the ground quality, the lower the effect of C/D on the bending moments;
- The absolute values of the normal forces increase with the increase of C/D ; the absolute discrepancies of the normal forces at the tunnel crown and invert arch are slightly higher than those of the normal forces at the tunnel sidewall when the support thickness changes from 0.20m to 0.50m;
- The larger the tunnel dimensions, the higher the impact of the support thickness on the shear forces and the higher the dependency of the shear forces with the C/D ratio.

Since the U-shaped tunnels without invert arch are common during the tunnel execution, in the following chapter, the behaviour of two different U-shaped tunnel linings (with and without invert arch) will be compared. In addition, a comparison will be made to investigate the difference of the results between two U-shaped tunnels and a circular tunnel. Two different cases of springs, only normal and normal plus shear springs, will be considered to simulate the external load scheme. The toe constraint conditions effect on the behaviour of U-shaped tunnel linings without invert arch will be highlighted.

CHAPTER 3 BEHAVIOUR OF TWO DIFFERENT U-SHAPED TUNNEL LININGS (WITH AND WITHOUT INVERT)

1. Introduction

The U-shaped tunnels without invert arch are common when a conventional method is used for the excavation of tunnels. The support design of this kind of tunnel was studied by some authors using different methods, e.g. the topology optimization method (Yin and Wei, 2000) or numerical modelling using a bedded-beam-spring model (which can also be called hyperstatic reaction method) (Barpi et al., 2011). However, the topology optimization method (Yin and Wei, 2000) is only able to give the tunnel deformation and cannot calculate the lining forces. Barpi et al. (2011) presented a method for the sensitivity analysis of U-shaped tunnel based on a fuzzy approach and the bedded-beam-spring model. However, they did not evaluate the behaviour of U-shaped tunnels without invert arch, in terms of structural forces and support displacements. Therefore, the HRM method is adopted in this chapter to study the behaviour of two different U-shaped tunnel linings (with and without invert arch).

It should be noticed that there are some differences between the present method and the one of Barpi et al. (2011). Firstly, the tunnel invert shape is modelled as a straight line by Barpi et al. (2011). In this chapter, more complex shapes can be considered like curved ones for the invert or no invert. Secondly, the stiffnesses of springs in Barpi et al. (2011) are linear and only depend on the equivalent radius R_{eq} of the tunnel, the elastic modulus E and the Poisson coefficient ν of the ground. However, in the present analysis, the stiffnesses of springs are non-linear and also depend on the cohesion c , friction angle φ , Poisson's ratio ν_s of the ground, and of the active loads (see Eqs. 2-24 and 2-25 in Chapter2). Thirdly, the studied contents are different: Barpi et al. (2011) focused on the sensitivity analysis based on a fuzzy approach and an entire set of imprecise parameters (e.g. spring stiffness and elastic modulus of lining are considered to be fuzzy). In contrast, the present method presents the estimation of the tunnel support behaviour, in terms of structural forces and support displacements along the tunnel support, considering the effect of different parameters (e.g. ground elastic modulus E_s , the cohesion c , friction angle φ of the ground, lateral earth pressure factor K_0 , cover-to-diameter C/D values, support thickness t , tunnel crown radius R_c).

In this chapter, the results of two kinds of U-shaped tunnels obtained by HRM are compared with the circular shape ones to highlight the effect of tunnel shape. Two different cases of springs, only normal and normal plus shear springs, are considered to simulate the external load scheme. The effect of shear springs on the tunnel lining behaviour is highlighted. In addition, the toe constraint conditions effect on the behaviour of U-shaped tunnel linings without invert arch is studied. The varying loads and two different U-shaped tunnels (with and without the inverted arch) are also considered in this study (Fig. 3-1). The active loads are independent of the displacements that develop in the support and at the ground-support interface.

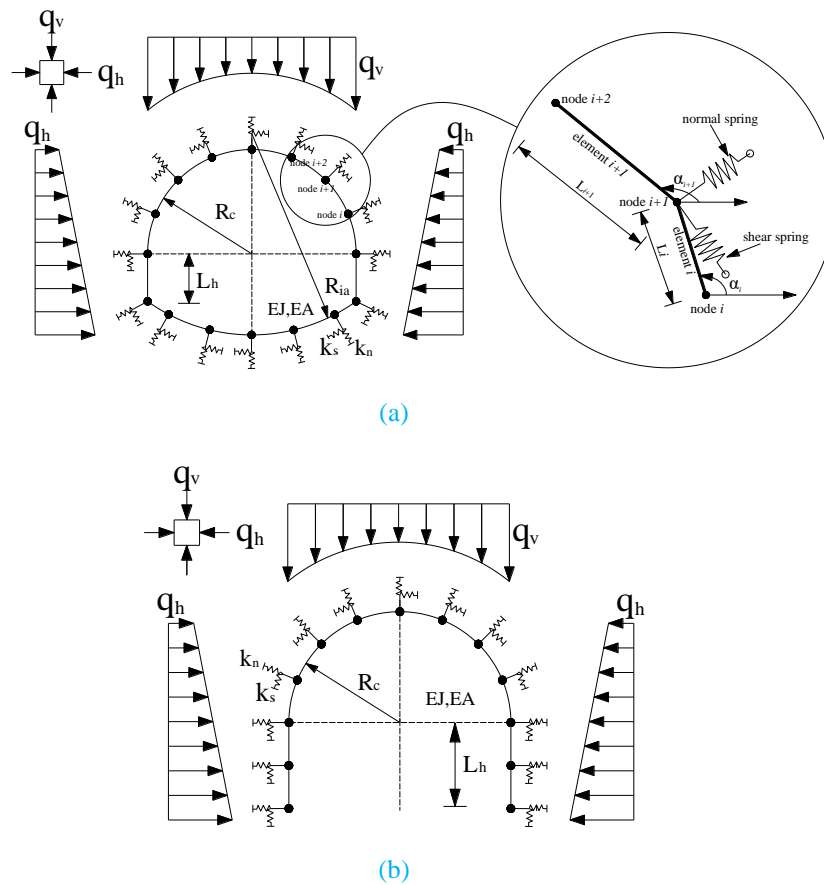


Fig. 3-1 Calculation scheme of two different U-shaped support structures with the HRM: (a) U-shaped tunnel with invert arch and scheme of the ground-support interaction through springs connected to the support nodes and (b) U-shaped tunnel without invert arch. With: q_v : vertical loads; q_h : horizontal loads; k_n : stiffness of the Winkler-springs; R_{ia} : radius of the inverted arch; R_c : crown radius; L_h : vertical length from the point of tunnel cross-section to the spring line (x-axis); EJ and EA : bending and normal stiffness of the support

The developed HRM model (U-shaped tunnel without inter arch) is validated on the basis of the comparison with results obtained from finite difference numerical models $FLAC^{3D}$. Taking the Geometry2 in

Fig. 3-2 with the clamped constraint condition in Fig. 3-3d (which corresponds to the worst internal forces case) as the reference case, a parametric investigation was conducted considering the change in stiffness of the springs, loads on the support, geometries and bending stiffness of the support structures. Note that the mathematical procedure of the HRM method has been shown in Chapter 2 in detail. Therefore, the introduction to the HRM method in this chapter will not be given.

2. Validation of the HRM method for a U-shaped tunnel without invert arch

In the first subsection, the comparisons of results obtained from two different U-shaped tunnels with only normal springs and normal springs plus shear springs are firstly given. Then the effect of constraint conditions on the tunnel lining behaviour of Geometry2 is discussed. Lastly, considering the effect of normal and shear springs, the comparison between circular and two U-shaped tunnels obtained by the HRM calculations are presented.

In the second subsection, the validation of the HRM method for a U-shaped tunnel without invert arch is given.

2.1 Calculation code and the dimensioning of the support

The HRM calculation code is able to consider the support geometry (Fig. 3-2) and the type of constraint at the base of the tunnel support (Fig. 3-3), which makes this code possible for the dimensioning of preliminary supports. Due to the symmetry of the problem, only half of the tunnel is considered. Since only vertical displacements are possible in the positions of the initial and final nodes of Geometry1, the constraint (e) in Fig. 3-3 is therefore chosen. Similarly, the constraint (e) is also used as the type constraint for Geometry2. In contrast, as the final node of Geometry2 can have different modes of displacements, e.g. rolling displacement, horizontal displacement or no displacement, the constraint types (a)-(d) can be used for the constraint condition of the final node of Geometry2.

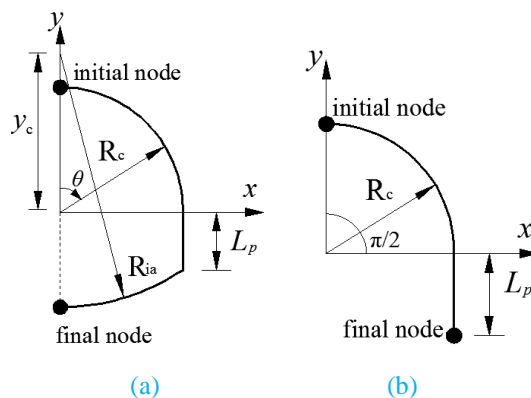


Fig. 3-2 Support geometries considered in the HRM calculation codes: (a) Geometry1 (U-shaped tunnel with invert arch) and (b) Geometry2 (U-shaped tunnel without invert arch). With: L_p : sidewall length; y_c : height of the invert arch centre; θ : the angle between the vertical axis of cross-section of tunnel and the element axis (θ is 0° at the initial node; θ is 90° at the connection of sidewall and crown)

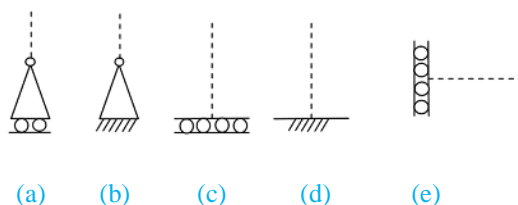


Fig. 3-3 Type of constraints: (a) horizontal hinged-roller, (b) fixed hinge, (c) horizontal clamped-roller, (d) clamped, and (e) vertical clamped-roller

An analysis for the verification of the preliminary support is here given as an example (Toulon tunnel, France) using the HRM calculation code. To reduce the length of this chapter, only the clamped constraint condition in Fig. 3-3d, which corresponds to the worst internal forces case (see Fig. 3-4), is adopted as a reference case to investigate the tunnel lining behaviour for next sections.

The geometrical and geomechanical parameters of the tunnel, the soil and the adopted support structure are shown in Table 3-1. Using the reference case with the clamped constraint condition (Fig. 3-3d), comparisons of the results obtained from those two different U-shaped tunnels with only normal springs and normal plus shear springs are presented in Fig. 3-4.

Fig. 3-4 shows that the maximum absolute values of the bending moments and of the shear forces are located at the sidewall for both two considered U-shaped tunnels. The normal forces of Geometry1 in the case of considering only normal springs are smaller than the ones taking into account both normal and shear springs. These normal forces are slightly higher at the tunnel invert arch. In contrast, the normal forces of

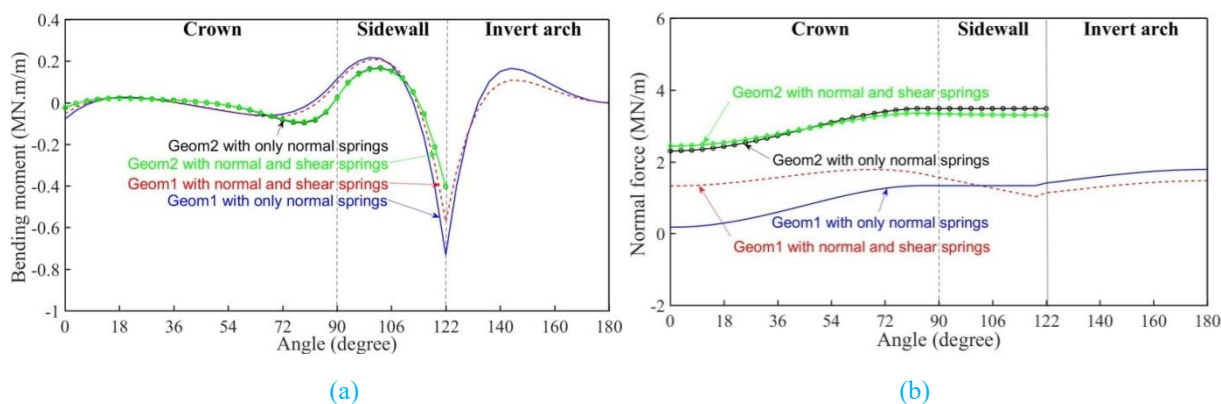
Geometry2 in the case of considering only normal springs are only smaller at the tunnel crown than the ones taking into account both normal and shear springs.

Table 3-1 Geometric parameters of the Toulon tunnel (Oreste and Dias, 2012)

Parameter	Symbol	Value	Unit
<i>Properties of tunnel</i>			
Crown radius	R_c	6.02	m
Invert arch radius	R_{ia}	20.22	m
Height of the invert arch centre	y_c	15.00	m
Height of the sidewall	L_p	3.80	m
Scale parameter in the x -direction	m_x	1.00	-
Scale parameter in the y -direction	m_y	1.00	-
Support thickness	t	0.22	m
Poisson's ratio	ν	0.15	-
Elastic modulus of concrete	E_0	35,000	MPa
<i>Properties of the ground</i>			
Cohesion	c	50	kPa
Unit weight	γ_s	22	kN/m ³
Poisson's ratio	ν_s	0.3	-
Internal friction angle	ϕ	20	°
Elastic modulus	E	300	MPa
Lateral earth pressure factor	K_0	0.5	-
Overburden	H	40	m

The radial displacements obtained in the case of Geometry2 are smaller than those of Geometry1. The maximum radial displacements of Geometry1 are located at the tunnel crown centre and at the sidewall and invert arch connection. Same maximum radial displacements for Geometry2 can be observed at the tunnel sidewall centre.

In addition, Fig. 3-4 also gives that the structural forces and displacements of Geometry2 have no significant change when considering only normal springs, which means that the spring type has a small effect on the internal forces and displacements of Geometry2.



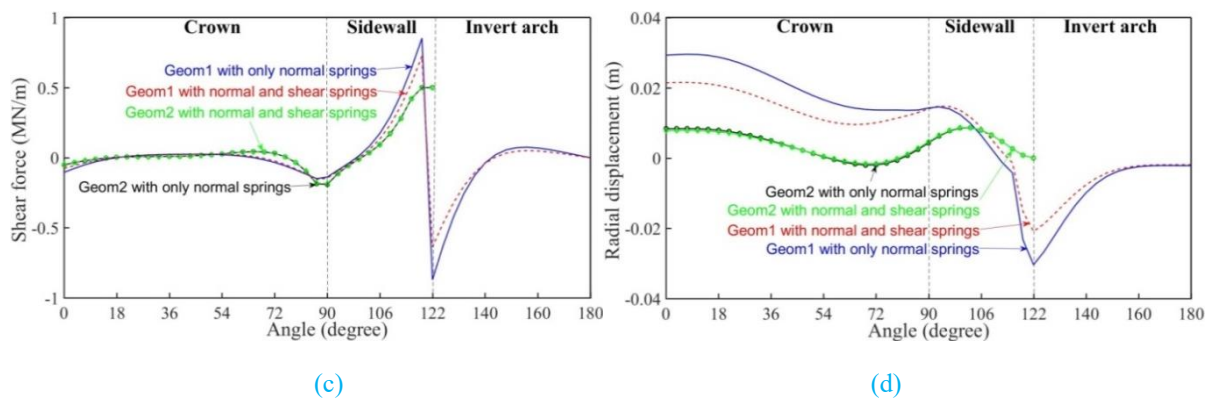


Fig. 3-4 Comparisons of results obtained from two different U-shaped tunnels with only normal springs and normal springs plus shear springs: (a) Bending moment, (b) Normal force, (c) Shear Force, and (d) Radial displacement (positive towards the inside of the tunnel)

Furthermore, Fig. 3-4 shows that the Geometry1 and Geometry2 almost give the same values of bending moments and shear forces at the tunnel crown. Nevertheless, the differences of bending moments and shear forces are obvious at the tunnel sidewall, and the results of Geometry1 are higher than that of Geometry2. The normal forces obtained from Geometry1 are clearly lower than that of Geometry2 at the tunnel crown and sidewall. In contrast, the radial displacements obtained from Geometry1 are higher than that of Geometry2 at the tunnel crown and sidewall. An analysis is also conducted to show the effect of the constraint conditions on the tunnel lining behaviour of Geometry2 (see Fig. 3-5).

From Fig. 3-5, it can be seen that the effect of the constraint conditions on the structural forces and on the displacements at the tunnel crown can be neglected. However, they affect the bending moments, the shear forces, and the radial displacements at the tunnel sidewall. The constraint d gives the largest bending moment (Fig. 3-5a) because of the restrained rotation at the tunnel lining bases (Fig. 3-5f). On the other hand, the smallest bending moments are found in the cases of constraints (a) and (b) where tunnel lining bases are free for rotation (Fig. 3-5f). The maximum shear forces are observed at the tunnel sidewall in the case of constraint (d). It should be noticed that the radial displacements of tunnel lining are clearly different for those four constraint cases at the tunnel sidewall. In addition, it can also be found that Geometry 2 almost has the same shear displacements under those four constraints condition, which means that the effect of the constraint types on shear displacements could be neglected.

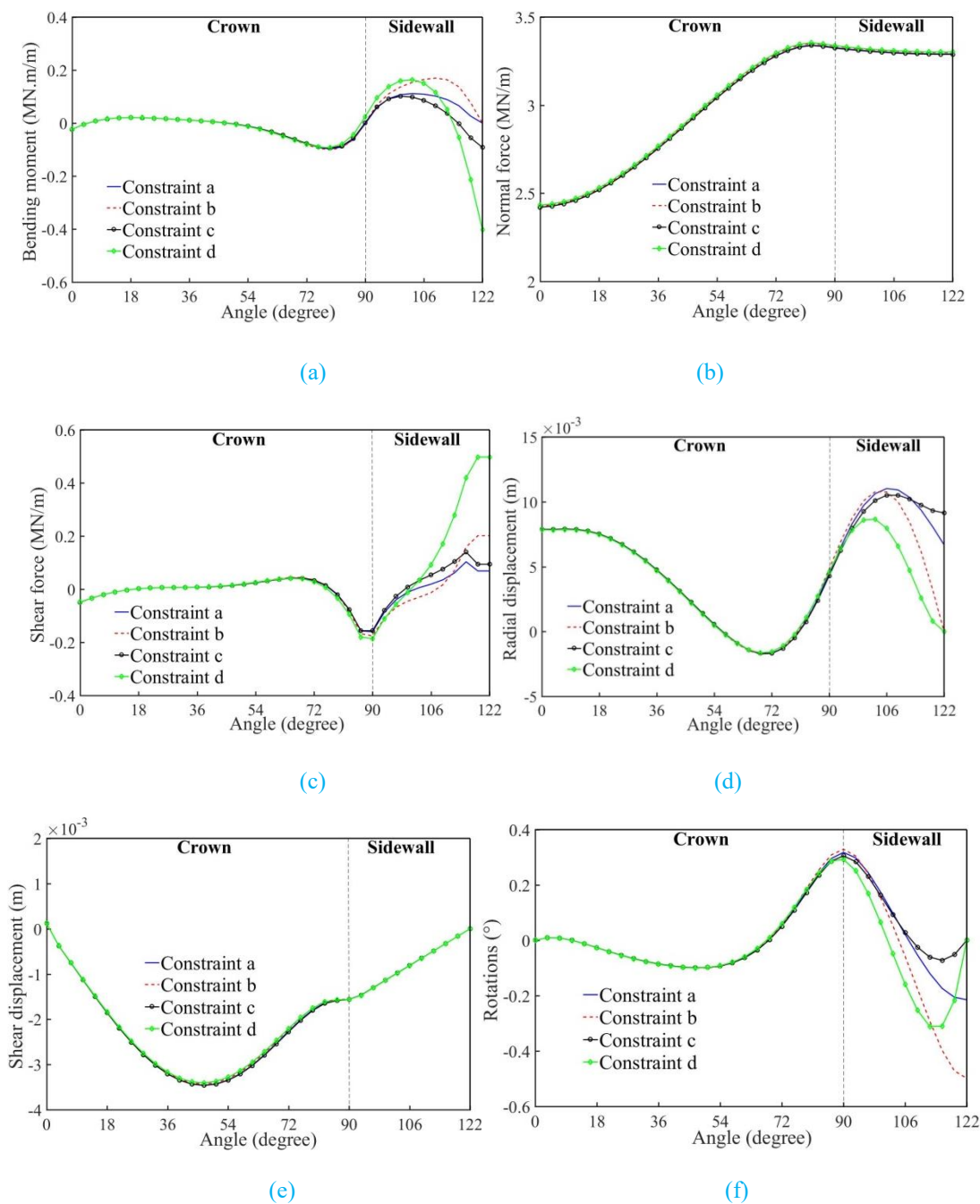


Fig. 3-5 Effect of constraint conditions on the tunnel lining behaviour of Geometry2: (a) Bending moment, (b) Normal force, (c) Shear Force, (d) Radial displacement, (e) Shear displacement, and (f) Rotations

Considering the effect of normal and shear springs, the comparisons of results between circular and two U-shaped tunnels obtained by the HRM calculations are also shown in Fig. 3-6. The parameters used in the comparison are the same as presented in Table 1 and the Geometry2 in Fig. 3-2 under the reference case of clamped constraint condition (Fig. 3-3d) is considered.

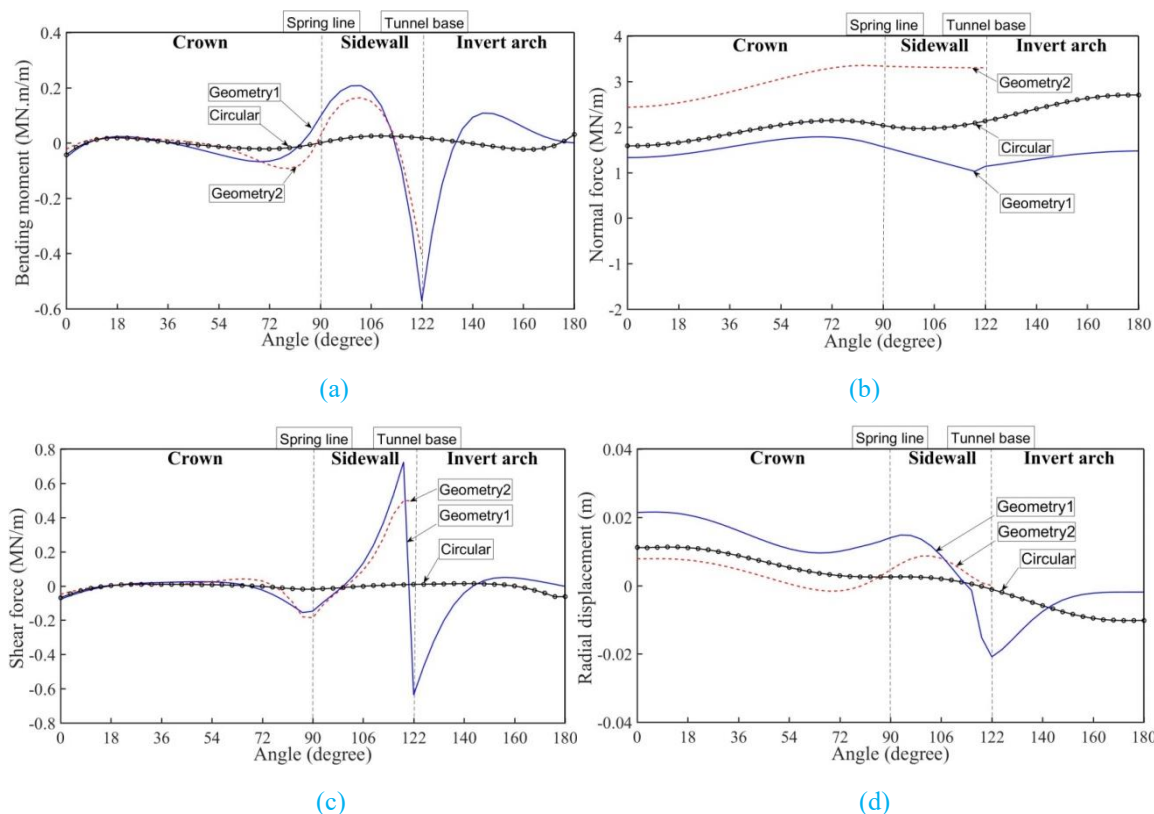


Fig. 3-6 Comparisons of the results between circular and two different U-shaped tunnels obtained by the HRM: (a) Bending moment, (b) Normal force, (c) Shear Force, and (d) Radial displacement (positive towards the inside of the tunnel)

It can be seen from Fig. 3-6 that the internal forces and displacements obtained from the three different geometries have the similar trend at the tunnel crown, and the results of normal forces and radial displacements obtained from the circular tunnel are between the ones of Geometry1 and Geometry2 cases. The normal forces of the Geometry2 case are higher than that of Geometry1 and the Circular cases at the tunnel crown and sidewall. However, the bending moments and shear forces have approximately values at the tunnel crown and sidewall for Geometry 1 and Geometry2. The trends of the internal forces and displacements obtained from the circular tunnel are smoother than that of Geometry1 and Geometry2 cases at the tunnel sidewall and invert arch.

2.2 Validation of the HRM method for a U-shaped tunnel without invert arch

A comparison between the HRM and a 2D numerical model (U-shaped tunnel without invert arch) is shown in this section, which makes it possible to estimate the accuracy achieved by means of the present

improved HRM. The 2D numerical simulation was done using the finite difference program FLAC^{3D} (Itasca Consulting Group, 2012) under the hypothesis of plane strain conditions. Materials are represented by polyhedral elements within a three-dimensional grid that is adjusted by the user to fit the shape of the object to be modelled. The structural response of a mechanical system that is composed of a solid continuum and a framework of load-carrying members can be simulated. The support is represented by a collection of structural elements (shells), each of them is associated with a set of nodes. It interacts with the solid continuum by means of links which connect the structural nodes to the soils mass nodes. In the present comparison, the ground is assumed to follow a linear elastic-perfectly plastic constitutive relation based on the Mohr-Coulomb shear failure criterion under plane-strain conditions.

Parameters from the Toulon tunnel project in the city of Toulon are adopted (Oreste and Dias, 2012). The geometrical parameters of the tunnel, the soil and the adopted support structure are shown in Table 3-1.

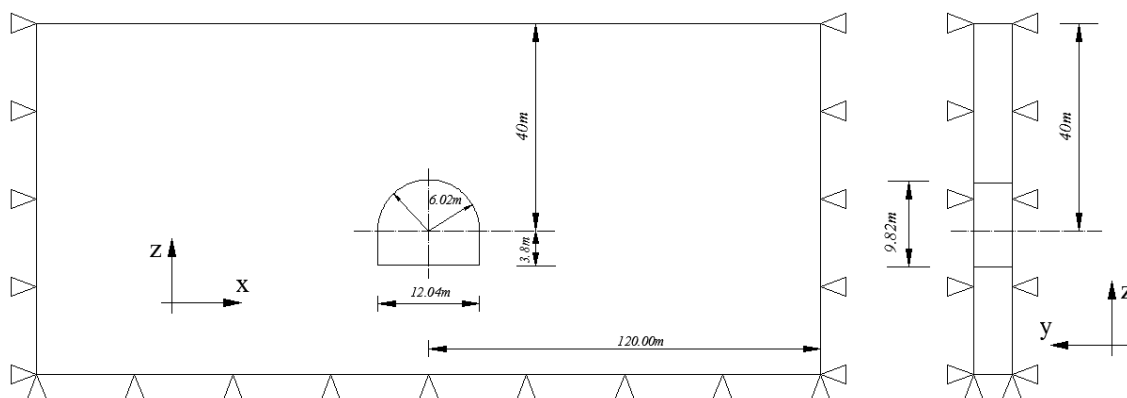


Fig. 3-7 Numerical geometry model of the U-shaped tunnel without invert arch

The 2D numerical model of the U-shaped tunnel without invert arch (taking Geometry2 in Fig. 3-2 as an example) is shown in Fig. 3-7 and Fig. 3-8. The dimension of the mesh elements increases with the distance to the tunnel. The FLAC^{3D} model is 60m long in the z -direction, 240m wide in the x -direction and consists of 6,082 zones and 12,362 grid points. Liner elements are embedded along the tunnel boundary and attached to the surrounded ground zones. A continuous support is simulated to compare with the results of the HRM in this chapter.

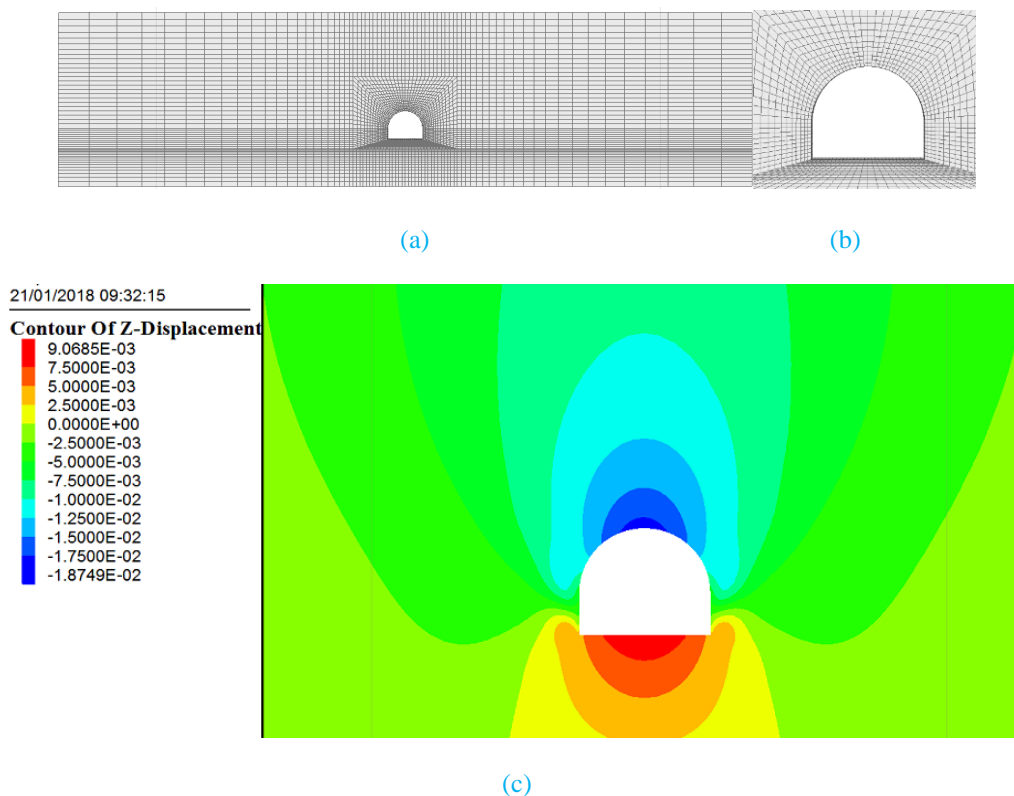


Fig. 3-8 Numerical model: (a) Two-dimensional numerical mode, (b) U-shaped tunnel without invert arch, and (c) Vertical displacements in FLAC^{3D}

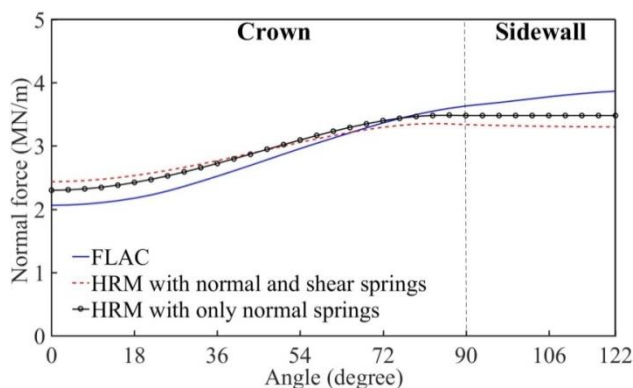
Comparing both methods: HRM and FLAC^{3D}, one can find that the lining is divided into a number of elements in both methods. The main difference lies on the fact that the presence of ground is considered through the external loads (caused by the ground gravity). These loads act directly and explicitly on the nodes of the beam elements through the springs in the HRM method. In contrast, the loads in the numerical method using FLAC^{3D} are applied at the tunnel support through the continuous media, arching effects can then be simulated.

Similar results were obtained by HRM and FLAC for all the five constraint conditions shown in Fig. 3-3. Considering the clamped constraint condition in Fig. 3-3d as an example, the results obtained from two methods are shown in Fig. 3-9.

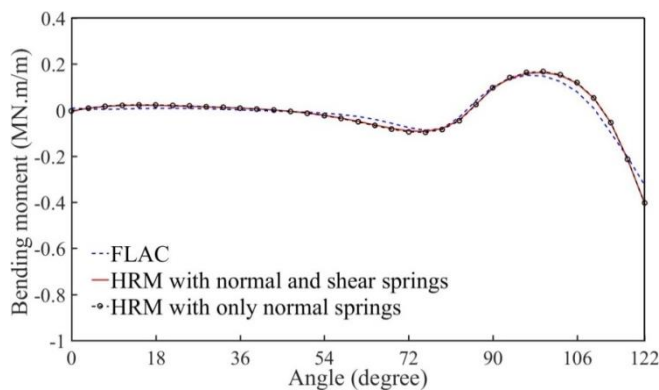
Fig. 3-9 illustrates the structural forces and displacements of the tunnel support. While no slip, which means a completely shear resistance, is assumed in FLAC^{3D} model, the HRM model considers both cases of only normal springs (case 1) and normal springs plus shear springs (case 2). It can be shown that the normal forces in the case of considering normal and shear springs (case 2) are larger than the ones in the case of

considering only normal springs (case 1) at the tunnel crown, but smaller at the tunnel sidewall. Moreover, it can be clearly found that FLAC^{3D} gives slightly lower normal forces than HRM at the tunnel crown, but slightly higher at the tunnel sidewall. The maximum difference (between FLAC and HRM with normal and shear springs) is equal to 12.3% and is located at the tunnel sidewall. This difference could be related to the different ways the ground surrounding the tunnel is considered. However, the bending moments in the case of considering the normal and shear springs are slightly smaller than that in the case of only normal springs along the whole tunnel. The bending moments calculated by HRM almost have the same trend compared with the FLAC^{3D} ones for the whole tunnel. Similarly, the results of radial displacements obtained from FLAC^{3D} are nearly close to the ones of HRM along the whole tunnel.

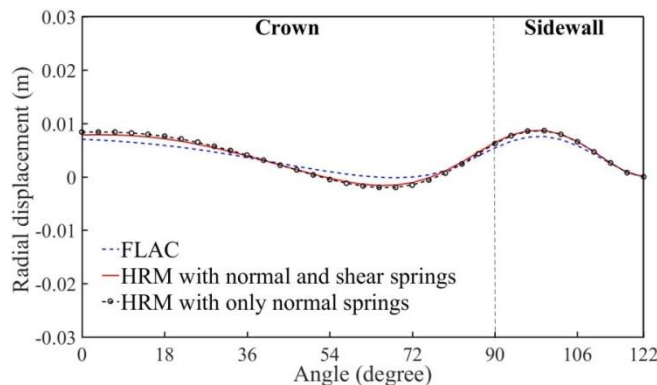
Based on the results mentioned above, it is, therefore, reasonable to conclude that the support displacements and structural internal forces obtained from the HRM are basically in good agreement with the ones of the numerical FLAC^{3D} with respect to the positions along the tunnel boundary.



(a)



(b)



(c)

Fig. 3-9 Comparison of structural forces and displacements in the U-shaped tunnel support (Geometry2 in Fig.3) between the HRM and FLAC^{3D} model: (a) Normal force, (b) Bending moment, and (c) Radial displacement

3. Results and parametric analysis for U-shaped tunnel without invert arch

Taking the Geometry2 in Fig. 3-2b with the clamped constraint condition (Fig. 3-3d) as the reference case, a parametric analysis is developed to study the effect of the different stiffness of the springs, different loads on the support, different geometries and different bending stiffness of the support structures on the structural forces and displacements of U-shaped tunnel without invert arch. It can be found that the stiffness of the springs is related to the ground elastic modulus and tunnel radius from Eq. (2-20) in chapter 2. The details of the cases adopted for the parametric analyses are shown in Table 3-2. Two values of lateral earth pressure factor K_0 are considered ($K_0=0.5$ and 1.5) and the tunnel dimension is changed in a range from 2m to 5m. Four different types of ground are considered and the parametric analyses are done using the HRM calculation code.

Table 3-2 Details of the cases adopted for the parametric analyses

Descriptions/Case	1	2	3	4	5	6	7	8
Properties of tunnel	A	A	B	B	C	C	D	D
Ground Elastic modulus E_s (MPa)	50	50	150	150	500	500	1500	1500
Friction angle φ (degree)	28		31		35		45	
Cohesion c (MPa)	0.005		0.02		0.5		0.75	
Lateral earth pressure factor K_0	0.5	1.5	0.5	1.5	0.5	1.5	0.5	1.5
Ground's unit weight γ (kN/m ³)	22							
Liner Young's modulus E_s' (GPa)	35							
Tunnel crown radius R_c (m)	Changed for three cases: $R_1=2.0\text{m}$; $R_2=3.5\text{m}$; $R_3=5.0\text{m}$							
Cover-to-diameter C/D values	Five values were considered: 2, 4, 10, 20, 40							
Support thickness t (m)	Two cases were considered: $t_1=0.20\text{m}$; $t_2=0.50\text{m}$							

The values of the bending moments, normal forces and normal displacements at the tunnel sidewall and the tunnel crown have been determined. The results obtained from those four different types of ground are illustrated in Figs. 3-10 to 3-13. Some interesting conclusions are obtained from the parametric analyses:

1. The higher the ground quality (the higher the stiffness of springs), the lower the bending moments, normal forces and normal displacements.
2. The thicker the tunnel support (the higher the bending stiffness of the support structures), the higher the normal forces and the bending moments, but the lower the normal displacement.
3. The bigger the loads (the cover-to-diameter C/D) on the support, the higher the normal forces, the bending moments and the normal displacements.
4. The bigger the radius of the tunnel, the higher the normal forces, the bending moments and the normal displacements.
5. The absolute values of the structural forces and displacements increase with the increase of the cover-to-diameter C/D .
6. For four types of ground, the values of normal forces at the tunnel sidewall are higher than that of normal forces at the tunnel crown; the higher the ground quality, the higher the effect of support thickness on the normal forces (Figs. 3-10c and d, Figs. 3-13c and d).
7. For a weak ground (ground type A), the bigger the tunnel radius, the higher the absolute values of normal displacements at the tunnel sidewall (Fig. 3-10e).
8. For strong ground (ground type D), the bigger the tunnel radius and the thinner the tunnel thickness, the higher the absolute values of bending moments at the tunnel crown (Fig. 3-13b).

In this parametric analysis, once the ground parameters, the tunnel dimensions, the thickness of the supports and the values of the cover-to-diameter C/D ratio, are assumed to be known, the structural internal forces and displacements can then be estimated. It is, therefore, possible to conduct a detailed design of the support structure of a U-shaped tunnel and then decided such as necessary reinforcements, concrete quality, etc. According to the proposed design figures, it is also possible to verify the effect of the various calculation parameters on the structure behaviour for a U-shaped tunnel support.

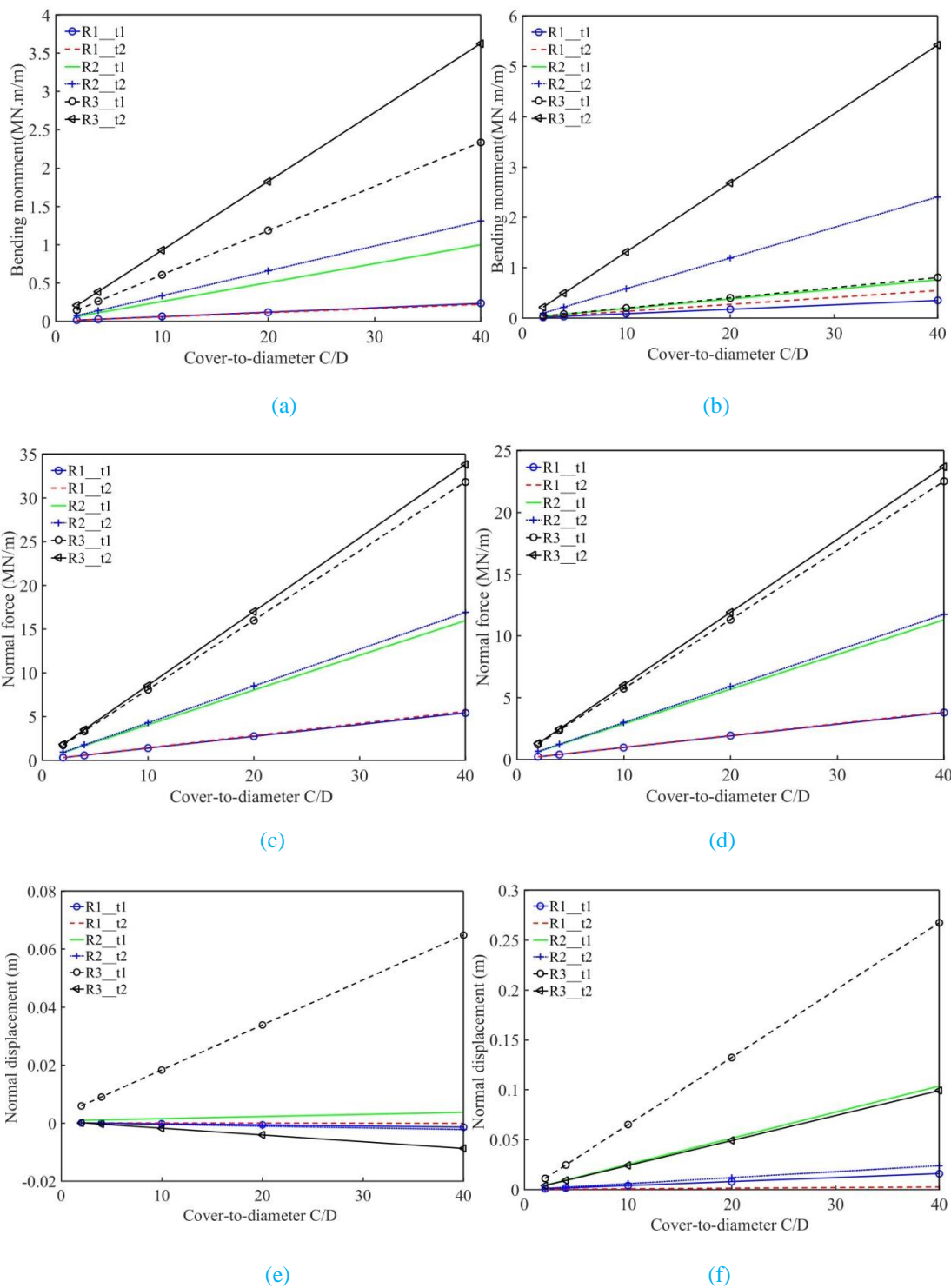


Fig. 3-10 Structural forces and displacement considering different stiffness of the springs, different loads on the support, different geometries and different bending stiffness of the support structures (Case1): (a) Bending moments at the tunnel sidewall, (b) Bending moments at the tunnel crown, (c) Normal force at the tunnel sidewall, (d) Normal force at the tunnel crown, (e) Normal displacement at the tunnel sidewall, and (f) Normal displacement at the tunnel crown

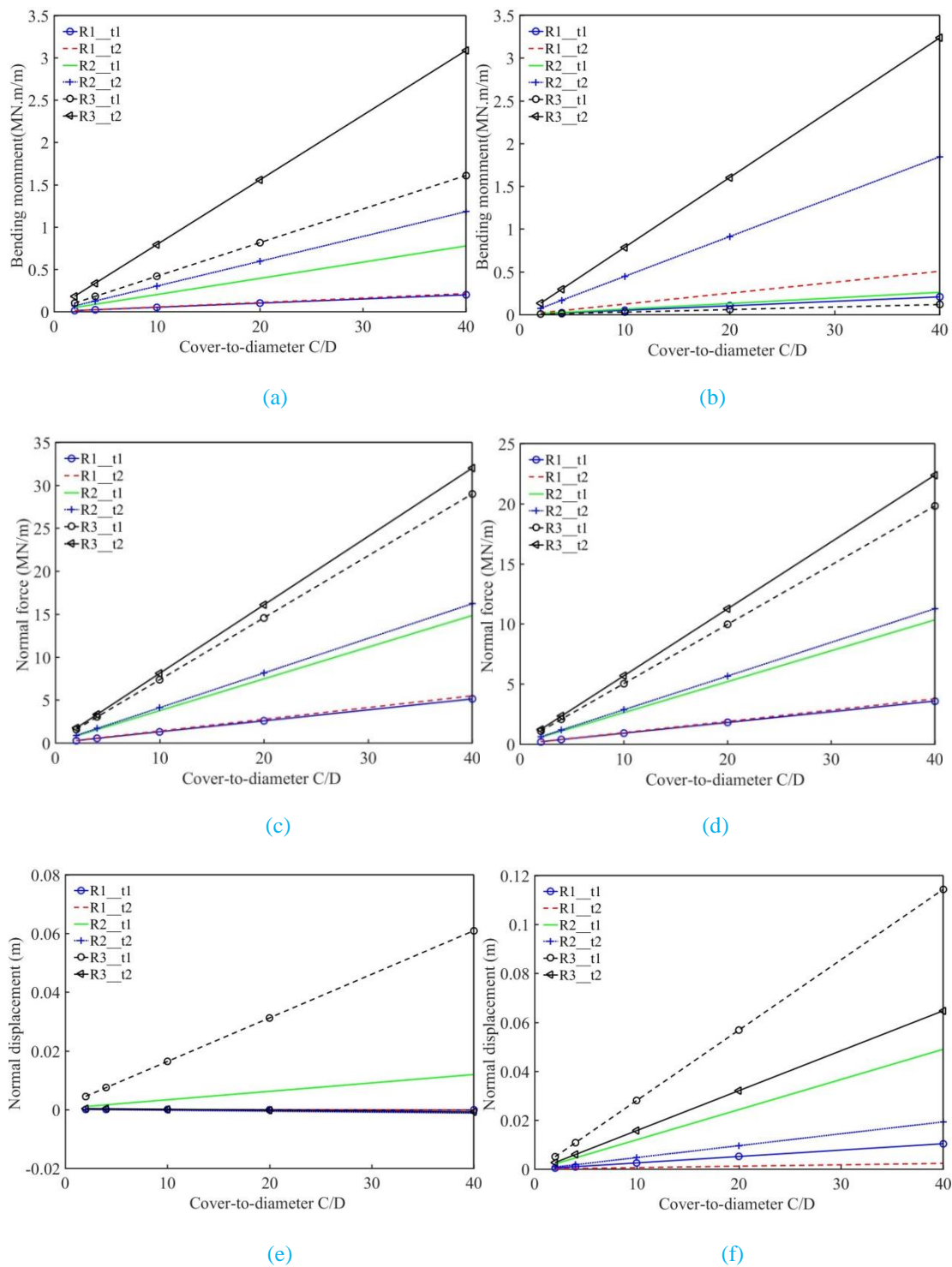


Fig. 3-11 Structural forces and displacement considering different stiffness of the springs, different loads on the support, different geometries and different bending stiffness of the support structures (Case3): (a) Bending moments at the tunnel sidewall, (b) Bending moments at the tunnel crown, (c) Normal force at the tunnel sidewall, (d) Normal force at the tunnel crown, (e) Normal displacement at the tunnel sidewall, and (f) Normal displacement at the tunnel crown

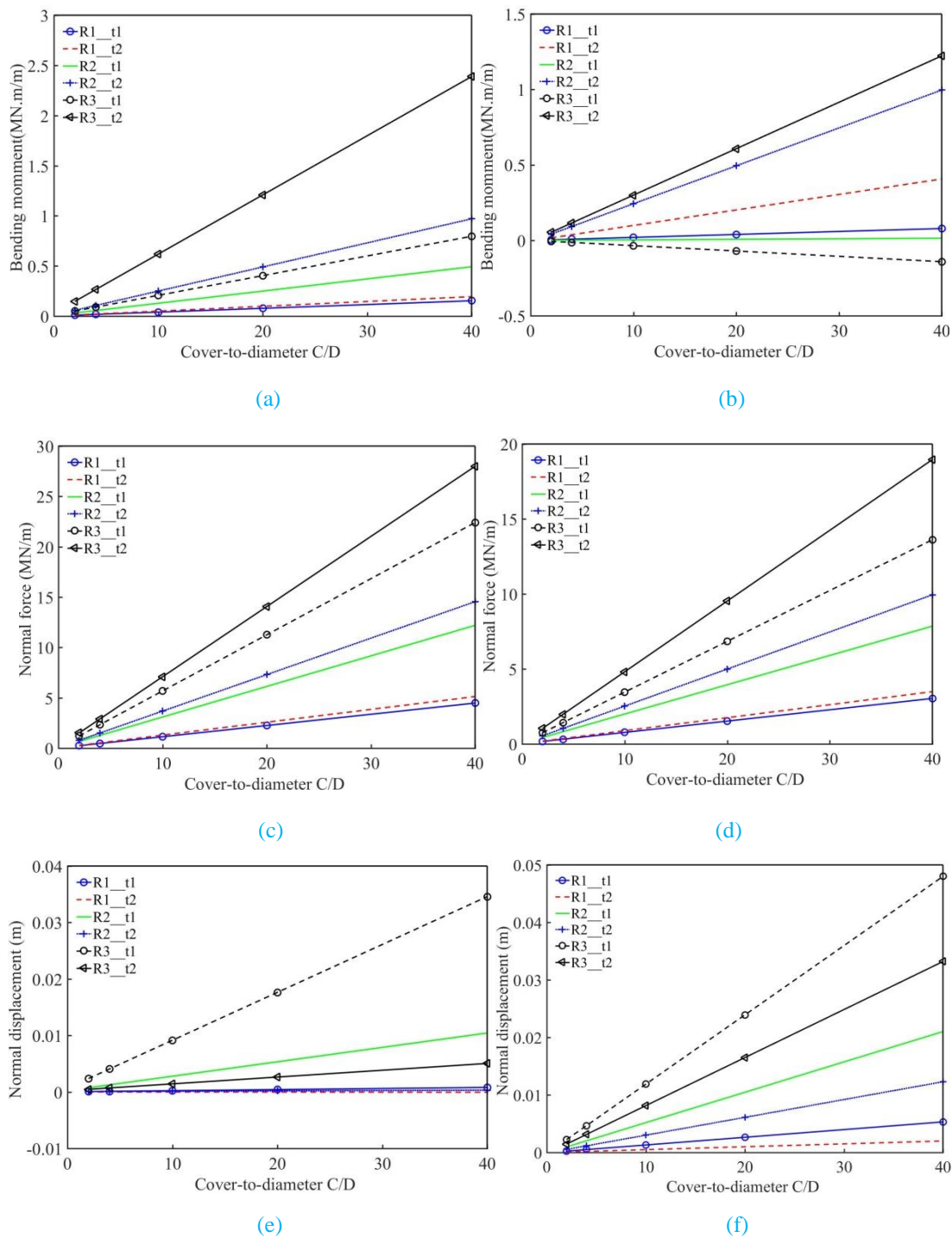


Fig. 3-12 Structural forces and displacement considering different stiffness of the springs, different loads on the support, different geometries and different bending stiffness of the support structures (Case5): (a) Bending moments at the tunnel sidewall, (b) Bending moments at the tunnel crown, (c) Normal force at the tunnel sidewall, (d) Normal force at the tunnel crown, (e) Normal displacement at the tunnel sidewall, and (f) Normal displacement at the tunnel crown

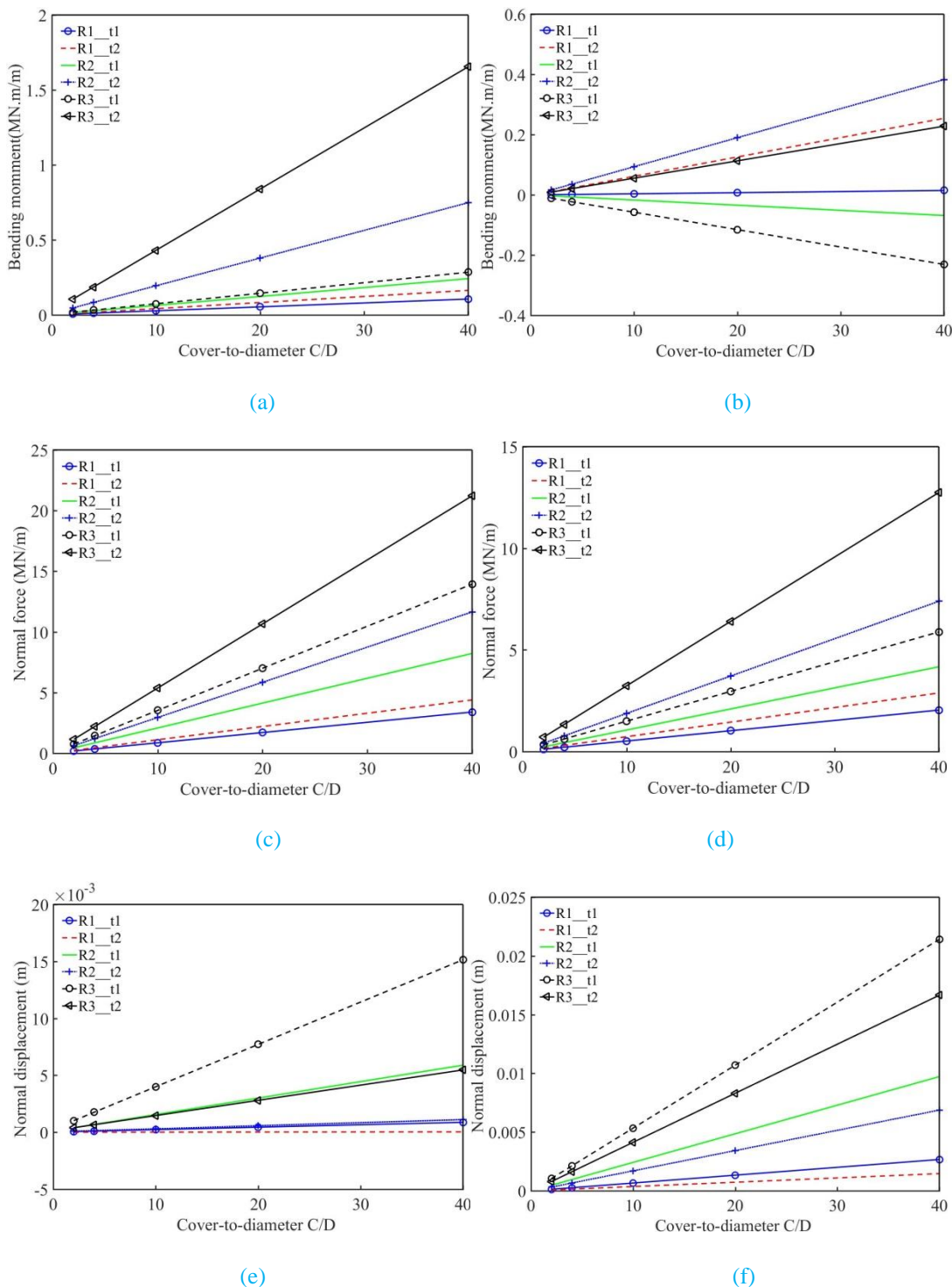


Fig. 3-13 Structural forces and displacement considering different stiffness of the springs, different loads on the support, different geometries and different bending stiffness of the support structures (Case7): (a) Bending moments at the tunnel sidewall, (b) Bending moments at the tunnel crown, (c) Normal force at the tunnel sidewall, (d) Normal force at the tunnel crown, (e) Normal displacement at the tunnel sidewall, and (f) Normal displacement at the tunnel crown

4. Conclusions

A comparison of two different cases of springs, only normal springs, and normal plus shear springs, is made in this chapter. The obtained conclusion is that the spring type has a small effect on the internal forces and displacements of Geometry2. The analysis is also made to show the effect of constraint conditions (Fig. 3-5) on the lining behaviour of Geometry2. One can find that the effect of constraint conditions on the bending moments, the shear forces, and radial displacements at the tunnel sidewall should not be neglected.

The results given by the present method are compared with the ones of the numerical model FLAC^{3D}. The small result differences founded between these two models allow the HRM method to be validated.

The parametric analysis permits to estimate the support behaviour of U-shaped tunnel without invert arch. The effect of four typical types of grounds, of three values of tunnel crown radius, of two values of tunnel support thickness and of five values of cover-to-diameter, was investigated. The results presented as design figures can be used for the preliminary estimation of the structural internal forces induced in a U-shaped tunnel support without invert arch under the action of active loads. It should be noticed that before using the proposed figures for a preliminary U-shaped tunnel support design, the external loads applied to the tunnel structure should be known, in terms of vertical load and lateral earth pressure coefficient.

Comparing with other numerical methods, one can be easily found that:

Firstly, the computational efficiency is greatly improved using the HRM method which makes it possible to do extensive parametric and reliability analyses considering the parameters influence of the surrounding ground mass and tunnel lining.

Secondly, different support conditions are also easily implemented using the proposed method. Loads coming from the surrounding soil mass to the tunnel lining can be modified, which allows considering complex loadings in terms of loading direction and magnitude.

Lastly, all boundary conditions and loading scenarios are explicitly applied in the HRM method. Hence, tunnel designers could easily control the input parameters which are used.

In the following chapter, the HRM method will be developed to study the behaviour of U-shaped on a layered media.

CHAPTER 4 EFFECT OF MULTI-LAYERED SOILS ON THE DESIGN OF TWO KINDS OF U-SHAPED TUNNEL LININGS

1. Introduction

Even though a lot of works have been done to develop tunnel lining design methods, it can be found that most of the analyses assumed that the tunnels are excavated in only one homogeneous soil. However, in real scenarios, it is very rare to meet tunnels built in only one layered soil. In most of the cases, layered soils are encountered which induces variations in terms of geomechanical properties (soil unit weight, Young modulus, cohesion and friction angle) for in each sub-layer. There are few studies which consider the effect of multi-layered soil mediums on the structural behaviour of the tunnel lining. Hagiwara et al. (1999) and Grant and Taylor (2000) presented data from a series of centrifuge model tests to investigate the effect of stiffness of an overlying layer on ground response around a tunnel. They found that the stability of a tunnel in the lower clay layer may be influenced by the presence of an upper layer depending on the type, state and thickness of the overlying material, and the cover depth above the tunnel crown. A topology optimization method was proposed by Yin and Yang (2000) for the design of tunnel support in layered geological media. This method makes the computer-aided design for the supports of underground tunnels embedded within layered geological media feasible. An experimental study was first conducted to investigate the bending stresses developed in tunnel lining by Nunes and Meguid (2009) through a series of 1-g model tests. The reduction of the moment was to a great extent dependent on the relative stiffness between the sand layer and the clay deposit around the tunnel. Yang and Yao (2017) proposed an axisymmetric failure mechanism to investigate the roof stability of deep tunnels in layered soils. In spite of this, no one of the methods mentioned above can provide an efficient way to estimate the tunnel behaviour in layered soils.

In fact, due to the variation of soil properties, the effect of the multi-layered environment on the internal forces and displacements of tunnel lining is not clear, especially when the contact surfaces of the multilayers is located between the tunnel crown and the invert. It is therefore interesting to find a simple and effective way to study the effect of the stratified soil mediums on tunnel lining behaviour (Zhang et al., 2015; Yang and Yan, 2015; Do and Dias, 2017; Do et al., 2018).

Since the HRM method simulates the structure-soil interaction by means of the springs which can easily simulate load transfer around tunnels excavated considering different rigidities of soil layers, this method is therefore used in this chapter to investigate the influence of multi-layered soils on the U-shaped tunnel lining design in terms of the internal forces and displacements of lining. Two different U-shaped tunnel linings (with and without invert arch shown in Fig. 4-1) are considered in this chapter.

The performance of the presented method is investigated by comparing its results with the ones of a finite difference program. Different stratified soil conditions are considered to investigate the U-shaped tunnel lining behaviour, e.g. one homogeneous layer, one layer with a linear cohesion with depth, two layers, and three layers considering a variation of the position and of the thickness of the intermediate layer. The results of two different U-shaped tunnels are compared and analysed for these different stratified soils. In the case of a U-shaped tunnel without invert, the effect of the lining constraint conditions (shown in Fig. 3-3 of the Chapter 3) is also investigated.

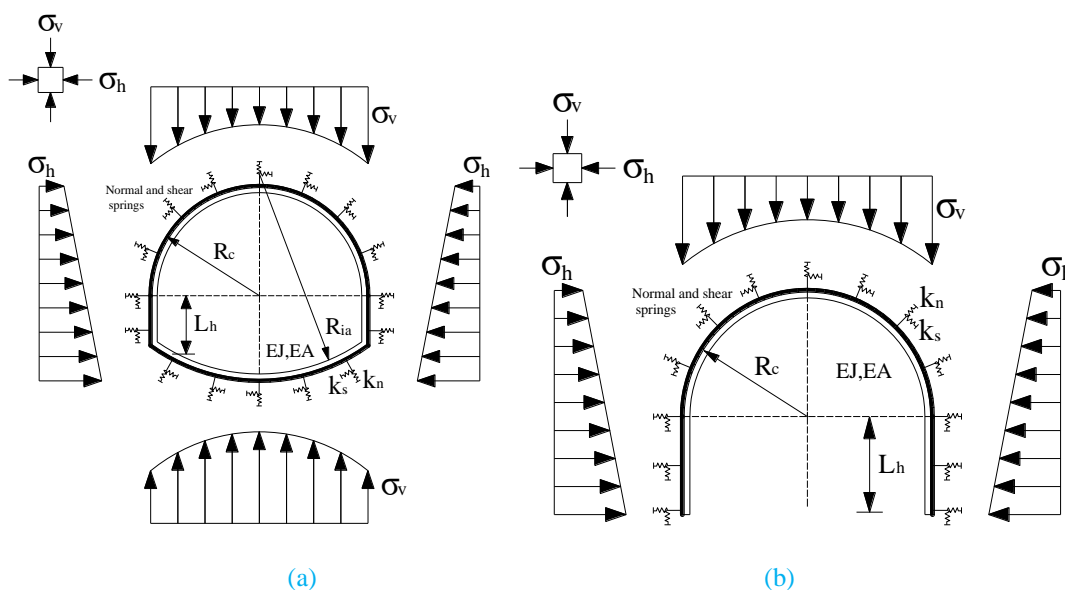


Fig. 4-1 Two different U-shaped tunnel linings: (a) with invert arch and (b) without invert arch. σ_v and σ_h are vertical and horizontal loads, respectively; k_n : normal spring stiffness; k_s : shear spring stiffness; R_c : radius of the tunnel crown; R_{ia} : radius of the tunnel invert arch; L_h : vertical distance from the point of tunnel cross-section to the tunnel centre; EA and EJ are the normal and bending stiffness of the structure, respectively

2. Tunnel design models

Only half of the tunnel is considered because of the symmetry of the problem. The HRM code could consider the support geometry (Fig. 4-2). The clamped constraint for the Geometry2 is adopted to investigate the behaviour of the tunnel lining in the following part of this chapter.

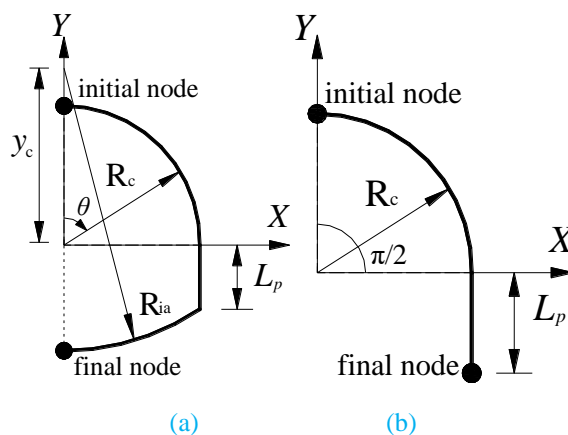


Fig. 4-2 Support geometries considered in the analysis: (a) Geometry1: tunnel with invert arch and (b) Geometry2: tunnel without invert arch. R_{ia} : radius of the tunnel invert arch; R_c : tunnel crown radius; L_p : tunnel sidewall length; y_c : height of the tunnel invert arch centre; θ : angle between the element axis and the vertical axis of tunnel cross-section. X and Y are the global Cartesian coordinates

Table 4-1 Tunnel parameters used in this chapter

Parameter	Symbol	Value	Unit
<i>Properties of tunnel</i>			
Crown radius	R_c	6.02	m
Invert arch radius	R_{ia}	20.22	m
Height of invert arch centre	y_c	15.00	m
Height of the sidewall	L_p	3.80	m
Support thickness	t	0.22	m
Poisson's ratio	ν	0.15	-
Elastic modulus of concrete	E_0	35,000	MPa
Tunnel diameter	D	10.74	m

Multi-layered grounds are usually encountered in practice such as the cases of Möller and Vermeer (2008) and Do and Dias (2017). The aim of this section is to investigate the influence of different layers position on the structural forces induced in the tunnel lining. There are four different layered soil cases considered in the HRM model for each kind of U-shaped tunnels (with and without invert arch):

- Case 1: Homogeneous medium including one soil layer with a constant cohesion,

- Case 2: Inhomogeneous medium including one soil layer as in case 1, whose cohesion varies linearly with depth (Yang and Du, 2016). This case is investigated in order to highlight the effect of cohesion change in depth.

- Case 3: Inhomogeneous medium including two layers with their contact surface located at the tunnel spring line. The upper layer and the lower layer are respectively classified as a soft ground and a bed rock.

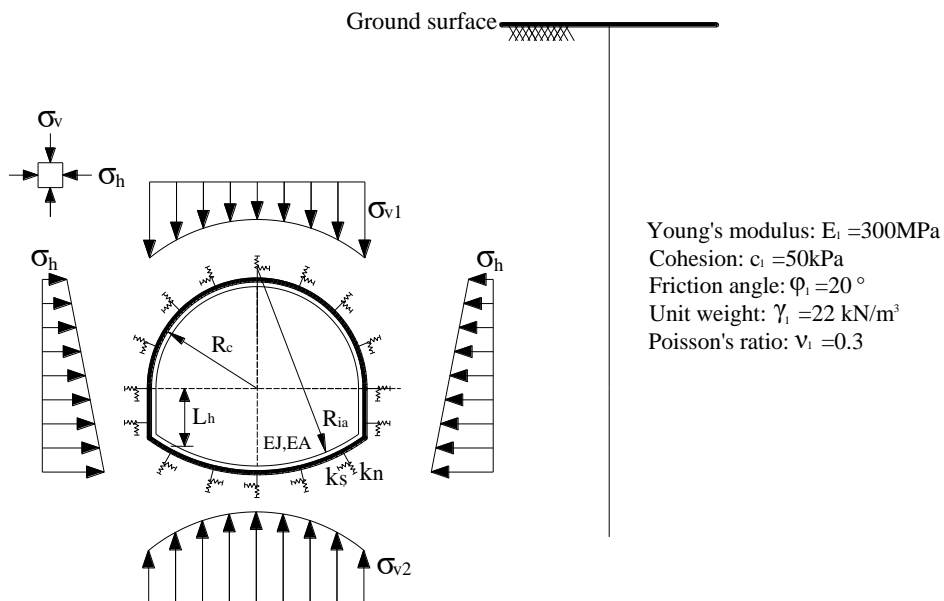
- Case 4: Inhomogeneous medium including three layers with a variation of the position and thickness of layer 2 (only the U-shaped tunnel with an invert arch is shown in Fig. 4-3). The middle layer is the weaker layer while the lower layer could be considered as the bed rock.

Table 4-2 Soil mass properties

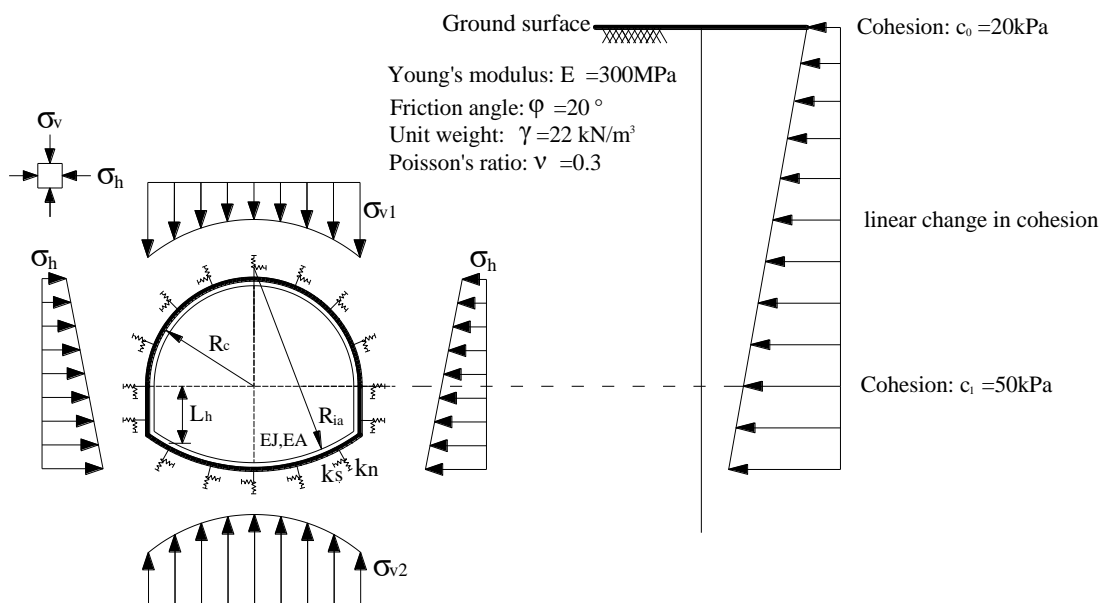
Properties	Symbol	Value	Unit
<i>Properties of the layer 1</i>			
Cohesion	C_1	50	kPa
Unit weight	γ_{s1}	22	kN/m ³
Poisson's ratio	ν_{s1}	0.3	-
Internal friction angle	φ_1	20	degrees
Elastic modulus	E_1	300	MPa
Lateral earth pressure factor	K_{01}	0.5	-
Thickness	H_1	changed	m
<i>Properties of the layer 2 in case4</i>			
Cohesion	C_2	10	kPa
Unit weight	γ_{s2}	20	kN/m ³
Poisson's ratio	ν_{s2}	0.3	-
Internal friction angle	φ_2	20	degrees
Elastic modulus	E_2	75	MPa
Lateral earth pressure factor	K_{02}	0.5	-
Thickness	H_2	changed	m
<i>Properties of the layer 2 in case3 and the layer 3 in case4</i>			
Cohesion	C_3	100	kPa
Unit weight	γ_{s3}	23	kN/m ³
Poisson's ratio	ν_{s3}	0.35	-
Internal friction angle	φ_3	45	Degrees
Elastic modulus	E_3	5,000	MPa
Lateral earth pressure factor	K_{03}	0.5	-
Thickness	H_3	changed	M

Three kinds of ground layers are adopted whose parameters are the ones of a soft soil, a hard soil and a bed rock, respectively. The geometrical parameters of the tunnel lining and layers soils are respectively shown in Table 4-1 and Table 4-2, which are adopted from the Toulon tunnel (Oreste and Dias, 2012). In addition, as the soil and structural parameters are different, the values of β in Eq. (2-20) are chosen on the basis of the comparison between the results of the HRM model and those of the FLAC^{3D}: $\beta=1$ for the one-layered

condition (Case1 and Case2); $\beta=1$ for the layer1 and $\beta=8$ for the layer2 under the two-layered condition (Case3); $\beta=1$ for the layer1 and layer2 and $\beta=8$ for the layer3 under the three-layered condition (Case4).



(a)



(b)

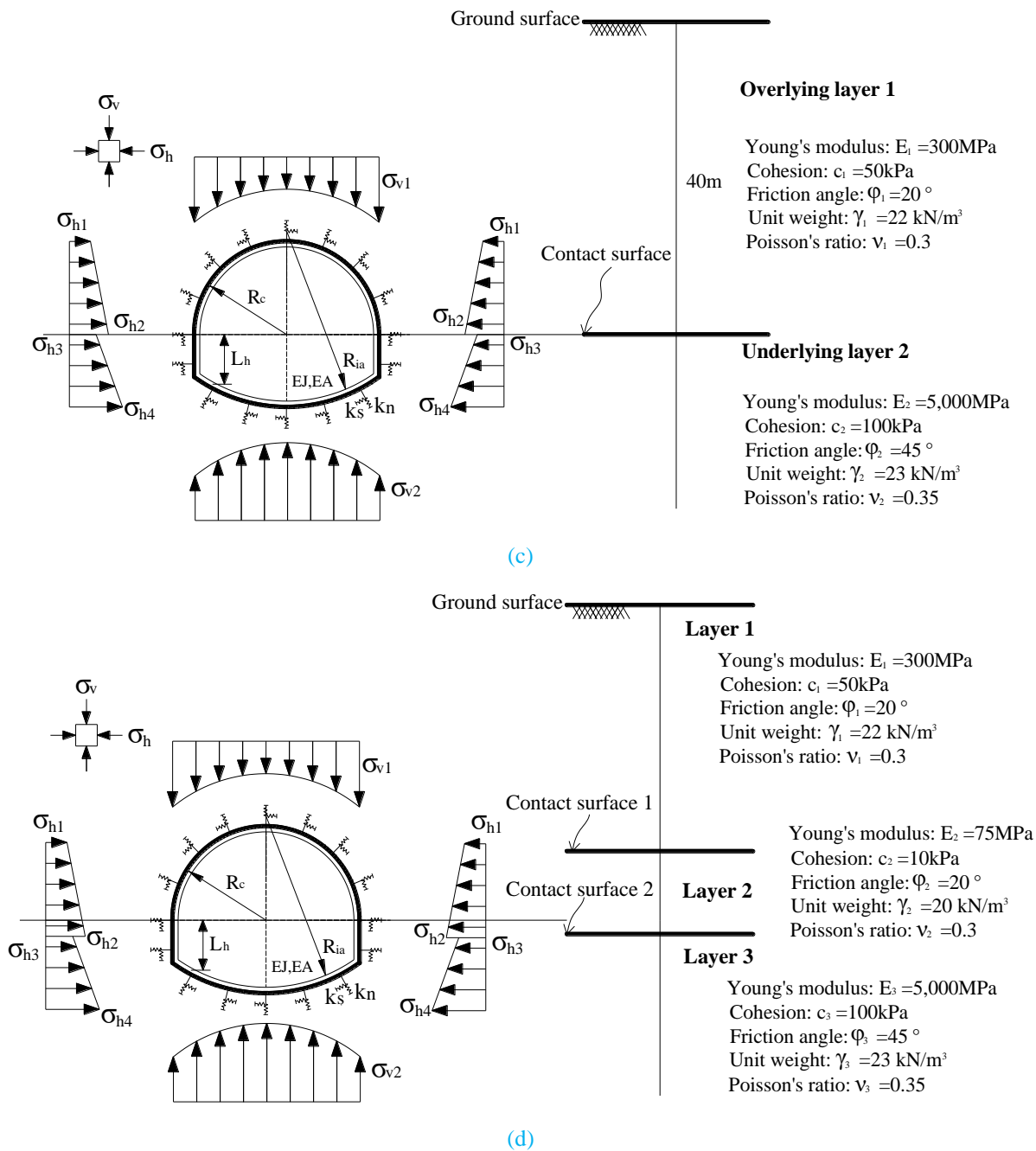


Fig. 4-3 Layered soil cases of U-shaped tunnel with invert arch: (a) Case1: all soil mass in one layer with a constant cohesion; (b) Case2: all soil mass in one layer with a linear cohesion variation with depth (20kPa at the surface, 50kPa at the centre of the tunnel); (c) Case3: two layers with a contact surface located at the spring line of tunnel; and (d) Case4: three layers with changed position and thickness of layer 2

3. Estimation the performance of the HRM Method

The accuracy of the HRM method is estimated in this section on the basis of a comparison with the finite difference program FLAC^{3D} (Itasca Consulting Group, 2012). Similar results are obtained by HRM and FLAC^{3D} for all the four layered soil cases as shown in Fig. 4-3. Only the Case3 (U-shaped tunnel with invert arch, two layers) is taken as an example to illustrate the obtained results. The parameters shown in Tables 4-1 and 4-2 are adopted for this evaluation.

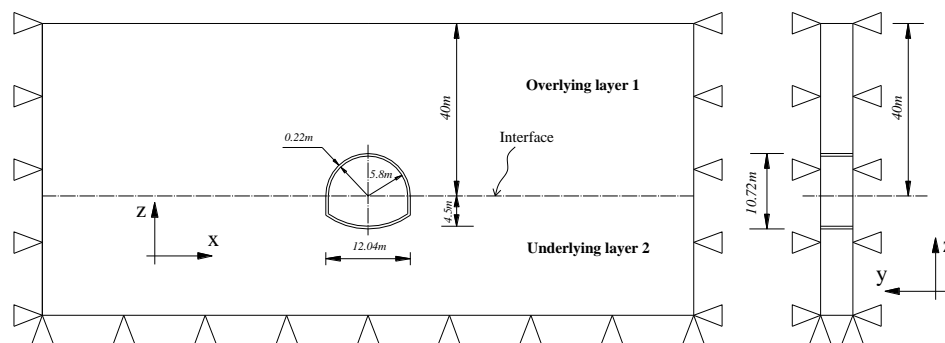


Fig. 4-4 Numerical geometry model of U-shaped tunnel with invert arch

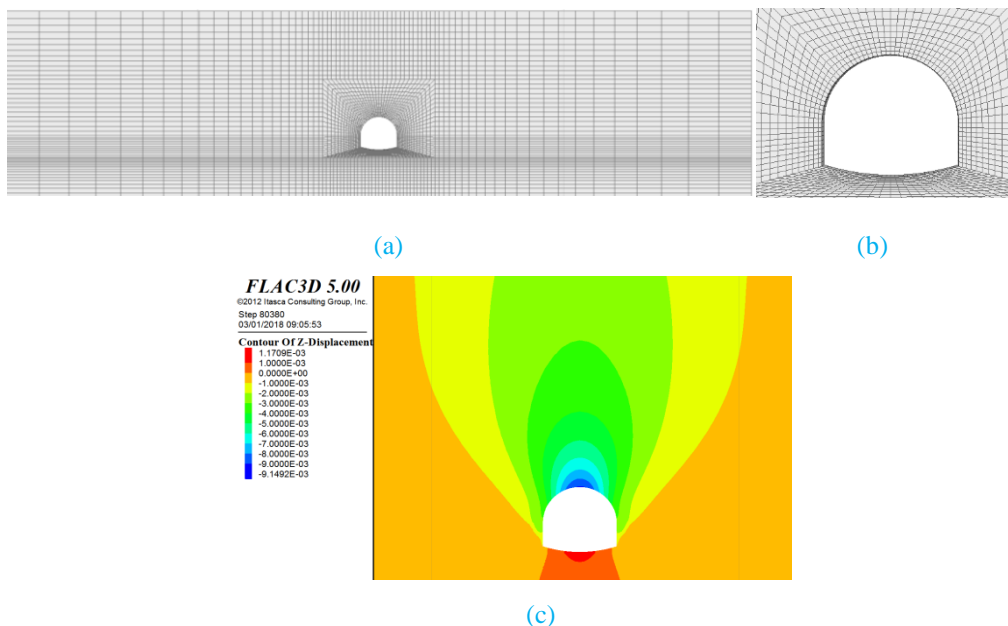


Fig. 4-5 Numerical model in FLAC^{3D}: (a) Two-dimensional mode; (b) tunnel with invert arch; and (c) Vertical displacement of this model

Figs. 4-4 and 4-5 show the numerical model of the U-shaped tunnel with invert arch (Geometry1 in Fig. 4-2) with the assumption of plane-strain conditions. The dimension of the elements increases with the distance

from the tunnel (Fig. 4-5). This model consists of about 6,100 zones and 12,400 grid points with 60m long in the z -direction, 240m wide in the x -direction.

Fig. 4-6 shows the internal forces and displacements of the U-shaped tunnel lining. The results were obtained from the FLAC^{3D} model and the HRM method, respectively. It can be found that the normal forces obtained from the FLAC^{3D} model are larger than the ones of HRM method at the tunnel crown and sidewall, but smaller at the tunnel invert arch. Although there are some small discrepancies between the results of HRM and FLAC^{3D}, the bending moments calculated by HRM have the similar trend compared with the results of FLAC^{3D} along the whole tunnel. The maximum absolute value of the bending moment for both of two results is located at the connection of tunnel sidewall and invert arch.

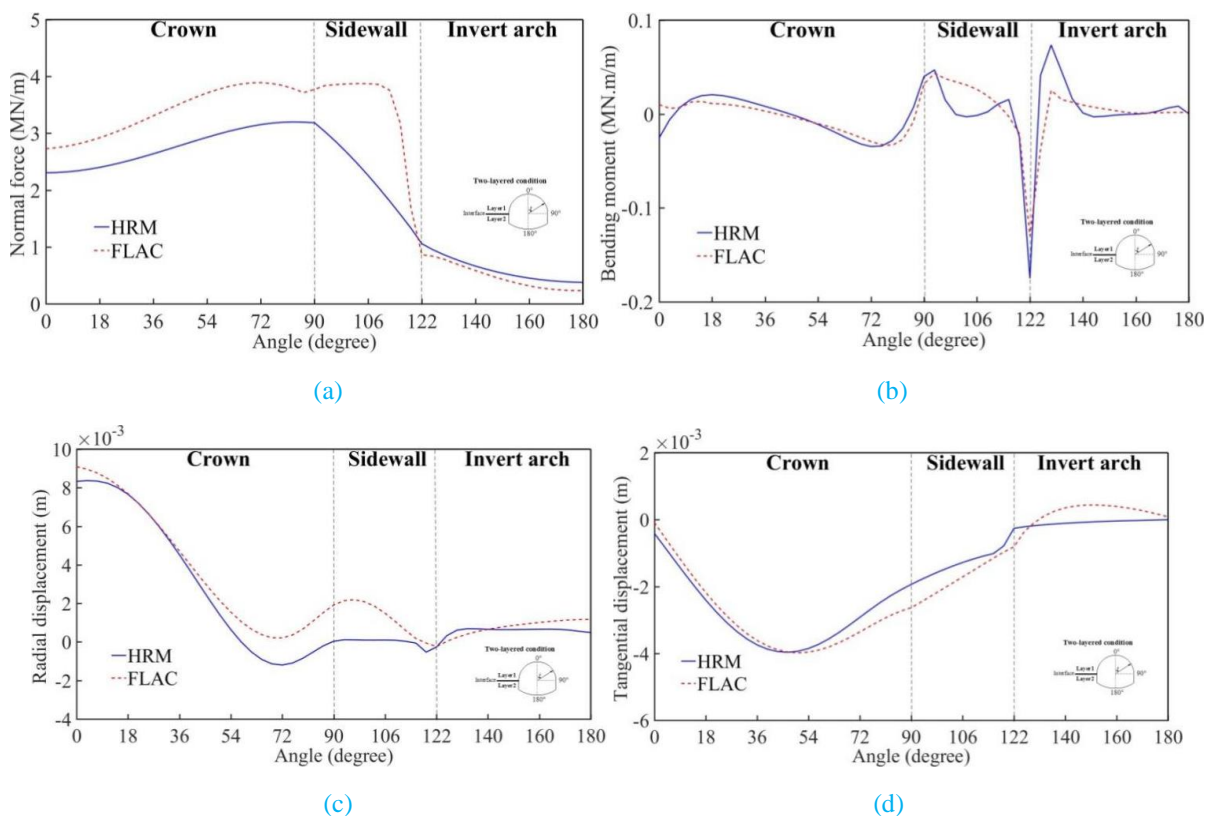


Fig. 4-6 Comparisons of internal forces and displacements in the U-shaped tunnel support (Geometry1 in Fig. 4-2). Key: (a) normal force; (b) bending moment; (c) radial displacement; and (d) tangential displacement

The results of radial displacements obtained from FLAC^{3D} give values close to the ones of HRM at the tunnel crown and invert arch. However, the results of tangential displacements obtained from FLAC^{3D} are similar to the ones of HRM along the whole tunnel. The maximum difference of tangential displacements happens at the spring line with 7.87%.

The small discrepancies between the results of HRM and FLAC can be explained by two reasons:

- The way the loading is applied on the tunnel support is different. The external loads of HRM method act directly and explicitly on the nodes of beam elements. In contrast, the loads in the FLAC analysis are applied at the tunnel support through the continuous soil.
- The tunnel arching effect developed in the FLAC model is not considered in the HRM model.

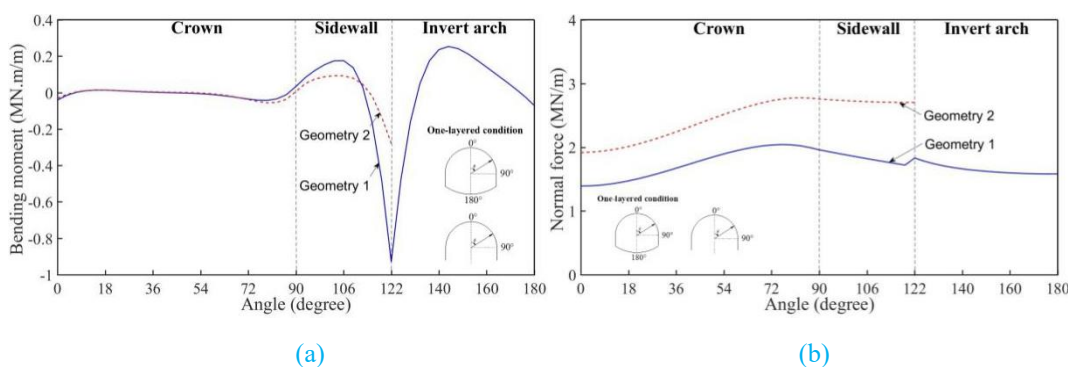
On the basis of the results mentioned above, it could be concluded that the displacements and internal forces results of supports obtained using the HRM are in good agreement with the ones of FLAC^{3D}. It is therefore reasonable and feasible to analyse the behaviour of U-shaped tunnel supports in layered soils using the HRM method.

4. Results and parametric analysis

This section gives the results of present method and the parametric analysis considering four layered soil cases of U-shaped tunnel, which has been shown in Fig. 4-3.

4.1. One soil (constant parameters)

Fig. 4-7 illustrates the results of the displacements and internal forces of two different U-shaped tunnels obtained from the HRM method with the Case1 (Fig. 4-3a). Only the clamped constraint condition is used for Geometry2 when doing this comparison.



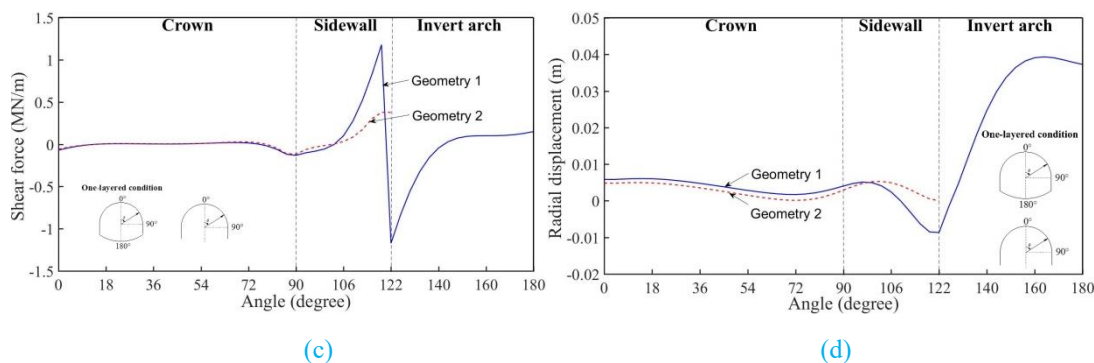
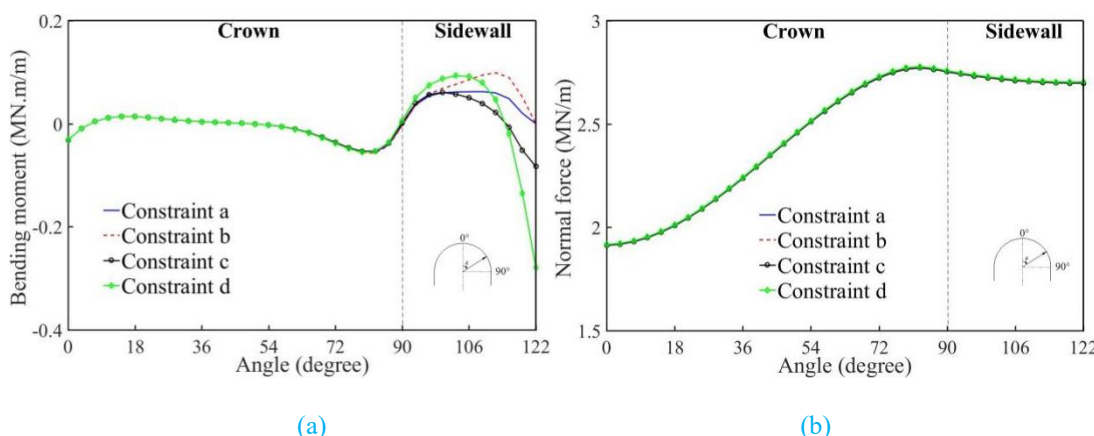


Fig. 4-7 Comparisons of the HRM results between two different U-shaped tunnels: (a) Bending moment; (b) Normal force; (c) Shear Force; and (d) Radial displacement

It can be found from Fig. 4-7 that the normal forces and displacements of the Geometry2 almost have the same trend compared with the Geometry1. There is no clear difference at the tunnel crown between the values of bending moments and displacements for the two tunnel shapes. The radial displacements of Geometry1 are slightly higher than the ones of Geometry2 at the tunnel crown, but smaller at the sidewall. Similarly, discrepancies for the shear forces and bending moments are also obvious at the sidewall. The normal forces of Geometry2 are higher than the ones for Geometry1 along the whole tunnel.

A comparison is also conducted to illustrate the effect of the constraint type (shown in Fig. 3-3 of Chapter 3) on the tunnel lining behaviour of Geometry2 (see Fig. 4-8). Fig. 4-8 shows that the effect of the constraint type on the internal forces and displacements at the tunnel crown can be neglected. However, its effect on bending moments, radial displacements and, rotations at the tunnel sidewall needs to be considered. It almost gives the same values of normal forces for the four constraint types along the whole tunnel.



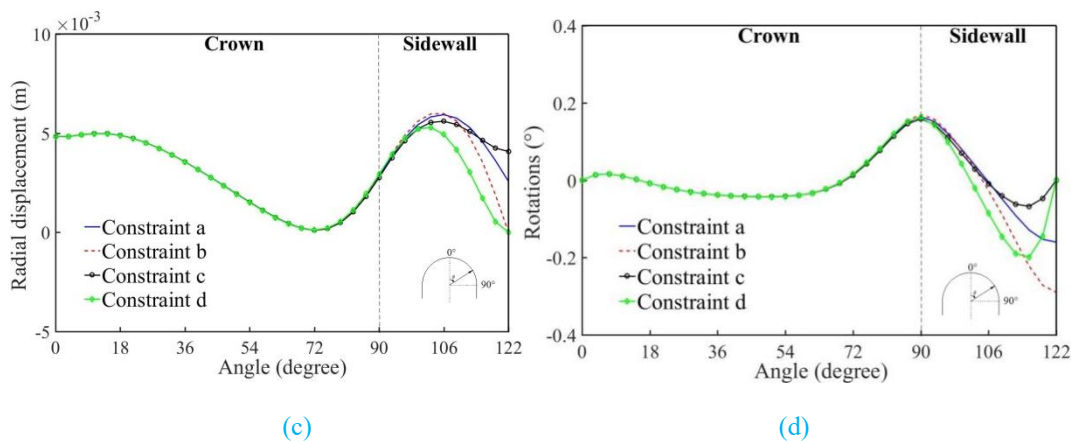


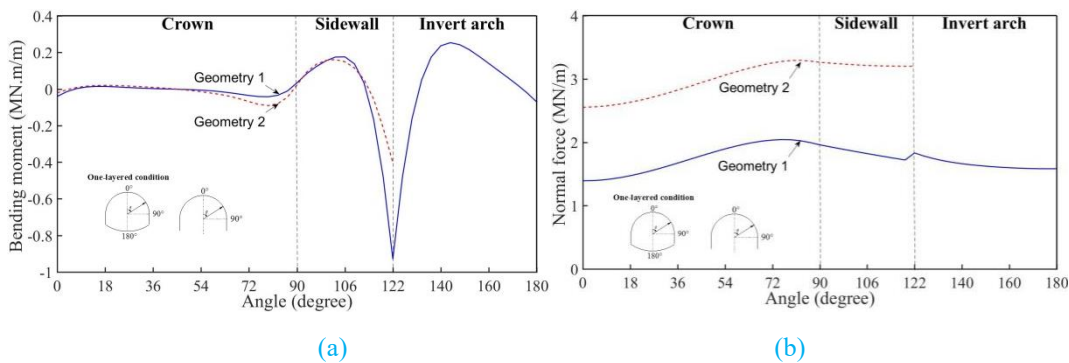
Fig. 4-8 Effect of constraint types on the tunnel lining behaviour of Geometry2: (a) Bending moment; (b) Normal force; (c) Radial displacement; and (d) Rotations

The largest bending moment is found in the case of constraint d due to the restrained rotation at the tunnel lining base. The smallest bending moments are found in the cases of constraints (a) and (b) where tunnel lining bases are free to rotate (Fig. 4-8d). In addition, the radial displacements of tunnel lining are also clearly different for those four constraint cases at the tunnel sidewall.

4.2. One soil with a linear cohesion variation with depth

Fig. 4-9 illustrates the results of the displacements and internal forces of two different U-shaped tunnels obtained using HRM under the condition of the one soil with a linear cohesion variation (Case2 in Fig. 4-3b).

Like the values of Case1 shown in Fig. 4-7, Fig. 4-9 illustrates that the normal forces and displacements of the Geometry2 almost have the same trend compared with Geometry1. However, the discrepancies of bending moments are smaller and the ones of normal forces are greater. The absolute values of radial displacements of Geometry2 are slightly higher than the ones of Geometry1 at the tunnel sidewall and centre of crown.



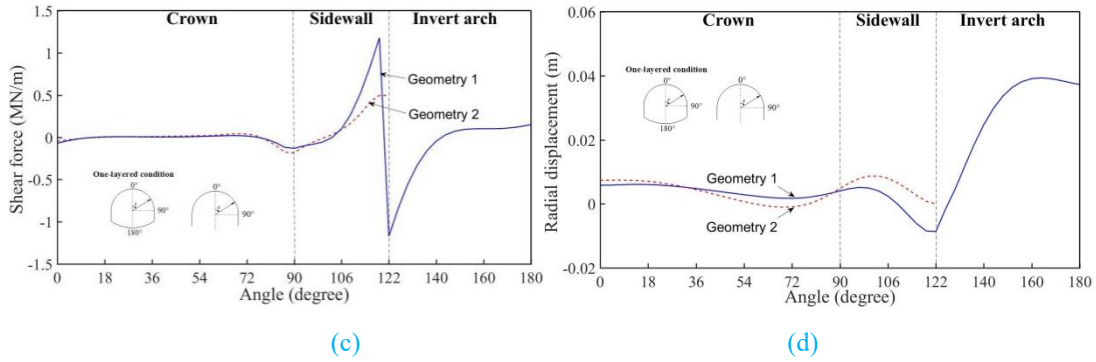
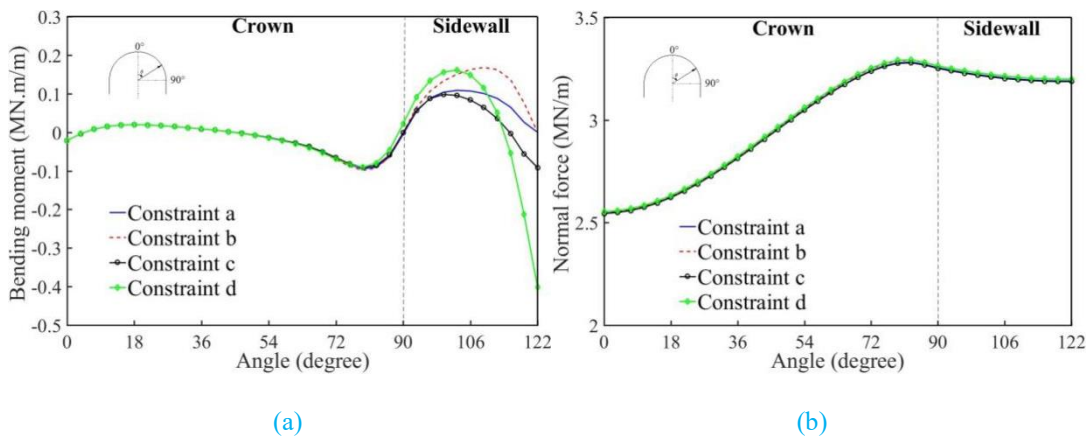


Fig. 4-9 Comparisons of the HRM results between two different U-shaped tunnels of cases 1 and 2: (a) Bending moment; (b) Normal force; (c) Shear Force; and (d) Radial displacement

The effect of constraint types under the condition of Case2 on the tunnel lining behaviour of Geometry2 is also shown in Fig. 4-10. Fig. 4-10 gives the similar conclusions as Fig. 4-8. It should be noticed that Case2 with a linear cohesion variation gives larger absolute values than Case1 with constant soil parameters, though both two Figures have the similar trend.

Fig. 4-11 shows the results of internal forces and displacements of Geometry2 obtained by HRM under the conditions of Cases 1 and 2. The linear varying cohesion with depth has a great effect on the internal forces and displacements of Geometry2 from Fig. 4-11. The normal forces under the condition of Case2 are clearly higher than the ones of Case1 along the whole tunnel. In addition, Case2 gives higher values of bending moments, shear forces and radial displacements at the sidewall. Clearly, there are no clear discrepancies between the values of bending moments and shear forces at the tunnel crown for both cases. In contrast, the radial displacements of Case2 are higher than those of Case1 at the centre of tunnel crown.



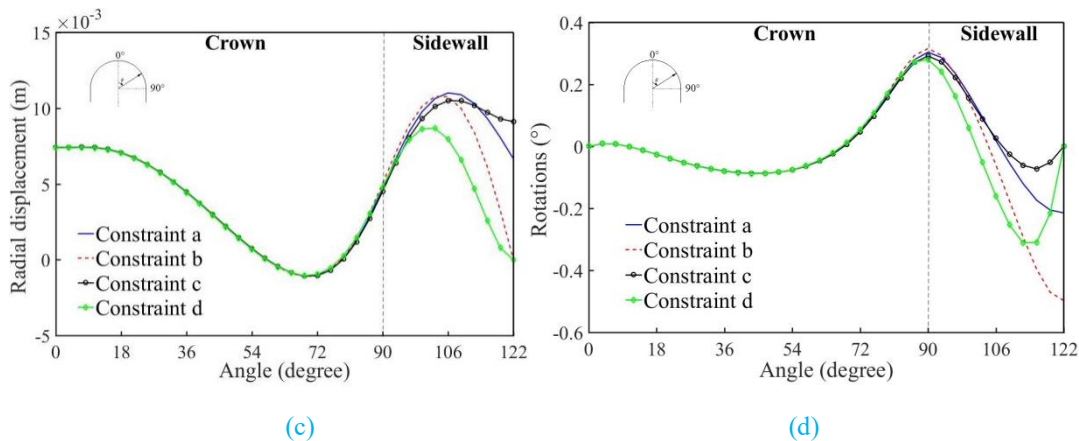


Fig. 4-10 Effect of constraint conditions on the tunnel lining behaviour of Geometry2: (a) Bending moment; (b) Normal force; (c) Radial displacement; and (d) Rotations

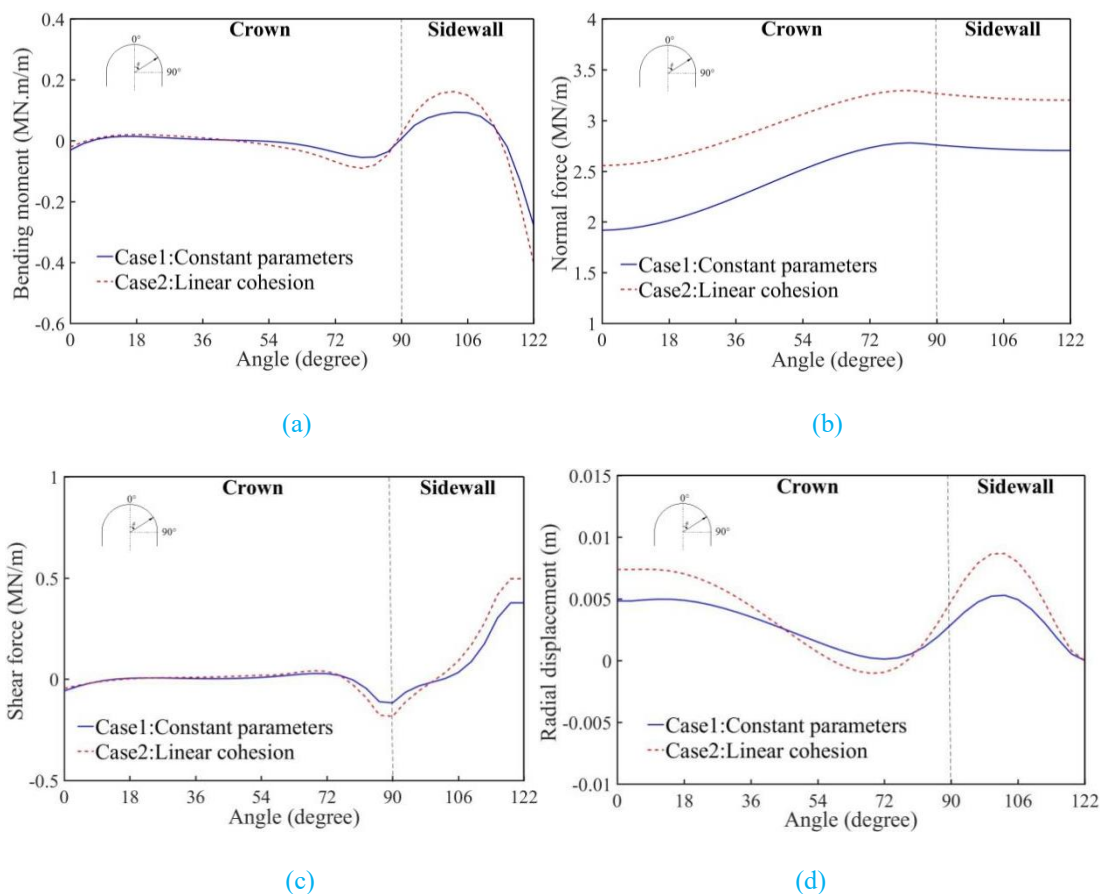


Fig. 4-11 Comparisons of the HRM results of Geometry2 under the cases 1 and 2: (a) Bending moment; (b) Normal force; (c) Shear Force; and (d) Radial displacement

4.3. Two-layered soil (contact surface located at the spring line of tunnel)

Fig. 4-12 shows the results of the displacements and internal forces of two different U-shaped tunnels obtained from HRM under the two-layered soil condition (Fig. 4-3c).

It is observed from Fig. 4-12 that the results of internal forces and displacements of Geometry2 are consistent with the ones of Geometry1. There is no clear difference for the bending moments and shear forces between the two shapes. However, the values of normal forces of Geometry2 are higher at the tunnel crown but lower at the sidewall than that of Geometry1. On the contrary, the values of radial displacement of Geometry2 are lower than that of Geometry1 at the centre of tunnel crown.

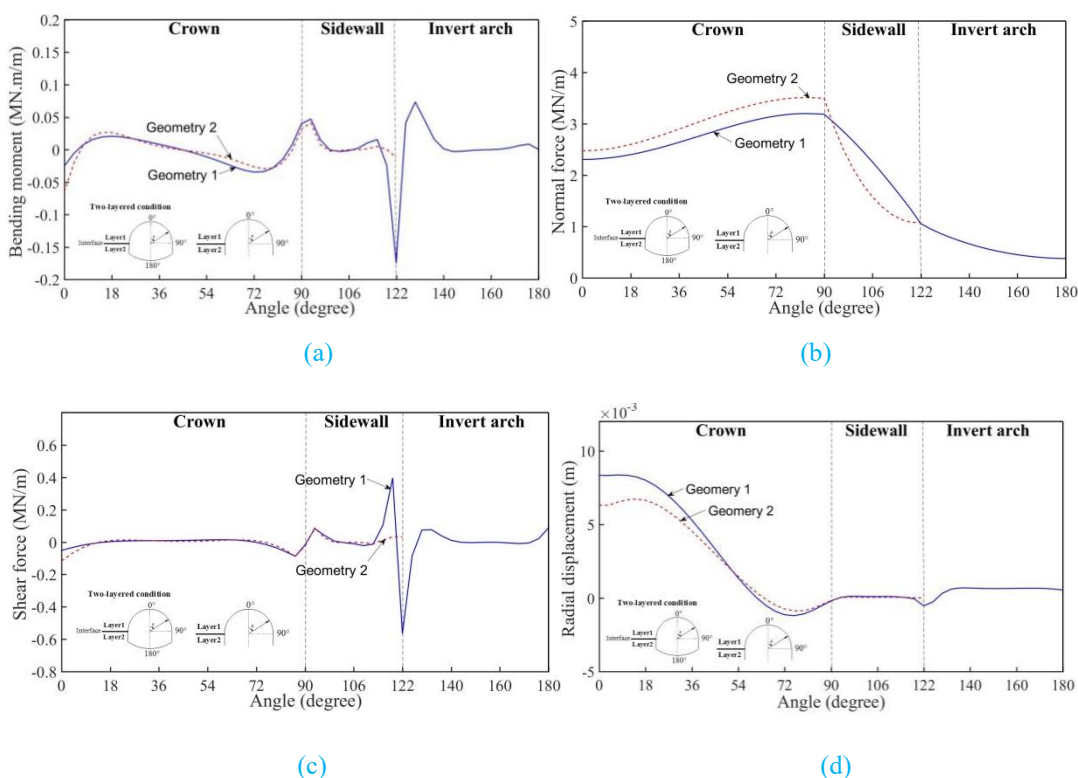


Fig. 4-12 Comparisons of the HRM results between two different U-shaped tunnels: (a) Bending moment; (b) Normal force; (c) Shear Force; and (d) Radial displacement

Similarly, a comparison is also conducted to study the effect of constraint types (shown in Fig. 3-3 of Chapter 3) on the tunnel lining behaviour of Geometry2 (Fig. 4-13). Compared with Figs. 4-8 and 4-10, Fig. 4-13 shows that the effect of the different constraint types on the lining behaviour is less obvious under the two-layered soil condition.

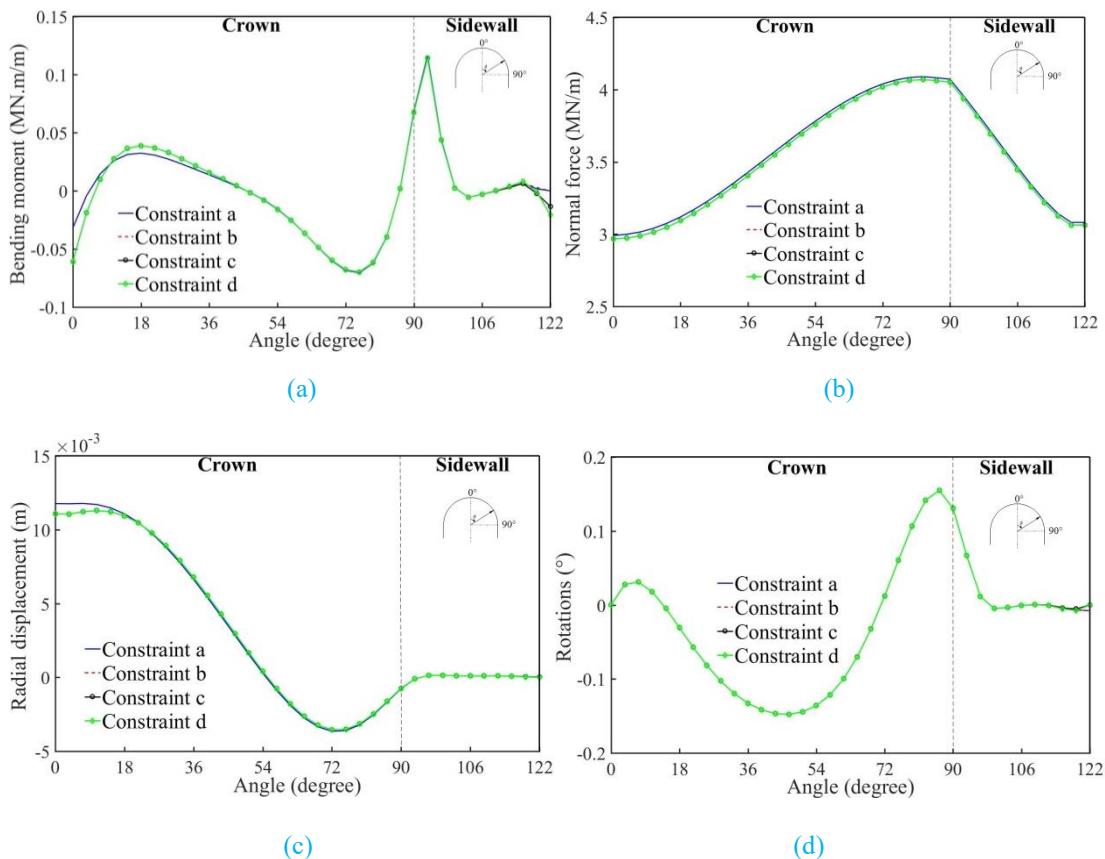
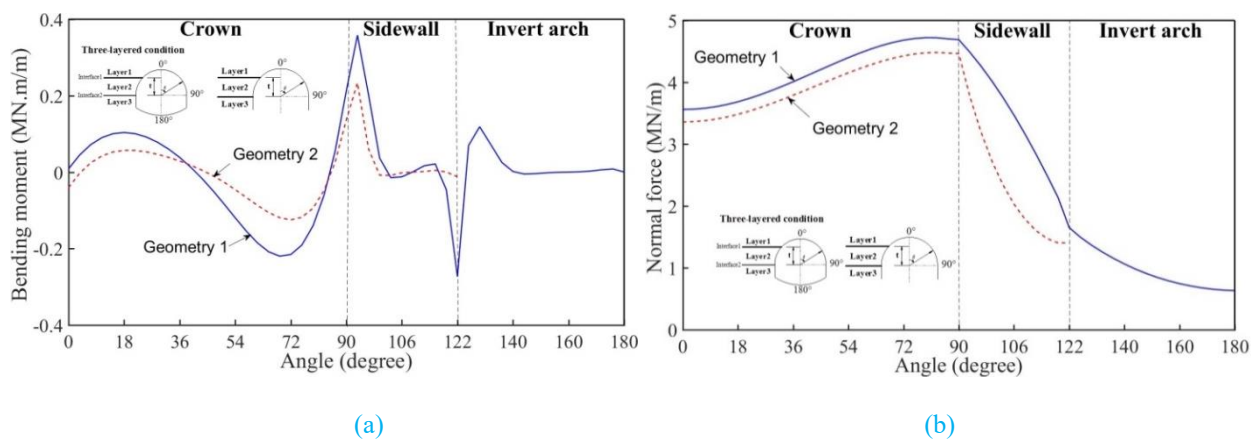


Fig. 4-13 Effect of constraint types on the tunnel lining behaviour of Geometry2: (a) Bending moment; (b) Normal force; (c) Radial displacement; and (d) Rotations

4.4. Three-layered soil

Fig. 4-14 illustrates the results of the displacements and internal forces of two different U-shaped tunnels under the three-layered soil condition with layer2 unchanged (special case: thickness of layer2 is equals to R_c).



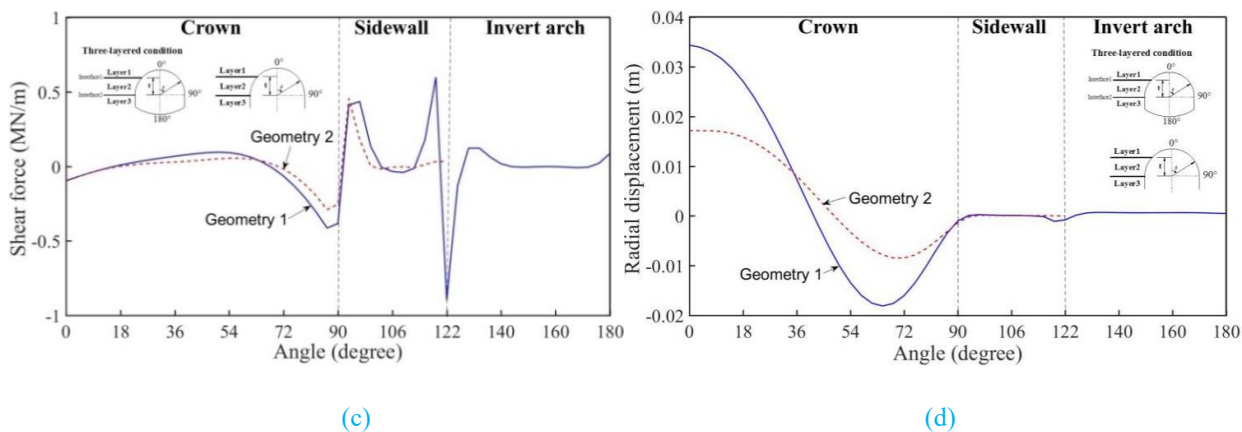


Fig. 4-14 Comparisons of the HRM results between two different U-shaped tunnels: (a) Bending moment; (b) Normal force; (c) Shear Force; and (d) Radial displacement

As shown in Fig. 4-14, although there are some discrepancies for the internal forces and displacements between the two lines, the tendencies between them are similar. Also, the discrepancies of the results between two geometries under the three-layered soil condition are higher than the ones under two-layered soil condition.

Similar to the results presented in Fig. 4-13, the effect of constraint types (shown in Fig. 3-3 of Chapter 3) on the tunnel lining behaviour of Geometry2 is also shown in Fig. 4-15. The same conclusion could be obtained from Fig. 4-15 that the tunnel lining behaviour is not significantly affected by the different constraint types under Case4. However, the three-layered soil condition (see in Fig. 4-15) gives larger absolute values than the two-layered soil condition.

In addition, for the three-layered soil condition, the other case (changing the position and thickness of layer2) is also considered. To study the influence of the position and thickness of layer2, the relative thickness of layer2 t/D is defined by the thickness (t) of layer2 over the tunnel diameter D . Note that the position of layer 2 is moving from the tunnel crown to the bottom and the layer2 thickness is taken equal to 1/5, 1/4, 1/3, 1/2 of the tunnel height. Taking the Geometry1 as an example, Fig. 4-16 shows the effect of the position and thickness of layer2 on the tunnel lining behaviour of Geometry1. The results of HRM are plotted as a function of the t/D in Fig. 4-16(a) for bending moments, in Fig. 4-16(b) for normal forces, in Fig. 4-16(c) for shear forces and in Fig. 4-16(d) for normal displacements.

As shown in Fig. 4-16, the effect of the thickness of layer2 on the bending moments and displacements of tunnel lining at the tunnel crown is not significant. The magnitude of the normal force increases nearly 20% as the relative thickness increases from 1/3 to 1/2, as shown in Fig. 4-16(b).

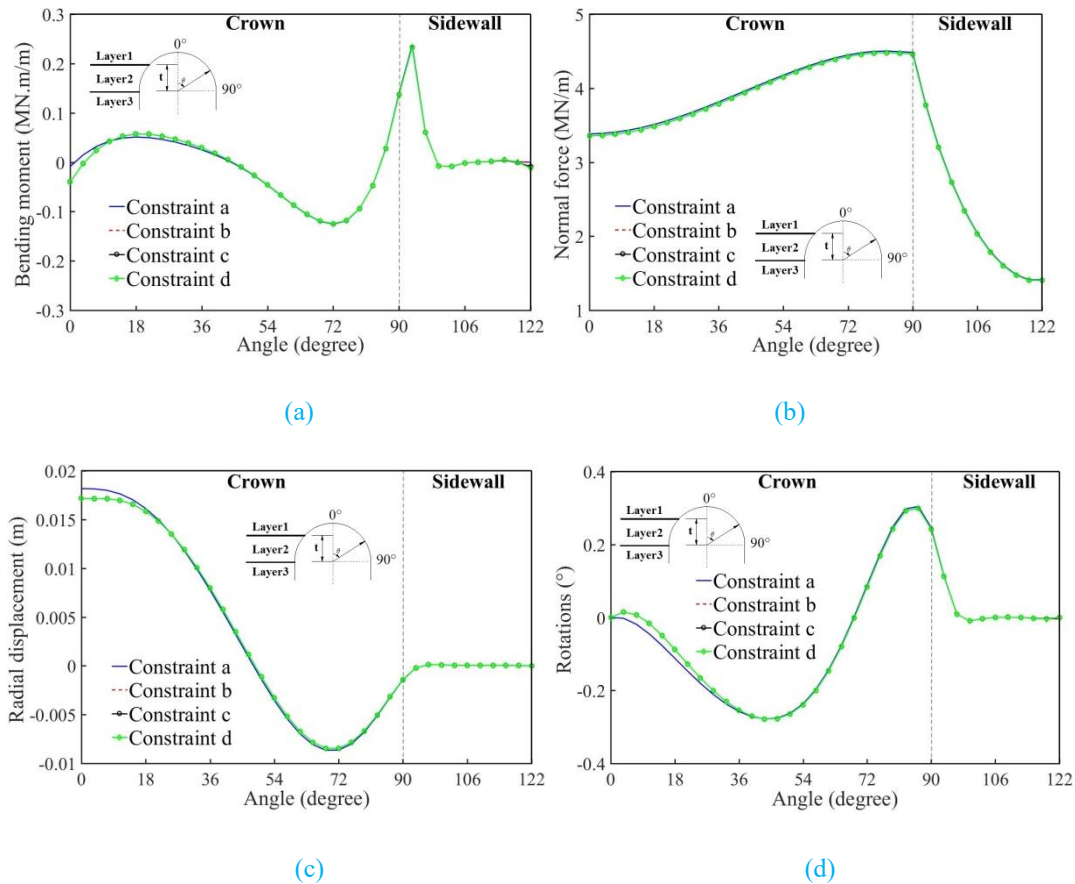


Fig. 4-15 Effect of constraint types on the tunnel lining behaviour of Geometry2: (a) Bending moment; (b) Normal force; (c) Radial displacement; and (d) Rotations

However, the lining behaviour at the tunnel sidewall is to a great extent affected by the thickness of layer2. The magnitude of the bending moment under the condition2 and condition3 (Condition1 represents layer2 is totally located at tunnel crown; Condition2 represents layer2 is located at tunnel crown and sidewall; Condition3 represents layer2 is located at tunnel sidewall and invert arch) decreases as the relative thickness increases from 1/5 to 1/3. Nevertheless, it increases as the relative thickness increase from 1/3 to 1/2. In contrast, the increase of the bending moment under Condition1 is not obvious when the relative thickness increases from 1/5 to 1/2, as shown in Fig. 4-16(a). As for the magnitude of the shear force, it increases as the relative thickness increases from 1/5 to 1/3 under the Condition2 and Condition3, but decreases as the relative thickness increases from 1/3 to 1/2 (Fig. 4-16c). However, the magnitude of the shear force under the

Condition1 increases with the increase of the relative thickness. Fig. 4-16 also shows that the magnitudes of normal force and normal displacement have a non-linear increase with the increase of the relative thickness from 1/5 to 1/2.

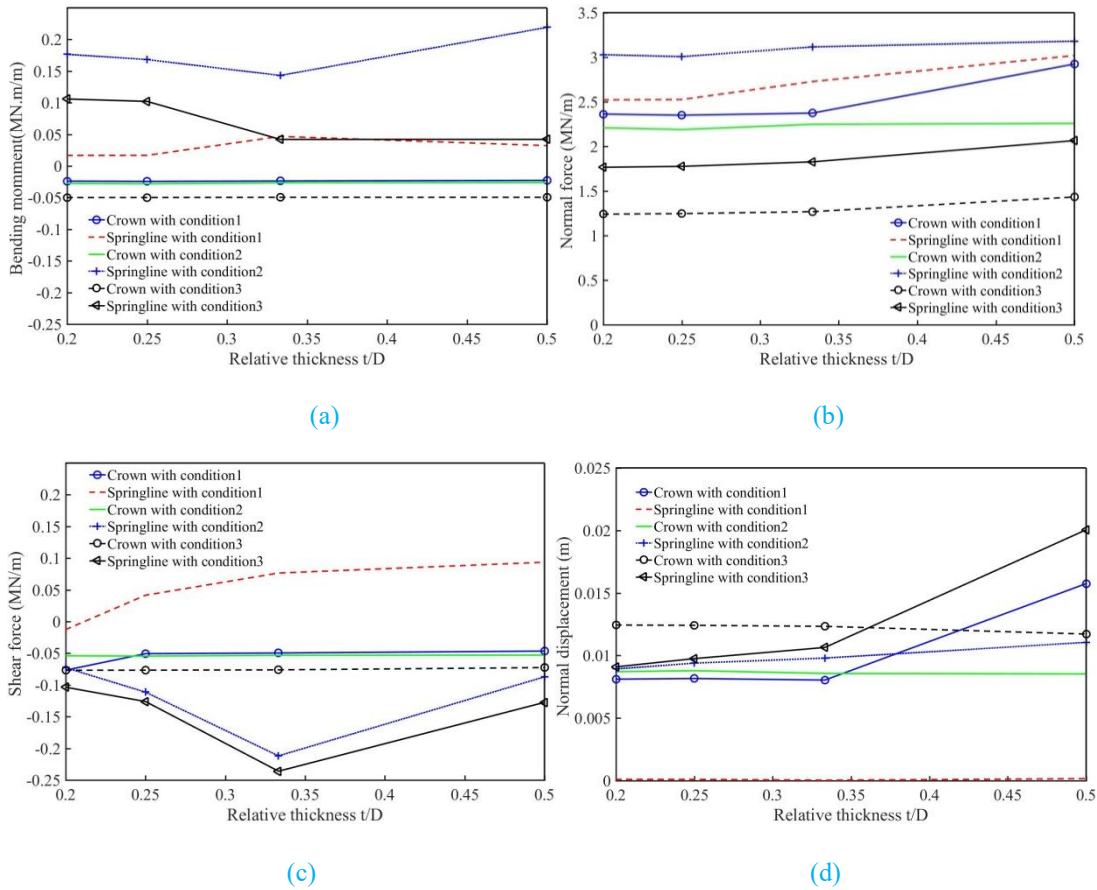


Fig. 4-16 Effect of the position and thickness of layer2 on the tunnel lining behaviour of Geometry1: (a) Bending moment; (b) Normal force; (c) Shear Force; and (d) Normal displacement. Key: Condition1 represents layer2 is totally located at tunnel crown; Condition2 represents layer2 is located at tunnel crown and sidewall; Condition3 represents layer2 is located at tunnel sidewall and invert arch

It could be concluded that the influence of the position of the layer2 is significant on the tunnel behaviour. Generally, the lower position of the layer2 causes smaller absolute values of normal forces, but higher absolute values for the bending moments, shear forces and normal displacements at the tunnel crown.

5. Conclusions

The HRM method is extended in this chapter to estimate the effect of multi-layered soil conditions on the U-shaped tunnel support behaviour. Two different geometries, a U-shaped tunnel with and without invert arch, are considered. Multi-layered soil conditions are considered and their influence on the U-shaped tunnel lining behaviour is presented. Compared with previous studies, more cases for soil layered conditions are studied. The results of HRM are compared with the ones of the numerical model FLAC^{3D}, a good agreement between these two approaches was found.

The comparisons between the results obtained from both of two different U-shaped tunnels under each soil condition are presented. In addition, the analysis is also made to show the effect of constraint types on the behaviour of U-shaped tunnel without invert arch. Some conclusions were obtained:

- The normal forces and displacements obtained from Geometry2 almost have the similar trend compared with the one of Geometry1.
- The effect of constraint types on the internal forces and displacements of tunnel linings can be neglected at the tunnel crown. However, their effect on the bending moments, shear forces and, radial displacements at the tunnel sidewall should be considered. The four constraint types considered almost give the same values of normal forces.
- The effect of relative thickness t/D of the mid-layer (layer2) on the bending moments and displacements at the tunnel crown are not significant. The magnitude of the normal force increases nearly 20% as the t/D increases from 1/3 to 1/2.
- The relative thickness t/D of mid-layer has a great effect on the lining behaviour at the tunnel sidewall.
- The influence of the position of the mid-layer is significant on the tunnel behaviour. Generally, the greater the depth of the mid-layer, the smaller the absolute values of the normal forces, but the higher the absolute of the bending moment, shear forces and normal displacement at the tunnel crown.

In the following chapter, the effect of the surcharge loading on the behaviour of a U-shaped tunnel excavated in saturated ground will be investigated.

CHAPTER 5 EFFECT OF A SURCHARGE LOADING ON HORSESHOE SHPAED TUNNELS EXCAVATED IN SATURATED GROUND

1. Introduction

More and more underground facilities, such as subway tunnels, are constructed under existing buildings or buildings are constructed over existing underground structures. In addition, in practical situations, tunnels are often constructed beneath the phreatic surface, like cross-river tunnels and urban tunnels near rivers. Tunnel linings should therefore sustain the loads transferred from the surrounding ground, surface buildings and groundwater (Takano, 2000; Nam and Bobet, 2006; Do et al. 2014b, c; Miranda et al., 2015). It is necessary to study the impact of those loads on the lining behaviour (Li et al., 2016; Aalianvari, 2017; Ding and Liu, 2018; Wu et al., 2018).

Some works have been presented to evaluate the surface loading effect on a tunnel located below the water table. Bobet (2001) presented a complete analytical solution to estimate the ground deformations and lining stresses of shallow circular tunnels in saturated ground. Later, an analytical solution for a deep circular tunnel in a saturated poroelastic soil mass was obtained under static and seismic loading conditions (Bobet 2003). Using a mathematical formulation, Bobet (2003) found that the stresses in the lining would not be affected if the drainage conditions change from full drainage to no-drainage or vice versa. However, the stresses and displacements of the soil mass are quite different from the drainage to the no-drainage condition. Shin et al. (2005) investigated the pore-water pressure role and its effect on the tunnel support using a finite element method. The pore-water pressure effect on the tunnel lining depends on the lining permeability and the deterioration of the drainage system. Bian et al. (2009) proposed a coupling method based on the three-dimension elasto-plastic finite element method to study the coupled seepage and stress fields in the concrete lining with high water pressure. Other numerical studies have also been done to evaluate the impact of surface loading on the lining efforts by Katebi et al. (2013, 2015). They show that the mechanical and geometrical parameters of the buildings, tunnels and surrounding ground have a considerable effect on the lining loads, which should not be neglected in tunnel design. The effect of surface loading on the hydro-mechanical (H-M) response of a tunnel in saturated ground was examined by Prassetyo and Gutierrez (2016). They found that a

linear permeability and the long-term H-M soil response have a large effect on the tunnel stability in saturated ground.

Although the analytical solutions are very useful, they are complex to develop when dealing with the complex non-circular tunnels shapes. Meanwhile numerical simulations can override this difficulty but need heavier calculation time. It is therefore imperative to find an accurate and efficient way to evaluate the impact of surface loadings on the tunnel linings in saturated soil conditions. The HRM method is presented in this chapter to calculate the internal forces and displacements of the horseshoe shaped tunnel linings considering the surface loading and pore-water pressure.

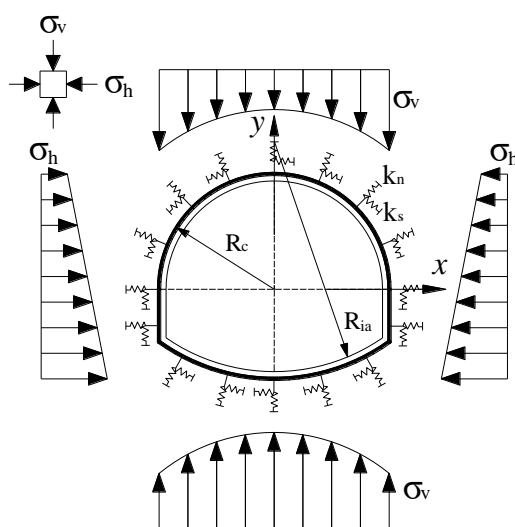


Fig. 5-1 Schematic diagram for a horseshoe shaped tunnel lining: σ_v and σ_h are respectively the vertical and horizontal loads; k_n and k_s are the normal and shear stiffness of springs, respectively; R_{ia} is the radius of the inverted arch; R_c is the crown radius

Tunnelling in saturated ground is subjected to the effect of groundwater, which depends on the lining permeability. When the tunnel lining is fully drained, the pore water pressure applied to the structures is equal to zero. Nevertheless, when the liner is impermeable, the structures should carry the full hydrostatic pore pressure as well as the stresses transferred from the soil mass (Bobet, 2003; Lee and Nam, 2001). Therefore, in order to study the pore water pressure effect, two extreme permeable cases are considered in this chapter: fully permeable (no pore water pressure) and impermeable (considering the full water load). Comparing with the results of a finite difference numerical model, the results of the present HRM method show good agreements with the numerical ones. This latter point permits to validate the HRM method. Then the effects of

pore water pressure, surcharge loading value, surcharge loading width and phreatic surface position on the internal forces and displacements of a horseshoe shaped tunnel lining are discussed. It is found that the normal forces and radial displacements are more sensitive to the water pressure, surcharge loading value and width, and the phreatic surface position than the bending moments. Fig. 5-1 shows the model used in the analysis of this chapter.

Active loads

The mathematical procedure of the HRM method can be referred to chapter 2. The active loads used in the HRM method are emphasized here, since the surface buildings and groundwater will be considered in this chapter. Therefore, the active loads should take into consideration the soil mass gravity loads, the pore pressure u_f and the additional loads due to the surcharge loading. It is assumed that the surface load is a uniform load and the analysis is done under plane-strain conditions. Considering the saturated unit weight γ_s of the soil mass, the pore pressure u_f and the surcharge loading P_0 , the active vertical load σ_v can be obtained by Terzaghi's formula (Takano, 2000):

$$\sigma_v = \gamma_s h + u_f + K_z \cdot P_0 \quad (5-1)$$

where h denotes the overburden height of one point on the tunnel lining; K_z refers to the coefficient of the vertical additional loads of surface pressure (Li et al., 2013), which is equal to:

$$K_z = \frac{1}{\pi} \cdot \left[\arctg\left(\frac{x}{z}\right) - \arctg\left(\frac{x-B}{z}\right) + \frac{x \cdot z}{x^2+z^2} - \frac{z \cdot (x-B)}{z^2+(x-B)^2} \right] \quad (5-2)$$

where x and z are the horizontal and vertical distance to point O (Fig. 5-3), respectively; B represents the width of the surcharge loading.

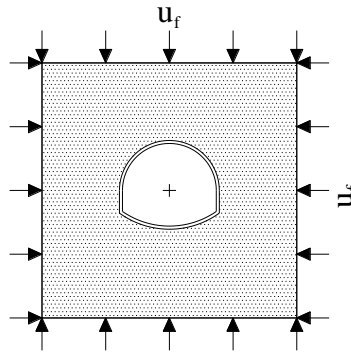


Fig. 5-2 Pore water pressure

The horizontal loads σ_h in the HRM model depend on the lateral earth pressure coefficient K_0 and the horizontal additional loads coefficient K_x of surcharge loading P_0 . σ_h can therefore be determined by the formula: $\sigma_h = K_0 \cdot \gamma_s h + u_f + K_x \cdot P_0$, where K_x is calculated as follows:

$$K_x = \frac{1}{\pi} \cdot \left[\arctg\left(\frac{x}{z}\right) - \arctg\left(\frac{x-B}{z}\right) - \frac{x \cdot z}{x^2+z^2} + \frac{z \cdot (x-B)}{z^2+(x-B)^2} \right] \quad (5-3)$$

In addition, the pore pressure u_f at the soil-structure interface in saturated ground should be calculated. When the tunnel lining is assumed to be impermeable, the lining supports have to support the full load caused by water. With respect to the pore water pressure u_f , a simple way is introduced to calculate (Bishop, 1954; Bishop and Morgenstern, 1960): $u_f = \gamma_w \cdot H_w$, where γ_w denotes the unit weight of water and H_w denotes the vertical distance from the tunnel crown to the phreatic surface (Fig. 5-3).

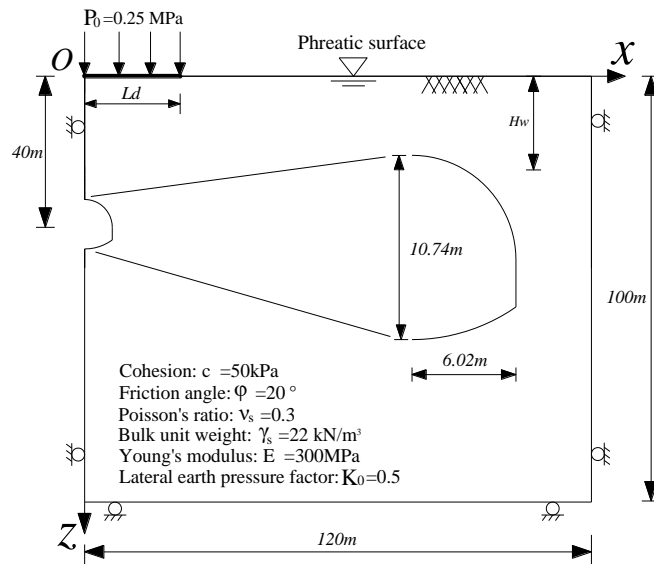


Fig. 5-3 Cross-section of the numerical adopted model with the adopted boundary conditions

2. Design model of tunnel and validation

To assess the accuracy of the present method, a comparison between a numerical simulation and the HRM is shown in this section.

2.1 Design model of tunnel

Numerical simulation is performed using the finite difference code FLAC (Itasca Consulting Group, 2012). Parameters from the Toulon tunnel in France are adopted. The ground profile and material properties of the Toulon tunnel are shown in Table 1 and Fig. 5-3.

Table 5-1 Tunnel parameters

Parameter	Symbol	Value	Unit
Crown radius	R_c	6.02	m
Invert arch radius	R_{ia}	20.22	m
Height of the invert centre	y_c	15.00	m
Height of the sidewall	L_p	3.80	m
Support thickness	t	0.22	m
Poisson's ratio	ν	0.15	-
Elastic modulus of concrete	E_0	35,000	MPa
Overburden	H	40	m

As it is assumed to be a symmetrical problem, only half of the model is set up. Fig. 5-3 shows the 2D numerical model under plane-strain conditions. The numerical model dimensions of the horseshoe shaped tunnel are 10.74 m by 12.04 m. A surcharge loading P_0 of 0.25MPa with a width L_d of 10m is applied on the ground surface above the tunnel. The size of the numerical model is taken to be 120 m in the X direction, 100 m in the Z direction. This size permits to avoid boundary effects. The soil is considered as fully saturated. For the boundary conditions, the horizontal (X) displacements of the nodes in the $x=0$ plane and $x=120$ plane are fixed, while the vertical (Z) displacements of the nodes at the base of the model are fixed. An impermeable tunnel lining modelled by a finite number of structural elements (liners in FLAC) is considered in the numerical model. Along the tunnel boundary the liner elements are attached to the soil zones.

The procedure of simulation in FLAC^{3D} is done as the following steps:

1. Setup of the numerical model, such as generating grid model, setting up boundary conditions, defining material properties, setting up initial conditions and balancing the initial state of stresses,
2. Simulation of the tunnel excavation, liner installation, then numerical calculations to reach the new equilibrium state.

2.2 Validation of the HRM method

Fig. 5-4 shows the mesh and the vertical displacements which occur above the tunnel after excavation. The numerical model is made up of 3535 zones for a total of 7288 nodes. The dimension of each element increases with the distance from the tunnel centre. The tunnel lining and ground properties used in this numerical analysis are presented in Table 5-1 and Fig. 5-3. Fig. 5-5 illustrates the lining geometry considered in this study.

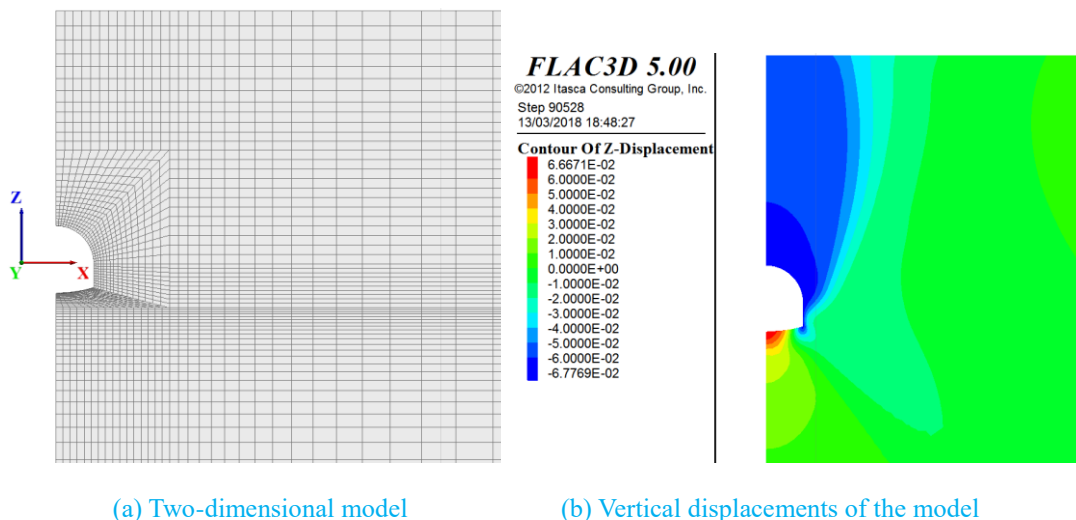


Fig. 5-4 Numerical model in FLAC^{3D}

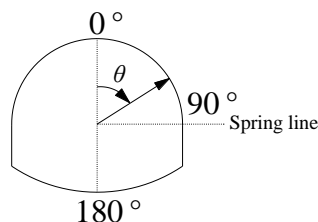
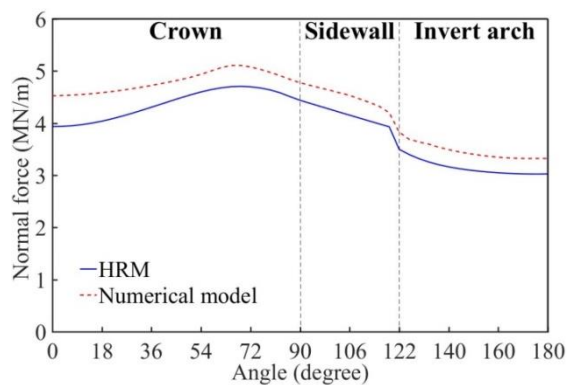


Fig. 5-5 Location θ (degrees)

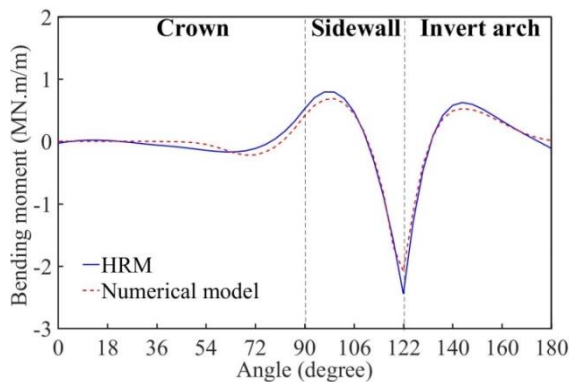
Fig. 5-6 illustrates the internal forces and displacements of the tunnel lining. The results were obtained from the numerical and the HRM models. From Fig. 5-6, it can be found that the normal forces of the HRM show a good agreement with the ones of the numerical model. The maximum absolute discrepancy (13.0%) for normal force occurs at the centre of the tunnel crown. Fig. 5-6b shows also a good agreement of the bending moments between the results of HRM and the numerical ones. The maximum absolute discrepancy (7.2%) in terms of bending moments is located at the connection of sidewall and inverted arch. In addition, noticeable differences for the radial displacements are obtained at the tunnel crown. This could be caused by

the arching tunnel lining effect developed in the numerical model, which is not considered in the HRM one. The values of radial displacements of the HRM are slightly higher than the numerical ones at the tunnel sidewall and invert arch. The maximum discrepancy (31%) happens at the centre of the tunnel crown.

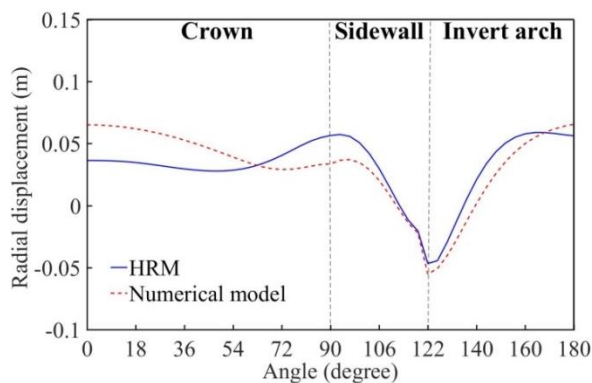
According to the above mentioned analysis, the lining displacements and internal forces results obtained from the HRM are in a good agreement with the numerical ones. Therefore, the HRM can be effectively used to evaluate the impact of surface loadings on the lining behaviour of horseshoe shaped tunnels in saturated soil conditions, in terms of lining displacements and structural forces. In the following section, the effect of the water pressure, the surcharge loading value and width, and the phreatic surface position, will be presented by means of the HRM method.



(a) Normal forces



(b) Bending moments

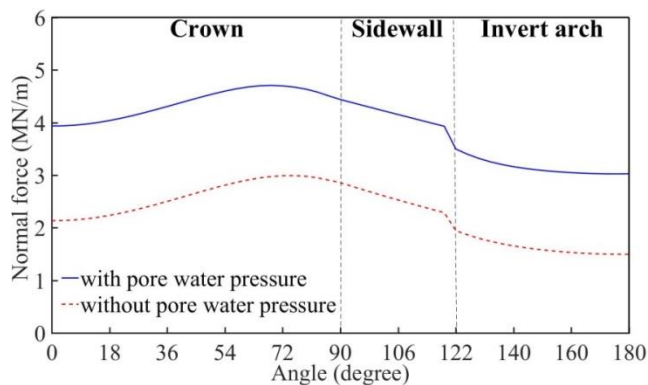


(c) Radial displacements

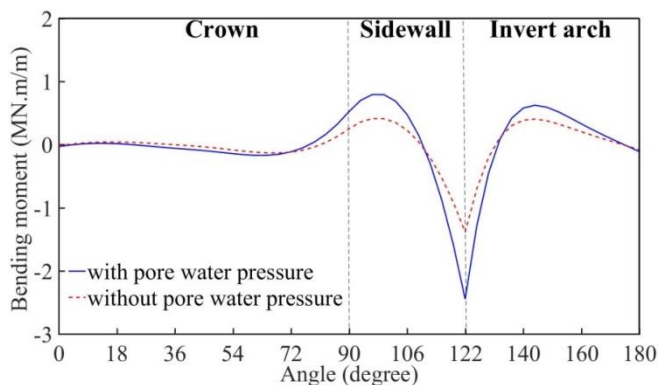
Fig. 5-6 Comparison of structural forces and displacements between the HRM and numerical model

3. Results analysis of the parametric studies

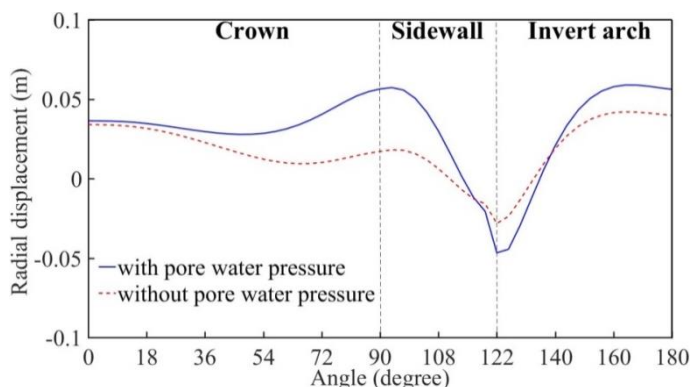
Firstly, the internal forces and displacements of a horseshoe shaped tunnel support considering the pore water pressure are presented in Fig. 5-7. When considering the pore water pressure, the absolute values of the HRM results (internal forces and displacements) are always higher than the ones without considering the pore water pressure. The peak value of normal forces when considering the pore water pressure occurs near the connection of the tunnel crown and sidewall, i.e. $\theta = 70^\circ$. This maximum normal force is approximately 57% larger than the one without considering the pore water pressure. The impact of pore water pressure on the bending moment at the tunnel crown and invert arch is not significant. However, significant differences in bending moments are found in the tunnel sidewall, as shown in Fig. 5-7b. A maximum bending moment of $2.45 \text{ MN}\cdot\text{m/m}$ occurs at the corner of the lining ($\theta = 32^\circ$) when considering the pore water pressure. This maximum bending moment is about 76% larger than the one without considering the pore water pressure. In contrast, the influence of pore water on the radial displacements along the whole tunnel except the centre of tunnel crown is significant. It is shown in Fig. 5-7c. The maximum radial displacement of 0.057 m occurs near the spring line.



(a) Normal forces



(b) Bending moments

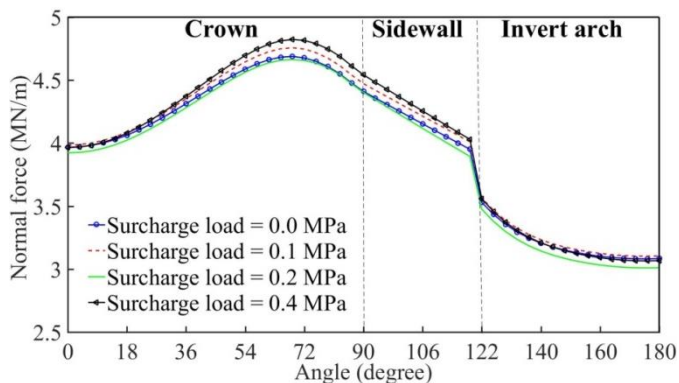


(c) Radial displacements

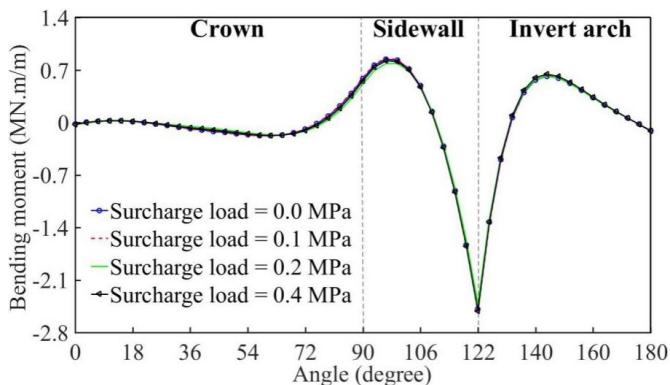
Fig. 5-7 Behaviour of tunnel lining considering and without considering the pore water pressure

Secondly, the impact of the surcharge loading on the internal forces and displacements of horseshoe shaped tunnel support under the water table is indicated in Fig. 5-8. It can be found from Fig. 5-8 that the surcharge loading has a significant impact on the normal forces and radial displacements at the tunnel crown and sidewall. However, the effect of the surcharge loading on the bending moments could be neglected. No matter what the value of the surcharge loading is, the maximum normal force always occurs near the

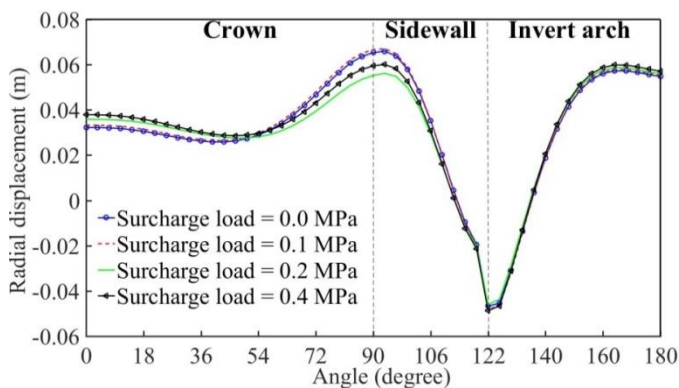
connection of the tunnel crown and the sidewall. In contrast, the maximum radial displacement is found at the tunnel spring line.



(a) Normal forces



(b) Bending moments



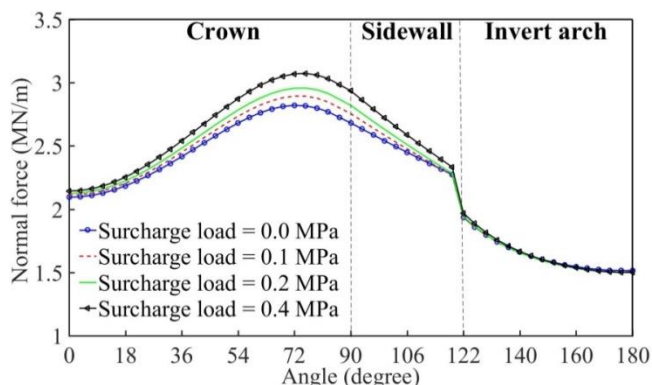
(c) Radial displacements

Fig. 5-8 Behaviour of tunnel lining when considering both the surcharge loading P_0 and the pore pressure

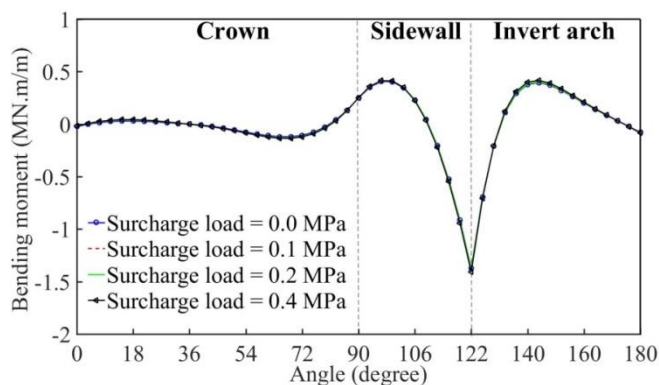
Thirdly, the effect of the surcharge loading on the internal forces and displacements without considering the pore water pressure is also investigated in Fig. 5-9. It can be clearly found that the surcharge loading has a great influence on the normal forces (tunnel crown and sidewall). Although the differences in bending

moments do not appear to be large, significant changes in normal forces and radial displacements are induced in the tunnel crown and sidewall. An increase of the surcharge loading results in a significant increase of the normal forces at the tunnel crown and sidewall. The effect of the surcharge loading on the normal forces of the tunnel invert arch could be neglected. However, the increase of the surcharge loading causes an increase of the radial displacements of the tunnel crown and invert arch. A decrease of the radial displacements at the tunnel sidewall is also observed. Compared with the results of Fig. 5-8c, the maximum radial displacement happens at the tunnel invert arch rather than at the tunnel sidewall when neglecting the pore water pressure.

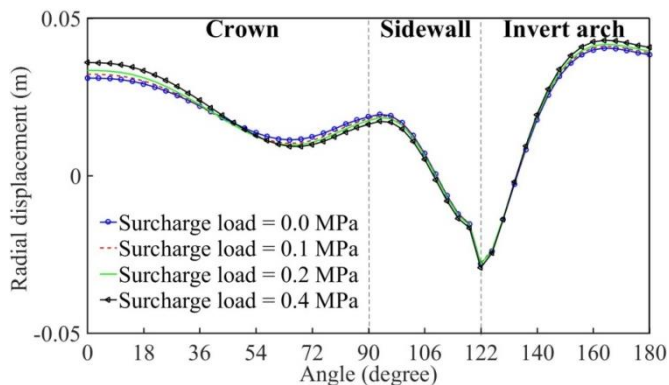
Comparing Fig. 5-8 to Fig. 5-9, the effect of the surcharge loading on the normal forces and displacements is significantly different. When considering the pore water pressure, the absolute values of internal forces and displacements are always higher than the ones without considering the pore water pressure. This conclusion is consistent with the numerical analysis of [Shin et al. \(2005\)](#) who found that the magnitudes of lining internal forces increased as the permeability of the drainage layer reduces.



(a) Normal forces



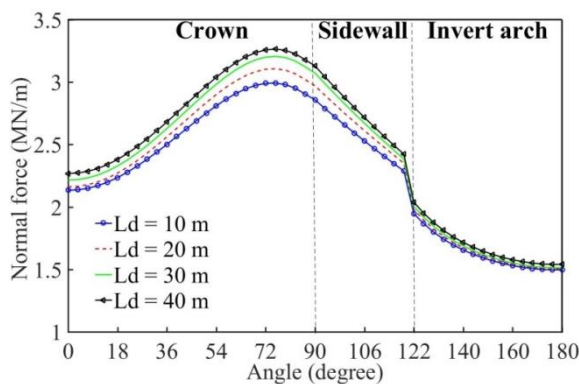
(b) Bending moments



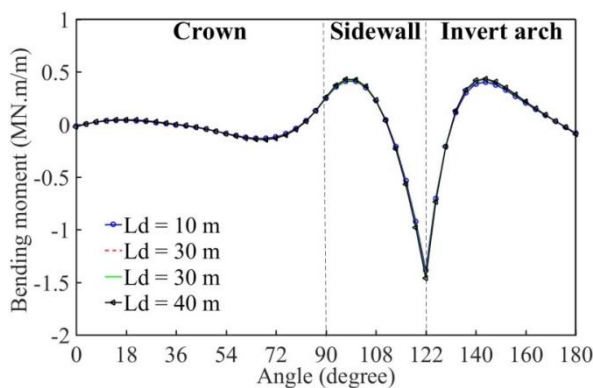
(c) Radial displacements

Fig. 5-9 Behaviour of tunnel lining when considering only the surcharge loading

Then, the influence of the applied width L_d of the surcharge load on the tunnel behaviour is studied, and shown in Fig. 5-10. While the surcharge loading P_0 is fixed to 0.25MPa, the widths L_d of surcharge loading of half model are considered to be in the range from 10 to 40m. Fig. 5-10 gives that the width of surcharge loading has a considerable effect on the normal forces of lining. As the surcharge loading width becomes wider, the normal forces increase. The bending moment is less sensitive to the changes of surcharge loading width compared to the radial displacements.



(a) Normal forces



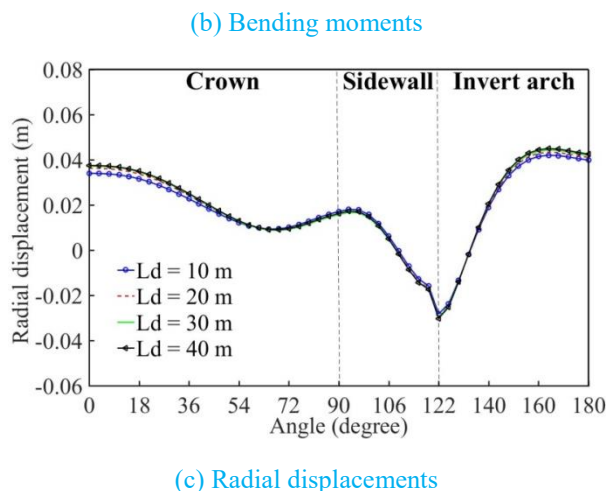
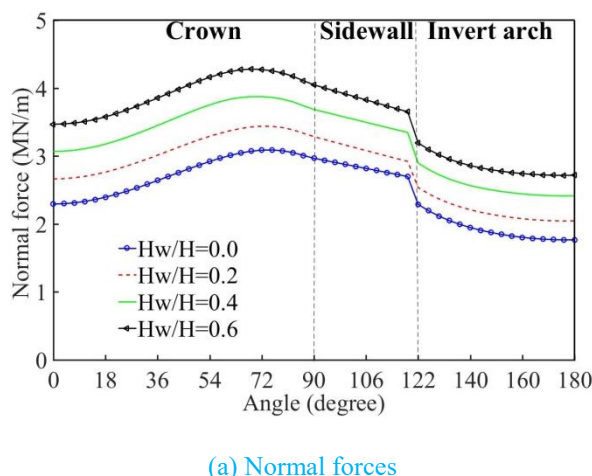


Fig. 5-10 Effect of the surcharge load width on the tunnel behaviour without considering the pore water pressure

Lastly, the effect of the phreatic surface position on the internal forces and displacements of the horseshoe shaped tunnel below the phreatic surface are presented. The calculations are conducted with H_w/H changing from 0.0 to 0.6. The internal forces and displacements of the horseshoe shaped tunnel lining are presented in Fig. 5-11 for the case of $P_\sigma=0.25$ MPa. As expected, the H_w/H ratio greatly influences the internal forces and lining displacements. It can be seen from Fig. 5-11 that the normal forces increase with the increase of the H_w/H ratio along the whole tunnel. However, although the effect of H_w/H ratio on the bending moments at the tunnel sidewall is obvious, its effect on the bending moments at the tunnel crown and invert is not significant. The absolute values of the bending moment increase with the increase of the H_w/H ratio at the tunnel sidewall. A significant influence of the H_w/H ratio on the radial displacements can also be seen near the connection of the tunnel crown and sidewall. The radial displacement increases as the H_w/H ratio increases.



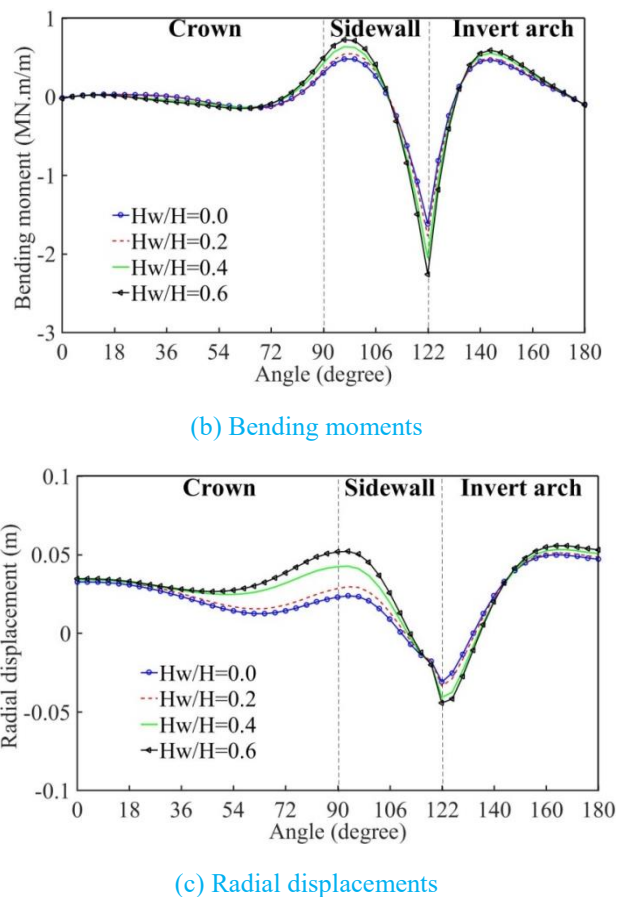


Fig. 5-11 Effect of phreatic surface position on tunnel behaviour

4. Conclusions

The effect of surface loading on a horseshoe shaped tunnel in a saturated soil mass is studied in this chapter using the HRM method. Comparisons between the results of the HRM and numerical ones are made and have permitted to validate the HRM method. Although it remains some discrepancies between the results of these two methods, the differences are admissible for an engineering point of view.

Parametric studies permit to investigate the influence of the surface loadings and the pore water pressure on the tunnel behaviour. Some conclusions can be drawn:

- The absolute values of the internal forces or displacements when considering the pore water pressure are always higher than the ones without considering the pore water pressure,
- No matter considering the pore water pressure or neglecting the pore water pressure, the surcharge loading has a significantly impact on the normal forces and radial displacements. However, the effect of

the surcharge loading on the bending moments is negligible,

- The width of surcharge loading has a considerable effect on the lining normal forces. As the surcharge loading width becomes wider, the value of normal forces increases. Nevertheless, the bending moments and radial displacements are not sensitive to the changes of the surcharge loading width,
- The phreatic surface position greatly influences the internal forces and displacements. The normal forces along the whole tunnel decrease with the increase of the phreatic surface position. The impact of the phreatic surface position on the bending moments is only visible at the tunnel sidewall. The normal forces and radial displacements of the lining are more sensitive to the water pressure, surcharge loading, surcharge loading width and phreatic surface position than the bending moments.

In the following chapter, an optimization analysis for the shape of a sub-rectangular tunnel by means of the HRM method will be presented.

CHAPTER 6 OPTIMIZATION OF SUB-RECTANGULAR TUNNEL USING HYPERSTATIC REACTION METHOD

1. Introduction

Nowadays, the increasing large-diameter and variety of cross-section geometry of tunnels are being employed to construct underground space projects. Sub-rectangular tunnels are especially suitable for underground engineering projects with a sub-rectangular cross-section, like subway entrance passages, underground pedestrian crossings. It is becoming a common cross-section in practice with the support of technology. Sub-rectangular tunnels have a lower probability of rolling (Li, 2017) and a higher utilization of the section ratio than the circular ones. However, in spite of this till now, there is no efficient way to design sub-rectangular tunnels. Very limited studies have dealt with sub-rectangular tunnels. Nakamura et al. (2003) performed full-scale loading tests on lining segments to confirm the adequacy of the rectangular shape tunnel design. Huang et al. (2018) assessed the mechanical behaviour of sub-rectangular segmental lining subject to self-weight in a full-scale loading test. Liu et al. (2018) conducted a full-scale ring test to investigate the mechanical behaviour of sub-rectangular segmental tunnel linings. All the studies mentioned above do not mention how the sub-rectangular tunnels are designed. Therefore, finding an effective way to optimize the sub-rectangular tunnel shapes in terms of internal forces is becoming important to facilitate the development of this kind of tunnels.

Since HRM method can provide results that are as valuable as the ones of FEM (Finite Element Model) or FDM (Finite Difference Model), but with less computational cost. Therefore, this chapter presents an optimization analysis for the shape of a sub-rectangular tunnel by means of the HRM method.

In this chapter, taking a twin-lane metro tunnel as an example, which is very common in relatively developed cities, the optimization process of sub-rectangular cross-sections in terms of tunnel lining forces is introduced using the HRM method. The static area (the simplified tunnel construction clearance) of a twin-lane metro tunnel is firstly determined. The intrados of sub-rectangular tunnel lining should at least cover this static area. Considering this requirement, a series of mathematical functions is proposed to optimize the sub-rectangular tunnel shape in terms of internal forces induced in the tunnel lining. Finally, the effect of different

parameters, e.g. the coefficient of lateral earth pressure at rest K_0 , Young's modulus of soil E_s , tunnel depth C , surface loads P_0 on the internal forces and the shape of sub-rectangular tunnel is investigated.

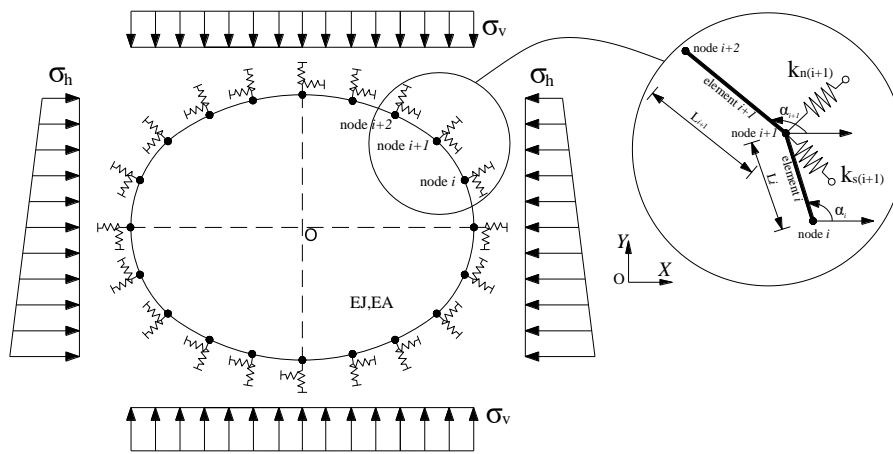


Fig. 6-1 An illustrate of sub-rectangular support structures in the HRM method. With: σ_v : the vertical loads; σ_h : the horizontal loads; k_n : normal stiffness of springs; k_s : shear stiffness of springs; EJ and EA : bending and normal stiffness of the support; X and Y are the global Cartesian coordinates. Note: every node has three degrees of freedom

2. Optimization of sub-rectangular tunnel shape

2.1 Determining the static area of a sub-rectangular tunnel and establishing optimizing procedure

The original static area of twin lanes metro tunnels is firstly determined according to the Vietnamese specifications (TCVN). A series of tunnel shapes with different dimensions has been investigated. Then the optimization of the tunnel shape is achieved by minimizing the lining forces (the maximum bending moment M_{max}). Finally, the effect of different parameters, like coefficient of lateral earth pressure at rest K_0 , Young's modulus E_s of soil, tunnel depth C , and surface load P_0 on the rectangular tunnel shape is investigated.

The construction clearance of twin lanes metro tunnels used for electrical trains based on the Vietnamese specification (TCVN) is shown in Fig. 6-2. For the convenience of this study, the tunnel construction clearance (the red line in Fig. 6-2) is simplified to the shape (blue line) shown in Fig. 6-3a.

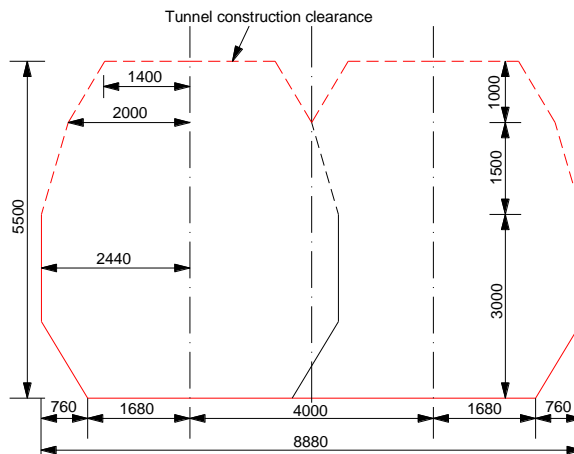


Fig. 6-2 Tunnel construction clearance (mm) of twin lanes metro tunnels

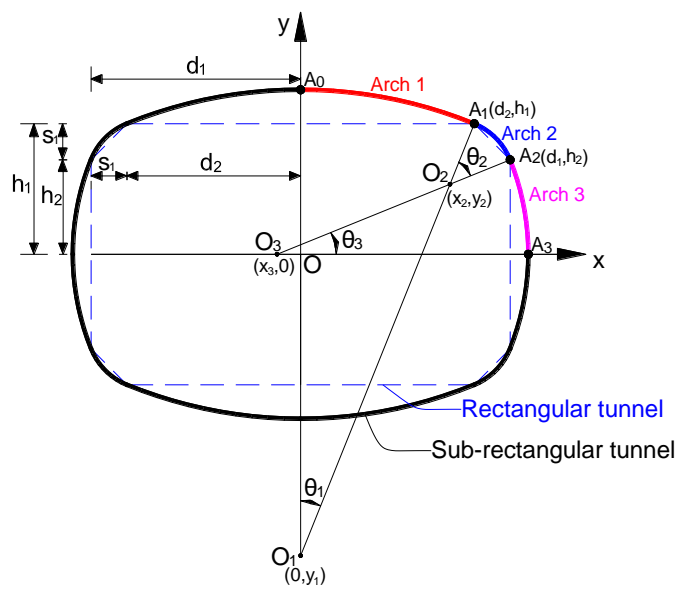
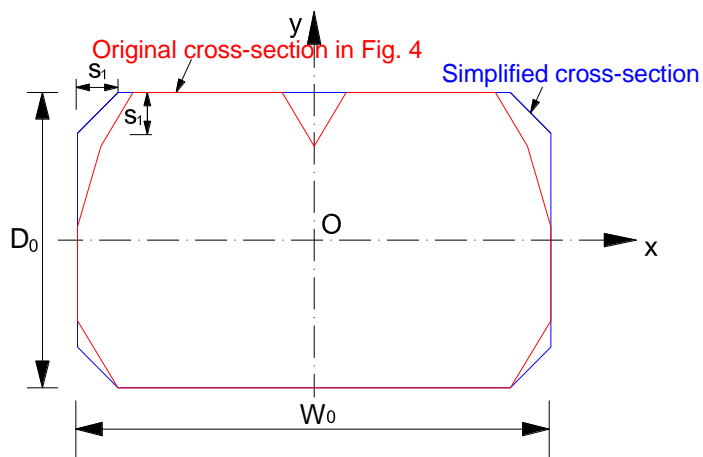


Fig. 6-3 Simplified considered tunnels: (a) Static area (blue line) of twin lane metro tunnels (b) Schematic diagram of sub-rectangular shape. $W_0 = 8.88\text{m}$; $D_0 = 5.50\text{m}$; $s_l = 0.76\text{m}$; $d_1 = 4.44\text{m}$; $d_2 = 3.68\text{m}$; $h_1 = 2.75\text{m}$; $h_2 = 1.99\text{m}$. Noted that the red line in Fig. 6-3a represents the original cross-section in Fig.6-2 and the blue line in Fig. 6-3b means the simplified cross-section

Since the tunnel shape is symmetric, a quarter of rectangular shape is considered to present the optimization formulas (Fig. 6-3b). Once the tunnel lining of the quarter rectangular shape is determined, the whole tunnel lining can be defined, as shown in Fig. 6-4.

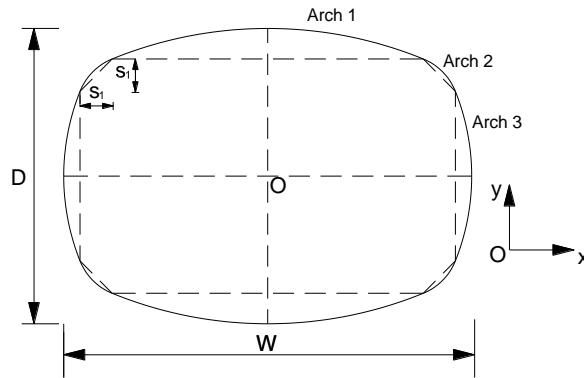


Fig. 6-4 Entire tunnel lining obtained by optimization

The geometry of the sub-rectangular tunnel is defined using the height D , and width W . The centre $O_1(0, y_1)$ of Arch1 is located on the vertical axis y ; the centre $O_3(x_3, 0)$ of Arch3 is located on the horizontal axis x ; the centre $O_2(x_2, y_2)$ of Arch2 is the intersection point of line O_1A_1 and line O_3A_2 . As $d_1 - d_2 = h_1 - h_2 = s_1$, based on the geometric relationship, one can find that O_2 is located on the line $y = -\frac{d_1-d_2}{h_2-h_1}x + \frac{1}{2} \cdot [(h_1 + h_2) - (d_1 + d_2)]$.

Note that in the optimization process, firstly, the lining boundary should cover the tunnel construction clearance of the twin lanes metro tunnel. Secondly, the lining boundary should be as small as possible to ensure the smaller excavated area. Lastly, the internal forces induced in the tunnel lining should be as small as possible. Therefore, the optimization constraints are the following ones:

- 1) O_2 is the intersection of line O_3A_2 and line O_1A_1 (Fig. 6-3);
- 2) Centre O_2 is on the line $y = -\frac{d_1-d_2}{h_2-h_1}x + \frac{1}{2}[(h_1 + h_2) - (d_1 + d_2)]$;
- 3) The lining is convex outwards.

Then it can be easily obtained that x_3 and y_1 should meet the following conditions:

$$x_3 < d_1 - h_2 * \frac{(h_1 - h_2)}{(d_1 - d_2)} \quad (6-1)$$

$$y_1 < h_1 - d_2 * \frac{(d_1 - d_2)}{(h_1 - h_2)} \quad (6-2)$$

Assumed x_3 is known, according to the geometric relationship shown in Fig. 6-3, one can obtain that x_2 and y_2 are the functions of x_3 :

$$x_2 = \left(\frac{h_2 \cdot x_3}{d_1 - x_3} + \frac{h_1 + h_2 - d_1 - d_2}{2} \right) / \left(\frac{h_2}{d_1 - x_3} + \frac{d_1 - d_2}{h_2 - h_1} \right) \quad (6-3)$$

$$y_2 = \frac{h_2}{d_1 - x_3} \cdot x_2 - \frac{h_2 \cdot x_3}{d_1 - x_3} \quad (6-4)$$

$O_1(0, y_1)$ is on the line O_2A_1 which is:

$$y = \frac{h_1 - y_2}{d_2 - x_2} \cdot x + h_1 - \frac{h_1 - y_2}{d_2 - x_2} \cdot d_2 \quad (6-5)$$

Since O_1 is also the intersection of line O_2A_1 and vertical axis y , then one obtains y_1 :

$$y_1 = h_1 - \frac{h_1 - y_2}{d_2 - x_2} \cdot d_2 \quad (6-6)$$

Therefore, all the unknown parameters, x_2 , y_2 and y_1 , are the functions of x_3 . Once x_3 is known, O_1 and O_2 can also be determined uniquely.

Given that R_1 is the radius of Circle O_1 ; R_2 is the radius of Circle O_2 ; R_3 is the radius of Circle O_3 ; θ_1 is the angle of OO_1O_2 ; θ_2 is the angle of $A_1O_2A_2$; θ_3 is the angle of OO_3O_2 (Fig. 6-3). Then the following formulas can be obtained:

$$R_1 = \sqrt{(h_1 - y_1)^2 + d_2^2} \quad (6-7)$$

$$R_2 = \sqrt{(y_2 - h_1)^2 + (x_2 - d_2)^2} \quad (6-8)$$

$$R_3 = \sqrt{(d_1 - x_3)^2 + h_2^2} \quad (6-9)$$

$$\theta_1 = \arctan \frac{d_2}{h_1 - y_1} \quad (6-10)$$

$$\theta_2 = 2 \cdot \arcsin \frac{\sqrt{(d_1 - d_2)^2 + (h_2 - h_1)^2}}{2 \cdot R_2} \quad (6-11)$$

$$\theta_3 = \arctan \frac{h_2}{d_1 - x_3} \quad (6-12)$$

It can be found from Eqs. 6-7 to 6-12 that θ and R are functions of the unknown parameters y_1 and x_3 .

The area A_{rect} of rectangular tunnel shown in Fig. 6-3a is:

$$A_{rect} = D * W - 4 * s_1^2 / 2 \quad (6-13)$$

The area A_{sr} of the sub-rectangular one shown in Fig. 6-3b is:

$$A_{sr} = 4 * (h_1 * d_1 - s_1^2 / 2 + A_{s1} + A_{s2} + A_{s3}) \quad (6-14)$$

in which

$$A_{s1} = \theta_1 * R_1 * R_1 / 2 - d_2 * (h_1 - y_1) / 2 \quad (6-15)$$

$$A_{s2} = \theta_2 * R_2 * R_2 / 2 - R_2 * R_2 * \sin(\theta_2 / 2) * \cos(\theta_2 / 2) \quad (6-16)$$

$$A_{s3} = \theta_3 * R_3 * R_3 / 2 - h_2 * (d_1 - x_3) / 2 \quad (6-17)$$

Fig. 6-5 presents the optimization procedure based on the HRM method. A_{per} is the change of area between the sub-rectangular and rectangular tunnel, which is equal to:

$$A_{per} = (A_{sr} - A_{rect}) / A_{rect} \quad (6-18)$$

The basic idea of the present optimization is based on searching the optimum sub-rectangular tunnel shape in terms of the smaller bending moment by changing the radius of Arch3 under the specific soil parameters.

Each optimization step is determined by using an iteration step of 0.01 for x_3 and the constraint $A_{per} \leq 5\%$ (see section 3.3). A parametric study was done in these two parameters and will be presented in the following part. For one given value of x_3 , there is only one corresponding shape of the sub-rectangular tunnel. Then on the basis of the HRM method, a set of maximum internal forces (M_{max} and N_{max}) for this corresponding shape can be obtained. An iteration step of 0.01 for x_3 is adopted (Fig. 6-5). Repeating the optimization procedure shown in Fig. 6-5 until the condition $A_{per} \leq 5\%$, it permits to obtain all the maximum internal forces. Since the tunnel lining should work in compression and tensile stresses should be avoided as far as possible, the optimal shape of the sub-rectangular tunnel is determined by the minimum M_{max} .

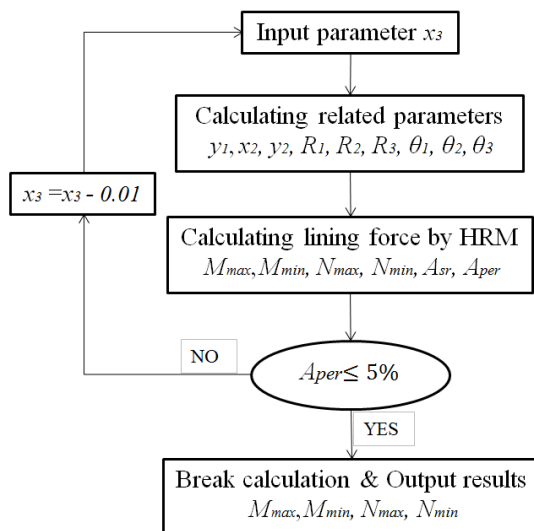


Fig. 6-5 Optimization procedure of sub-rectangular tunnels. M_{max} : maximum bending moment; M_{min} : minimum bending moment; N_{max} : maximum normal force; N_{min} : minimum normal force

2.2 Reference case

2.2.1 Presentation of the reference case

Two-line metro tunnels are very common in urban environments. Fig. 6-6 gives the schematic diagram of the sub-rectangular tunnel and the soil parameters used for the optimization analysis. The parameters are taken from the metro line 4 in Shanghai (Zhu et al., 2018). The Young’s modulus E_s of the soil is taken equal to 3.6 MPa; the Poisson’s ratio ν_s of the soil to 0.495; the coefficient of lateral earth pressure at rest K_0 to 0.6; the weight γ of soil to 18 kN/m³; tunnel depth $C=10$ m; a uniform surface load $P_0=20$ kPa. The friction angle ϕ and cohesion c of soil are respectively equal to 16.5 degrees and 25.6 kPa. This analysis is named “reference case” in the following study.

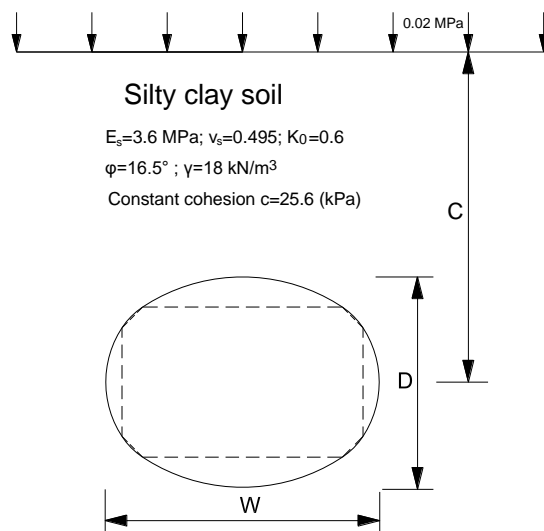


Fig. 6-6 Schematic diagram of sub-rectangular and soil parameters in the optimization. Height of sub-rectangular tunnel

$$D = 2 * (R_1 - \sqrt{y_1^2}); \text{ width of sub-rectangular tunnel } W = 2 * (R_3 + x_3)$$

2.2.2 Associated numerical model

In order to validate the presented HRM method, a comparison between the HRM method and 2D numerical simulations using FLAC^{3D} using parameters of above reference case is conducted under plane-strain condition. The soil is assumed to follow a linear elastic-perfectly plastic constitutive relation based on the Mohr-Coulomb shear failure criterion. The properties of tunnel and soil used in the optimization are adopted in the numerical modelling. Note that the dimensions of tunnels are determined by the values of the optimum radius of the present method. Fig. 6-7 gives an example of numerical model as $C=5D_0$, in which the model is shown with 200m width in the x-direction, 67.5m height in the z-direction. The tunnel centre is located at a distance of 40m from the bottom of the model. The size chosen for the model is large enough to avoid the boundary effects. The nodes at sides of the models are fixed in the horizontal directions (i.e. $y=0$, $x=-100$ and $x=100$), and the nodes at the base of the model are fixed in the vertical direction. Note that the numerical model is three dimensional and 1 m thick “slice” is modelled. This model is composed of around 9,500 grid points. The dimension of the mesh elements increases as the distance from the tunnel increases.

The procedure of the excavation simulation is done using the following steps:

1. Setup of the numerical model, such as generating grid model, setting up boundary conditions, defining material properties, setting up initial conditions and equilibrium of the initial state of stresses,
2. Excavation of the tunnel, installation of the liner, then a new equilibrium state is reached.

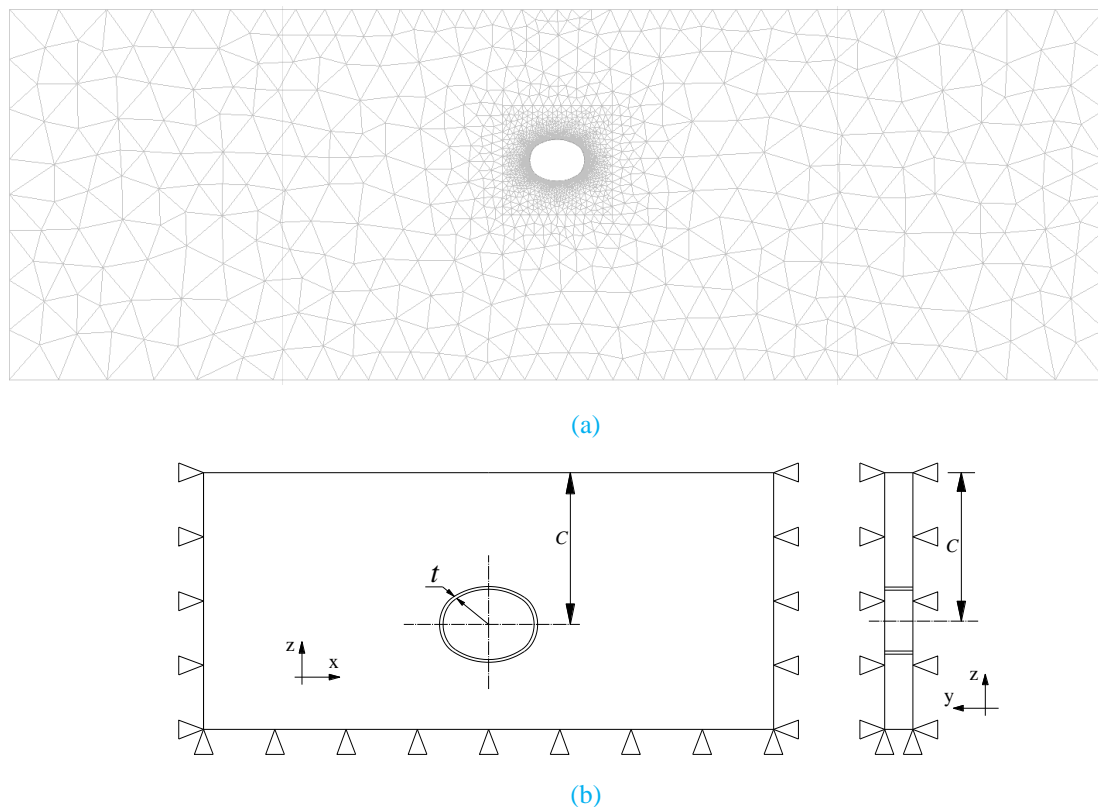


Fig. 6-7 Numerical model as $C=5D_0$: (a) Mesh diagram in FLAC model; (b) Plane strain model under consideration

2.2.3 Comparison results between the present HRM method and $FLAC^{3D}$ model

For a comparison analysis, the results obtained from the present HRM method and $FLAC^{3D}$ model are listed in Table 6-1. Fig. 6-8 presents the comparisons of internal forces at the tunnel right spring for different cases of tunnel depth.

From the Fig. 6-8 and Table 6-1, one can find that the outcomes of internal forces obtained by the present HRM method are always smaller than those obtained from $FLAC^{3D}$ model, except for the normal force at tunnel crown as $C/D_0=30$. It can also be found that the difference between the results of both methods is small, which is less than 9% while $C/D_0 \geq 2$. This agreement indicates that the present approach is valid in the evaluation of the effect of tunnel depth on internal forces of sub-rectangular tunnel.

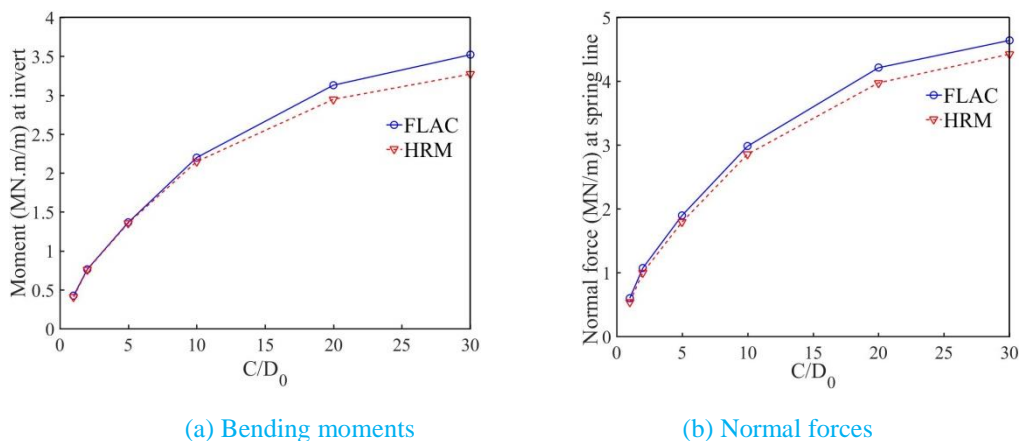


Fig. 6-8 Effect of tunnel depth C on the internal forces of sub-rectangular tunnel obtained by FLAC^{3D} and HRM

Table 6-1 Comparison of internal forces of HRM and FLAC considering different tunnel depth C in terms of normal forces (T) and bending moment (M)

C/D_0	T (MN/m) at crown			T (MN/m) at spring line			M (MN.m/m) at invert			M (MN.m/m) at spring line		
	HRM	FLAC	Errors	HRM	FLAC	Errors	HRM	FLAC	Errors	HRM	FLAC	Errors
1	0.244	0.291	16.15%	0.536	0.597	10.22%	0.407	0.424	4.01%	-0.397	-0.479	17.12%
2	0.484	0.525	7.81%	1.000	1.072	6.72%	0.756	0.762	0.79%	-0.753	-0.823	8.51%
5	0.893	0.933	4.29%	1.794	1.902	5.68%	1.357	1.388	2.23%	-1.356	-1.435	5.51%
10	1.440	1.463	1.57%	2.855	2.981	4.23%	2.146	2.198	2.37%	-2.165	-2.254	3.95%
20	2.022	1.989	-1.66%	3.973	4.214	5.72%	2.947	3.128	5.78%	-3.031	-3.248	6.68%
30	2.256	2.142	-5.32%	4.422	4.638	4.66%	3.270	3.519	7.07%	-3.378	-3.701	8.73%

3. Parametric analyses

This section presents the tunnel shape optimization results under different geometry configurations and geotechnical parameters. The effect of the coefficient of lateral earth pressure at rest K_0 , Young’s modulus E_s of soil, tunnel depth C and, surface load P_0 on the sub-rectangular tunnel shape is discussed.

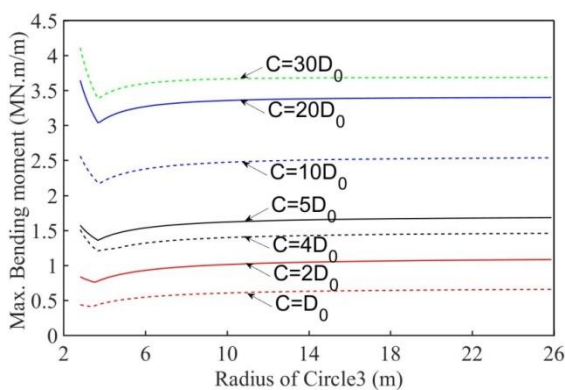
As mentioned above, it should be noted that the optimal shape of the sub-rectangular tunnel is determined by the minimum M_{max} . A parametric study on the iteration step and A_{per} is also done to investigate the role of these parameters.

If the iteration step is set equal to 0.001, the calculating time is 10 times longer than that as it was with 0.01. In fact, when the iteration step is set equal to 0.01 and $A_{per} \leq 5\%$, the calculation time for the optimization is about 8340s (on an Intel Xeon CPU E5-2609 v4 1.7GHz with 2 processors PC, the same below). The obtained optimum result for M_{max} is equal to 0.69308 MN.m/m (reference case). However, if the iteration parameter is set equal to 0.001, the optimum result is equal to 0.69285 MN.m/m. The difference between these two optimum values is very low (0.0332%) and it is why we consider iteration step 0.01 in the

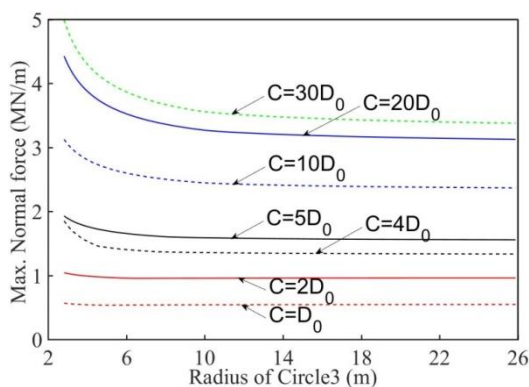
following parts. Similarly, the smaller the value of A_{per} , the longer the calculation time. It is also found that the optimum solution always occurs for $A_{per} \leq 5\%$. For example, a value of 5% and 2% was used for A_{per} . For $A_{per} \leq 2\%$, it is found that the calculating time is equal to 52980s and however, the optimum results are the same as $A_{per} \leq 5\%$ with a calculation time of about 8340s. Therefore, an iteration step for x_3 of 0.01 and $A_{per} \leq 5\%$, are taken in following optimization analyses.

3.1 Effect of the tunnel depth on the lining forces and on the sub-rectangular tunnel shapes

The influence of tunnel depth is considered by a parametric study on the parameter C while the other parameters are kept constant. Values of C changed from 1 to $30D_0$ ($D_0 =$ height of static area of tunnel) are considered. The impact of C on the lining forces and on the sub-rectangular tunnel shape is shown in Fig. 6-9 and Fig. 6-10.



(a) Bending moments



(b) Normal forces

Fig. 6-9 Effect of tunnel depth C on the Maximum internal forces obtained by HRM

It can be seen from Fig. 6-9 that the maximum bending moment of sub-rectangular tunnels decreases firstly, such as till a value of R_3 equal to 3.74m corresponding to $C/D_0=10$, and then increases slowly with the increase of R_3 . Generally, the maximum bending moment increases as C/D_0 increases. Unlike the maximum bending moment, the maximum normal force increases with the increase of C/D_0 as well, but it decreases as R_3 increases. This is because the increase of C/D_0 results in the increase of active loads (see Eq. 2-28 in chapter 2), which leads to an increase of the tunnel lining forces. When R_3 increases, the tunnel width (W) will also decrease. As a consequence, the total vertical earth loading applied on the crown part of the tunnel will decrease and therefore a smaller maximum bending moment M_{max} and normal force N_{max} will occur as seen in Fig. 6-9. However, when R_3 increases, it also causes a decrease of the transmission effect of the lateral loads from the tunnel side to the tunnel crown. This transmission effect plays an important role in the increase of normal forces and the decrease of bending moments induced in the tunnel crown part. Consequently, when R_3 value exceeds a certain value (i.e. the optimum value of R_3), the lining shape then becomes less optimal, which induces higher bending moment and smaller normal force (see Fig. 6-9). For example, when R_3 tends to infinity, the lining is close to be a rectangle, which results in a larger maximum bending moment.

Fig. 6-10 presents the minimum M_{max} depending on the tunnel depth. They increase with the increase of C/D_0 . However, the relation between the minimum M_{max} and C/D_0 is not linear. R_3 increases rapidly till a value of $C/D_0 = 10$ and then decreases slowly as C/D_0 increases, which means that the tunnel depth effect on the sub-rectangular tunnel shape becomes insignificant when $C/D_0 > 10$. In other words, the optimum shape of sub-rectangular tunnels does not significantly change when $C/D_0 > 10$.

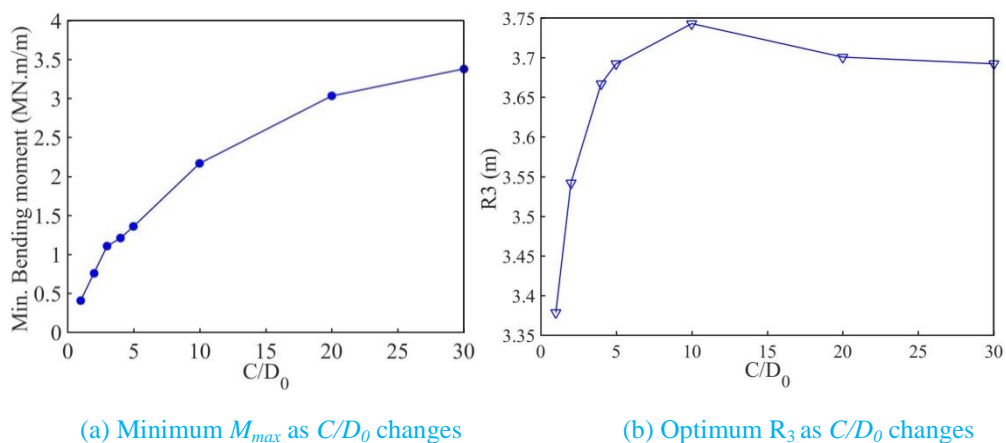


Fig. 6-10 Effect of the tunnel depth C on the minimum M_{max} value and on the sub-rectangular tunnel shape

To be concise, Fig. 6-11 only presents the distribution of bending moment and normal force when $C=D_0$ and $C=30D_0$, respectively. The optimum radius of circle3 (R_3) and corresponding values of normal forces induced at the tunnel crown and at the left tunnel spring line, the bending moments induced at the tunnel invert and at the left spring lines, determined in the following cases of $C/D_0 = 1, 2, 4, 5, 10, 20, 30$, are shown in Table 6-2.

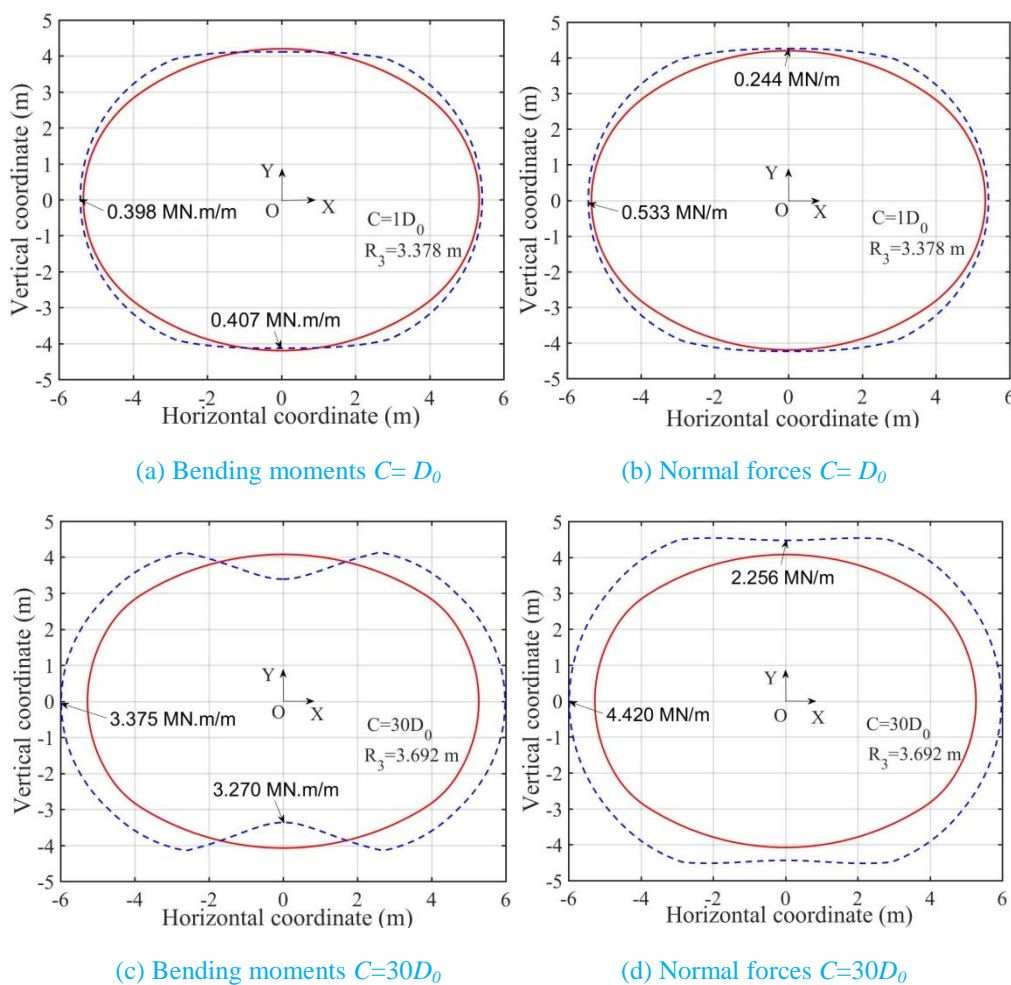


Fig. 6-11 Optimum sub-rectangular tunnel shapes and internal forces as $C=D_0$ and $C=30D_0$, respectively. The red solid line corresponds to the sub-rectangular lining shape

It is obvious that the normal forces at the tunnel crown and the left spring line increase with the increase of C/D_0 . Similarly, the bending moments at the tunnel invert and the left spring line increase as well as C/D_0 increases. This is because the earth loadings increase with the increase of C/D_0 (see Eq. 2-28), which causes an increase of the tunnel lining forces.

Table 6-2 Optimum internal forces considering different tunnel depth C obtained by present method

C/D_0	1	2	4	5	10	20	30
R_3 (m)	3.378	3.542	3.667	3.692	3.743	3.704	3.692
T (MN/m) at the crown	0.244	0.484	0.790	0.893	1.440	2.022	2.256
T (MN/m) at the spring line	0.533	0.997	1.590	1.791	2.852	3.971	4.420
M (MN.m/m) at the invert	0.407	0.756	1.206	1.357	2.146	2.947	3.270
M (MN.m/m) at the spring line	-0.398	-0.754	-1.204	-1.356	-2.164	-3.028	-3.375

In addition, Fig. 6-12 shows the comparison between the results of HRM and FLAC^{3D} in terms of bending moments and normal forces along the entire tunnel for the case of $C/D_0=5$. It can be found that the present method gives very similar values of bending moments at the tunnel crown, invert and spring line. However, there are some differences at the tunnel shoulders and knees. In contrast, both methods give very similar values for the normal forces along the whole tunnel. The present method is verified once again.

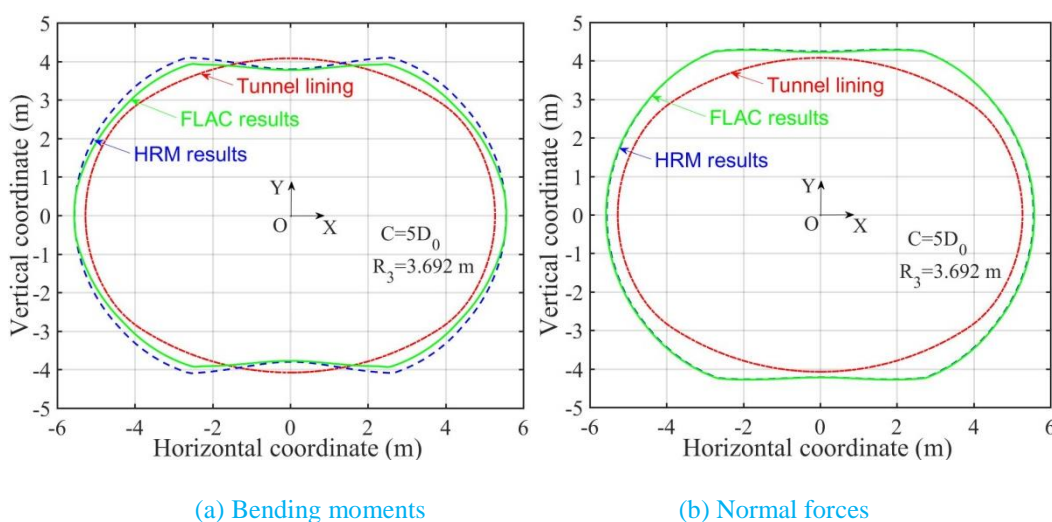


Fig. 6-12 Comparison between the results of HRM and FLAC^{3D} in terms of bending moments and normal forces along the whole tunnel for the case of $C/D_0=5$

3.2 Effect of coefficient of lateral earth pressure on internal forces and shape of sub-rectangular tunnel

The influence of coefficient of lateral earth pressure at rest K_0 ($K_0 = 0.1; 0.25; 0.5; 0.75; 1; 1.25; 1.5$) on the internal forces and shape of sub-rectangular tunnel is shown in Figs. 6-13 and 6-14, respectively. It should be noted that the values of K_0 are usually over 0.5 under normally consolidated conditions, therefore, these values ($K_0 = 0.1; 0.25; 0.5$) are only adopted here as theoretical studies. The following set of parameters from

the metro line 4 in Shanghai (Zhu et al. 2018) is considered: $E_s=3.6$ MPa, $C=10$ m, $P_0=0.02$ MPa, $\nu=0.495$, $\varphi=16.5^\circ$, $c=25.6$ kPa, $\gamma=18$ kN/m³, thickness of lining $t=0.5$ m, elastic modulus of lining $E_0=35000$ MPa, Poisson's ratio of lining $\nu_0=0.15$, is adopted in the analysis.

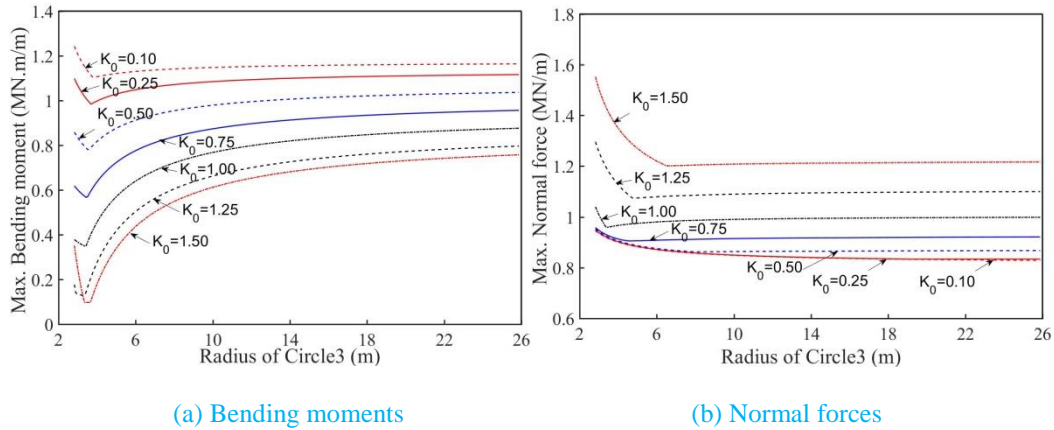


Fig. 6-13 Internal forces of sub-rectangular tunnel considering different K_0

Fig. 6-13 shows that the influence of coefficient of lateral earth pressure at rest K_0 on the internal forces of sub-rectangular tunnel is significant when $K_0 > 0.25$. The bending moment of sub-rectangular tunnel decreases as K_0 increases. However, the normal force of sub-rectangular tunnel increases as K_0 increases. This is because of the lateral earth pressure transmission effect mentioned above. Indeed, the lateral pressure tends to push the waists inwards and it increases with the coefficient of lateral earth pressure at rest K_0 . Therefore, the bending moment decreases and the normal force increases as K_0 increases. Note that the normal force of sub-rectangular tunnel when $K_0 = 0.25$ is slightly higher than that when $K_0 = 0.10$, which means that the influence of K_0 on the normal force of sub-rectangular tunnel is insignificant when $K_0 < 0.25$.

For each case of K_0 value, the bending moment of sub-rectangular tunnel decreases firstly and then increases with the increase of R_3 . The reason is the same as that mentioned in Section 2.2. Therefore, for any given value of K_0 , there is only one corresponding R_3 which supplies minimum M_{max} . Once R_3 is known, the optimal shape of the sub-rectangular tunnel can be obtained according to the mathematical formulas derived in Section 2.1. In addition, the normal force of sub-rectangular tunnel decreases as R_3 increases when $K_0 < 0.5$. However, the normal force firstly decreases rapidly and then increases very slowly as R_3 increases when $K_0 > 0.5$. It means that the effect of lateral pressure on the values of normal force is much more significant when $K_0 > 0.5$.

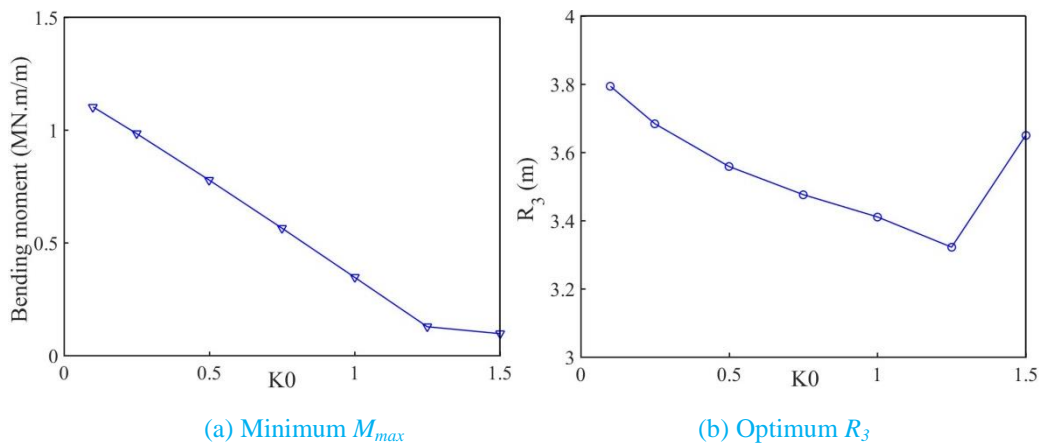


Fig. 6-14 Effect of K_0 on minimum M_{max} and sub-rectangular tunnel shape

Fig. 6-14 gives that the minimum M_{max} decreases with the increase of K_0 . The reason is just like that mentioned above. Specially, while K_0 is less than 1.25, it is nearly linear relationship between M_{max} and K_0 . In addition, the optimum R_3 decreases with the increase of K_0 when K_0 is less than 1.25. However, R_3 increases with the increase of K_0 when K_0 is over 1.25.

Fig. 6-15 only presents the distributions of bending moment and normal force when K_0 is 0.25 and K_0 is 1.5, respectively. The radius of circle 3 (R_3), the normal forces at tunnel crown and at left spring line, the bending moments at tunnel invert and at left spring lines are shown in Table 6-3 corresponding $K_0 = 0.25; 0.5; 0.75; 1; 1.25; 1.5$. Note that the maximum positive moment happens close to the middle point of the crown and invert areas, and the largest negative moment occurs to near the tunnel spring line as $K_0 = 0.25$; whereas the largest negative moment occurs at the four corners and the bending moment at the spring line is relatively small and becomes positive as $K_0 = 1.5$. This is because the lateral pressure tends to push the tunnel waists inwards. As K_0 increases, both of the lateral pressure and the lateral confinement will increase. Therefore, the stress concentration is formed at the four corners. Due to the same reason, the minimum normal force happens near the invert and crown areas as K_0 is 0.25, however, the minimum normal force appears near the spring line as K_0 is 1.5. In general, the normal force increases with the increase of K_0 . Specially, the normal forces at the tunnel crown and invert areas increase obviously as K_0 increases from 0.25 to 1.5.

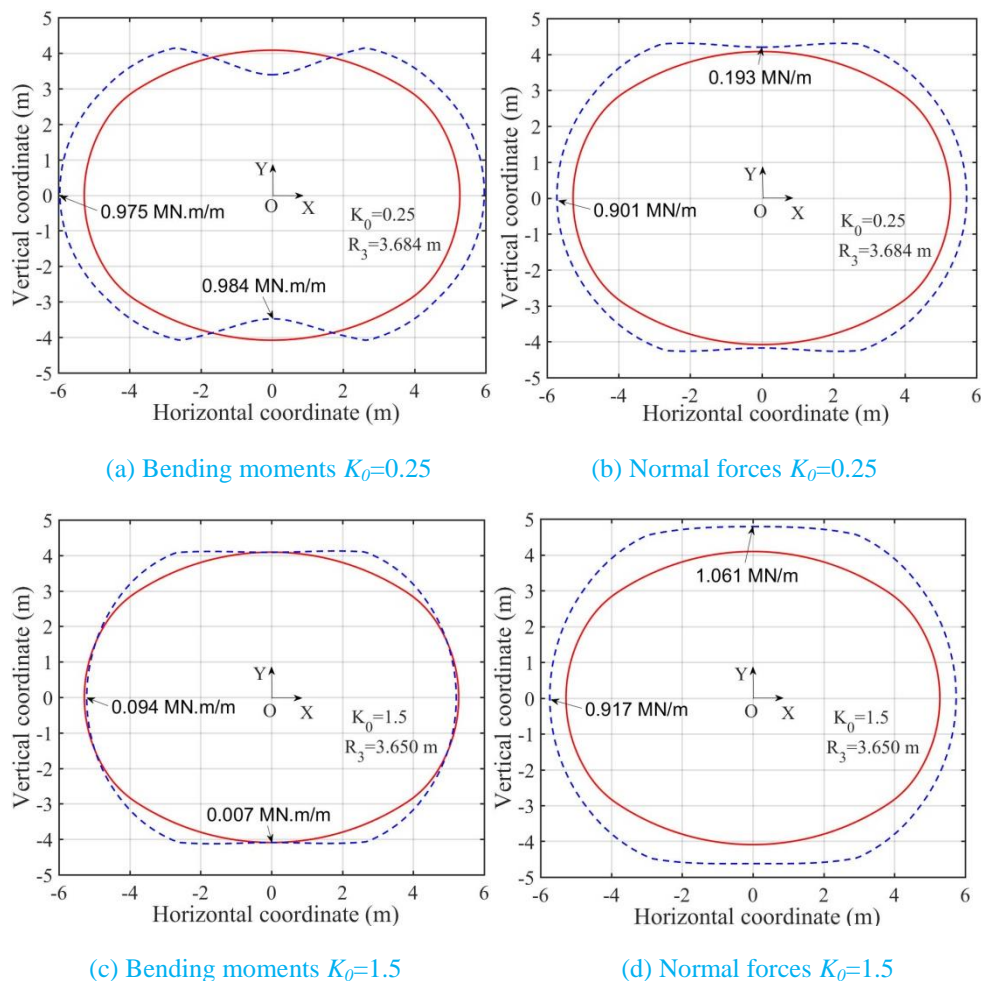


Fig. 6-15 Optimum sub-rectangular tunnel shapes and internal forces as $K_0=0.25$ and $K_0=1.5$, respectively. Note red solid line is the diagram of corresponding sub-rectangular lining

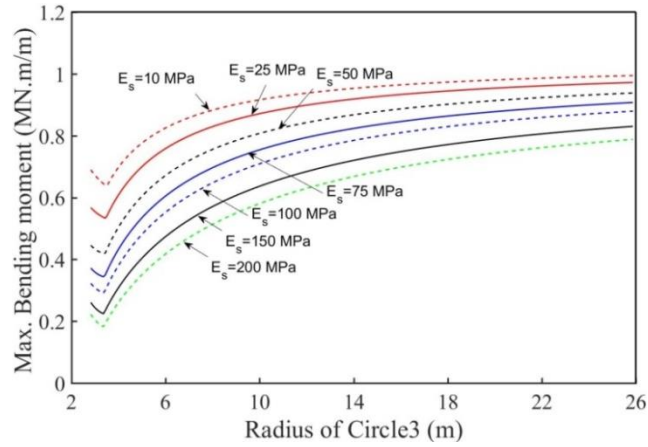
Table 6-3 Optimum internal forces considering different K_0

K_0	0.10	0.25	0.50	0.75	1.0	1.25	1.5
R_3 (m)	3.794	3.684	3.558	3.476	3.411	3.322	3.650
T (MN/m) at the crown	0.088	0.193	0.370	0.548	0.728	0.912	1.061
T (MN/m) at the spring line	0.896	0.901	0.908	0.914	0.920	0.927	0.917
M (MN.m/m) at the invert	1.102	0.984	0.778	0.565	0.346	0.111	0.007
M (MN.m/m) at the spring line	-1.092	-0.975	-0.771	-0.560	-0.346	-0.127	0.094

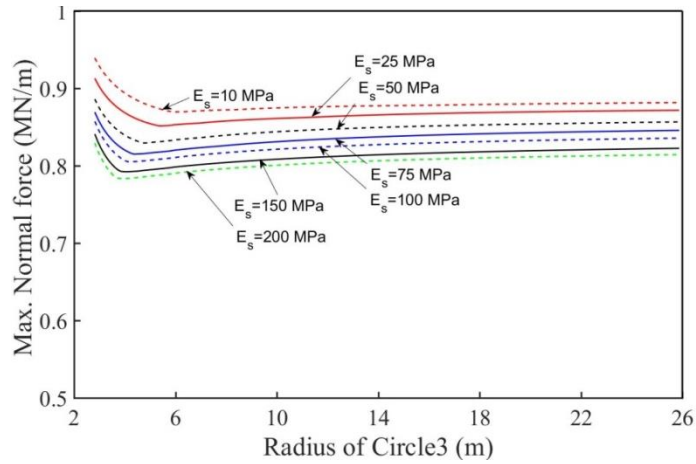
It can be found from Table 6-3 that the normal force at tunnel crown increases as K_0 increases. However, the normal force at spring line increases firstly and then decreases as K_0 increases. The bending moment at tunnel invert decreases as K_0 increases. It should be noticed that the bending moment at spring line decreases as K_0 increases, but the bending moment changes from negative to positive while K_0 is 1.25.

3.3 Effect of Young’s modulus E_s of soil on internal forces and shape of sub-rectangular tunnel

In this subsection, the influence of Young’s modulus of soil $E_s = 10, 25, 50, 75, 100, 150, 200$ MPa on the internal forces and shape of sub-rectangular tunnel is presented in Fig. 6-16 and Fig. 6-17, respectively, corresponding to $K_0=0.6, C=10\text{m}, P_0= 0.02\text{MPa}, \nu=0.495, \varphi =16.5^\circ, c=25.6\text{kPa}, \gamma=18\text{kN/m}^3, E_0=35000$ MPa, $\nu_0=0.15$ and $t=0.5\text{m}$.



(a) Bending moments



(b) Normal forces

Fig. 6-16 Effect of Young’s modulus E_s of soil on the Maximum internal forces

Fig. 6-16a presents that Young’s modulus E_s of soil has a significant influence on the bending moment of sub-rectangular tunnel. The bending moment of sub-rectangular tunnel decreases as E_s increases. The bending moment of sub-rectangular tunnel decreases firstly and then increases with the increase of R_3 . For any given value of E_s , there is only one corresponding R_3 which supplies minimum M_{max} . Once R_3 is known, the optimal shape of the sub-rectangular tunnel can be obtained. Fig. 6-16b gives that the normal force of sub-rectangular

tunnel decreases as E_s increases. The normal force of sub-rectangular tunnel decreases rapidly and then increases slowly as R_3 increases.

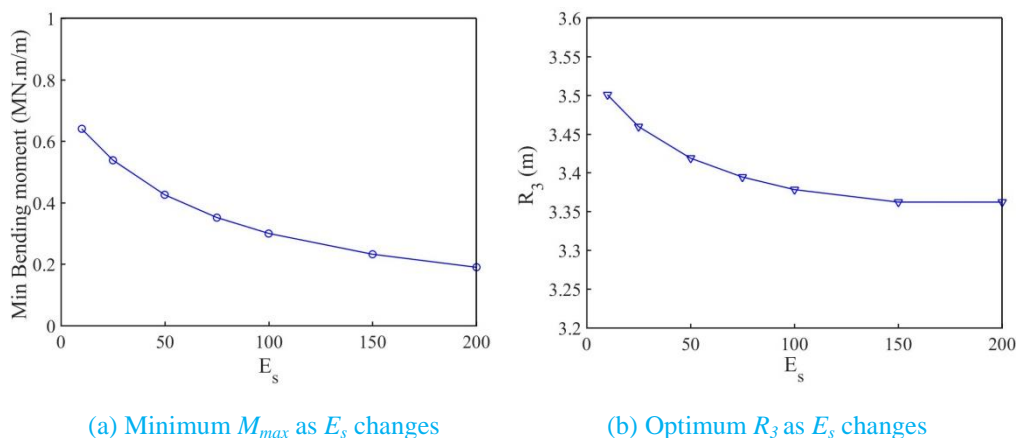


Fig. 6-17 Effect of Young’s modulus E_s of soil on minimum M_{max} and sub-rectangular tunnel shape

Fig. 6-17 shows that the minimum M_{max} decreases with the increase of E_s . Similarly, the optimum R_3 decreases with the increase of E_s as well.

Table 6-4 Optimum internal forces considering different Young’s modulus of soil E_s

E_s (MPa)	10	25	50	75	100	150	200
R_3 (m)	3.501	3.460	3.419	3.394	3.378	3.362	3.362
T (MN/m) at the crown	0.456	0.484	0.514	0.532	0.543	0.557	0.563
T (MN/m) at the spring line	0.898	0.872	0.843	0.824	0.810	0.790	0.776
M (MN.m/m) at the invert	0.637	0.533	0.417	0.343	0.291	0.223	0.183
M (MN.m/m) at the spring line	-0.633	-0.528	-0.412	-0.337	-0.285	-0.217	-0.175

Fig. 6-18 only presents the distributions of bending moment and normal force when E_s is 10 MPa and E_s is 200 MPa, respectively. All the radius of circle R_3 , the normal forces at tunnel crown and at left spring line, the bending moments at tunnel invert and at left spring lines, are shown in Table 6-4, corresponding to $E_s = 10, 25, 50, 75, 100, 150, 200$ MPa. It is obvious that the normal force at tunnel crown increases as E_s increases. However, the normal force at left spring line decreases with the increases of E_s . The bending moments at tunnel invert and at left spring line decrease as E_s increases.

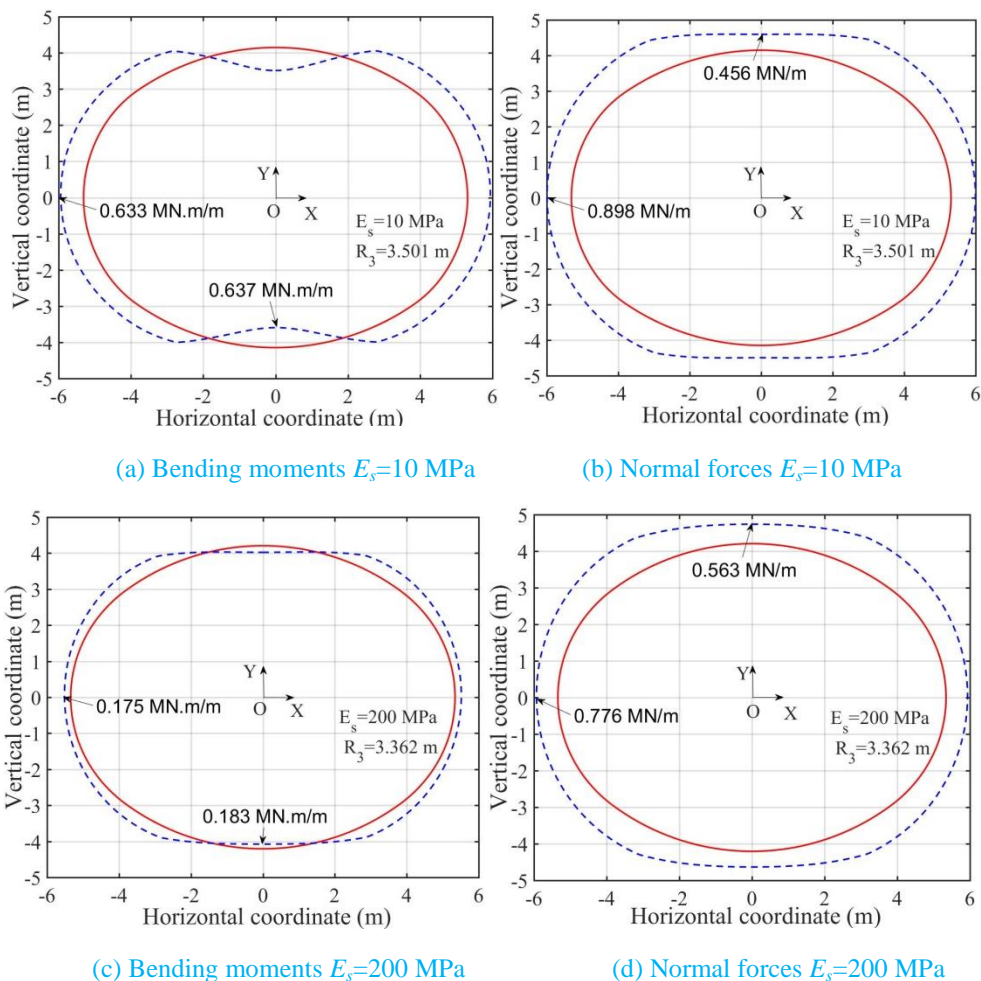
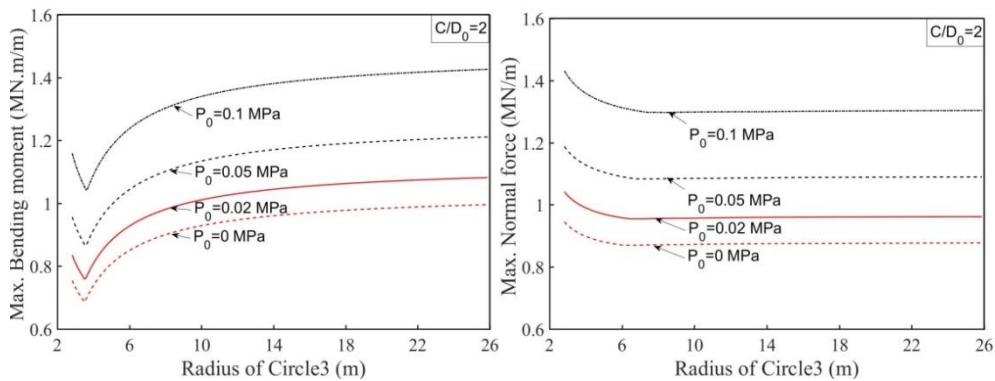


Fig. 6-18 Optimum sub-rectangular tunnel shapes and internal forces as $E_s=10$ MPa and $E_s=200$ MPa, respectively

3.4 Effect of surface loads on internal forces and shape of sub-rectangular tunnel

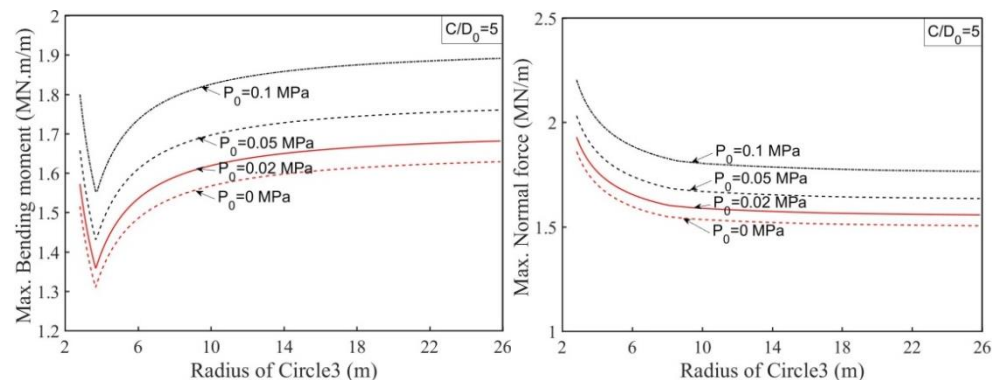
From Eq. 2-28, one finds that when the tunnel depth is over two times of the external diameter of the tunnel lining, an effective depth should be considered. However, the effective depth h_0 depends on the surface loads P_0 . Therefore, the effect of surface loads on internal forces and shape of sub-rectangular tunnel is studied in this subsection considering different tunnel depth C (e.g. $C/D_0= 2, 5, 10, 20$).

The influence of surface load $P_0= 0, 0.02, 0.05, 0.1$ MPa on the internal forces and shape of sub-rectangular tunnel is shown in Fig. 6-19, corresponding to $K_0=0.6, E_s=3.6$ MPa, $\nu=0.495, \varphi =16.5^\circ, c=25.6$ kPa, $E_0=35000$ MPa, $\nu_0=0.15, \gamma=18$ kN/m³, $t=0.5$ m, $C=2D_0, 5D_0, 10D_0, 20D_0$. The other outcomes of internal forces are presented in Table 6-5.



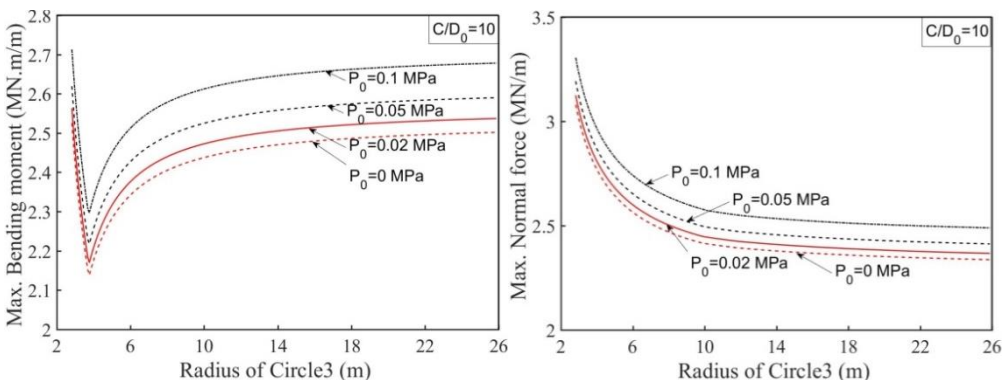
(a) Bending moments $C=2D_0$

(b) Normal forces $C=2D_0$



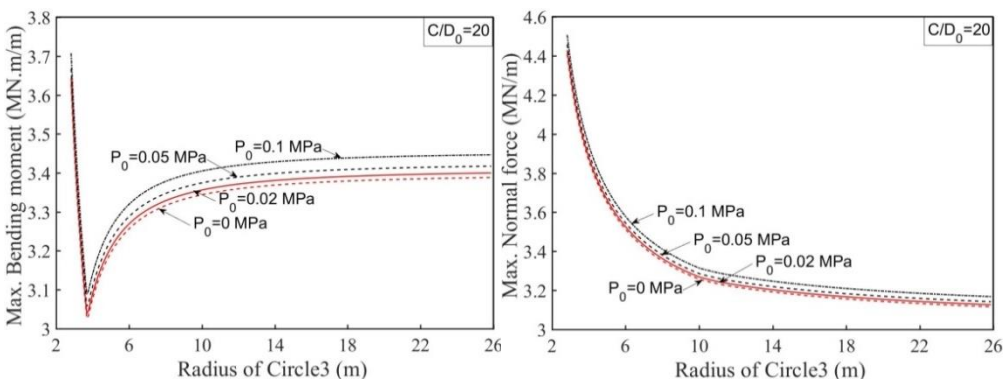
(c) Bending moments $C=5D_0$

(d) Normal forces $C=5D_0$



(e) Bending moments $C=10D_0$

(f) Normal forces $C=10D_0$



(g) Bending moments $C=20D_0$

(h) Normal forces $C=20D_0$

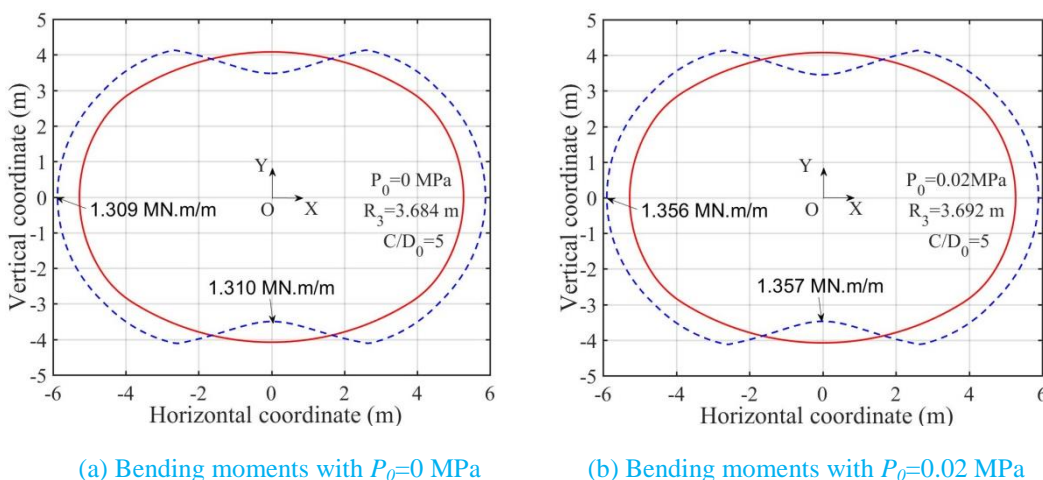
Fig. 6-19 Effect of surface loads on the Maximum internal forces considering different C

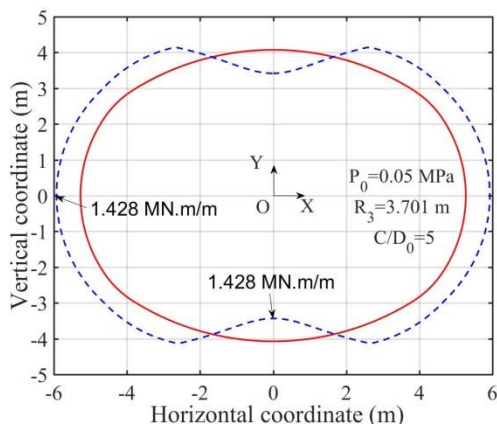
Clearly, from Fig. 6-19 and Table 6-5, one obtains that the internal forces increase with the increase of surface load P_0 . Also, the influence of P_0 on the internal forces of sub-rectangular tunnel is closely related to the values of C/D_0 . As the increase of C/D_0 , the influence of P_0 on the internal forces is less obvious. Note that the impact of P_0 on the shape of sub-rectangular tunnel disappears as C/D_0 is over 10 (e.g. R_3 keeps constant as C/D_0 is over 10). It means that the sub-rectangular tunnel can be designed without considering the effect of P_0 as C/D_0 is over 10.

Table 6-5 Effect of surface loads on internal forces and shape of sub-rectangular tunnel considering different C

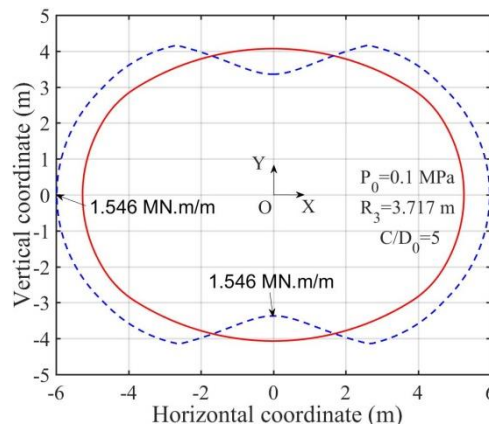
P_0 (MPa)	$C/D_0=2$				$C/D_0=5$				$C/D_0=10$				$C/D_0=20$			
	0	0.02	0.05	0.1	0	0.02	0.05	0.1	0	0.02	0.05	0.1	0	0.02	0.05	0.1
R_3 (m)	3.517	3.542	3.575	3.625	3.684	3.692	3.701	3.717	3.743				3.701			
T (MN/m) at the crown	0.436	0.484	0.557	0.677	0.861	0.893	0.942	1.022	1.420	1.440	1.471	1.525	2.014	2.022	2.035	2.056
T (MN/m) at the spring line	0.903	0.997	1.137	1.370	1.728	1.791	1.885	2.042	2.812	2.853	2.913	3.015	3.954	3.971	3.995	4.035
M (MN.m/m) at the invert	0.686	0.756	0.862	1.038	1.310	1.357	1.428	1.546	2.117	2.146	2.190	2.262	2.935	2.947	2.965	2.994
M (MN.m/m) at the spring line	-0.683	-0.754	-0.861	-1.037	-1.309	-1.356	-1.428	-1.546	-2.134	-2.164	-2.210	-2.289	-3.016	-3.028	-3.047	-3.078

Fig. 6-19 also gives that the surface loads P_0 has the similar effect on the internal forces under the condition of different C/D_0 . Because of this, only considering $C/D_0=5$, the distributions of internal forces considering different surface loads are shown in Figs. 6-20 and 6-21, respectively. Clearly, the maximum positive moment occurs close to the middle point of the crown and invert areas, and the largest negative moment appears to near the tunnel spring line. In contrast, the minimum normal force occurs close to the middle point of the crown and invert areas.



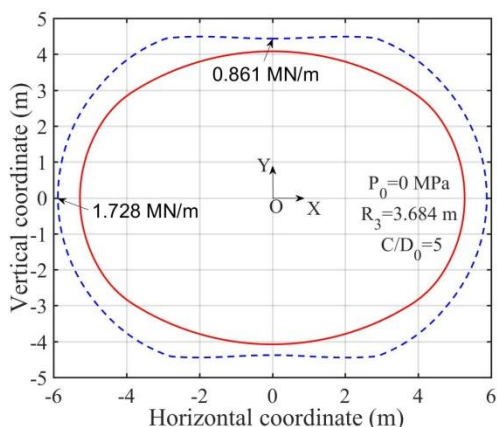


(c) Bending moments with $P_0=0.05$ MPa

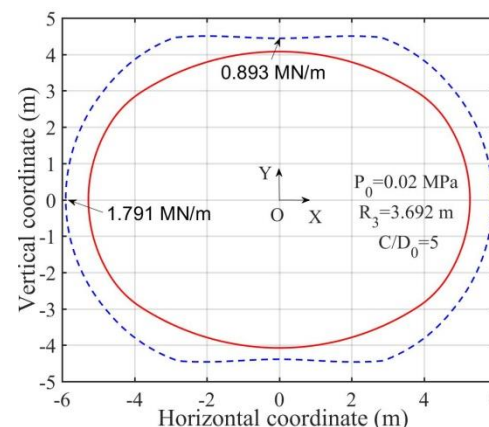


(d) Bending moments with $P_0=0.1$ MPa

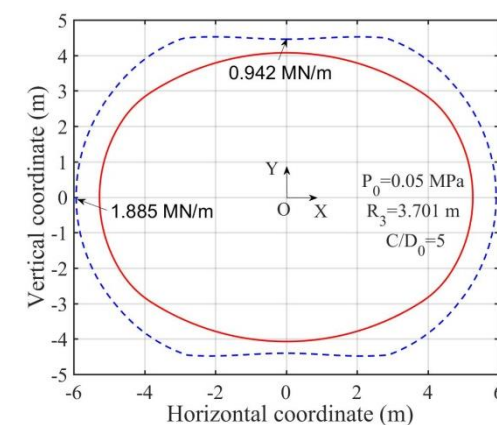
Fig. 6-20 Distributions of bending moment considering different surface loads when $C/D_0=5$



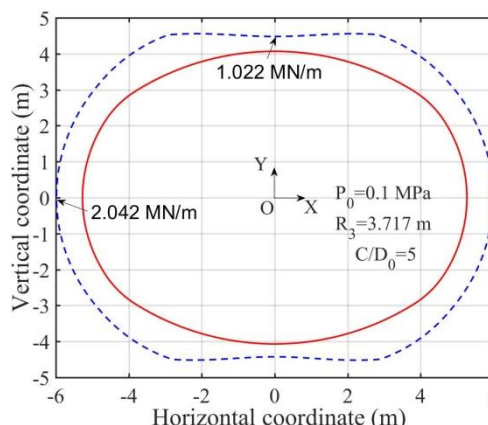
(a) Normal forces with $P_0=0$ MPa



(b) Normal forces with $P_0=0.02$ MPa



(c) Normal forces with $P_0=0.05$ MPa



(d) Normal forces with $P_0=0.1$ MPa

Fig. 6-21 Distributions of normal force considering different surface loads when $C/D_0=5$

4. Conclusions

The increasing large-diameter and variety of cross-section geometry of tunnels are being employed to construct underground space projects, e.g. the tunnels with sub-rectangular cross-section. In spite of that, there are limited studies dealt with the design of sub-rectangular tunnels. Therefore, an optimization process on the basis of hyperstatic reaction method was deduced in this chapter, which provides an effective way to optimize the sub-rectangular tunnel shape.

Taking a twin-lane metro tunnel with the Vietnamese specifications as an example, a series of mathematical functions used in the optimization progress of sub-rectangular tunnel shape were deduced. Since the maximum bending moment of sub-rectangular tunnel always decreases firstly and then increases with the increase of R_3 under the effect of different parameters, the optimal shape of the sub-rectangular tunnel is determined by the minimum M_{max} .

According to the mathematical formulas derived in this chapter, the effect of different parameters, like coefficient of lateral earth pressure, Young's modulus of soil, tunnel depth, surface loads, on the internal forces and shape of sub-rectangular tunnel was investigated. The present method was validated by comparing the results to the ones of FLAC^{3D}. Some conclusions are given:

1. The optimum R_3 of sub-rectangular tunnel increases rapidly and then decreases slowly as C/D_0 increases. The bending moment of sub-rectangular tunnel increases with the increase of C/D_0 . However, the relation of bending moment and C/D_0 is not linear but approximately parabolic. The normal force of sub-rectangular tunnel increases with the increase of C/D_0 .

2. The optimum R_3 of sub-rectangular tunnel decreases with the increase of K_0 when K_0 is less than 1.25. However, R_3 increases with the increase of K_0 when K_0 is over 1.25. The bending moment of sub-rectangular tunnel decreases as K_0 increases. However, the normal force of sub-rectangular tunnel increases as K_0 increases. Note that as $K_0 = 0.75$, the maximum positive moment happens close to the middle point of the crown and invert areas, and the largest negative moment occurs to near the tunnel spring line; whereas as K_0 increases (e.g. $K_0=1.5$), the largest negative moment occurs at the four corners and the bending moment at the spring line is relatively small and becomes positive. This is because the lateral pressure tends to push the tunnel waists inwards. As K_0 increases, the stress concentration is then formed at the four corners.

3. The optimum R_3 of sub-rectangular tunnel decreases with the increase of E_s . The bending moment of sub-rectangular tunnel decreases with the increase of E_s . The normal force of sub-rectangular tunnel decreases as E_s increases as well.

4. The internal forces of sub-rectangular tunnel increase with the increase of surface load P_0 . The influence of P_0 on the internal forces of sub-rectangular tunnel is closely related to the values of C/D_0 . As the increase of C/D_0 , the influence of P_0 on the internal forces is less obvious. Specially, the impact of P_0 on the shape of sub-rectangular tunnel disappears as C/D_0 is over 10 (e.g. R_3 keeps constant as C/D_0 is over 10).

In the next chapter, the thermos-mechanical analysis of the tunnel lining behaviour will be presented using the HRM method.

CHAPTER 7 THERMO-MECHANICAL BEHAVIOUR OF TUNNELS

1. Introduction

Although tunnels are widely used for transportation, such as water, road and rail traffic, less attention has been given to thermal stresses in tunnels caused by a temperature change. In practice, during the life of a tunnel, the temperature changes in the tunnel lining and the surrounding ground. Several studies have presented the reasons which may cause a temperature change of the lining, e.g. (1) the seasonal changes in ambient temperature, (2) the heating from the passage of cars, trucks or trains, (3) the geothermal issues and (4) the fires.

This temperature modification will induce a variation of the tunnel lining forces. The stresses caused by the change of temperature are called thermal stresses. Thermal stresses generated by temperature may cause cracks and can also lead to damages of the lining. If large enough (when caused by fire) they can have a major factor on the damage of tunnels. In fact, there are a number of tunnels that suffered cracking damage due to thermal loading, such as in 1996 (Channel Tunnel fire in France). This incident resulted in considerable damage over 480 m (Maraveas and Vrakas, 2014). The 1999 Mont Blanc tunnel fire seriously damaged the tunnel roof over a length of 900 m, especially, a part of the tunnel roof lining completely has collapsed and exposed the rock mass (Voeltzel and Dix, 2004).

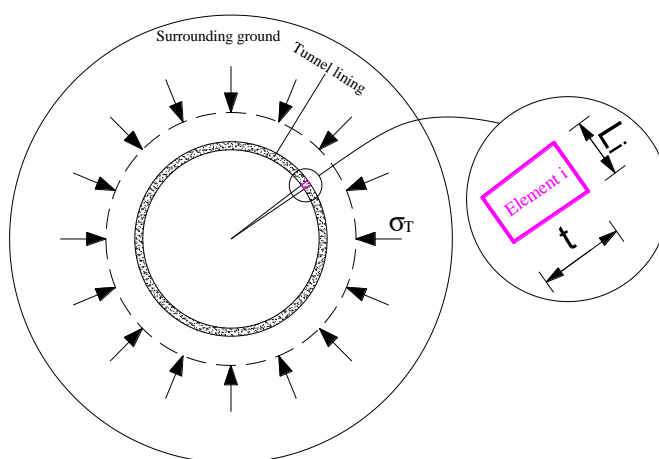
Even though the change in temperature has an influence on the tunnel lining forces, few research works which focus on the thermo-mechanical behaviour of tunnels can be found. On the basis of the finite element method, Nicholson et al. (2014) reported on the work carried out in designing thermal energy segments in the Crossrail project of London. Barla and Di Donna (2018) investigated the possibility of the thermal activation of tunnel linings and shown how thermo-mechanical numerical analyses were used to achieve a proper and effective design of tunnels. Considering *in-situ* monitoring strain on a tunnel lining in the Shaanxi Province, Luo et al. (2010) analysed the tunnel lining forces under the ambient temperature changing in one year. In spite of this, none of them propose an efficient way to estimate the effect of a temperature change on the tunnel behaviour. Efficient and rigorous calculation procedures are required to provide an appropriate design of such structures.

This chapter presents an improvement of the HRM method to introduce the thermal stresses calculation. The effective strain coefficient of lining is deduced from the *in-situ* results and then used to calculate the effective lining thermal stresses combined with the mechanical ones. The implementation of the thermal behaviour of tunnel lining and surrounding mass is then presented. A parametric study is proposed to investigate the effect of the temperature change on the tunnel lining forces by means of the present method. Several factors are considered, such as the tunnel lining thickness, lining elastic modulus and ground coefficient of thermal expansion. Thereafter, the effect of fire which can modify the soil lining parameters is studied as well. The tunnel lining collapse caused by a fire event is predicted.

2. Hyperstatic reaction method considering the temperature

The tunnel lining should be subjected to its own weight, surrounding rock pressure and temperature stress. When investigating the thermo-mechanical behaviour of tunnels, ignoring the lining weight, only the surrounding rock pressure and temperature stress are considered in the analysis. It is assumed that 1) the parameters of ground, like Poisson’s ratio ν_s , cohesion c , internal friction angle φ and Young’s modulus E_s are assumed to be constant under the effect of temperature; 2) the change of temperature in the lining is assumed to be the same as the one of the surrounding ground.

Since the change in temperature is considered, the loads applied to the lining should include two parts: 1) the earth active loads (σ_v and σ_h shown in Fig. 7-1b) applied directly by the surrounding ground; 2) the additional thermal loads (ground and lining σ_T shown in Fig. 7-1a) caused by the change of temperature.



(a)

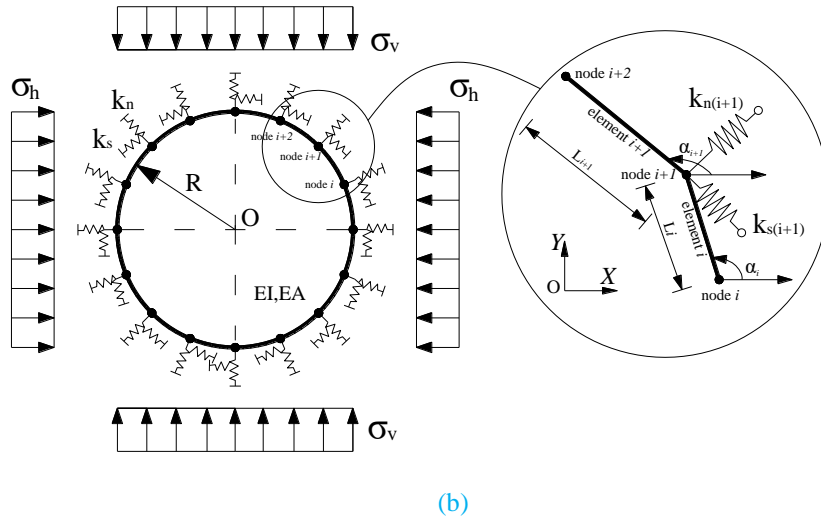


Fig. 7-1 Simplified structure of circular tunnel considering additional thermal loads caused by the temperature change in the HRM method. With: σ_T : the additional thermal loads caused by the change of temperature; σ_v : the vertical loads; σ_h : the horizontal loads; k_n : normal stiffness of springs; k_s : shear stiffness of springs; L_i : length of element i ; t : thickness of lining; EI and EA : bending and normal stiffness of lining; X and Y are the global Cartesian coordinates

2.1 Additional thermal loads

The temperature in tunnels and surrounding soils usually changes in time. The lining temperature change causes induced strains in the concrete by thermal expansion or shrinkage. The lining is restrained by the surrounding ground and lining stresses will therefore change with the temperature. The stresses caused by the change of temperature are called thermal stresses.

It is assumed that the additional thermal load σ_T caused by the change of temperature is a uniform load (Fig. 7-1a) and the structures are always contacted with the ground no matter how much the temperature changes. Generally, heating will yield a uniform compression load and cooling causes a uniform tension load (Bourne-Webb, 2013). In the analysis, σ_T is the sum of the additional thermal load σ_{T_s} from the soil mass and the additional thermal load σ_{T_l} from the lining. Therefore, the total thermal load σ_T is therefore obtained as follows:

$$\sigma_T = \sigma_{T_s} + \sigma_{T_l} \tag{7-1}$$

Given that the surrounding ground is perfectly restrained by the lining and the ground-lining contact is perfectly rigid, the potential soil strains caused by the change of temperature are totally converted to

additional thermal stresses. Therefore, the additional soil thermal stresses caused by the change of temperature can be expressed by:

$$\sigma_{TS} = E_s \cdot \varepsilon^{ths} \quad (7-2)$$

in which E_s indicates the Young's modulus of ground; ε^{ths} represents the radial soil restrained thermal strain caused by the temperature change, which can be given by:

$$\Delta\varepsilon^{ths} = \alpha_{TS} \cdot \Delta T \quad (7-3)$$

where α_{TS} is the soil coefficient of thermal expansion ($^{\circ}\text{C}$); ΔT the change of temperature.

Unlike the soil thermal strains, the lining strains caused by the change of temperature cannot be completely converted to additional tunnel lining thermal stresses. This is because only the outer surface of the lining which is in contact with the soil mass is constrained, while the inner surface of the lining is free. Meanwhile, [Amatya et al. \(2012\)](#) pointed out that only the restrained structure strains induce thermal stresses which should be considered in a structural design. Therefore, the additional thermal stresses σ_{TL} of the tunnel lining can be expressed by:

$$\sigma_{TL} = E \cdot (\beta_{TL} \cdot \varepsilon^{th}) \quad (7-4)$$

where E indicates the Young's modulus of tunnel lining; β_{TL} is the effective strain coefficient of lining which means the proportion of strain converted into thermal stress; ε^{th} represents the radial thermal strain of structure due to the change of temperature, which can be given by:

$$\varepsilon^{th} = \alpha_{TL} \cdot \Delta T \quad (7-5)$$

in which α_{TL} is the lining coefficient of thermal expansion ($^{\circ}\text{C}$); ΔT means the change of temperature.

Therefore, to calculate the additional thermal stress σ_{TL} , the key point is to determine the value of β_{TL} . [Amatya et al. \(2012\)](#) studied the thermo-mechanical behaviour of energy piles and found that the end restraint of piles is important. However, no author has provided a specific formulation to estimate the value of β_{TL} of tunnel lining. Relied on the *in-situ* monitoring of tunnel lining concrete strain of the Liujiaping No.3 tunnel in the Shaanxi Province of China, [Luo et al. \(2010\)](#) studied the tunnel lining forces under ambient temperature during one year. By comparing the internal forces of the present method to the *in-situ* results of [Luo et al. \(2010\)](#), the value of β_{TL} in this chapter can then be determined. The properties of the materials used in [Luo et al. \(2010\)](#) are shown in Table 7-1.

Table 7-1 Properties of the materials used in Luo et al. (2010)

Properties of lining	Symbol	Value	Unit
Radius	R	6.08	m
Thickness	t	0.45	m
Poisson's ratio	ν	0.16	-
Elastic Modulus	E	29,500	MPa
Coefficient of thermal expansion	α_{Tl}	0.9×10^{-5}	$^{\circ}\text{C}^{-1}$

It should be noted that the initial temperature of the lining concrete is equal to 12°C in Luo et al. (2010). Given that the Young's modulus E_s of the ground is taken equal to 300MPa; the Poisson's ratio ν_s of the ground to 0.3; the overburden thickness h of tunnel to 40m; the lateral earth pressure factor K_0 to 0.8; the unit weight γ of soil to 22kN/m^3 ; the friction angle φ and cohesion c of soil are respectively equal to 20 degrees and 50 kPa.

Table 7-2 gives the inner lining thermal forces obtained from the in-situ data due to the change of temperature (Luo et al. 2010). When only considering the effect of the temperature change, the normal forces obtained by the present method are also shown in Table 7-2 corresponding to β_{Tl} with t/R^2 . It can be found that the results calculated by the present method are in good agreement with those of Luo et al. (2010) and their difference is lower than 8.5%. So β_{Tl} is taken as t/R^2 in the following analysis. Therefore, the thermal stresses depend on the temperature change, the coefficient of thermal expansion, the thickness of lining and the elastic modulus of the lining concrete (Luo et al., 2010).

Table 7-2 Inner thermal forces of lining concrete (Luo et al. 2010)

Change of temperature ΔT ($^{\circ}\text{C}$)	Normal force N (kN/m)		Error
	Luo et al. (2010)	Present method	
-10.1	207.45	190.11	8.36%
-11.6	222.53	218.35	1.88%

Fig. 7-2 shows the positive direction of the structural forces (bending moment M , normal force N) in the analysis.

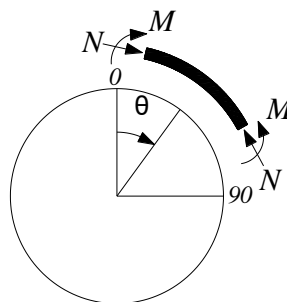


Fig. 7-2 Positive direction of the structural forces (bending moment M , normal force N). θ : the angle between the vertical axis of cross-section of tunnel and the element axis

The effect of active loads applied directly by the surrounding ground on the internal forces of a circular tunnel has been studied by Do et al. (2014d). Therefore, only the thermal loads are considered in the following analysis to present the temperature change effect on the incremental internal forces induced in the tunnel lining of a circular tunnel.

Table 7-3 Properties of the materials used in the analysis

	Symbol	Value	Unit
Properties of lining			
Radius	R	6.02	m
Thickness	t	0.50	m
Poisson's ratio	ν	0.15	-
Elastic Modulus	E	35,000	MPa
Coefficient of thermal expansion	α_{TL}	1.2×10^{-5}	$^{\circ}\text{C}^{-1}$
Overburden thickness	h	40	m
Properties of the soil mass			
Elastic Modulus	E_s	300	MPa
cohesion	c	50	kPa
Internal friction angle	φ	20	degree
Unit weight	γ_s	22	kN/m^3
Poisson's ratio	ν_s	0.30	-
Lateral earth pressure factor	K_0	0.8	-
Coefficient of thermal expansion	α_{TS}	5×10^{-6}	$^{\circ}\text{C}^{-1}$

In the following analysis, both the soil mass and tunnel lining are assumed to behave in linear thermo-elastic conditions. The Young's modulus of the soil mass is taken equal to 300 MPa and the lining Young's modulus to 35 GPa. The coefficients of thermal expansion are taken equal to $5 \times 10^{-6} \text{ }^{\circ}\text{C}^{-1}$ for the soil and $1.2 \times 10^{-5} \text{ }^{\circ}\text{C}^{-1}$ for the concrete lining.

The properties of the soil and lining are taken from the Toulon tunnel in France (Oreste and Dias, 2012). They are summarized in Table 7-3.

3. Effect of the temperature change on the tunnel lining forces

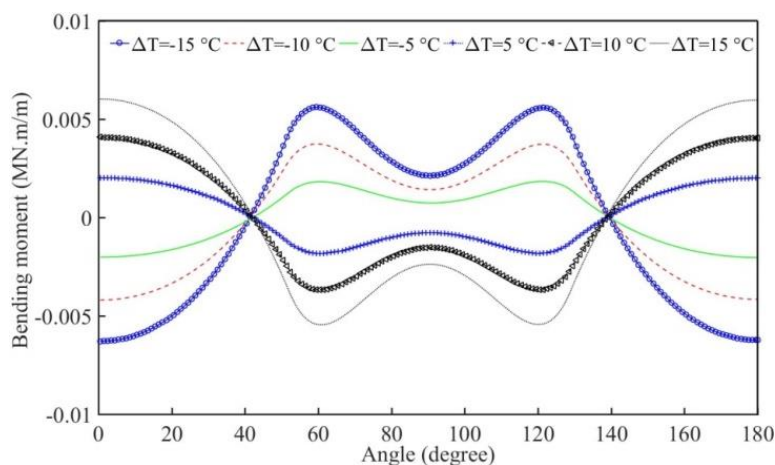
Barla and Di Donna (2018) found that the typically ground temperature in most continental Europe countries at depths being higher than 5-8 m varies between 8 °C and 16 °C, but remains constant over the whole year, down to approximately 50 m. Toulon tunnel is located at the south of France, so it is assumed a constant temperature equal to 20 °C. Luo et al. (2010) found that the temperature change is about 15°C when they studied the mechanical behaviour of the lining concrete. Therefore, it is assumed that the lining is subjected to a temperature change which varies from -15°C to +15°C and the thermal expansion coefficient and elastic modulus of the concrete structure stays constant in this temperature range. The properties presented in Table 7-3 are adopted in the analysis.

3.1 Considering only the additional thermal loads of lining

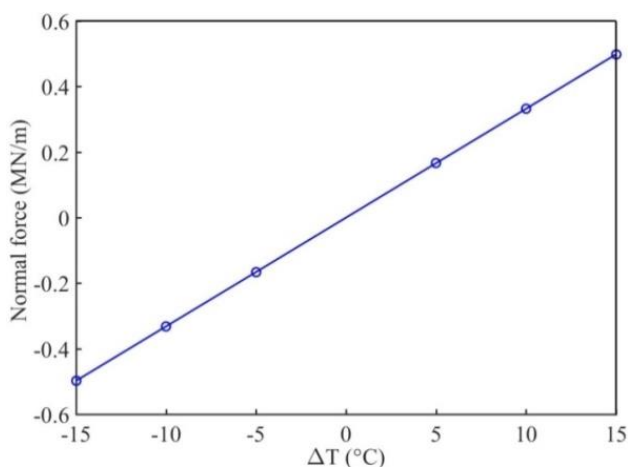
When considering only the additional thermal loads, the coefficient of thermal expansion of the lining α_{TL} is considered to be equal to $1.2 \times 10^{-5} \text{ } ^\circ\text{C}^{-1}$ and the coefficient of thermal expansion of the soil α_{TS} to $0 \text{ } ^\circ\text{C}^{-1}$. The other properties in Table 7-3 are adopted. This case occurs when temperature change happens in a very short period of time, like the significant heat generated by underground trains when braking, stopping at platforms and accelerating, so that there is no enough time to transmit the temperature change from lining to surrounding soil. Fig. 7-3 presents the effect of temperature change on the incremental forces induced in the tunnel lining while only considering the additional lining thermal loads. As can be seen in this figure, cooling the lining generates tensile normal forces, whereas heating the lining leads to compressive normal forces. Since the additional thermal loads are applied uniformly to the tunnel lining along the tunnel radial direction (see Fig. 7-1a), similar normal forces can be obtained along the whole tunnel when the value of temperature change is constant. Therefore, Fig. 7-3b gives the relation of normal force and temperature change. In contrast, the bending moments highly change along the whole lining. The maximum absolute bending moment values occur at the centre of the tunnel crown and at the invert. It is known that the lateral pressure tends to push the

waists inwards and it increases with the lateral earth pressure factor K_0 . As the considered coefficient K_0 is equal to 0.8 in the analysis, therefore, the absolute bending moment values at the tunnel crown and at the invert are higher than the spring line ones.

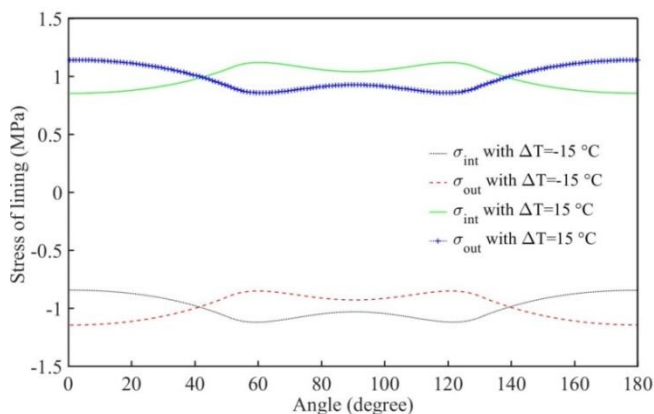
It is worth noting that the greater the temperature change, the greater the internal forces of lining. And for the same value of temperature difference, a cooling load will produce the similar response as a heating one. The absolute values of the extrados lining stresses are higher than the intrados ones at the tunnel crown (Fig. 7-3c). However, the absolute values of the intrados stress are higher than the extrados ones at the tunnel sidewall. This is due to the fact that the bending moment and the axial force have the same sign (positive or negative) at the crown, whereas their signs are opposite at the side wall.



(a) Bending moment



(b) Normal force

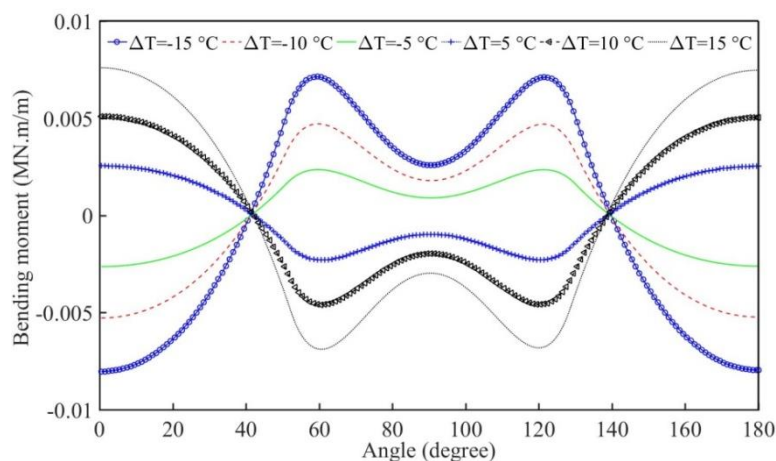


(c) Stress of lining

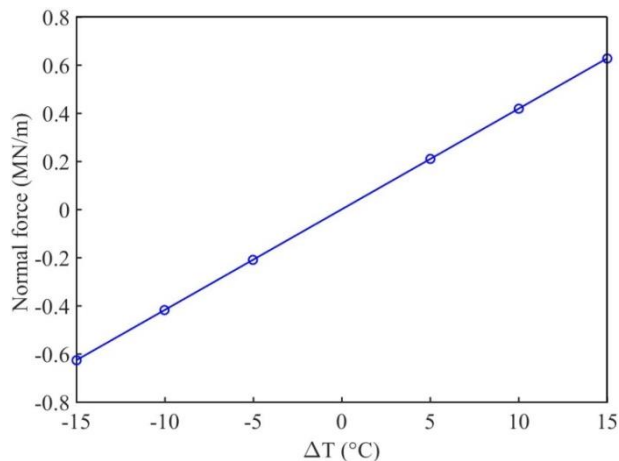
Fig. 7-3 Effect of the temperature change on the incremental tunnel lining forces when only considering the additional lining thermal loads

3.2 Considering the additional thermal loads of the soil mass and lining

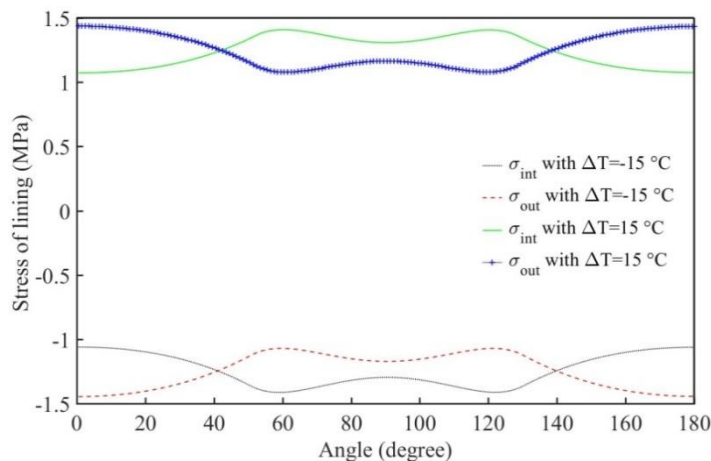
While considering the additional thermal loads of the soil mass and lining, the coefficient of thermal expansion of lining α_{TL} is set equal to $1.2 \cdot 10^{-5} \text{ }^\circ C^{-1}$ and the coefficient of thermal expansion of ground α_{TS} to $5 \cdot 10^{-6} \text{ }^\circ C^{-1}$. Fig. 7-4 shows the effect of the temperature change on the tunnel lining forces when considering the additional thermal loads of the lining and soil mass. Comparing them with the results of Fig. 7-3, the absolute force values considering the additional thermal loads of lining and soil mass are higher than of the ones while only considering the additional lining thermal loads.



(a) Bending moment



(b) Normal force



(c) Stress of lining

Fig. 7-4 Effect of the temperature change on the tunnel lining forces of when considering the additional thermal loads of the soil mass and lining

3.3 Effect of other factors on the tunnel lining forces

In this section, the effect of other factors, such as the change of lining thickness, lining modulus and soil type, on the tunnel lining forces is presented. The coefficient of thermal expansion of lining α_{TL} is set equal to $1.2 \times 10^{-5} \text{ } ^\circ\text{C}^{-1}$.

Note that the forces along the whole tunnel have been shown in Figs. 7-3 and 7-4 when considering different temperature changes. As it is found that the maximum force caused by temperature change occurs at the tunnel crown, only the internal forces at the tunnel crown are therefore presented in the following study.

3.3.1 Lining thickness

The effect of temperature change on the tunnel lining forces for different lining thicknesses is studied in this subsection. The lining thickness varies in a range from 0.3m to 0.6m.

Fig. 7-5 shows the tunnel lining forces at the tunnel crown for different temperature change and lining thickness. As can be seen from this figure, although the absolute values of bending moments and normal forces increase with the increase of the lining thickness, the intrados and extrados stresses decrease as the lining thickness increases. This is because the stress induced in the cross section of the tunnel lining strongly depends on the lining thickness. Indeed, stresses are calculated based on the following formula:

$$\sigma = \frac{N}{A} \pm \frac{My}{I} \quad (7-6)$$

where: N are the normal forces; M the bending moment; A the cross-sectional area of the lining along the direction of the tunnel excavation; y is $t/2$ and I is the moment of inertia which also depends on the thickness.

Consequently, the thicker the lining is, the smaller the stress value is. In addition, the greater the temperature change, the greater the internal forces at the tunnel crown. Cooling the lining causes tensile forces, whereas heating the lining generates compressive forces. The effect of thickness on the bending moments is more obvious than that on the normal forces. For example, when ΔT is equal to 15°C , the bending moment reaches 2.8 kN.m/m corresponding to a lining thickness $t = 0.30\text{m}$, whereas it becomes 10.9kN.m/m corresponding to the case $t = 0.6\text{m}$. Obviously, the bending moment increases almost three times when the thickness varies from 0.3m to 0.6m. Differently, the normal force only increases less than two times from 47.7kN/m to 73.9kN/m. Note that the similar conclusion about the normal force can be obtained at the other parts of the tunnel, e.g., the normal force increases from 42.4kN/m to 71.2kN/m with the same conditions at the sidewall.

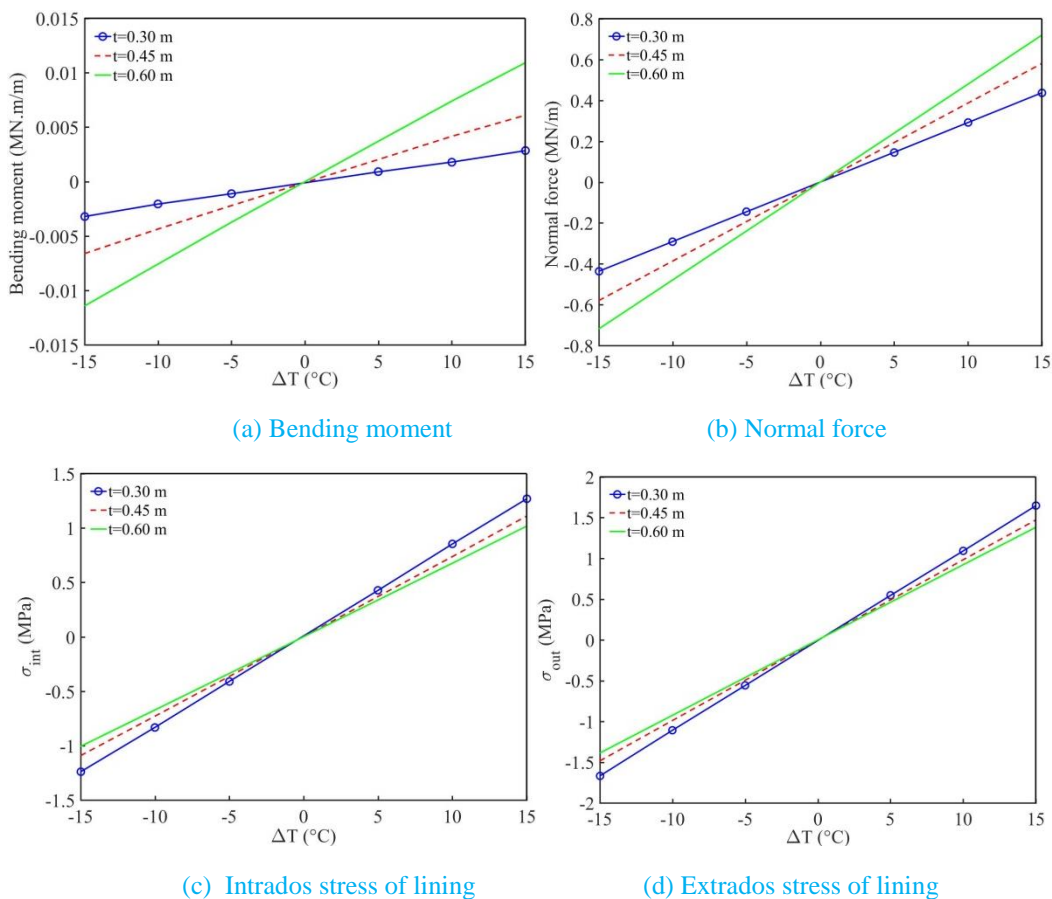


Fig. 7-5 Effect of the temperature change on the tunnel lining forces at the tunnel crown while considering the lining thickness

3.3.2 Elastic modulus of lining

The effect of temperature change on the tunnel lining forces considering different values of lining concrete’s modulus is presented in this subsection. The elastic modulus of lining varies in a range from 20 GPa to 50 GPa. Fig. 7-6 gives the effect of the temperature change on the tunnel lining forces at the tunnel crown considering different elastic modulus of lining. It can be found that the absolute values of the forces increase as the elastic modulus increases. In fact the bending and normal stiffness (EI and EA) of the lining depend on the elastic modulus of lining. The larger the elastic modulus is, the greater the stiffness of lining is. The forces that the lining can support are then larger.

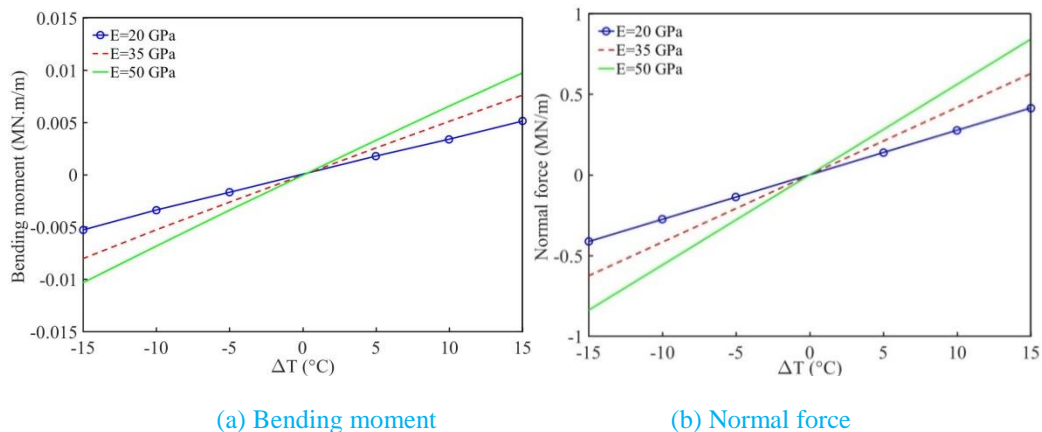
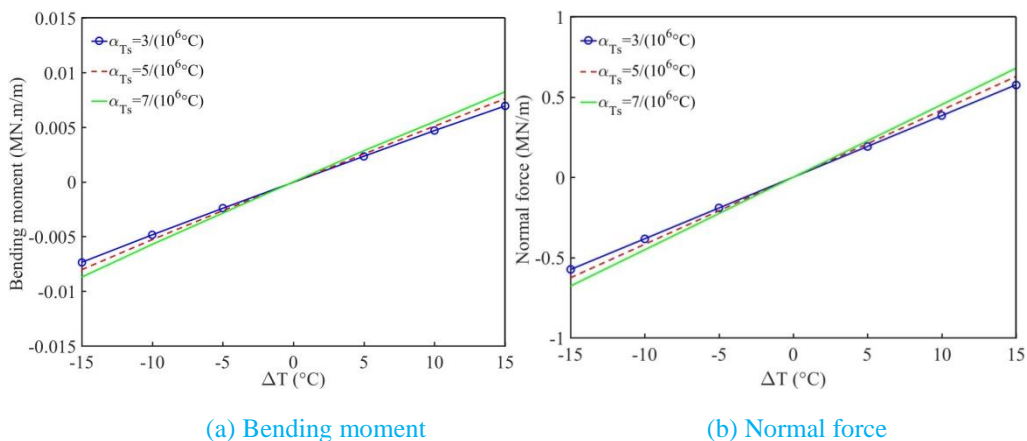


Fig. 7-6 Effect of the temperature change on the tunnel lining forces at the tunnel crown considering different elastic modulus of lining

3.3.3 Coefficient of thermal expansion of the soil mass

The coefficient of thermal expansion of the soil mass depends on the type of ground (Mroueh et al., 2018). Therefore, the effect of temperature change on the tunnel lining forces for different soil’s coefficient of thermal expansion is investigated. Given that σ_{Ts} varies from 3 to $7 \times 10^{-6} \text{ } ^\circ\text{C}^{-1}$, Fig. 7-7 gives the effect of temperature change on the tunnel lining forces at the tunnel crown considering different σ_{Ts} . It can be seen from Fig. 7-7 that the maximum difference is lower than 15.7%, when ΔT is equal to 15°C . The absolute values of internal forces increase with the increase of σ_{Ts} .



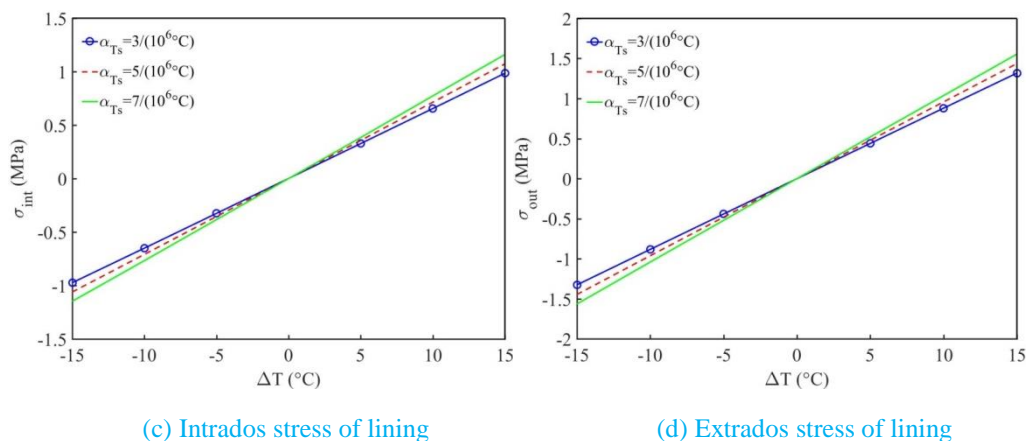


Fig. 7-7 Effect of the temperature change on the tunnel lining forces at the tunnel crown while considering different soil coefficients of thermal expansion

4. Effect of a fire on the tunnel lining forces

The behaviour of tunnel linings subjected to severe fire exposure is studied in this section. In the event of fire, the temperature in the tunnel rises rapidly within a short time, which is able to cause an irreversible loss of stiffness and strength (Maraveas and Vrakas, 2014). Furthermore, a lot of fire tests, e.g. EUREKA fire test (Kaundinya, 2006), were executed in the past decades in order to determine the temperature development and the damage pattern during a tunnel fire. Fire tests have shown that, at the tunnel ceiling, gas temperature rises to temperatures of 800 to 1000 °C after about 5 to 10 minutes and can reach temperatures of 1200 °C or even greater (Kaundinya, 2006). It usually results in concrete spalling of the tunnel lining. Therefore, it is of importance to study the tunnel lining behaviour at elevated temperatures.

The influence of a fire on the relevant tunnel lining properties, e.g. elastic modulus, is firstly introduced and then its effect on the behaviour of the tunnel lining is presented.

To study the fire effect on the tunnel lining forces, it is assumed that the temperature of tunnel changes from 100 °C to 800 °C (Aslani and Samali, 2014). Since the temperature in a tunnel rises rapidly within a very short amount of time, the assumption that there is no enough time for tunnel lining to transmit the heat generated by fire to the surrounding soil is considered. Therefore, the additional thermal load from soil is neglected in the analysis of fire case.

In addition, Guo et al. (2010) studied the fire thermal stress of twin-tube tunnels assuming that the coefficient of thermal expansion of the tunnel structure is not sensitive to temperature. This assumption is also adopted in the analysis.

4.1 Effect of a fire on the lining elastic modulus

Tunnel lining is usually prefabricated by steel fibre reinforced concrete (SFRC). Many studies on the degradation of tunnel lining concrete when it is exposed to high temperature have been reported. When studying the effect of elevated temperatures on the behaviour of reinforced concrete, Aslani and Samali (2014) developed a constitutive relationship for high strength SFRC subjected to fire. The relationship was proposed to evaluate the elasticity modulus of SFRC at elevated temperatures using regression analyses conducted on experimental data. This relationship is adopted in the following analysis (Fig. 7-8), which is expressed as:

$$E_T = E \cdot \left\{ \begin{array}{ll} 1.0 & 20^\circ\text{C} \\ 1.1344 - 0.0017T + 5 \cdot 10^{-7}T^2 & 100^\circ\text{C} \leq T \leq 800^\circ\text{C} \end{array} \right\} \quad (7-7)$$

where E_T is the lining elastic modulus at different temperatures; E is the lining elastic modulus at the room temperature.

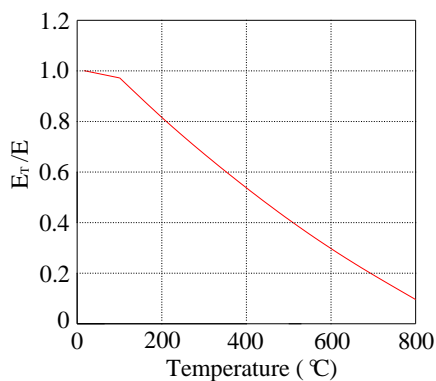


Fig. 7-8 Young's modulus lining used in analysis (Aslani and Samali, 2014)

4.2 Effect of a fire on the tunnel lining forces

According to Kaundinya (2006), the damage of tunnels is caused particularly by the spontaneous development of great amounts of heat and aggressive fire gases. The EUREKA (1995) fire tests found that the maximum hot gas temperature in a tunnel cross section occurs at the tunnel crown. In addition, Section 3 has shown that the maximum forces caused by temperature changes occur at the tunnel crown. Therefore, this

section presents the effect of a fire on the tunnel lining forces and radial displacements at the tunnel crown, which is shown in Fig. 7-9. The other mechanical properties of lining and ground are given in Table 7-3.

It can be found from Fig. 7-9 that the maximum stresses occur when the temperature is approximately equal to 400°C during the fire event. The bending moments caused by a fire at the tunnel crown increase firstly with the increase of temperature when the temperature is lower than 300°C, then decrease when the temperature is over 300°C. Especially, when the temperature reaches 500°C, the induced bending moment becomes negative. Fig. 7-9b shows that the normal lining forces increase firstly and reach a peak of 6.80 MN/m when the temperature is equal to 400°C. However, the normal forces decrease as the temperature is over 400°C. This could be due to the fact that the lining elastic modulus decreases as the temperature increases. Consequently, thermal-induced stresses in the tunnel lining will decrease as seen in Fig. 10 c and d.

Fig. 7-9e shows that the radial displacements increase as the temperature increases. This also permits to explain why the lining forces increase firstly and then decrease with the increase of temperature. As the temperature increases, a greater proportion of the lining strain caused by the temperature change is converted into lining radial displacements.

Since the absolute values of the axial forces are significantly larger than the ones of bending moments, the intrados and extrados stresses of lining have the similar trend with normal forces.

It should be noted that for the parameters of lining used in this section (see Table 7-3), the maximum normal force which can be supported by the lining is equal to 7.75 MN/m and the maximum bending moment to 1250 kN. m/m. Since only the additional thermal load caused by temperature change is considered in this study, the earth active loads applied directly by the surrounding ground is not considered. If also considering earth active loads, the bending moment reaches 192.6 kN.m/m and the normal lining force is equal to 7.751 MN/m, when the temperature reaches 200°C. This normal force is superior to the maximum admissible lining value and then the structure will collapse if the temperature is over 200°C. The limit state of the structures is then verified for the design of such structures subjected to a thermal loading.

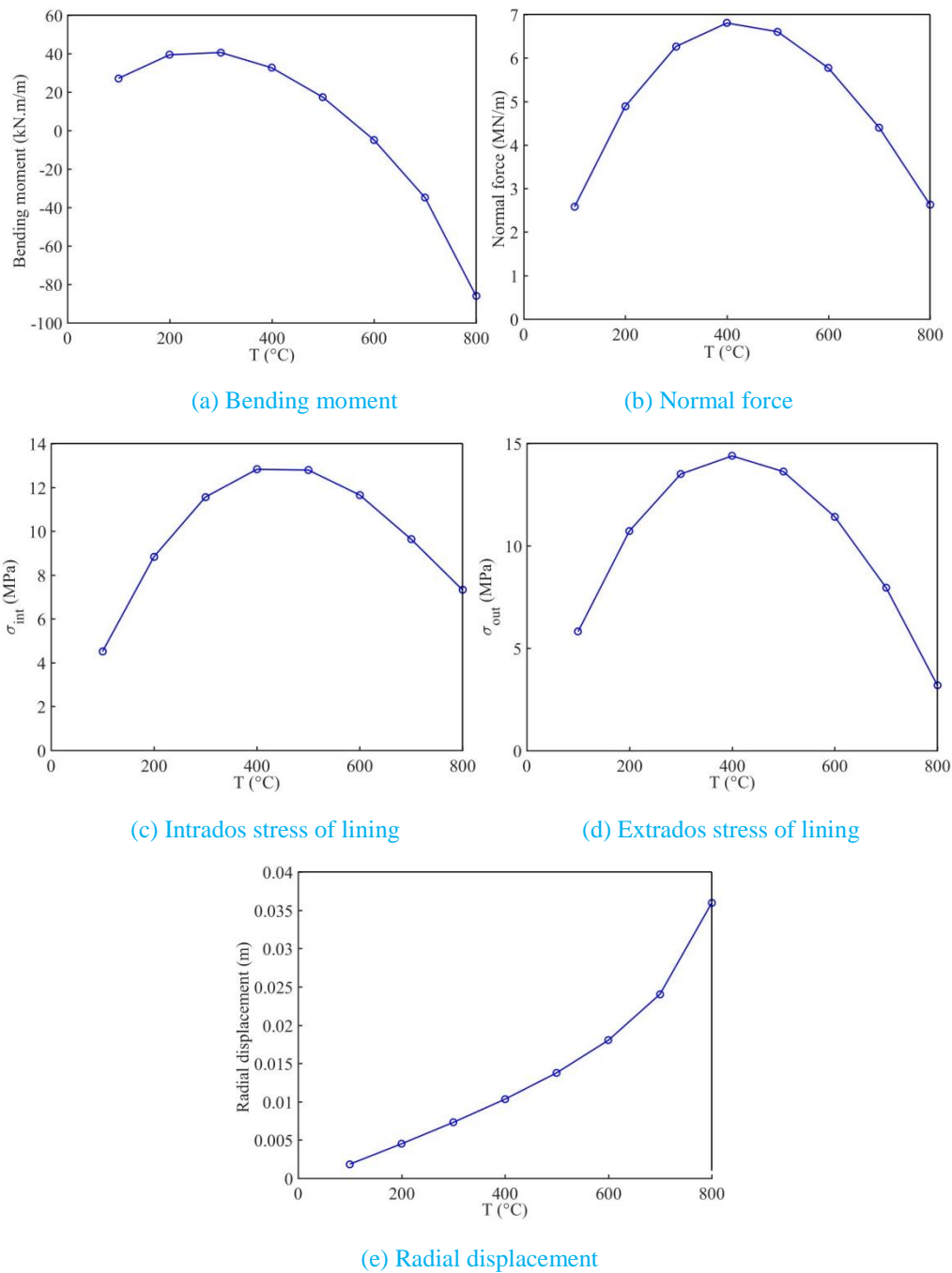


Fig. 7-9 Effect of the temperature change on the tunnel lining forces at the tunnel crown considering different coefficient of thermal expansion

In addition, it was observed (Hertz, 2003; Kaundinya, 2006) that the spalling of lining starts when the temperature rises during the first 5 minutes from the beginning of the fire event. Fig. 7-10 presents the ETK/ISO curve shown in Kaundinya (2006). It can be found from Fig. 7-10 that the temperature is over 400°C at the 5th minute when the spalling happens. Therefore, this paper permits to give a possible explanation from

the lining structural point of view. It provides that it is of importance to design tunnel collapses in the case of a fire event.

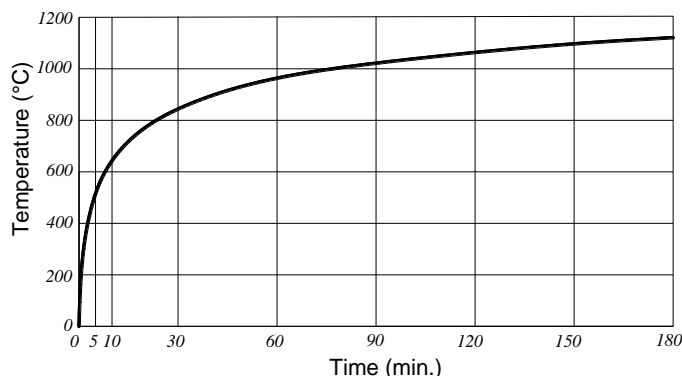


Fig. 7-10 Temperature-time ETK/ISO curve (Kaundinya, 2006)

In summary, the fire has a significantly negative influence on the tunnel lining. The first 5 minutes when the temperature can reach 400 °C represent the worst time for the tunnel lining. If the lining is subjected to fire without any protection, the tunnel lining damage will occur. Therefore, it requires that preventive measures should be taken to prevent fires. Kaundinya (2006) proposed several possibilities of structural fire protection measures in tunnels: 1) high strength concrete with an extremely tight texture; 2) fire-proof panels installed on the outer side of the lining; 3) sprayed fire protection (e.g. fire-proof render); 4) novel concrete mixtures containing polypropylene fibers. Maraveas and Vrakas (2014) also presented a summary of the various prevention measures, e.g. thermal barrier, compressive stress control, supplementary reinforcement, choice of section type/shape.

5. Conclusions

This chapter presents an efficient way to estimate the effect of a temperature change on the tunnel lining behaviour on the basis of the HRM method. The effective strain coefficient β_{Tl} of lining is used to calculate the effective thermal lining stresses in a first step. This parameter is determined by *in-situ* results. Then the influence of the temperature change on the tunnel lining forces by means of the present method is investigated, considering different factors. Thereafter, the effect of a fire is also studied. Some conclusions are obtained:

- Cooling the lining leads to tensile forces, whereas heating the lining generates compressive forces;

- The normal forces caused by the temperature change have a low fluctuation along the whole tunnel. In contrast, the caused bending moments change greatly along the whole lining. The maximum absolute bending moment values occur at the tunnel crown and invert;

- The absolute values of bending moments and normal forces increase with the increase of lining thickness, whereas the intrados and extrados stresses decrease as the lining thickness increases;

- The absolute forces values increase as the elastic modulus increases;

- The impact of the soil thermal expansion coefficient on the internal forces of lining is insignificant;

- The maximum forces occur when the temperature is approximately equal to 400°C in the case of a fire.

Clearly, the temperature change has a significant influence on the forces of a tunnel lining. Specially, a fire event could lead to a tunnel collapse.

GENERAL CONCLUSIONS

This manuscript focuses on the design of tunnel lining in terms of internal forces and displacements induced in the lining using the Hyperstatic Reaction Method (HRM).

Firstly, a HRM model is developed for the behaviour analysis of a U-shaped tunnel structure (with invert). The results of the HRM method are validated by comparing with the ones of numerical models using FLAC^{3D}. A comparison of two different active loads, constant and varying loads, is made. It has permitted to show that the absolute discrepancy of two solutions obtained from the two different loads is almost null when the cover-to-diameter $C/D = 3.0$. A parametric analysis is made to estimate the U-shaped tunnel support behaviour. It is shown that **1)** The higher the ground mass quality, the lower the support displacements, bending moments, shear forces and normal forces. **2)** The thicker the tunnel support, the lower the shear forces and tunnel support displacements, but the higher the normal forces and bending moments. **3)** The absolute values of the bending moments and normal forces increase with the increase of C/D . **4)** The larger the tunnel dimensions, the higher the impact of the support thickness on the shear forces and the higher the dependency of the shear forces with the C/D ratio.

Secondly, the behaviour of two different U-shaped tunnel linings (Geometry1 and Geometry2) is studied using the HRM method. A comparison of two different cases of springs, only normal springs, and normal plus shear springs, indicates that the spring type has a small effect on the internal forces and displacements of Geometry2. The effect of constraint conditions on the lining behaviour of Geometry2 is discussed. One can find that the effect of constraint conditions on the bending moments, shear forces, and radial displacements at the tunnel sidewall should not be neglected. The comparison of the results between circular and two U-shaped tunnels show that the internal forces and displacements obtained from the three different geometries have the similar trend at the tunnel crown. However, the bending moments and shear forces have not only a similar trend, but also approximately the same values at the tunnel crown and sidewall for Geometry 1 and Geometry2. Also, the trends of the internal forces and displacements obtained from the circular tunnel are smoother than that of Geometry1 and Geometry2 cases at the tunnel sidewall and invert arch.

Thirdly, the effect of horizontally multi-layered soil conditions on the U-shaped tunnel behaviour is studied by the HRM method. Two different geometries and multi-layered soil conditions are considered. The

results of HRM have a good agreement with the numerical ones. The influence of multi-layered soil conditions on the U-shaped tunnel lining behaviour is presented. The analysis permits to show the effect of the constraint types on the behaviour of U-shaped tunnel without invert arch. The obtained results highlight that **1)** the normal forces and displacements obtained from Geometry2 almost have the similar trend compared with the one of Geometry1. **2)** The effect of constraint types on the internal forces and displacements of tunnel linings can be neglected at the tunnel crown. However, their effect on the bending moments, shear forces, and radial displacements at the tunnel sidewall should be considered. **3)** The effect of the relative thickness t/D of the mid-layer (layer2) on the bending moments and displacements at the tunnel crown are not significant. However, the relative thickness t/D of the mid-layer has a great effect on the lining behaviour at the tunnel sidewall. **4)** The influence of the position of the mid-layer is significant on the tunnel behaviour. Generally, the greater the depth of the mid-layer, the smaller the absolute values of the normal forces, but the higher the absolute values of the bending moments, shear forces and normal displacements at the tunnel crown.

Fourthly, the effect of a surface loading on a horseshoe shaped tunnel in a saturated soil mass is studied using the HRM method. Comparisons between the results of the HRM and numerical ones have permitted to validate the HRM method. Parametric studies have permitted to investigate the influence of the surface loadings and pore water pressures on the tunnel behaviour: **1)** the absolute values of the internal forces or displacements when considering the pore water pressure are always higher than the ones without considering the pore water pressure. **2)** Whether or not considering the pore water pressure, the surcharge loading has a significantly impact on the normal forces and radial displacements. However, the effect of the surcharge loading on the bending moments can be negligible. **3)** The phreatic surface position greatly influences the internal forces and displacements. In contrast, its effect on the bending moments is only visible at the tunnel sidewall. In general, the normal forces and radial displacements of the lining are more sensitive to the water pressure, surcharge loading, surcharge loading width and phreatic surface position than the bending moments.

Fifthly, the optimization process of sub-rectangular tunnel is presented on the basis of the HRM method. A series of mathematical functions used in the optimization progress of sub-rectangular tunnel shapes are deduced. According to the mathematical formulas, the effect of different parameters, like the lateral earth pressure coefficient, soil Young's modulus, tunnel depth, surface loads, on the internal forces and shape of sub-rectangular tunnels is investigated. It is shown that **1)** the optimum R_3 of sub-rectangular tunnel increases

rapidly and then decreases slowly as the tunnel depth C/D_0 increases. The internal forces of sub-rectangular tunnels increase with the increase of C/D_0 . **2)** The optimum R_3 of sub-rectangular tunnel decreases with the increase of K_0 when K_0 is lower than 1.25 and then increases with the increase of K_0 when K_0 is over 1.25. The bending moments of sub-rectangular tunnels decrease as K_0 increases. However, the normal forces of sub-rectangular tunnels increase as K_0 increases. **3)** The optimum R_3 of sub-rectangular tunnel decreases with the increase of E_s . The internal forces of sub-rectangular tunnel decrease with the increase of E_s . **4)** The internal forces of sub-rectangular tunnel increase with the increase of surface load P_0 . The influence of P_0 on the internal forces of sub-rectangular tunnel is closely related to the values of C/D_0 . As the increase of C/D_0 , the influence of P_0 on the internal forces is less obvious. Specially, the impact of P_0 on the shape of sub-rectangular tunnel disappears as C/D_0 is over 10.

At the end of this manuscript, a thermo-mechanical analysis of the tunnel lining behaviour is presented using the HRM method. The effective strain coefficient β_{Tl} of lining is used to calculate the effective thermal lining stresses. Then the influence of the temperature change on the tunnel lining forces by means of the present method is investigated. Thereafter, the effect of a fire is studied. Some conclusions are obtained: **1)** Cooling the lining leads to tensile forces, whereas heating the lining generates compressive forces. **2)** The normal forces caused by the temperature change have a low fluctuation along the whole tunnel. In contrast, the bending moments change greatly along the whole lining. The maximum absolute bending moment values occur at the tunnel crown and invert. **3)** The absolute values of bending moments and normal forces increase with the increase of the lining thickness, whereas the intrados and extrados stresses decrease as the lining thickness increases. **4)** The absolute forces values increase as the elastic modulus increases. **5)** The impact of the soil thermal expansion coefficient on the internal forces of lining is insignificant. **6)** The maximum forces occur when the temperature is approximately equal to 400°C in the case of a fire.

In conclusion, this research work presents the design of tunnel linings based on the HRM method. It focuses on the analysis of U-shaped tunnel behaviour in terms of internal forces and displacements of lining under different conditions, the optimization of sub-rectangular tunnel shape, and the effect of temperature change on circular tunnel lining behaviour. This thesis has permitted to show that the HRM method is particularly suitable for the estimation of the tunnel lining behaviour, in terms of structural forces and lining

displacements along the support profile. This research can provide valuable references for the related tunnel designers at the preliminary design.

REFERENCES

- AFTES. (2011). Recommendations on the Convergence Confinement Method.
- Amatya, B., Soga, K., & Bourne-Webb, P. J. (2012). Thermo-mechanical behaviour of energy piles. *Géotechnique*, 62(6), 503–519.
- Andre P. A., (2004). Development of Urban Underground Infrastructures in the world. Lecture presented by ITA Past-President in 18th National TAC Conference, Edmonton Canada.
- Aslani, F., & Samali, B. (2014). Constitutive relationships for steel fibre reinforced concrete at elevated temperatures. *Fire Technology*, 50(5), 1249-1268.
- Barla, M., & Di Donna, A. (2018). Energy tunnels: concept and design aspects. *Underground Space*, 3(4), 268-276.
- Barpi, F., Barbero, M., & Peila, D. (2011). Numerical modelling of ground-tunnel support interaction using bedded-beam-spring model with fuzzy parameters. *Gospodarka Surowcami Mineralnymi*, 27, 71-87.
- Bobet, A. (2003). Effect of pore water pressure on tunnel support during static and seismic loading. *Tunnelling and Underground Space Technology*, 18, 377–393.
- Bobet, A. (2011). Lined circular tunnels in elastic transversely anisotropic rock at depth. *Rock mechanics and rock engineering*, 44(2), 149-167.
- Bourne-Webb, P. J., Bodas Freitas, T. M., & Freitas Assunção, R. M. (2015). Soil–pile thermal interactions in energy foundations. *Géotechnique*, 66(2), 167-171.
- Bian, K., Xiao, M. and Chen, J. T. (2009). Study on coupled seepage and stress fields in the concrete lining of the underground pipe with high water pressure. *Underground Space Technology*, 24, 287–295.
- Bishop, A. W. (1954). The use of pore-water coefficients in practice. *Géotechnique*, 4(4), 148–152.
- Bishop, A. W., & Morgenstern, N. (1960). Stability coefficients for earth slopes. *Géotechnique*, 10(4), 129–153.
- British Tunnelling Society. Tunnel Lining Design Guide. *Institution of Civil Engineers (Great Britain)*, 4.6.1 Effects of tunnel type and shape.
- Brown, E. T., Bray, J. W., Ladanyi, B., & Hoek, E. (1983). Ground response curves for rock tunnels. *Journal of Geotechnical Engineering*, 109(1), 15-39.

- Ding, W. Q., Duan, C., Zhu, Y. H., Zhao, T. C., Huang, D., & Li, P. (2019). The behaviour of synchronous grouting in a quasi-rectangular shield tunnel based on a large visualized model test. *Tunnelling and Underground Space Technology*, 83, 409–424.
- Do, N. A., Dias, D., Oreste, P., & Djeran-Maigre, I. (2014a). 2D tunnel numerical investigation: the influence of the simplified excavation method on tunnel behaviour. *Geotechnical and Geological Engineering*, 32(1), 43-58.
- Do, N. A., Dias, D., Oreste, P., & Djeran-Maigre, I. (2014b). A new numerical approach to the hyperstatic reaction method for segmental tunnel linings. *International Journal for Numerical and Analytical Methods in Geomechanics*, 38(15), 1617-1632.
- Do, N. A., Dias, D., Oreste, P., & Djeran-Maigre, I. (2014c). Three-dimensional numerical simulation of a mechanized twin tunnels in soft ground. *Tunnelling and Underground Space Technology*, 42, 40-51.
- Do, N. A., Dias, D., Oreste, P., & Djeran-Maigre, I. (2014d). The behaviour of the segmental tunnel lining studied by the hyperstatic reaction method. *European Journal of Environmental and Civil Engineering*, 18(4), 489-510.
- Do, N. A., & Dias, D. (2017). A comparison of 2D and 3D numerical simulations of tunnelling in soft soils. *Environmental Earth Sciences*, 76(3), 102.
- Do, N. A., Dias, D., & Oreste, P. (2018). Simplified Approach to the Design of Segmental Tunnel Linings. *Proceedings of ICE - Geotechnical Engineering*, 171(3), 209-214.
- Du, D. C., Dias D., & Yang, X. (2018). Analysis of earth pressure for shallow square tunnels in anisotropic and nonhomogeneous soils. *Computers and Geotechnics*, 104, 226-236.
- Duddeck, H., & Erdmann, J. (1985). Structural design models for tunnels in soft soil. *Underground Space*; (United States), 9, 246–259.
- Duddeck, H. (1988). Guidelines for the design of tunnels. *Tunnelling and Underground Space Technology*, 3(3), 237–249.
- Einstein, H. H., & Schwartz, C. W. (1979). Simplified analysis for tunnel supports. *Journal of Geotechnical and Geoenvironmental Engineering*, 105(4), 499–518.
- Eman, A. E., Gouda, A., Hesham, F. & Khaled, A. H. (2013). Behaviour of different shapes of twin tunnels in soft clay soil. *International Journal of Engineering and Innovative Technology*, 2(7), 297–302.
- EUREKA. (1995). Project EU 499 FIRETUN; Fires in Transport Tunnels; Report on Full-Scale Tests; editor: Studiengesellschaft Stahlanwendung e.V., Düsseldorf.

- González-Nicieza, C., Alvarez-Vigil, A. E., Menendez-Diaz, A., & Gonzalez-Palacio, C. (2008). Influence of the depth and shape of a tunnel in the application of the convergence-confinement method. *Tunnelling and Underground Space Technology*, 23, 25–37.
- Grant, R. J., & Taylor, R. N. (2000). Stability of tunnels in clay with overlying layers of coarse grained soil. In: *GeoEng 2000: An International Conference on Geotechnical & Geological Engineering*, Melbourne, Australia.
- Guo, J., Jiang, S. P., & Zhang, Z.Y. (2016). Fire thermal stress and its damage to subsea immersed tunnel. *Procedia Engineering*, 166, 296-306.
- Hagiwara, T., Grant, R. J., & Calvello, M. (1999). The effect of overlying strata on the distribution of ground movements induced by tunnelling in clay. *Soils and Foundations*, 39(3), 63–73.
- Hertz, K. D. (2003). Limits of spalling of fire-exposed concrete. *Fire safety journal*, 38(2), 103-116.
- Hoek, E., & Brown, E. T. (1980). *Underground Excavations in Ground*. The Institution of Mining and Metallurgy, London, 527.
- Huang, X., Zhu, Y., Zhang, Z., Zhu, Y., Wang, S., & Zhuang, Q. (2018). Mechanical behaviour of segmental lining of a sub-rectangular shield tunnel under self-weight. *Tunnelling and Underground Space Technology*, 74, 131-144.
- Huebner, K. H., Dewhirst, D. L., Smith, D. E., & Byrom, T. G. (2001). *The Finite Element Method for Engineers*. John Wiley and Sons, inc, New York.
- ITA-Group2 (2000). Guidelines for the design of shield tunnel lining. *Tunnelling and Underground Space Technology*, 15(3), 303-331.
- International Tunnelling Association (ITA). Guidelines for structural fire resistance for road tunnels. 2004.
- Itasca Consulting Group Inc. (2012). *FLAC3D fast Lagrangian analysis of continua in 3 Dimensions (Version 5.0)*. User's manual. Minneapolis, MN: Author.
- Katebi, H., Rezaei, A. H., & Hajjalilue-Bonab, M. (2013). The influence of surface buildings and ground stratification on lining loads applying the finite element method. *Electronic Journal of Geotechnical Engineering*, 18, 1845–1861.
- Katebi, H., Rezaei, A. H., Hajjalilue-Bonab, M., & Tarifard, A. (2015). Assessment the influence of ground stratification, tunnel and surface buildings specifications on shield tunnel lining loads (by FEM). *Tunnelling and Underground Space Technology*, 49, 67–78.
- Kaundinya I. (2006). Protection of road tunnel linings in cases of fire /Federal Highway.
- Lanka, S. (2018). Guideline for design of road tunnel. Japan International Cooperation Agency (JICA).

- Leca, E., & Clough, G. W. (1992). Preliminary design for NATM tunnel support in soil. *Journal of geotechnical engineering*, 118(4), 558-575.
- Lee, I. M., & Nam, S. W. (2001). The study of seepage forces acting on the tunnel lining and tunnel face in shallow tunnels. *Tunnelling and Underground Space Technology*, 16(1), 31-40.
- Li, G.X., Zhang, B.Y., & Yu, Y.Z. (2013). Soil Mechanics. Beijing: Tsinghua University Press, 1-366.
- Li, J. (2017). Key Technologies and Applications of the Design and Manufacturing of Non-Circular TBMs. *Engineering*, 3(6), 905-914.
- Li, P. F., Fang, Q., & Zhang, D. L. (2014). Analytical solutions of stresses and displacements for deep circular tunnels with liners in saturated ground. *Journal of Zhejiang University SCIENCE A*, 15(6), 395-404.
- Liu, X., Liu, Z., Ye, Y., Bai, Y., & Zhu, Y. (2018). Mechanical behaviour of quasi-rectangular segmental tunnel linings: Further insights from full-scale ring tests. *Tunnelling and Underground Space Technology*, 79, 304-318.
- Luo, Y. B., Chen, J. X., Qiao, X., & Wang, M. S. (2010). Mechanics state analysis of secondary lining concrete structure on tunnel based on temperature effect. *China Journal of Highway and Transport*, 23(2), 64-69.
- Maraveas, C., & Vrakas, A. A. (2014). Design of concrete tunnel linings for fire safety. *Structural Engineering International*, 24(3), 319-329.
- Mashimo H, Ishimura T (2005) Numerical modelling of the behaviour of shield tunnel support during assembly of a tunnel ring. In: 5th International Symposium Geotechnical Aspects of Underground Construction in Soft Ground.
- Miranda, T., Dias, D., Pinheiro, M. and Eclaircy-Caudron S. (2015), Methodology for real-time adaptation of tunnels support using the observational method. *Geomechanics and engineering*, 8(2), 153-171.
- Molins, C., & Arnau, O. (2011). Experimental and analytical study of the structural response of segmental tunnel linings based on an in situ loading test. Part 1: Test configuration and execution. *Tunnelling Underground Space Technol.*, 26(6), 764-777.
- Möller, S. C. (2006). Tunnel induced settlements and structural forces in linings. Ph.D. thesis, Univ. Stuttgart, Inst. f. Geotechnik, Stuttgart, Germany.
- Möller S. C., & Vermeer P. A. (2008). On numerical simulation of tunnel installation. *Tunnelling and Underground Space Technology*, 23, 461-475.

- Nakamura, H., Kubota, T., Furukawa, M., & Nakao, T. (2003). Unified construction of running track tunnel and crossover tunnel for subway by rectangular shape double track cross-section shield machine. *Tunnelling and underground space technology*, 18(2-3), 253-262.
- Nam, S. W., & Bobet, A. (2006). Liner stresses in deep tunnels below the water table. *Tunnelling and Underground Space Technology*, 21(6), 626-635.
- Nicholson, D. P., Chen, Q., de Silva, M., Winter, A., & Winterling, R. (2014). The design of thermal tunnel energy segments for Crossrail, UK. *In Proceedings of the Institution of Civil Engineers-Engineering Sustainability*, 167(3), 118-134.
- Nunes, M. A., & Meguid, M. A. (2009). A study on the effects of overlying soil strata on the stresses developing in a tunnel lining. *Tunnelling and Underground Space Technology*, 24(6), 716-722.
- O'Rourke, T. D. (1984). Guidelines for tunnel lining design. *American Society of Civil Engineers*, Reston, Va.
- Oreste, P. P. (2003). Analysis of structural interaction in tunnels using the convergence–confinement approach. *Tunnelling and Underground Space Technology*, 18(4), 347-363.
- Oreste, P. P. (2007). A numerical approach to the hyperstatic reaction method for the dimensioning of tunnel supports. *Tunnelling and Underground Space Technology*, 22(2), 185-205.
- Oreste, P., Dias, D. (2012) Stabilisation of the excavation face in shallow tunnels using fibreglass dowels. *Ground mechanics and ground engineering*, 45(4), 499-517.
- Pan, Q., & Dias, D. (2017). Upper-bound analysis on the face stability of a non-circular tunnel. *Tunnelling and Underground Space Technology*, 62, 92-102.
- Panet, M. (1995). Le calcul des tunnels par la méthode convergence confinement. Presses de l'école nationale des Ponts et chaussées, Paris.
- Prasetyo, S. H., & Gutierrez, M. (2016). Effect of surface loading on the hydro-mechanical response of a tunnel in saturated ground. *Underground Space*, 1(1), 1-19.
- Peck, R. B. (1969). Deep excavations and tunnelling in soft ground-state of the art. *In Proceedings of the 7th International Conference on Soil Mechanics and Foundation Engineering*, State of the Art Volume, 225–290.
- Plizzari, G. A., & Tiberti, G. (2006). Steel fibers as reinforcement for precast tunnel segments. *Tunnelling and Underground Space Technology*, 21(3), 438-439.

- Shin, J. H., Potts, D. M., & Zdravkovic, L. (2005). The effect of porewater pressure on NATM tunnel linings in decomposed granite soil. *Canadian Geotechnical Journal*, 42, 1585–1599.
- Takano, Y. H. (2000). Guidelines for the design of shield tunnel lining. *Tunnelling and Underground Space Technology*, 15(3), 303-331.
- TCVN. Hàm đường sắt và hàm đường ô tô - Tiêu chuẩn thiết kế. 4527-1988
- ÜÇER, S. (2006) Comparison of 2D and 3D finite element models of tunnel advance in soft ground: A case study on Bolu tunnels. Thesis, Middle East Technical University.
- Voeltzel, A., & Dix, A. (2004). A comparative analysis of the Mont Blanc, Tauern and Gotthard tunnel fires. *Routes/Roads*, 17, 129-132.
- Yang, X. L., & Du, D. C. (2016). Upper bound analysis for bearing capacity of nonhomogeneous and anisotropic clay foundation. *KSCE Journal of Civil Engineering*, 20, 2702-2710.
- Yang, X. L., & Yao, C. (2017). Axisymmetric failure mechanism of a deep cavity in layered soils subjected to pore pressure. *International Journal of Geomechanics*, 17(8), 04017031.
- Yang, X. L., & Yan, R. M. (2015). Collapse mechanism for deep tunnel subjected to seepage force in layered soils. *Geomechanics and Engineering*, 8(5), 741-756.
- Yin, L., & Yang, W. (2000). Topology optimization for tunnel support in layered geological structures. *International Journal for Numerical Methods in Engineering*, 47, 1983–1996.
- Yoon, J., Han, J., Joon, E., & Shin, J. (2014). Effects of Tunnel Shapes in Structural and Hydraulic Interaction. *KSCE Journal of Civil Engineering*, 18(3), 735–741.
- Zhang, D. M., Huang, H. W., Hu, Q. F., & Jiang, F. (2015). Influence of multi-layered soil formation on shield tunnel lining behaviour. *Tunnelling and Underground Space Technology*, 47, 123-135.
- Zhu, Y. T., Zhu, Y. F., Zhang, Z. X., & Huang, X. (2018). Computational model and mechanical characteristics of linings of special-shaped shield tunnels. *Chinese Journal of Geotechnical Engineering*, 40(7), 1230-1236.